FRACTURE MECHANICS

NESTOR PEREZ

FRACTURE MECHANICS

This page intentionally left blank

FRACTURE MECHANICS

by

Nestor Perez
Department of Mechanical Engineering
University of Puerto Rico

Created in the United States of America

Visit Kluwer Online at: http://kluweronline.com
and Kluwer's eBookstore at: http://ebooks.kluweronline.com

Contents

Foreword

I had the pleasure and the privilege of reading the original book, particularly some of the important chapters of the book on Fracture Mechanics by Dr. Nestor Perez. I find the book, in general, very well written for the academicians as well as for the practitioners in the field of engineering fracture mechanics. The language is simple, clear and to the point. Each chapter is developed in such a way that the mathematical treatment supports the main physical mechanism of fracture. The equations are arranged in an orderly fashion in harmony with the descriptive concepts of a phenomenon that is highly complex, very nonlinear and often unpredictable. The main objective of a mathematical analysis is to explain and clarify a physical phenomenon, and definitely not to jeopardize it by undue and unwanted complexity at the cost of brevity. If this is true for a textbook or any treatise for that matter, Dr. Perez's book has done the job quite elegantly.

This book is suitable as a textbook for a senior undergraduate and graduate textbook of a one-semester course in Mechanical, Civil, Chemical and Industrial Engineering, Materials Science as well as in Applied Physics and Applied Chemistry programs.

Each chapter is self-contained and self-sufficient in descriptive details, but it keeps a smooth continuity with its preceding and following chapters. The numerical and the algebraic illustrations are just in place with the theoretical analyses and the empirical examples. Unlike many voluminous works on fracture mechanics, in this book mathematics does not overburden the physics of fracture mechanics, and thus shows a more realistic route to solve a particular problem. Hence, practicing engineers in consulting firms and design offices can use this book in a very handy and straightforward fashion. Also it is a good reference book in the personal library of many retired professionals and professors who still like to keep in touch with the reality as a hobby, pastime or pleasure.

I highly recommend this book to any technical publishing house for the timely birth of this solid but simple work on engineering fracture mechanics.

Jay K. Banerjee, Ph.D., P.E., M.Ed.
Editor (2003)
Journal of Mechanical Behavior of Materials

This page intentionally left blank

Preface

The purpose of this book is to present, in a closed form, analytical methods in deriving stress and strain functions related to Fracture Mechanics. This book contains a compilation of work available in the literature in a scatter form and, to a certain extent, selected experimental data of many researchers to justify the theoretical fracture mechanics models in solving crack problems. It is a self-contained and detailed book for the reader (senior and graduate students, and engineers) involved in the analysis of failure using a mathematical approach for designing against fracture. However, it is important that the reader understands the concept of modeling, problem solving, and interpreting the meaning of mathematical solution for a particular engineering problem or situation. Once this is accomplished, the reader should be able to think mathematically, foresee metallurgically the significance of microstructural parameters on properties, analyze the mechanical behavior of materials, and recognize realistically how dangerous a crack is in an stressed structure, which may fail catastrophically.

In spite of the advances in fracture mechanics, many principles remain the same. Dynamic Fracture Mechanics is included through the field of fatigue and Charpy impact testing. The material included in this book is based upon the development of analytical and numerical procedures pertinent to particular fields of linear elastic fracture mechanics (LEFM) and plastic fracture mechanics (PFM), including mixed-mode-loading interaction. The mathematical approach undertaken herein is coupled with a brief review of several fracture theories available in cited references.

Fracture mechanics of engineering materials deals with fracture of solids undergoing large deformation (ductile materials) and/or fracture (brittle material) when subjected to extreme loading. The analysis of a solid responding to loads is concerned partly with microscopic mechanisms of fracture, establishing fracture criteria, and predicting the fracture stress from a macroscopic approach.

Nestor Perez, Ph.D.
Department of Mechanical Engineering
University of Puerto Rico, Mayaguez, PR 00680

This page intentionally left blank

Dedication

To my wife Neida

    To my daughters Jennifer and Roxie

    To my son Christopher

This page intentionally left blank

Chapter 1

THEORY OF ELASTICITY

1.1   INTRODUCTION

The definition of variables such as force, load, stress, strain, and displacement is vital for the understanding of state properties of solid materials, and for characterizing the mechanical behavior of crack-free or cracked solids. Clearly, the latter have a different mechanical behavior than the former and it is characterized according to the principles of fracture mechanics, which are divided into two areas. Linear Elastic Fracture Mechanics (LEFM) considers the fundamentals of linear elasticity theory, and Plastic Fracture Mechanics (PFM) is for characterizing plastic behavior of ductile solids. In order to characterize cracked solids, knowledge of the aforementioned variables is necessary. For instance, the term dynamic force defined by Newton's second law as $F = ma$, depends on the acceleration of a moving mass.

However, if this mass is stationary and susceptible to be deformed a quasi-static force or mechanical force must be defined. Both dynamic and mechanical forces have the same units, but different physical meaning. Moreover, this mechanical force is analogous to load (P). Obviously, this is the point of departure in this chapter for defining an important engineering parameter called elastic stress, $\sigma = P/A$, which in turn it is related to Hooke's law as $E = \sigma/\epsilon$. Then, ϵ is the elastic strain and E is the elastic modulus of elasticity.

Now, the strain is defined as $\epsilon = d\mu/dx$ where $d\mu$ is the change of displacement, say, in the x-direction. The intent here is to indicate how certain parameters or variables are related to one another. Nevertheless, if two variables are known, the third one can be estimated or predicted. This is one of the benefits of mathematics for solving engineering problems, which have their own constraints for dictating the magnitude of a particular variable. In fact, one or more variables may define a material property, while a property depends on the microstructure of a solid material.

1.2   DEFINITIONS

This section is concerned with some definitions the reader needs to assimilate before the fracture mechanics theories and mathematical definitions are introduced in a progressive manner. It is important to have a clear and precise definition of vital concepts in the field of applied mechanics so that the learning process for understanding fracture mechanics becomes obviously easy. However, basic concepts such as stress, strain, safety factor, deformation and the like are important in characterizing the mechanical behavior of solid materials subjected to forces or loads in service. Hence,

DEFORMATION: The movement of points in a solid body relative to each other.

DISPLACEMENT: The movement of a point in a vector quantity in a body subjected to loading.

STRAIN: This is a geometric quantity, which depends on the relative movement of two or three points in a body.

STRESS: The stress at a point on a body represents the internal resistance of a body due to an external force. Thus, load (P) and the cross-sectional area (A) are related to stress as indicated by the equation of equilibrium of forces. Thus,

$$\sum F_y \; = \; P - \sigma A = 0 \tag{1.1}$$

$$\sigma \; = \; \frac{P}{A} \tag{1.2}$$

If A is the original cross-sectional area (A_o), then σ is an engineering stress; otherwise, it is a local stress. In addition, the theory of elasticity deals with isotropic materials subjected to elastic stresses, strains, and displacements. The relationships between stresses and strains are known as constitutive equations, which are classified as Equilibrium Equations, Compatibility Equations and Boundary equations. The reader should consult a book on Theory of Elasticity [1].

Safety Factor: This is an important parameter used in designing structural components to assure structural integrity. Simply stated, the safety factor is a design factor defined by [2]

$$Stress = \frac{Strength}{S_F} \qquad \text{For } S_F > 1 \tag{1.3}$$

Here, the strength may represent a material's property, such as the yield strength, and the stress is the variable to be applied to a structure. The role of S_F in this simple relationship is to control the design stress so that

Usually, the safety factor is in the order of two, but its magnitude depends on the designer's experience.

1.3 STRAIN AND STRESS EQUATIONS

According to the theory of elasticity, the field equations are based on the normal strains (ϵ_{ij}) and the shear strains (γ_{ij}). These are related to displacements, which are illustrated in Figures 1.1 and mathematically defined by
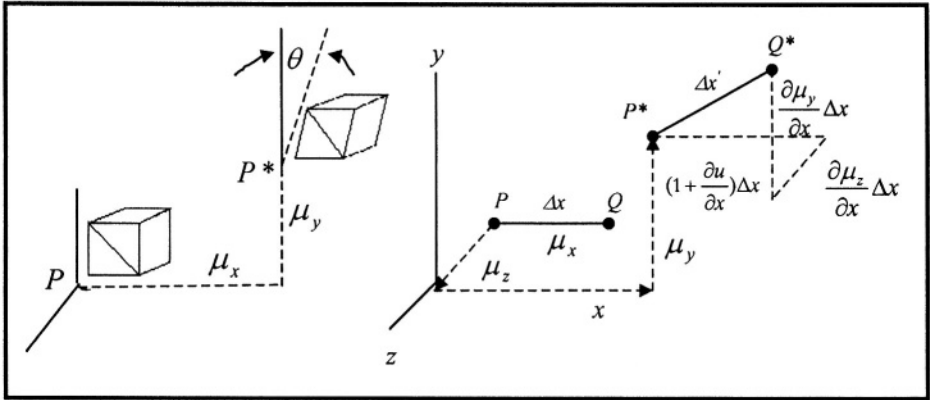
Figure 1.1 Distortion of a solid body

$$
\begin{aligned}
\epsilon_{xx} &= \frac{\partial \mu_x}{\partial x} & \gamma_{xy} &= \frac{\partial \mu_y}{\partial x} + \frac{\partial \mu_x}{\partial y} = \frac{\tau_{xy}}{G} \\
\epsilon_{yy} &= \frac{\partial \mu_y}{\partial y} & \gamma_{yz} &= \frac{\partial \mu_z}{\partial y} + \frac{\partial \mu_y}{\partial z} = \frac{\tau_{yz}}{G} \qquad (1.4) \\
\epsilon_{zz} &= \frac{\partial \mu_z}{\partial z} & \gamma_{zx} &= \frac{\partial \mu_x}{\partial z} + \frac{\partial \mu_z}{\partial x} = \frac{\tau_{zx}}{G}
\end{aligned}
$$

where G = Shear modulus (MPa)

According to the theory of elasticity, stresses and strains are generalized as $\epsilon_{ij} = f(\sigma_{ij})$, $\gamma_{ij} = f(\tau_{ij})$, $\sigma_{ij} = f(\epsilon_{ij})$, and $\tau_{ij} = f(\gamma_{ij})$. These quantities are treated as second-rank tensors and the matching mathematical framework of tensor analysis can be found elsewhere [3-4]. It is not intended herein to review the theory of elasticity, but include simplified forms of stresses and strains so that the reader is reminded about the use of these second-rank tensors as powerful tools for solving engineering problems or situations.

Problems, whose solutions require the analysis of stresses, strains, and displacements, are normally encountered in engineering structures, which are susceptible to develop dangerous cracks during service. Thus, it is important to visualize the stresses and strains as tridimensional entities that develop around discontinuities in microstructures, such as dislocations, composite materials, and uniquely in the vicinity of a crack tip due to an applied external loading

system. For instance, the resultant stresses in a three-dimensional element are shown in Figure 1.2. At equilibrium, the shear stresses are related as $\tau_{xy} = \tau_{yx}$, $\tau_{yz} = \tau_{zy}$ and $\tau_{zx} = \tau_{xz}$, and the tensile stresses are σ_{xx}, σ_{yy} and σ_{zz}.
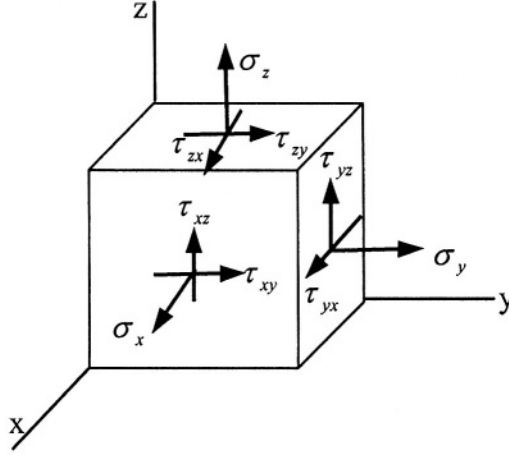
Figure 1.2 Three-dimensional stress element.

1.4 TRIAXIAL STRESS STATE

According to Hooke's law for isotropic solid materials, the strain components and the related elastic stresses are defined below as mathematical formulas. Hence, the tridimensional entities are

$$
\begin{aligned}
\epsilon_{xx} &= \frac{\sigma_{xx}}{E} & \epsilon_{yy} = \epsilon_{zz} &= -\frac{v\sigma_{xx}}{E} \\
\epsilon_{yy} &= \frac{\sigma_{yy}}{E} & \epsilon_{xx} = \epsilon_{zz} &= -\frac{v\sigma_{yy}}{E} \\
\epsilon_{zz} &= \frac{\sigma_{zz}}{E} & \epsilon_{xx} = \epsilon_{yy} &= -\frac{v\sigma_{zz}}{E} \\
v &= -\frac{\epsilon_{yy}}{\epsilon_{xx}} = -\frac{\epsilon_{zz}}{\epsilon_{xx}}
\end{aligned}
\tag{1.5}
$$

where $v =$ Poisson's ratio

Using the **Principle of Superposition**, the total stain and stress in one direction become

$$
\begin{bmatrix} \epsilon_{xx} \\ \epsilon_{yy} \\ \epsilon_{zz} \end{bmatrix} = \frac{1}{E} \begin{bmatrix} \sigma_{xx} - v(\sigma_{yy} + \sigma_{zz}) \\ \sigma_{yy} - v(\sigma_{xx} + \sigma_{zz}) \\ \sigma_{zz} - v(\sigma_{xx} + \sigma_{yy}) \end{bmatrix}
\tag{1.6}
$$

For convenience, the stresses as function of strains may be defined in a matrix form as indicated below. The stresses along the principal axes are

$$\begin{bmatrix} \sigma_{xx} \\ \sigma_{yy} \\ \sigma_{zz} \end{bmatrix} = \frac{E}{(1+v)(1-2v)} \begin{bmatrix} (1-v)\,\epsilon_{xx} + v\,(\epsilon_{yy} + \epsilon_{zz}) \\ (1-v)\,\epsilon_{yy} + v\,(\epsilon_{xx} + \epsilon_{zz}) \\ (1-v)\,\epsilon_{zz} + v\,(\epsilon_{xx} + \epsilon_{yy}) \end{bmatrix} \qquad (1.7)$$

and the shear stresses on planes axe

$$\begin{bmatrix} \tau_{xy} \\ \tau_{yz} \\ \tau_{zx} \end{bmatrix} = G \begin{bmatrix} \gamma_{xy} \\ \gamma_{yz} \\ \gamma_{zx} \end{bmatrix} = \frac{E}{2\,(1+v)} \begin{bmatrix} \gamma_{xy} \\ \gamma_{yz} \\ \gamma_{zx} \end{bmatrix} \qquad (1.8)$$

since the shear modulus of elasticity is

$$G = \frac{E}{2\,(1+v)} \qquad (1.9)$$

where E = Elastic modulus of elasticity (MPa)

1.5 BIAXIAL STRESS STATE

If $\sigma_{zz} = \tau_{zx} = \tau_{zy} = \gamma_{xz} = \gamma_{yz} = 0$, then the strain entities for the biaxial state are defined in matrix form

$$\begin{bmatrix} \epsilon_{xx} \\ \epsilon_{yy} \\ \epsilon_{zz} \end{bmatrix} = \frac{1}{E} \begin{bmatrix} \sigma_{xx} - v\sigma_{yy} \\ \sigma_{yy} - v\sigma_{xx} \\ \sigma_{xx} + \sigma_{yy} \end{bmatrix} \qquad (1.10)$$

$$\begin{bmatrix} \gamma_{xy} \\ \gamma_{xz} \\ \gamma_{yz} \end{bmatrix} = \frac{1}{G} \begin{bmatrix} \tau_{xy} \\ 0 \\ 0 \end{bmatrix} \qquad (1.11)$$

and the stresses are

$$\begin{bmatrix} \sigma_{xx} \\ \sigma_{yy} \\ \sigma_{zz} \end{bmatrix} = \frac{E}{(1-v^2)} \begin{bmatrix} \epsilon_{xx} + v\epsilon_{yy} \\ \epsilon_{yy} + v\epsilon_{xx} \\ 0 \end{bmatrix} \qquad (1.12)$$

$$\begin{bmatrix} \tau_{xy} \\ \tau_{yz} \\ \tau_{zx} \end{bmatrix} = \frac{E}{2\,(1+v)} \begin{bmatrix} \gamma_{xy} \\ 0 \\ 0 \end{bmatrix} \qquad (1.13)$$

In addition, the principal stresses and principal strains occur on principal axes, and their maximum and minimum values can be predicted using the Mohr's circle on a point. Mohr allows the determination of the normal and shear stress in a two dimensional plane.

Hence, if $\sigma_{zz} = 0$, then the principal stresses and strains can be predicted from the following expressions

$$\sigma_{1,2} = \frac{\sigma_{xx} + \sigma_{yy}}{2} \pm \sqrt{\left(\frac{xx - \sigma_{yy}}{2}\right)^2 + \tau_{xy}^2} \qquad (1.14)$$

$$\sigma_{1,2} = \frac{\sigma_{xx} + \sigma_{yy}}{2} \pm \tau_{\max} \qquad (1.15)$$

Recall that the third principal stress is perpendicular to the outward plane of the paper implying that $\sigma_3 = \sigma_{zz}$. In addition, if the shear stress $\tau_{xy}0$, then σ_1 and σ_2 are principal stresses, which are related to their principal directions. The angle between the principal directions is 90°.

Conversely, the principal strains are strains in the direction of the principal stresses. For a two-dimensional analysis, the principal strains are determined using the following quadratic expression

$$\epsilon_{1,2} = \frac{\epsilon_{xx} + \epsilon_{yy}}{2} \pm \sqrt{\left(\frac{\epsilon_{xx} - \epsilon_{yy}}{2}\right)^2 + \left(\frac{\gamma_{xy}}{2}\right)^2} \qquad (1.16)$$

1.6   SOUND BODIES UNDER TENSION

For uniaxial tension testing, the state of stress and the state of strain are described by the uniaxial relationships. From an engineering point of view, the tensile or longitudinal strain e is defined as elongation or stretching, which is related to Hooke's law of elastic deformation. For a uniaxial tensile test on a crack-free specimen shown in Figure 1.3, the strain and Hooke's law are

$$\epsilon = \int_{l_o}^{l} \frac{dl}{l} = \ln\left(\frac{l}{l_o}\right) \qquad \text{(Natural or true strain)} \qquad (1.17)$$

$$\epsilon = \frac{\Delta l}{l_o} \qquad \text{(Engineering strain)} \qquad (1.18)$$

$$\epsilon = \frac{\sigma}{E} \qquad \text{(Hooke's Law)} \qquad (1.19)$$

Here, Δl is the change in gage length of a line segment between two points on a solid and lo is the original gage length. It is clear that Hooke's law gives a linear stress-strain relationship. Most structural materials have some degree of plasticity, which is not defined by defined by Hooke's law.
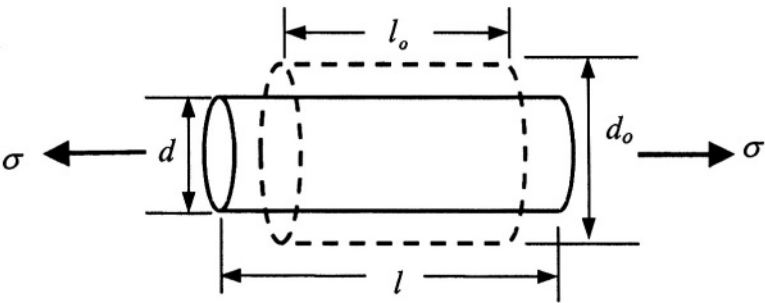
Figure 1.3 Schematic tensile crack-free round specimen.

In general, the mechanical behavior of a material under a stress-loading mode depends on the microstructure, strain rate, and environment. The behavior of an initially crack-free material is characterized by one of the typical stress-strain curves shown in Figure 1.4.
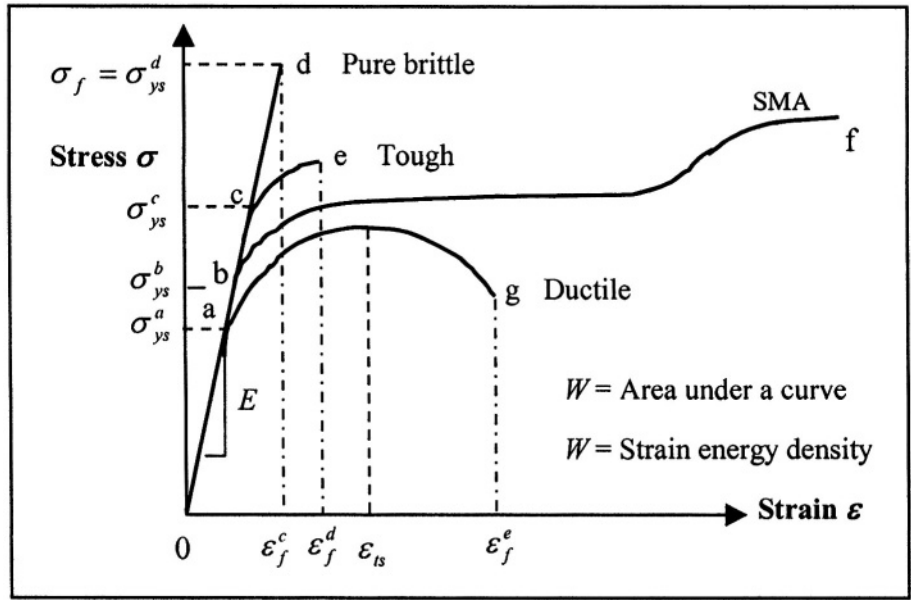
Figure 1.4 Schematic Stress-Strain curves.

Typical tension properties, such as yield strength, tensile strength, ductility, and the modulus of elasticity are obtained from these curves. The strength refers to a property and stress is a parameter related to an applied loading mode. Nevertheless, the area under the curve is a measure of fracture toughness in terms of strain energy density, which is not a common variable used by engineers

in structural analysis, but it may be used as a controlling parameter in classifying structural materials. Particularly, the SMA curve in Figure 1.4 is for a shape memory alloy (SMA), such as 55Ni-45Ti (Nitinol), which exhibits significant high strain to failure (superelastic) and high total strain energy density [5–6].

This strain energy density W $(Joules/m^3)$ is the energy required to deform the material. According to Figure 1.4, this energy is the area under the curve. For elastic behavior (up to the yield point), fracture toughness is the elastic strain energy density known as resilience and it is defined as

$$W = \int_o^\epsilon \sigma d\epsilon \qquad (1.20)$$

This expression represents an elastic behavior up to the yield strain for points a, b, c and d in Figure 1.4. Hooke's law, eq. (1.19), is used to solve the integral given by eq. (1.20). Thus, the elastic strain energy density becomes

$$W = \int_o^{\epsilon_{ys}} E\epsilon d\epsilon = \frac{1}{2}E\epsilon_{ys}^2 = \frac{\sigma_{ys}^2}{2E} \qquad (1.21)$$

On the other hand, **tough materials** have fracture toughness based on *oe* and SMA curves. Thus, the strain energy density for curve *oe* takes the form

$$W = \int_o^{\epsilon_f^e} \sigma d\epsilon = \int_o^{\epsilon_{ys}} \sigma d\epsilon + \int_{\epsilon_{ys}}^{\epsilon_f^e} \sigma d\epsilon \qquad (1.22)$$

$$W = \frac{\sigma_{ys}^2}{2E} + \int_{\epsilon_{ys}}^{\epsilon_f^e} \sigma d\epsilon \qquad (1.23)$$

This integral can be solved once a stress function in terms of strain, $\sigma = f(\epsilon)$, is available. The most common **plastic stress functions** applicable from the yield point to the ultimate tensile stress (σ_{ts}) (maximum stress on a stress-strain curves (Figure 1.4). are known as Ramberg-Osgood and Hollomon equations. These functions are defined by

$$\sigma = \sigma_{ys}\left(\frac{\epsilon}{\alpha'\epsilon_{ys}}\right)^{1/n'} \qquad \text{For } \sigma \geq \sigma_{ys} \quad \text{(Ramberg-Osgood)} \quad (1.24)$$

$$\sigma = k\epsilon^n \qquad\qquad \text{For } \sigma \geq \sigma_{ys} \quad \text{(Hollomon)} \qquad (1.25)$$

where $n, n' =$ Strain hardening exponents
$\quad\quad k =$ Strength coefficient or proportionality constant (MPa)
$\quad\quad \sigma =$ Plastic stress (MPa)
$\quad\quad \sigma_{ys} =$ Yield strength (MPa)
$\quad\quad \epsilon =$ Plastic strain
$\quad\quad \alpha' =$ Constant

For a strain hardenable material, the Hollomon or power-law equation may be used as an effective stress expression in eq. (10.3) so that the integral can

easily be solve. Combining eqs. (1.23) and (1.25) yields the total strain energy density up to the maximum stress

$$W = \frac{\sigma_{ys}^2}{2E} + \frac{k\epsilon^{n+1}}{n+1}\Big|_{\epsilon_{ys}}^{\epsilon_{ts}} \tag{1.26}$$

$$W = \frac{\sigma_{ys}^2}{2E} + \frac{k\left(\epsilon_{ts}^{n+1} - \epsilon_{ys}^{n+1}\right)}{n+1} \tag{1.27}$$

$$W = W_e + W_p \tag{1.28}$$

Here, the first and second terms are the elastic (W_e) and plastic (W_p) strain energy densities. Since Hooke's law applies up to the yield point, the total energy as per eq. (10.27) takes the form

$$W = \frac{\sigma_{ys}^2}{2E} - \frac{k}{n+1}\left(\frac{\sigma_{ys}}{E}\right)^{n+1} + \frac{k\epsilon_{ts}^{n+1}}{n+1} \tag{1.29}$$

An ideal tough material must exhibit high strength and ductility. Despite ductile materials are considered tough; they have low strength and high ductility. However, if a notched tensile specimen, made of a ductile material, is loaded in tension, the plastic flow is shifted upwards since a triaxial state of stress is developed at the root of the notch. This is a constraint against plastic flow, but it enhances the magnitude of the elastic stresses at the notch root [7].

In summary, the yield strength (material property) and the fracture toughness in terms of total strain energy density (variable) of crack-free materials can be compared using the inequalities shown below

$$\sigma_{ys}^{ductile} < \sigma_{ys}^{tough} < \sigma_{ys}^{brittle} \tag{1.30}$$

$$W_{brittle} < W_{tough} < W_{ductile} \tag{1.31}$$

This analogy implies that the yield strength decreases and the total strain energy density increases with increasing strength and decreasing strain to failure. This expressions can be used for classifying solid materials. However, an ideal material for practical engineering applications should be characterized according to the above inequalities, but slightly modified as indicated below for certain applications where high ductility is not desired

$$\sigma_{ys}^{ductile} < \quad < \sigma_{ys}^{tough} \approx \sigma_{ys}^{brittle} \tag{1.32}$$

$$W_{brittle} < \quad < W_{tough} \approx W_{ductile} \tag{1.33}$$

1.7   PLANE CONDITIONS

One important material's condition for characterizing the mechanical behavior of either a cracked or a crack-free specimen is its thickness. Thus, plane conditions are classified below

   PLANE STRESS: This is a stress condition used for thin bodies (plates), in which the specimen thickness must be $B << w$, where w is the width. Thus, the negligible stresses under the plane-stress condition are the through-thickness and the shear stresses

$$\sigma_{zz} = \tau_{yz} = \tau_{zx} = 0 \tag{1.34}$$

   This stress condition is vital in studying local stress fields near a crack tip in a solid body under a quasi-static or dynamic loading. The former loading is the most common in monotonic and fracture mechanics testing. This stress can be defined as $\sigma_{zz} = 0$ at the surface and $\sigma_{zz} \simeq 0$ at the mid-thickness plane.

   PLANE STRAIN: This particular condition is for thick bodies, which develop a triaxial state of local stress at the crack tip. The through-thickness stress in Cartesian coordinates is

$$\sigma_{zz} \simeq v\left(\sigma_{xx} + \sigma_{yy}\right) \tag{1.35}$$

1.8   EQUILIBRIUM EQUATIONS

The objective of this section is to show the equilibrium field equations used for deriving analytically solutions for the unknown stresses σ_{xx}, σ_{yy} and τ_{xy}. Subsequently, this requires an elementary treatment of the theory of elasticity. The equilibrium equations in Cartesian coordinates are the sum of forces at equilibrium

$$\frac{\partial \sigma_{xx}}{\partial x} + \frac{\partial \tau_{xy}}{\partial y} + F_x \quad = \quad 0 \tag{1.36}$$

$$\frac{\partial \sigma_{yy}}{\partial y} + \frac{\partial \tau_{xy}}{\partial x} + F_y \quad = \quad 0 \tag{1.37}$$

   For polar coordinates,

$$\frac{\partial \sigma_{rr}}{\partial r} + \frac{1}{r}\frac{\partial \tau_{r\theta}}{\partial \theta} + \frac{1}{r}\left(\sigma_{rr} - \sigma_{\theta\theta}\right) + F_r \quad = \quad 0 \tag{1.38}$$

$$\frac{1}{r}\frac{\partial \sigma_{\theta\theta}}{\partial \theta} + \frac{\partial \tau_{r\theta}}{\partial r} + \frac{2\tau_{r\theta}}{r} + F_\theta \quad = \quad 0 \tag{1.39}$$

where r = Radial direction
      θ = Tangential direction
      F_r = Body-force intensity in the r-direction
      F_θ = Body-force intensity in the θ-direction

1.9 AIRY'S STRESS FUNCTION

The Airy's stress function approach [8] will be used in order to analytically determine the unknown stresses σ_{xx}, σ_{yy} and τ_{xy} in two-dimensional elasticity problem. Use of the type of coordinates depends on the nature of the problem and the complexity of the needed analytical approach, in which the equilibrium and compatibility equations must be satisfied. For instance, Cartesian coordinates may be used on rectangular-shaped beams, while polar coordinates are used on curved beams. Solutions of elasticity problems require the determination of these stresses. This can be accomplished using the Airy's stress function ϕ, which must satisfy a biharmonic equation in the order of $\nabla^4 \phi = 0$. Hence, the objective of this section is to describe the method for finding solutions of engineering problems using the Airy's stress function ϕ, which must satisfy the equilibrium and compatibility equations, and boundary conditions. Assume that the stresses σ_{xx}, σ_{yy} and τ_{xy} can be represented by the Airy's stress function such that

$$
\begin{aligned}
\sigma_{xx} &= \frac{\partial^2 \phi}{\partial y^2} + \Omega \\
\sigma_{yy} &= \frac{\partial^2 \phi}{\partial x^2} + \Omega \\
\tau_{xy} &= -\frac{\partial^2 \phi}{\partial x \partial y}
\end{aligned}
\tag{1.40}
$$

Here, $\Omega = \Omega(x, y)$ is the body-force field. Once an Airy's stress function is selected, the stress solutions may not necessarily satisfy the equilibrium equation. Instead, the Airy's biharmonic equation for zero or constant body forces (such as those due to gravity, water pressure in porous materials, and centrifugal forces in rotating machine parts) is used in order to verify if the stress definitions meet the equilibrium requirements. The Airy's biharmonic equation is of the form

$$
\nabla^4 \phi = \frac{\partial^4 \phi}{\partial x^4} + 2\frac{\partial^4 \phi}{\partial x^2 \partial y^2} + \frac{\partial^4 \phi}{\partial y^4} = 0
\tag{1.41}
$$

The body-force intensities or the body force of magnitudes are

$$
\begin{aligned}
F_x &= -\frac{\partial \Omega}{\partial x} \\
F_y &= -\frac{\partial \Omega}{\partial y}
\end{aligned}
\tag{1.42}
$$

The stress compatibility equation is [1,9]

$$
\nabla^2 \left(\sigma_{xx} + \sigma_{yy} \right) = -\frac{\psi}{v} \left(\frac{\partial F_x}{\partial x} + \frac{\partial F_y}{\partial y} \right)
\tag{1.43}
$$

where $\psi = v$ for plane stress condition

$\psi = v/(1 - v)$ for plane strain condition

Any Airy's stress function ϕ used in the solution of engineering problems should satisfy eq. (1.41). Subsequently, the stresses can be derived using eq. (1.40). However, the type of ϕ function one chooses should be based on experience or trial and error so that ϕ satisfies eq. (1.41).

It should be mentioned that the Airy's stress function ϕ is also used for determining the stress field, and subsequently the strain field around edge dislocations in an isotropic and continuous media. A mathematical and theoretical treatment on this particular subject is given in a book written by Meyers and Chawla [3] in which clear isostress contours indicate the maximum tension, compression, and shear stresses.

1.10   AIRY'S POWER SERIES

Let the Airy's stress function be defined as an Airy's power series having a_i polynomial constants

$$\phi = \sum_{I=1}^{m} a_i x^{m-i} y^{i-1} \tag{1.44}$$

For convenience, the first order derivatives of this function, eq. (1.40), with respect to two-dimensional Cartesian coordinates are

$$\frac{\partial \phi}{\partial x} = \sum_{I=1}^{m} (m - i)\, a_i x^{m-i-1} y^{i-1} \tag{1.45}$$

$$\frac{\partial \phi}{\partial y} = \sum_{I=1}^{m} (i - 1)\, a_i x^{m-i} y^{i-2} \tag{1.46}$$

A polynomial described by eq. (1.44) must satisfy the Airy's biharmonic expression, eq. (1.41). For instance, let the order of the polynomial be

$$\phi = \sum_{i=1}^{5} a_i x^{5-i} y^{i-1} \tag{1.47}$$

$$\phi = a_1 x^4 + a_2 x^3 y + a_3 x^2 y^2 + a_4 xy^3 + a_5 y^4 \tag{1.48}$$

Thus, the pertinent derivatives are

$$\frac{\partial^4 \phi}{\partial x^4} = 24a_1$$

$$\frac{\partial^4 \phi}{\partial y^4} = 24a_5 \qquad (1.49)$$

$$\frac{\partial^4 \phi}{\partial x^2 \partial y^2} = 4a_3$$

Substituting eq. (1.49) into (1.41) yields a non-satisfactory results

$$\nabla^4 \phi = \frac{\partial^4 \phi}{\partial x^4} + 2\frac{\partial^4 \phi}{\partial x^2 \partial y^2} + \frac{\partial^4 \phi}{\partial y^4} \qquad (1.50)$$

$$\nabla^4 \phi = 24a_1 + 8a_3 + 24a_5 \neq 0 \qquad (1.51)$$

This problem can be solved by letting $\nabla^4 \phi = 0$ in eq. (1.51) so that $24a_1 + 8a_3 + 24a_5 = 0$. Thus, $a_5 = -(a_1 + a_3/3)$. Now, substituting a_5 in eq. (1.48) yields the redefined Airy's stress function is redefined

$$\phi = a_1 \left(x^4 - y^4 \right) + a_2 x^3 y + a_3 \left(x^2 y^2 - \frac{1}{3} y^4 \right) + a_4 xy^3 \qquad (1.52)$$

from which the fourth order derivatives are

$$\frac{\partial^4 \phi}{\partial x^4} = 24a_1$$

$$\frac{\partial^4 \phi}{\partial y^4} = -24a_1 - 8a_3 \qquad (1.53)$$

$$\frac{\partial^4 \phi}{\partial x^2 \partial y^2} = 4a_3$$

Substituting these fourth order derivatives, eq. (1.53), into the biharmonic expression, eq. (1.41), yields $\nabla^4 \phi = 0$. The reader should verify these partial results as an exercise. Therefore, eq. (1.52) satisfies the condition $\nabla^4 \phi = 0$. Subsequently, using eq. (1.52) and (1.40) gives the expected stress equations along with zero body-force field as

$$\sigma_{xx} = \frac{\partial^2 \phi}{\partial y^2} = -12a_1 y^2 + 2a_3 \left(x^2 - 2y^2 \right) + 6a^4 xy$$

$$\sigma_{yy} = \frac{\partial^2 \phi}{\partial x^2} = 12a_1 x^2 + 6a_2 xy + 2a_3 y^2 \qquad (1.54)$$

$$\tau_{xy} = -\frac{\partial^2 \phi}{\partial x \partial y} = -3a_2 x^2 - 4a_3 xy - 3a_4 y^2$$

An example can make this procedure sufficiently clear how to develop Airy's stresses for a cantilever beam.

EXAMPLE 1.1. *Find an Airy stress polynomial based on even functions of x and odd functions of y in Cartesian coordinates for the simple supported elastic beam of unit width, supported at ends. Now, assume plane stress condition, and a uniform distribution of the load P. (From Ref. [9]).*
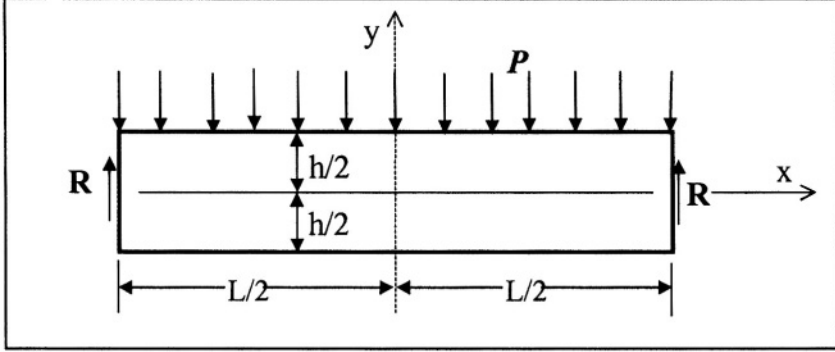
Figure E1.1

Loading conditions:

$$\sigma_{yy} = \tau_{xy} = 0 \quad @\ y = -h/2 \tag{a1}$$

$$\sigma_{yy} = -P \quad @\ y = \pm h/2 \tag{a2}$$

$$\tau_{xy} = 0 \quad @\ y = h/2 \tag{a3}$$

$$R = \int_{-h/2}^{h/2} \tau_{xy} dy = \frac{PL}{2} \quad @\ x = \pm\frac{L}{2} \tag{a4}$$

$$\int_{-h/2}^{h/2} \sigma_{xx} dy = 0 \quad @\ x = \pm\frac{L}{2} \tag{a5}$$

$$\int_{-h/2}^{h/2} \sigma_{xx} y\, dy = 0 \quad @\ x = \pm\frac{L}{2} \tag{a6}$$

Solution:
Eqs. (d) and (e) indicate that there is no longitudinal force and bending coupling at the ends of the beam. Now, select the following polynomial

$$\phi = a_1 x^2 + a_2 x^2 y + a_3 \left(x^2 y^3 - \frac{1}{5} y^5 \right) + a_4 y^3 \tag{1.55}$$

From which

$$\frac{\partial^4 \phi}{\partial x^4} = 0$$

$$\frac{\partial^4 \phi}{\partial y^4} = 24a_3 y \tag{a1}$$

$$\frac{\partial^4 \phi}{\partial x^2 \partial y^2} = 12a_3 y$$

These expressions satisfy the condition $\nabla^4 \phi = 0$. *Thus, the Airy's stresses take the form along with* $\Omega = 0$

$$\sigma_{xx} = \frac{\partial^2 \phi}{\partial y^2} = a_3 \left(6x^2 y - 4y^3\right) + 6a_4 y \tag{a2}$$

$$\sigma_{yy} = \frac{\partial^2 \phi}{\partial x^2} = 2a_1 + 2a_2 y + 2a_3 y^3 \tag{a3}$$

$$\tau_{xy} = -\frac{\partial^2 \phi}{\partial x \partial y} = -2a_2 x - 6a_3 x y^2 \tag{a4}$$

Let's use the given loading conditions in order to determine the polynomial constants a_i. *Using eq. (a3) along with the loading condition given by eq. (a1) and (a2) gives*

$$\sigma_{yy} = 2a_1 + 2a_2 y + 2a_3 y^3 = 0 \qquad @ \ y = -h/2 \tag{b1}$$
$$\sigma_{yy} = 2a_1 + 2a_2 y + 2a_3 y^3 = -p \qquad @ \ y = +h/2 \tag{b2}$$

or

$$a_1 - a_2 \left(\frac{h}{2}\right) - a_3 \left(\frac{h^3}{8}\right) = 0 \tag{b3}$$

$$a_1 - a_2 \left(\frac{h}{2}\right) - a_3 \left(\frac{h^3}{8}\right) = -P/2 \tag{b4}$$

Solving eqs. (b1) and (b2) simultaneously for a_1 *yields*

$$a_1 = -\frac{P}{4} \tag{b5}$$

Furthermore, using eq. (a4) along with (a1)

$$\tau_{xy} = -2a_2 x - 6a_3 x y^2 = 0 \qquad @ \ y = -h/2 \tag{c1}$$
$$0 = -a_2 - 3a_3 y^2 \tag{c2}$$
$$0 = a_2 + 3a_3 \left(-\frac{h}{2}\right)^2 \tag{c3}$$
$$a_2 = -\frac{3}{4}a_3 h^2 \tag{c4}$$

Substituting eqs. (b5) and (c4) into (b3) gives

$$a_3 = \frac{P}{h^3} \tag{c5}$$

Combining eqs. (a6) and (a2) yields

$$\int_{-h/2}^{h/2} \sigma_{xx} y \, dy = 0 \quad @ \; x = \frac{L}{2} \tag{d1}$$

$$\int_{-h/2}^{h/2} \left[a_3 \left(6x^2 y - 4y^3 \right) + 6a_4 y \right] y \, dy = 0 \quad @ \; x = \frac{L}{2} \tag{d2}$$

$$\int_{-h/2}^{h/2} \left[a_3 \left(6x^2 y^2 - 4y^4 \right) + 6a_4 y^2 \right] dy = 0 \quad @ \; x = \frac{L}{2} \tag{d3}$$

$$\int_{-h/2}^{h/2} \left[a_3 \left(\frac{3}{2} L^2 y^2 - 4y^4 \right) + 6a_4 y^2 \right] dy = 0 \tag{d4}$$

Solving this integral and using eq. (c5) gives

$$a_4 = a_3 \left(\frac{h^2}{10} - \frac{L^2}{4} \right) \tag{d5}$$

$$a_4 = \frac{P}{20h^3} \left(2h^2 - 5L^2 \right) \tag{d6}$$

Using the moment of inertia $I = h^3/12$ in eq. (d6) yields

$$a_4 = \frac{P}{240I} \left(2h^2 - 5L^2 \right) \tag{d7}$$

Inserting a_1 through a_4 into (1.56) through (1.58) yields the required stresses

$$\sigma_{xx} = \frac{P}{8I} \left(4x^2 - L^2 \right) y + \frac{P}{60I} \left(3h^2 y - 20y^3 \right) \tag{e1}$$

$$\sigma_{yy} = \frac{P}{24I} \left(4y^2 - 3h^2 y - h^3 \right) \tag{e2}$$

$$\tau_{xy} = \frac{Px}{8I} \left(h^2 - 4y^2 \right) \tag{e3}$$

Conventional strength of materials gives the stress in the x-direction as

$$\sigma_{xx} = \frac{My}{I} = \frac{P}{8I} \left(4x^2 - L^2 \right) y \tag{e4}$$

Here, M is the moment. For instance, eq. (e4) implies that the second term can be interpret as a correction term. Therefore, eq. (e1) is more accurate than eq. (e4) [3].

1.11 POLAR COORDINATES

Consider a two-dimensional and a small element in equilibrium of unit thickness shown in Figure 1.5. The sum of all forces in the radial r-directions is [9]
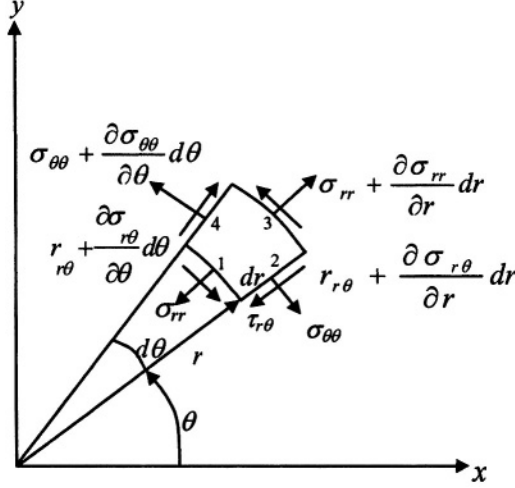
Figure 1.5 Stresses on a polar element of unit depth

$$
0 = \left(\sigma_{rr} + \frac{\partial \sigma_{rr}}{\partial r} dr\right)(r + dr)\,d\theta - \sigma_{rr} r\, d\theta - \frac{1}{2}\left[\sigma_{\theta\theta} dr + \left(\sigma_{\theta\theta} + \frac{\partial \sigma_{\theta\theta}}{\partial \theta} d\theta\right) dr\right] d\theta
$$
$$
+ \left(\tau_{r\theta} + \frac{\partial \tau_{r\theta}}{\partial \theta} d\theta - \tau_{r\theta}\right) dr + F_r r\, dr\, d\theta \tag{1.55}
$$

For an infinitely small element with $dr \to 0$ and $d\theta \to 0$, eq. (1.55) gives the first equilibrium equation

$$
\frac{\partial \sigma_{rr}}{\partial r} + \frac{1}{r}\frac{\partial \tau_{r\theta}}{\partial \theta} + \frac{1}{r}(\sigma_{rr} - \sigma_{\theta\theta}) + F_r = 0 \tag{1.56}
$$

Similarly, the equilibrium equation in the tangential direction yields the second equilibrium equation

$$
\frac{1}{r}\frac{\partial \sigma_{\theta\theta}}{\partial \theta} + \frac{\partial \tau_{r\theta}}{\partial r} + \frac{2\tau_{r\theta}}{r} + F_\theta = 0 \tag{1.57}
$$

Here, F_r and F_θ are body-force intensities. The resultant stress equations in polar coordinates are defined by [9]

$$\sigma_{rr} = \frac{1}{r}\frac{\partial\phi}{\partial r} + \frac{1}{r^2}\frac{\partial^2\phi}{\partial\theta^2}$$

$$\sigma_{\theta\theta} = \frac{\partial^2\phi}{\partial r^2} \tag{1.58}$$

$$\tau_{r\theta} = \frac{1}{r^2}\frac{\partial\phi}{\partial\theta} - \frac{1}{r}\frac{\partial^2\phi}{\partial r\partial\theta} = -\frac{\partial}{\partial r}\left(\frac{1}{r}\frac{\partial\phi}{\partial\theta}\right)$$

One particular Airy's stress function ϕ for a crack-free hollow cylinder is of the type [9]

$$\phi = a_1 + a_2 \ln(r) + a_3 r^2 + a_4 r^2 \ln(r) \tag{1.59}$$

For a plate containing a crack, the Airy's stress function may be of the form [10]

$$\phi = r^{\lambda+1} f(\theta) \tag{1.60}$$

In general, the Airy's stress function can be defined in a general form

$$\phi = g(r) f(\theta) \tag{1.61}$$

The biharmonic operator in polar coordinates is defined below. Expanding and simplifying this operator requires a step-by-step algebraic manipulation of the partial derivatives of any Airy's stress function. For convenience, the algebraic manipulation is carried out as indicated below by the nine multiplication steps

$$\nabla^4\phi = \left(\frac{\partial^2}{\partial r^2} + \frac{1}{r}\frac{\partial}{\partial r} + \frac{1}{r^2}\frac{\partial^2}{\partial\theta^2}\right)\left(\frac{\partial^2\phi}{\partial r^2} + \frac{1}{r}\frac{\partial\phi}{\partial r} + \frac{1}{r^2}\frac{\partial^2\phi}{\partial\theta^2}\right)$$

$$\tag{1.62}$$

1)
$$\frac{\partial}{\partial r^2}\left(\frac{\partial^2 \phi}{\partial r^2}\right) = \frac{\partial^4 \phi}{\partial r^4}$$

2)
$$\frac{\partial^2}{\partial r^2}\left(\frac{1}{r}\frac{\partial \phi}{\partial r}\right) = \frac{2}{r^3}\frac{\partial \phi}{\partial r} - \frac{2}{r^2}\frac{\partial^2 \phi}{\partial r^2} + \frac{1}{r}\frac{\partial^3 \phi}{\partial r^3}$$

3)
$$\frac{\partial^2}{\partial r^2}\left(\frac{1}{r^2}\frac{\partial^2 \phi}{\partial \theta^2}\right) = \frac{6}{r^4}\frac{\partial^2 \phi}{\partial \theta^2} - \frac{4}{r^3}\frac{\partial^3 \phi}{\partial r \partial \theta^2} + \frac{1}{r^2}\frac{\partial^4 \phi}{\partial r^2 \partial \theta^2}$$

4)
$$\frac{1}{r}\frac{\partial}{\partial r}\left(\frac{\partial^2 \phi}{\partial r^2}\right) = \frac{1}{r}\frac{\partial^3 \phi}{\partial r^3}$$

5)
$$\frac{1}{r}\frac{\partial}{\partial r}\left(\frac{1}{r}\frac{\partial \phi}{\partial r}\right) = \frac{1}{r}\left(-\frac{1}{r^2}\frac{\partial \phi}{\partial r} + \frac{1}{r}\frac{\partial^2 \phi}{\partial r^2}\right)$$

(1.63)

6)
$$\frac{1}{r}\frac{\partial}{\partial r}\left(\frac{1}{r^2}\frac{\partial^2 \phi}{\partial \theta^2}\right) = \frac{1}{r}\left(-\frac{2}{r^3}\frac{\partial^2 \phi}{\partial \theta^2} + \frac{1}{r^2}\frac{\partial^3 \phi}{\partial r \partial \theta^2}\right)$$

7)
$$\frac{1}{r^2}\frac{\partial^2}{\partial \theta^2}\left(\frac{\partial^2 \phi}{\partial r^2}\right) = \frac{1}{r}\frac{\partial^4 \phi}{\partial \theta^2 \partial r^2}$$

8)
$$\frac{1}{r^2}\frac{\partial^2}{\partial \theta^2}\left(\frac{1}{r}\frac{\partial \phi}{\partial r}\right) = \frac{1}{r^3}\frac{\partial^3 \phi}{\partial \theta^2 \partial r}$$

9)
$$\frac{1}{r^2}\frac{\partial^2}{\partial \theta^2}\left(\frac{1}{r^2}\frac{\partial^2 \phi}{\partial \theta^2}\right) = \frac{1}{r^4}\frac{\partial^4 \phi}{\partial \theta^4}$$

Thus, adding these expressions, it can easily be verified that $\nabla^4 \phi = 0$ for an appropriate function; otherwise, adjust the function or select another Airy's stress function ϕ. So far, the analytical definitions have been carried out assuming that the elastic material is sound, isotropic, and continuous. An example can make this mathematical treatment very clear and useful for solving a simple elastic beam problem. Thus, the reader's understanding of the distribution of stresses in two-dimensional beams is further expanded. In addition, the choice of Airy's stress function ϕ is vital for satisfying the fourth order operator $\nabla^4 \phi = 0$; otherwise, the analysis may be time consuming.

Example 1.2 *A large plate is subjected to a line of uniform distribution of load acting on the edge as indicated. Determine the Airy's stresses in polar coordinates.*
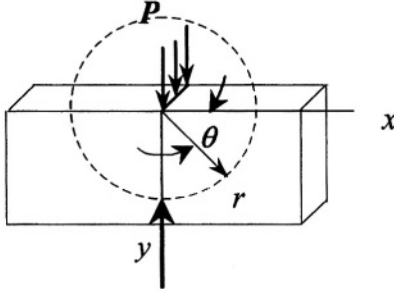
Boundary Conditions

$$\sigma_\theta = \tau_{r\theta} = 0$$
$$@ \; \theta = 0, \pi$$

$$P_r = \sigma_{rr} r d\theta \cos\theta$$

Figure E1.2

Solution:

$$\sum F_y \;\; = \;\; 0 \tag{a}$$

$$P - \int_o^\pi \sigma_{rr} r \cos\theta d\theta \;\; = \;\; 0 \tag{b}$$

Let the Airy's function be

$$\phi = ar \sin\theta \tag{c}$$

*Using eqs. (1.63) on (1.62) follows that*t

$$\nabla^4\phi \;\; = \;\; \left[\frac{\partial^4\phi}{\partial r^4}\right] + \left[\frac{2}{r^3}\frac{\partial\phi}{\partial r} - \frac{2}{r^2}\frac{\partial^2\phi}{\partial r^2}\right] + \left[\frac{6}{r^4}\frac{\partial^2\phi}{\partial\theta^2} - \frac{4}{r^3}\frac{\partial^3\phi}{\partial r\partial\theta^2} + \frac{1}{r^2}\frac{\partial^4\phi}{\partial r^2\partial\theta^2}\right]$$
$$+ \left[\frac{1}{r}\frac{\partial^3\phi}{\partial r^3}\right] + \left[\frac{1}{r}\left(-\frac{1}{r^2}\frac{\partial\phi}{\partial r} + \frac{1}{r}\frac{\partial^2\phi}{\partial r^2}\right)\right] + \frac{1}{r}\left(-\frac{2}{r^3}\frac{\partial^2\phi}{\partial\theta^2} + \frac{1}{r^2}\frac{\partial^3\phi}{\partial r\partial\theta^2}\right)$$
$$+ \left[\frac{1}{r}\frac{\partial^4\phi}{\partial r^2\partial\theta^2}\right] + \left[\frac{1}{r^3}\frac{\partial^3\phi}{\partial\theta^2\partial r}\right] + \left[\frac{1}{r^4}\frac{\partial^4\phi}{\partial\theta^4}\right] \tag{d}$$

and

$$\nabla^4\phi \;\; = \;\; [0] + \left[\frac{2a\theta}{r^3}\sin\theta\right] + \left[\frac{4a}{r^3}\cos\theta - \frac{2a\theta}{r^3}\sin\theta\right]$$
$$+ [0] + \left[-\frac{a\theta}{r^3}\sin\theta\right] + \left[-\frac{2a}{r^3}\cos\theta + \frac{a\theta}{r^3}\sin\theta\right] \tag{e}$$
$$+ [0] + \left[\frac{2a\theta}{r^3}\cos\theta - \frac{a\theta}{r^3}\sin\theta\right] + \left[-\frac{2a}{r^3}\cos\theta + \frac{a\theta}{r^3}\sin\theta\right] = 0$$

Therefore, eq. (c) satisfies $\nabla^4 \phi = 0$. Furthermore, the elastic stresses can be defined in terms of trigonometric functions. According to eq. (1.58), the elastic stresses in polar coordinates are

$$\sigma_{rr} = \frac{1}{r}\frac{\partial \phi}{\partial r} + \frac{1}{r^2}\frac{\partial^2 \phi}{\partial \theta^2} = \frac{2a}{r}\cos\theta \qquad (f)$$

$$\sigma_{\theta\theta} = \frac{\partial^2 \phi}{\partial \theta r^2} = 0 \qquad (g)$$

$$\tau_{r\theta} = \frac{1}{r^2}\frac{\partial \phi}{\partial \theta} - \frac{1}{r}\frac{\partial^2 \phi}{\partial r \partial \theta} = 0 \qquad (h)$$

These results imply that the boundary conditions were correct. Combining eqs. (b) and (f) provides the final expression for the load P and the constant a

$$P = -\int_o^\pi 2a\cos^2\theta d\theta = -2a\left[\frac{1}{2}\theta + \frac{1}{4}\sin 2\theta\right]_o^\pi \qquad (i1)$$

$$P = \pi a \qquad (i2)$$

$$a = P/\pi \qquad (i3)$$

Substituting eq. (i3) into (f) yields the radial stress

$$\sigma_{rr} = \frac{2P}{\pi r}\cos\theta \qquad (j)$$

1.12 PROBLEMS

1.1 A thin sheet made of an aluminum alloy having $E = 67GPa$, $G = 256GPa$ and $v = 1/3$ was used for two dimensional surface strain measurements. The measurements provided the strains as $\epsilon_{xx} = 10.5x10^{-5}$, $\epsilon_{yy} = -20x10^{-5}$ and $\gamma_{xy} = 240x10^{-5}$. Determine the corresponding stress in Cartesian coordinates. An element is shown below. [Solution: $\sigma_{xx} = 2.89\ MPa$, $\sigma_{yy} = 12.44\ MPa$ and $\tau_{xy} = 60.45\ MPa$].
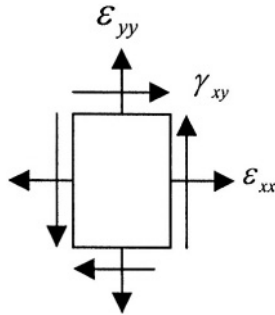
1.2 Determine a) the principal stresses and strains and b) the maximum shear stress for the case described in Problem 1.1.

1.3 Calculate the diameter of a 1-m long wire that supports a weight of 200 Newton. If the wire stretches 2 mm, calculate the strain and the stress induced by the weight. Let the modulus of elasticity be $E = 207 GPa$. [Solution: $\epsilon = 0.20\%$, $\sigma = 414\ MPa$ and $d = 0.78$ mm].

Fixed

200 N
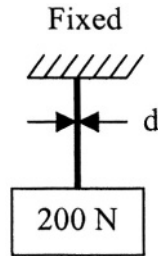
1.4 Derive an expression for the local uniform strain across the neck of a round bar being loaded in tension. Then, determine its magnitude if the original diameter is reduced 80%.

1.5 The torsion of a bar containing a longitudinal sharp groove may be characterized by a warping function of the type [after F.A McClintock, Proc. Inter. Conf. On Fracture of Metals, Inst. of Mechanical Eng., London, (1956) 538]

$$w = \mu_z = \lambda \int_o^r y dx - \lambda \int_o^r x dy$$

The displacements are $\mu_x = 0$ and $\mu_y = rz\lambda$, where λ and r are the angle of twist per unit length and the crack tip radius, respectively. The polar coordinates have the origin at the tip of the groove, which has a radius (R). Determine w, the shear strains γ_{rz} and $\gamma_{z\theta}$. In addition, predict the maximum of the shear strain [Solution: If $r \rightarrow 0$, then $\gamma_{rz} = \gamma_{\max} \rightarrow -\infty$].

Groove
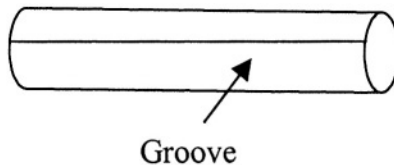
1.6 A cantilever beam having a cross-sectional area of 1.5 cm^2 is fixed at the left-hand side and loaded with a 100 Newton downward vertical force at the extreme end as shown in the figure shown below. Determine the strain in the strain gage located at 8 cm from the fixed end of the shown steel cantilever beam. The steel modulus of elasticity of is $E = 207GPa$.
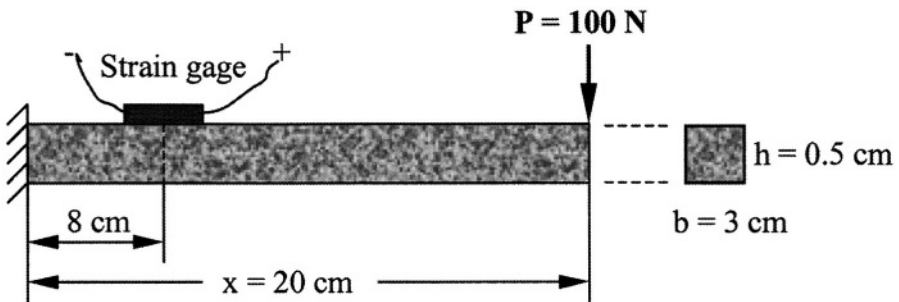
1.13 REFERENCES

[1] S.P. Timoshenko and J.N. Goodier, "Theory of Elasticity," McGraw-Hill, Third Ed., New York, (1970)

[2] J.E. Shigley and C.R. Mischke, "Mechanical Engineering Design," Fifth Ed., McGraw-Hill Book Company, New York, (1989) 14

[3] M.A. Meyers and K.K. Chawla, "Mechanical Metallurgy: Principles and Applications," Prentice-Hall, Inc., New Jersey, (1984)

[4] A. Kelly and G.W. Groves, "Crystallography and Crystal Defects," Addison-Wesley Publishing Co., California, (1970)

[5] R.L. Ellis, "Ballistic Impact Resistance of Graphite Epoxy Composites With Shape Memory Alloy And Extended Chain Polyethylene Spectra TM Hybrid Components," Ph.D. Dissertation, Virginia Polytechnic Institute and State University, (1996)

[6] H. Jia, "Impact Damage Resistance of Shape Memory Alloy Hybrid Composite Structures," Ph.D. Dissertation, Virginia Polytechnic Institute and State University, Mechanical Engineering Department, May 26, 1998

[7]   W.S. Peeling, "Design Options for Selection of Fracture Control Procedures in the Modernization of Codes, Rules, and Standards," Proceedings: Joint United States–Japan Symposium on Applications of Pressure Component Codes, Tokyo, Japan. (March 1973)

[8]   G.B. Airy, British Assoc. Adv. Sci. Report, (1862)

[9]   J.W. Dally and W.F. Riley, "Experimental Stress Analysis," Third edition, McGraw-Hill, New York, (1991)

[10] K. Hellan, "Introduction to Fracture Mechanics," McGraw-Hill Book company, New York, (1984)

Chapter 2

INTRODUCTION TO FRACTURE MECHANICS

2.1 INTRODUCTION

The theory of elasticity used in Chapter 1 served the purpose of illustrating the close form of analytical procedures in order to develop constitutive equations for predicting failure of crack-free solids [1]. However, when solids contain flaws or cracks, the field equations are not completely defined by the theory of elasticity since it does not consider the stress singularity phenomenon near a crack tip. It only provides the means to predict general yielding as a failure criterion. Despite the usefulness of predicting yielding, it is necessary to use the principles of fracture mechanics to predict fracture of solid components containing cracks.

fracture mechanics is the study of mechanical behavior of cracked materials subjected to an applied load. In fact, Irwin [2] developed the field of fracture mechanics using the early work of Inglis [3], Griffith [4], and Westergaard [5]. Essentially, fracture mechanics deals with the irreversible process of rupture due to nucleation and growth of cracks. The formation of cracks may be a complex fracture process, which strongly depends on the microstructure of a particular crystalline or amorphous solid, applied loading, and environment. The microstructure plays a very important role in a fracture process due to dislocation motion, precipitates, inclusions, grain size, and type of phases making up the microstructure. All these microstructural features are imperfections and can act as fracture nuclei under unfavorable conditions. For instance, **Brittle Fracture** is a low-energy process (low energy dissipation), which may lead to catastrophic failure without warning since the crack velocity is normally high. Therefore, little or no plastic deformation may be involved before separation of the solid. On the other hand, **Ductile Fracture** is a high-energy process in which a large amount of energy dissipation is associated with a large plastic deformation before crack instability occurs. Consequently, slow crack growth occurs due to strain hardening at the crack tip region.

2.2   THEORETICAL STRENGTH

Consider the predicament of how strong a perfect (ideal) crystal lattice should be under an applied state of stress, and the comparison of the actual and theoretical strength of metals. This is a very laborious work to perform, but theoretical approximations can be made in order to determine or calculate the stress required for fracture of atomic bonding in crystalline or amorphous crystals.

Assume a simple sinusoidal stress-displacement law with a half-period of 1/2 shown Figure 2.1 which predicts the simultaneous separation of atoms when the atomic separation reaches a critical value.
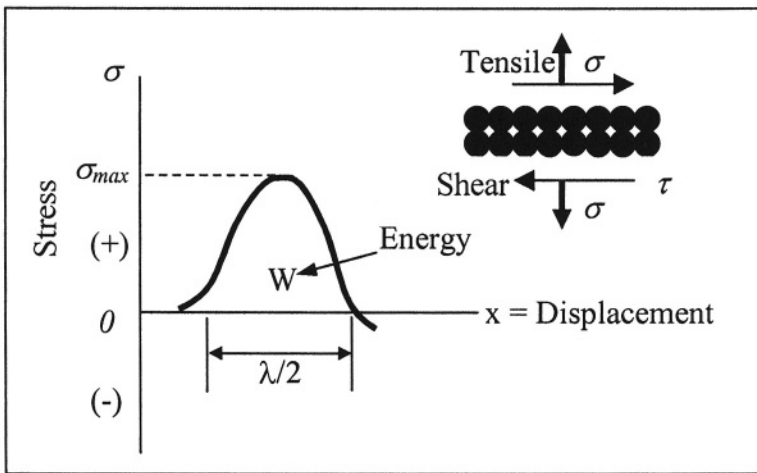
Figure 2.1 Sinusoidal stress vs. displacement.

For an ideal crystal subjected to a tensile load and a shear load, which generates small displacements, the sinusoidal stress functions are

$$\sigma \;=\; \sigma_{\max} \sin\left(\frac{2\pi x}{\lambda}\right) \simeq \left(\frac{2\pi x}{\lambda}\right)\sigma_{\max} \tag{2.1a}$$

$$\tau \;=\; \tau_{\max} \sin\left(\frac{2\pi x}{a_o}\right) \simeq \left(\frac{2\pi x}{a_o}\right)\tau_{\max} \tag{2.1b}$$

Thus, the maximum theoretical tensile stress becomes

$$\sigma_{\max} \;=\; \left(\frac{\lambda}{2\pi x}\right)\sigma \tag{2.2a}$$

$$\tau_{\max} \;=\; \left(\frac{a_o}{2\pi x}\right)\tau \tag{2.2b}$$

The interpretation of Figure 2.1 is that the strength to pull atoms apart increases with increasing atomic distance, reaches a maximum strength (peak

strength) equals to the theoretical (cohesive) tensile strength $\sigma_{max} = \sigma_c$ and then it decreases as atoms are further apart in the direction perpendicular to the applied stress. Consequently, atomic planes separate and the material cleaves perpendicularly to the tensile stress.

Assuming an elastic deformation process, Hooke's law gives the tensile and shear modulus of elasticity defined by

$$E = \frac{Tensile\ Stress}{Strain} = \frac{\sigma}{x/a_o} \tag{2.3a}$$

$$G = \frac{Shear\ Stress}{Strain} = \frac{\tau}{x/a_o} \tag{2.3b}$$

where $a_o = \lambda/2 = $ Equilibrium atomic distance (Figure 2.2)

Combining eqs. (2.2) and (2.3) yields the theoretical fracture strength of solid materials

$$\sigma_{max} \simeq \frac{E}{\pi} \tag{2.4}$$

$$\tau_{max} \simeq \frac{G}{2\pi} \tag{2.5}$$

Table 2.1 contains theoretical and experimental data for some elastic materials tested in tension.

Table 2.1 Theoretical and experimental fracture strength [6]

Material	E (MPa)	σ_{max}-Eq.(2.5)	σ_f-Exp.	σ_{max}/σ_f
Silica Fibers	97.10	30.90	24.10	1.28
Iron Whisker	295.20	94.00	13.10	7.18
Silicon Whisker	165.70	52.70	6.50	8.11
Alumina Whisker	496.20	158.00	15.20	10.39
Ausformed Steel	200.10	63.70	3.10	20.55
Piano Wire	200.10	63.70	2.80	22.75

The discrepancy between σ_{max} and σ_f values is due to the fact that the sinusoidal model assumes a concurrent fracture of atomic bonding until the atomic planes separate and σ_f is associated with plastic flow and dislocation motion. Physically, the discrepancy is due to the presence of small flaws or cracks on the surface or within the material.

Using the energy at fracture for a tension test, the fracture work per unit area can be defined by a simple integral

$$W = \int_o^{\lambda/2} \sigma_{max} \sin\left(\frac{\pi x}{\lambda/2}\right) dx = \left(\frac{\lambda}{\pi}\right)\sigma_{max} \tag{2.6}$$

Letting $2\gamma = W$ be the total surface energy required to form two new fracture surfaces and combining eqs. (2.4) and (2.6) yields the theoretical tensile strength in terms of surface energy and equilibrium spacing

$$\sigma_c = \sqrt{\frac{E\gamma}{a_o}} \qquad (2.7)$$

In addition, the atomic bonding in solids is related to bonding forces and energies. The bonding forces are interatomic forces (repulsive and attractive forces) that bind the atoms together to form symmetrical arrays of atoms. These forces as well as the potential energies depend on the interatomic spacing or distance between adjacent atoms. Figure 2.2 schematically shows the forces and the energies as functions of interatomic spacing (separation distance between centers of two atoms) for two ideal atoms. In general, atoms are considered spherical electric structures having diameters in the order of $0.1\ nm$. According to the theoretical plot depicted in Figure 2.2, both attractive and repulsive forces act together to keep the atoms at their equilibrium spacing. These forces depend on temperature and pressure.
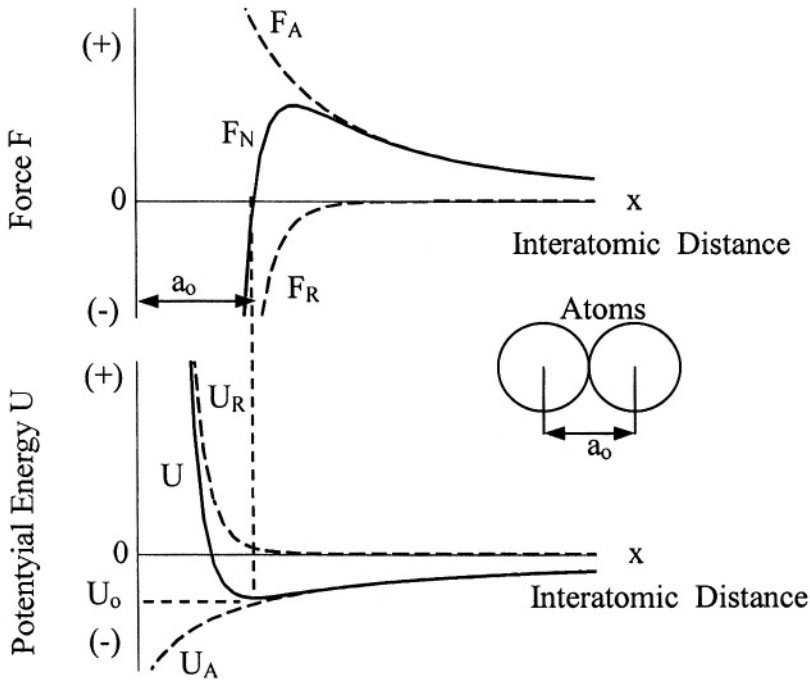

Figure 2.2 Schematic variation of bonding energy and bonding force as functions of interatomic spacing

The potential or bonding energy and forces are defined by

$$U = -\frac{C_a}{x^n} + \frac{C_b}{x^m} = U_A + U_B \tag{2.8}$$

$$F = \frac{dU}{dx} = F_A + F_B \tag{2.9}$$

where C_a = Attractive constant $\quad C_b$ = Repulsive constant
$\quad n, m$ = Exponents
$\quad U_A, U_B$ = Attractive and repulsive energies
$\quad F_A + F_B$ = Attractive and repulsive forces

The curves in Figure 2.2 are known as Condon-Morse curves and are used to explain the physical events of atomic displacement at a nanoscale. At equilibrium, the minimum potential energy and the net force are dependent of the interatomic spacing; that is, $U_o = f(a_o) < 0$ and $F_N = g(a_o) = 0$. However, if the interatomic spacing is slightly decreased $(x < a_o)$ or perturbed by the action of an applied load, a repulsive force builds up and the two atoms have the tendency to return to their equilibrium position at $x = a_o$. On the other hand, if $x > a_o$, an attractive force builds up so that $x = a_o$.

Conclusively, an array of atoms form a definite atomic pattern with respect to their neighboring atoms and as a result, all atoms form a specific space lattice consisting of unit cells, such as body-centered cubic (BCC), hexagonal., monoclinic and the like.

2.3 STRESS-CONCENTRATION FACTOR

Consider an infinite plate containing an elliptical hole with major axis 2a and minor axis 2b as shown in Figure 2.3, where the elliptical and Cartesian coordinates are (ξ, β) and (x, y), respectively. The equation of an ellipse, the Cartesian coordinates, and the radius of curvature are given below, respectively

$$\frac{x^2}{a^2} + \frac{y^2}{b^2} = 1 \tag{2.10}$$

and

$$x = c \cosh \xi \cos \beta \tag{2.11}$$
$$y = c \sinh \xi \sin \beta \tag{2.12}$$

The radius of the ellipse is defined in terms of semi-axes by

$$\rho = \frac{b^2}{a} \tag{2.13}$$

Figure 2.3 Elliptic coordinates in an infinite plate

PROBLEM STATEMENT: It is desirable to derive the maximum elastic stress component at an elliptical crack tip along the major axis $2a$ when the minor axis $2b \to 0$ [7]. Inglis [3] who derived the elastic stress distribution in an infinite plate studied this problem.   When a remote stress is applied perpendicular to the major axis 2a of the thin plate, the stress distribution expression for tan elliptical hole shown in Figure 2.3 is [8]

$$\sigma_x = \sigma \left[-\frac{1}{A^2} + \frac{x\left(x^2 - a^2 + b^2\right)^{-1/2}}{A^2} - \frac{a^2 x \left(x^2 - a^2 + b^2\right)^{-3/2}}{A} \right] \quad (2.14)$$

$$\sigma_y = \sigma \left[1 - B + Bx \left(x^2 - a^2 + b^2\right)^{-1/2} - \frac{a^2 x \left(x^2 - a^2 + b^2\right)^{-3/2}}{A} \right] (2.15)$$

where $A = 1 - b/a$
$\qquad B = \left(1 - 2b/a\right) / \left(1 - b/a\right)^2$
$\qquad \rho = $ Minimum radius at the end of the major a-axis

The resultant maximum axial stress at the edge of the ellipse is [3,9]

$$\sigma_{\text{max}} = \left(1 + \frac{2a}{b}\right) \sigma \qquad\qquad (2.16)$$

$$\sigma_{\text{max}} = K_t \sigma \qquad\qquad (2.17)$$

Here, K_t is the stress-concentration factor and σ is the nominal stress or the driving force. If $a = b$, then $K_t = 3$ and $\sigma_{\text{max}} = 3\sigma$ for a hole. On the other hand, if $b \to 0$, then $\sigma_{\text{max}} \to \infty$ is singular and it is meaningless, and a very

sharp crack is formed since $\rho \rightarrow 0$. In addition, K_t is used to analyze the a stress at a point in the vicinity of a notch having a radius $\rho >> 0$. However, if a crack is formed having $\rho \simeq 0$, the stress field at the crack tip is defined in terms of the stress-intensity factor (K_I) instead of the stress-concentration factor (K_t). In fact, microstructural discontinuities and geometrical discontinuities, such as notches, holes, grooves, and the like, are sources for crack initiation when the stress-concentration factor is sufficiently high. The degree of concentration of the stresses or strains is determined as the stress-concentration factor.

Symmetric Circular Hole in Finite Plate: Figure 2.4 shows the distribution of the axial and transverse normalized stresses along the x-axis near a circular hole in a wide thin plate loaded in tension. The equations for the normalized stresses in this particular case are based on Grover's analysis [10].
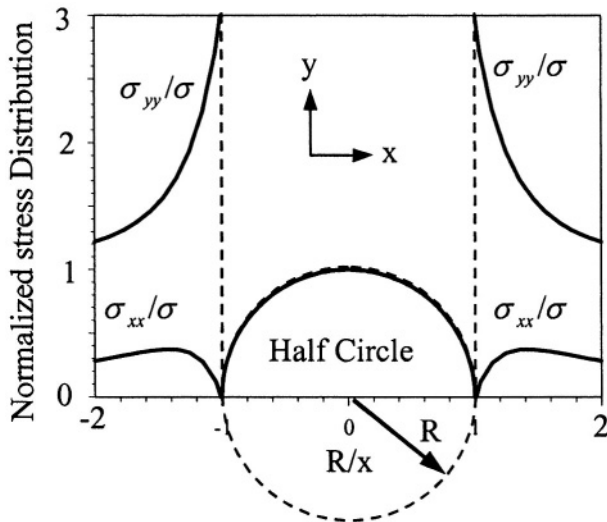

Figure 2.4 Normalized Axial and trasverse stresses along the x-axis near a circular hole in thin plate under tension loading

$$\frac{\sigma_x}{\sigma} = \frac{3}{2}\left(\frac{R}{x}\right)^2 - \frac{3}{2}\left(\frac{R}{x}\right)^4 \tag{2.18}$$

$$\frac{\sigma_y}{\sigma} = 1 + \frac{1}{2}\left(\frac{R}{x}\right)^2 + \frac{3}{2}\left(\frac{R}{x}\right)^4 \tag{2.19}$$

where R = Hole radius
σ = Nominal stress
σ_x = Transverse stress
σ_y = Axial stress

2.4   GRIFFITH CRACK THEORY

Griffith [4] noted in 1921 that when a stressed plate of an elastic material containing a crack, the potential energy decreased and the surface energy increased. Potential energy is related to the release of stored energy and the work done by the external loads. The "surface energy" results from the presence of a crack as shown in Figure 2.5. This energy arises from a non-equilibrium configuration of the nearest neighbor atoms at any surface in a solid [11-13].
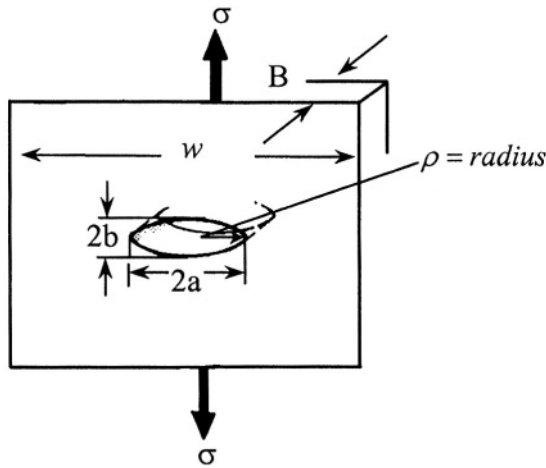

Figure 2.5 Through-thickness crack in a large plate containing an elliptical crack of crack tip radius ρ.

PROBLEM STATEMENT: A large plate containing a crack is subjected to a remote and uniform tensile load in the direction of the y-axis, and perpendicular to the crack line along the x-axis. What is the external stress that will cause crack instability (crack propagation) value?

Solution: Consider the configuration shown in Figure 2.5, which was used by Griffith to estimate the specific surface energy and the decrease in potential energy (upon using the stress analysis of Inglis [3]) when infinitely plate having a through-thickness crack of length $2a$ and it is loaded remotely from the crack face.

Thus, the total potential energy of the system is given by [4]

$$U = U_o - U_a + U_\gamma \tag{2.20}$$

$$U = U_o - \frac{\pi \beta a^2 \sigma^2 B}{E} + 2\left(2aB\gamma_s\right) \tag{2.21}$$

where U = Potential energy of the cracked body
$\quad\quad U_o$ = Potential energy of uncracked body
$\quad\quad U_a$ = Elastic energy due to the presence of the crack
$\quad\quad U_\gamma$ = Elastic-surface energy due to the formation of crack surfaces
$\quad\quad a$ = One-half crack length
$\quad\quad 4aB = 2(2aB)$ = Total surface crack area
$\quad\quad \gamma_s$ = Specific surface energy
$\quad\quad E$ = Modulus of elasticity
$\quad\quad \sigma$ = Applied stress and v = Poisson's ratio
$\quad\quad \beta = 1$ for plane stress and $\beta = 1 - v^2$ for plane strain

The equilibrium condition of eq. (2.21) is defined by the first order partial derive. The equilibrium condition of eq. (2.21) is defined by the first order derivative with respect to crack length. This derivative is of significance because the critical crack size may be predicted very easily. If $dU/da = 0$, the crack size and total surface energy are, respectively

$$a \;\; = \;\; \frac{(2\gamma_s)E}{\pi\beta\sigma^2} \tag{2.22}$$

$$2\gamma_s \;\; = \;\; \frac{\pi\beta a\sigma^2}{E} \tag{2.23}$$

Rearranging eq. (2.23) gives a significant expression in linear elastic fracture mechanics (LEFM)

$$\sigma\sqrt{\pi a} \;\; = \;\; \sqrt{\frac{(2\gamma_s)E}{\beta}} \tag{2.24}$$

$$K_I \;\; = \;\; \sigma\sqrt{\pi a} \tag{2.25}$$

The parameter K_I is called the stress intensity factor which is the crack driving force and its critical value is a material property known as fracture toughness, which in turn, is the resistance force to crack extension [14]. The interpretation of eq. (2.24) suggests that crack extension is brittle solids is completely governed by the critical value of the stress-intensity factor defined by eq. 2.25). In fact, K_I equation is applicable to a specimen containing other crack geometry subjected to a remotely applied tensile stress. Experimentally, the critical value of K_I, known as fracture toughness, can be determined at a fracture stress when the crack length reaches a critical or maximum value prior to rapid crack growth . Thus, $K_I \rightarrow K_{IC}$ as $\sigma \rightarrow \sigma_f$ when $a \rightarrow a_c$. This brief explanation is intended to make the reader be aware of the importance of fracture mechanics in analyzing cracked components.

In addition, taking the second derivative of eq. (2.21) with respect to the crack length yields

$$\frac{d^2U}{da^2} = -\frac{2\pi\beta\sigma^2 B}{E} \tag{2.26}$$

Denote that $d^2U/da^2 < 0$ represents an unstable system. Consequently, the crack will always grow.

Combining eqs. (2.13) and (2.16) yields the axial stress equation along with $\sigma_y = \sigma_{max}$

$$\sigma_{max} = \left(1 + 2\sqrt{\frac{a}{\rho}}\right)\sigma \tag{2.27}$$

For a sharp crack $a \gg \rho$ and $\sqrt{a/\rho} \gg 1$, eq. (2.27) yields the maximum axial stress as

$$\sigma_{max} = \left(2\sqrt{\frac{a}{\rho}}\right)\sigma \tag{2.28}$$

Thus, the theoretical stress concentration factor becomes

$$K_t = 2\sqrt{\frac{a}{\rho}} = \frac{\sigma_{max}}{\sigma} \tag{2.29}$$

In fact, the use of the stress-concentration approach is meaningless for characterizing the behavior of sharp cracks because the theoretical axial stress-concentration factor is $K_t \to \infty$ as $\rho \to 0$. Therefore, the elliptical hole becomes an elliptical crack and the stress-intensity factor K_I is the most useful approach for analyzing structural and machine components containing sharp cracks.

2.5   STRAIN-ENERGY RELEASE RATE

It is well-known that plastic deformation occurs in engineering metal, alloys and some polymers. Due to this fact, Irwin [2] and Orowan [15] modified Griffith's elastic surface energy expression, eq. (2.23), by adding a plastic deformation energy or plastic strain work γ_p in the fracture process. For tension loading, the total elastic-plastic strain-energy is known as the strain energy release rate G_I, which is the energy per unit crack surface area available for infinitesimal crack extension [14]. Thus,

$$G_I = 2\left(\gamma_s + \gamma_p\right) \tag{2.30}$$

$$G_I = \frac{\pi a \sigma^2}{E'} \tag{2.31}$$

Here, $E' = E/\beta$. Rearranging eq. (2.31) gives the stress equation as

$$\sigma = \sqrt{\frac{E'G_I}{\pi a}} \tag{2.32}$$

Combining eq. (2.25) and (2.31) yields

$$G_I = \frac{K_I^2}{E'} \tag{2.33}$$

This is one of the most important relations in the field of linear fracture mechanics. Hence, eq. (2.33) suggests that G_I represents the material's resistance (R) to crack extension and it is known as the crack driving force. On the other hand, K_I is the intensity of the stress field at the crack tip.

The condition of eq. (2.32) implies that $G_I = R$ before relatively slow crack growth occurs. However, rapid crack growth (propagation) takes place when $G_I \rightarrow G_{IC}$, which is the critical strain energy release rate known as the crack driving force or fracture toughness of a material under tension loading. Consequently, the fracture criterion by G_{IC} establishes crack propagation when $G_I \geq G_{IC}$. In this case, the critical stress or fracture stress σ_c and the critical crack driving force G_{IC} can be predicted using eq. (2.32) when the crack is unstable. Hence,

$$\sigma_c = \sqrt{\frac{E'G_{IC}}{\pi a}} \tag{2.34}$$

Griffith assumed that the crack resistance R consisted of surface energy only for brittle materials. This implies that $R = 2\gamma_s$, but most engineering materials undergo, to an extent, plastic deformation so that $R = 2\left(\gamma_s + \gamma_p\right)$. Figure 2.5 shows a plastic zone at the crack tip representing plasticity or localized yielding, induced by an external nominal stress. This implies that the energy γ_p is manifested due to this small plastic zone in the vicinity of the crack tip.
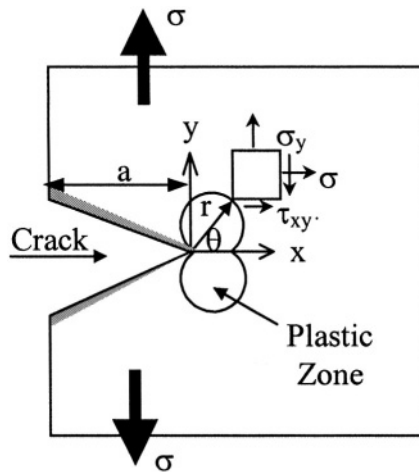

Figure 2.6 Crack showing the plastic zone and stress at the crack tip

It is clear that the internal stresses on an element of an elastic-plastic boundary are induced by plasticity and are temperature-dependent tensors. The stress in front of the crack tip or within the plastic zone exceeds the local microscopic yield stress, which may be defined as the theoretical or cohesive stress for breaking atomic bonds. If microscopic plasticity through activated slip systems does not occur, as in glasses, then a linear elastic fracture is achieved as the controlling fracture process. In essence, the fracture process is associated with plasticity at a microscopic level.

If large plasticity occurs at the crack tip, then the crack blunts and its radius of curvature increases. This plastic deformation process is strongly dependent on the temperature and microstructure. Regardless of the shape of the plastic zone, the irreversible crack tip plasticity is an indication of a local strain hardening process during which slip systems are activated and dislocations pile up and dislocation interaction occurs.

2.6   GRAIN-SIZE REFINEMENT

In addition, the grain size refinement technique is used to enhance the strength and fracture toughness of body-centered cubic (BCC) materials, such as low carbon steels. Letting a crack size be in the order of the average grain size $(d = a)$ it can be shown that both yield strength (σ_{ys}) and fracture toughness (G_{IC}) depend on the grain size. Using the Hall-Petch equation for σ_{ys} and eq. (2.34) for σ_f, it is clear that these stress entities depend on the grain size. Hence,

$$\sigma_{ys} = \sigma_o + k_y d^{-1/2} \tag{2.35}$$

$$\sigma_f = \left(\frac{E' G_{IC}}{\pi}\right)^{1/2} d^{-1/2} = k_f d^{-1/2} \tag{2.36}$$

where σ_o = Constant friction stress (MPa)
k_y = Dislocation locking term $(MPa\sqrt{m})$
k_f = Constant $(MPa\sqrt{m})$

Denote that eqs. (2.35) and (2.36) predict that $\sigma_{ys} = f(d)$ and $\sigma_f = f(d)$. The slopes of these equations, k_y and k_f, respectively, have the same units and they may be assumed to be related to fracture toughness. However, k_y is referred to as the dislocation locking term that restricts yielding from a grain to the adjacent one. Moreover, analysis of these equations for materials having temperature and grain size dependency indicate that both $\sigma_{ys} \to \infty$ and $\sigma_f \to \infty$ as $d \to 0$, but $\sigma_f > \sigma_{ys}$ due to the inherent friction stress so at a temperature T_1.

Furthermore, σ_o represents the stress required for dislocation motion along slip planes in BCC polycrystalline materials. One can observe that $\sigma_{ys} \to \sigma_o$ for

$d^{-1/2} = 0$, which means that σ_o is regarded as the yield stress of a single crystal. However, $\sigma_{ys} \to \sigma_o$ and $\sigma_f \to \sigma_o$ as $d \to \infty$ is an unrealistic case. Therefore, grain size refinement is a useful strengthening mechanism for increasing both σ_{ys} and σ_f. At a temperature $T_2 > T_1$, σ_{ys} decreases since σ_o and k_y also decrease, and G_{IC} increases. Therefore, σ_f must decrease.

Briefly, if a dislocation source is activated, then it causes dislocation motion to occur towards the grain boundary, which is the obstacle suitable for dislocation pile up. This pile up causes a stress concentration at the grain boundary, which eventually fractures when the local stress (shear stress) reaches a critical value. Therefore, another dislocation sources are generated. This is a possible mechanism for explaining the yielding phenomenon from one grain to the next. However, the grain size dictates the size of dislocation pile-up, the distance dislocations must travel, and the dislocation density associated with yielding. This implies that the finer the grains the higher the yield strength.

If a suitable volume of hard particles exists in a fine-grain material, the yield stress is enhanced further since three possible strengthening mechanisms are present. That is, solution strengthening, fine grain strengthening and particle (dispersion) strengthening. If these three strengthening mechanisms are activated, then the Hall-Petch model is not a suitable model for explaining the strengthening process, but the material strengthening is enhanced due to these mechanisms. This suitable explanation is vital in understanding that the grain size plays a major role in determining material properties such as the yield strength and fracture toughness.

2.7 PROBLEMS

2.1 Show that the applied stress is $\sigma \to 0$ when the crack tip radius is $\rho \to 0$. Explain.

2.2   In order for crack propagation to take place, the strain energy is defined by the following inequality $U(a) - U(a + \Delta a) \geq 2\Delta a\gamma$, where Δa is the crack extension. Show that the crack driving force at instability is defined by $G \geq 0.5 dU(a)/da$.

2.3   One $(1\text{-}mm)\text{x}(15\text{-}mm)\text{x}100\text{-}mm$ steel strap has a 3-mm long central crack. This strap is loaded in tension to failure. Assume that the steel is brittle having the following properties: $E = 207\ MPa\ \sigma_{ys} = 1,500\ PMa$ and $K_{IC} = 70\ MPa\sqrt{m}$. Determine a) the critical stress and b) the critical strain-energy release rate.

2.4   Suppose that a structure made of plates has one cracked plate. If the crack reaches a critical size, will the plate fracture or the entire structure collapse? Explain.

2.5 What is crack instability according to Griffith criterion?

2.6   Assume that a quenched 1.2%C-steel plate has. a penny-shaped crack. Will the Griffith theory be applicable to this plate?

2.7   Will the Irwin theory be valid for a changing plastic zone size during crack growth?

2.8   What are the major roles of the surface energy and the stored elastic energy during crack growth?

2.9   What does happen to the elastic energy during crack growth?

2.10   What does $dU/da = 0$ mean?

2.8   REFERENCES

[1]   J.W. Dally and W.F. Riley, "Experimental Stress Analysis," third edition, McGraw-Hill, Inc., New York, (1991)

[2]   G.R. Irwin, "Fracture I," in S. Flugge (ed), Handbuch der Physik VI, Springer-Verlag, New York, (1958) 558-590

[3]   C.E. Inglis, "Stresses in a Plate due to the Presence of Cracks and Sharp Corners," Trans. Institute of Naval Architecture, 55 (1913) 219-241

[4]   A.A. Griffith, "The Phenomena of Rupture and Flows in Solids," Phil. Trans. Royal Soc., 221 (1921) 163-167

[5]   H.M. Westergaard, "Bearing Pressures and Cracks," Journal of Applied Mechanics, G1 (1939) A49 - A53

[6]   W.J. McGregor Tegart, "Elements of Mechanical Metallurgy," Macmillan, NY, (1966)

[7]   A.P. Boresi and O.M. Sidebottom, "Advanced Mechanics of Materials", John Wiley & Sons, New York, (1985) 534-538

[8]   J.A. Collins, "Failure of Materials in Mechanical Design: Analysis, Prediction, Prevention," Second Edition, John Wiley & Sons, New York (1993) 422

[9]   S.P. Timoshenko and J.N. Goodier, "Theory of Elasticity," Third edition, McGraw-Hill Co., New York, (1970) 193

[10] H.J. Grover, "Fatigue Aircraft Structures," NAVIR 01-1A-13 Department of the Navy, US, (1966)

[11] D. Broek, "Elementary Engineering Fracture Mechanics," fourth edition, Kluwer Academic Publisher, Boston, (1986)

[12] K. Hellan, "Introduction to Fracture Mechanics," McGraw-Hill, New York, (1984)

[13] R.W. Hertzberg, " Deformation and Fracture Mechanics of Engineering Materials," Third edition, John Wiley & Sons, New York, (1989)

[14] J.M. Barsom and S.T. Rolfe, "Fracture and Fatigue Control in Structures: Applications of Fracture Mechanics," Third edition, American Society For Testing and Materials, West Conshocken, PA, (199) Chapter 2

[15] E. Orowan, "Fatigue and Fracture of Metals," MIT Press, Cambridge, MA, (1950) 139

Chapter 3

LINEAR ELASTIC FRACTURE MECHANICS

3.1   INTRODUCTION

Solid bodies containing cracks can be characterized by defining a state of stress near a crack tip and the energy balance coupled with fracture. Introducing the Westergaard's complex function and will allow the development a significant stress analysis at the crack tip. These particular functions can be found elsewhere [1]. For instance, Irwin [2] treated the singular stress field by introducing a quantity known as the **stress intensity factor**, which is used as the controlling parameter for evaluating the critical state of a crack.

The theory of linear-elastic fracture mechanics (LEFM) is integrated in this chapter using an analytical approach that will provide the reader useful analytical steps. Thus, the reader will have a clear understanding of the concepts involved in this particular engineering field and will develop the skills for a mathematical background in determining the elastic stress field equations around a crack tip. The field equations are assumed to be within a small plastic zone ahead of the crack tip. If this plastic zone is sufficiently small, the small-scale yielding approach is used for characterizing brittle solids and for determining the stress and strain fields when the size of the plastic zone is sufficiently smaller than the crack length; than is, $r << a$. In contrast, a large-scale yielding is for ductile solids, in which $r \geq a$.

Most static failure theories assume that the solid material to be analyzed is perfectly homogeneous, isotropic and free of stress risers or defects, such as voids, cracks, inclusions and mechanical discontinuities (indentations, scratches or gouges). Actually, fracture mechanics considers structural components having small flaws or cracks which are introduced during solidification, quenching, welding, machining or handling process. However, cracks that develop in service are difficult to predict and account for preventing crack growth.

3.2   MODES OF LOADING

A crack in a body may be subjected to three different types of loading, which involve displacements of the crack surfaces. The mechanical behavior of a solid containing a crack of a specific geometry and size can be predicted by evaluating the stress intensity factors $(K_I, K_{II}, \text{and } K_{III})$ shown in Figure 3.1.
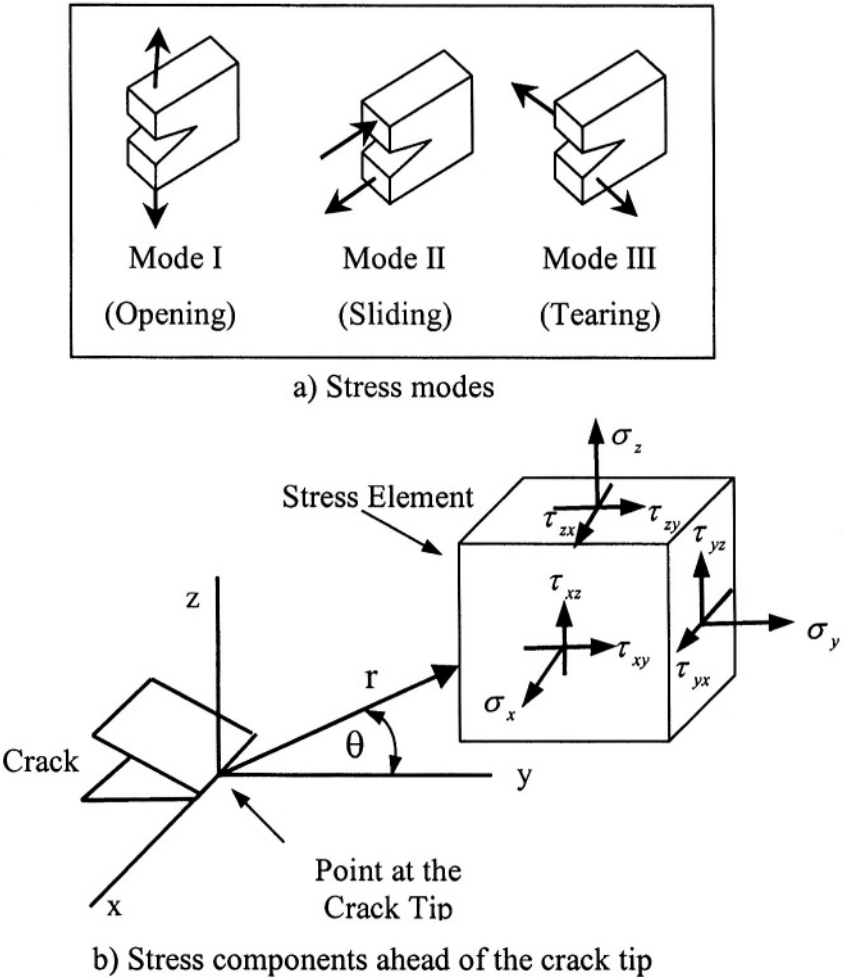

a) Stress modes

b) Stress components ahead of the crack tip

Figure 3.1 Stress loading modes and crack coordinate system

If crack growth occurs along the crack plane perpendicular to the direction of the applied external loading mode, then the stress intensity factors are defined according to the American Society for Testing Materials (ASTM) E399 Standard Test Method as

$$K_I = \lim_{r \to 0} \left(\sigma_{yy} \sqrt{2\pi r} \right) f_I (\theta) = \sigma_{yy} \sqrt{2\pi r} \quad @ \quad \sigma_{yy} = \sigma_{yy} (r, \theta = 0) \quad (3.1)$$

$$K_{II} = \lim_{r \to 0} \left(\tau_{xy} \sqrt{2\pi r} \right) f_{II} (\theta) = \tau_{xy} \sqrt{2\pi r} \quad @ \quad \tau_{xy} = \tau_{xy} (r, \theta = 0) \quad (3.2)$$

$$K_{III} = \lim_{r \to 0} \left(\tau_{yz} \sqrt{2\pi r} \right) f_{III} (\theta) = \tau_{yz} \sqrt{2\pi r} \quad @ \quad \tau_{yz} = \tau_{yz} (r, \theta = 0) \quad (3.3)$$

Here, $f_I (\theta)$, $f_{II} (\theta)$ and $f_{III} (\theta)$ are trigonometric functions to be derived analytically and K_I was developed by Irwin [2].

Thus, specimens and structural components having flaws or cracks can be loaded to various levels of the applied stress-intensity factor for a particular stress mode shown in Figure 3.1. This is analogous to unflawed components being loaded to various levels of the applied stress σ. In fact, the parameters r and θ are the polar coordinates of a plastic zone that forms ahead of the crack tip. If $\theta = 0$ in Figure 3.1, then the stresses can be evaluated along the crack plane.

The stress intensity factor(s) for a particular crack configuration can be defined as a general function

$$K_i = f \left(Stress, \ Crack \ Geometry, \ Specimen \ Configuration \right) \quad (3.4)$$

where $i = I, \ II, \ III$ which stand for mode 1, mode 2, and mode 3, respectively

The parameter K_i can be used to determine the static or dynamic fracture stress, the fatigue crack growth rate and corrosion crack growth rate. For elastic material, the strain-energy release rate G_i, known as the crack driving force, is related to the stress intensity factor and the modulus of elasticity as indicated by the relationship given by eq. (2.34). For convenience, the relationship is

$$G_i = \frac{K_i^2}{E'} \quad (3.5)$$

where $E' = E$ for plane stress (MPa)
$E' = E / \left(1 - v^2 \right)$ for plane strain (MPa)
E = Elastic modulus of elasticity (MPa)
v = Poisson's ratio

This expression, eq. (3.5), is a fundamental mathematical model in the fracture mechanics field, specifically for mode I.

3.3   WESTERGAARD'S STRESS FUNCTION

Using mode I as a basis, the coordinate system defining a double-ended crack in a complex form is shown in Figure 3.2. This is a classical representation of Westergaard's approach for developing stress functions near an elliptical crack of total length $2a$.
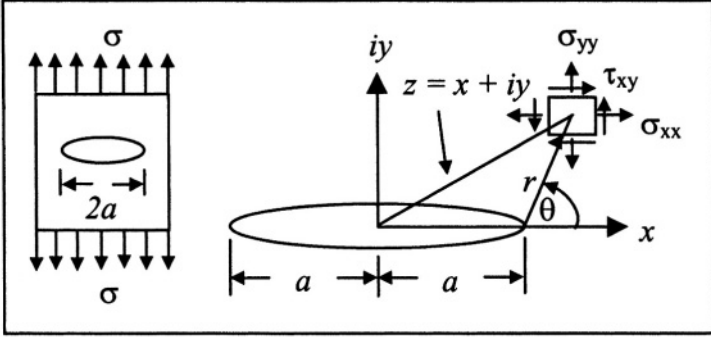

Figure 3.2 The crack tip stress field in complex coordinates

The Airy's complex function and Westergaard's complex function are, respectively [1,11]

$$\phi \;=\; \operatorname{Re}\overline{Z'} + y\operatorname{Im}\overline{Z} \qquad \text{(Airy's)} \qquad (3.6)$$

$$Z(z) \;=\; \operatorname{Re}Z + i\operatorname{Im}Z \qquad \text{(Westergaard's)} \qquad (3.7)$$

where $\operatorname{Re}\overline{Z}$ = Real part
$\operatorname{Im}\overline{Z}$ = Imaginary part
Z = Analytic stress function
$i = \sqrt{-1}$
$i^2 = -1$

Below are some supportive and useful expressions for developing the elastic stress functions. Hence,

$$\overline{Z'} \;=\; \int \overline{Z}\,dz \qquad \overline{Z} = \int \overline{Z}\,dz \qquad (3.8a)$$

$$Z' \;=\; \frac{dZ}{dz} \qquad Z = \int Z'\,dz \qquad (3.8b)$$

$$\frac{\partial\left(\operatorname{Re}Z\right)}{\partial x} \;=\; \operatorname{Re}Z' \qquad \frac{\partial\left(\operatorname{Re}Z\right)}{\partial y} = -\operatorname{Im}Z' \qquad (3.9a)$$

$$\frac{\partial\left(\operatorname{Im}Z\right)}{\partial x} \;=\; \operatorname{Im}Z' \qquad \frac{\partial\left(\operatorname{Im}Z\right)}{\partial y} = \operatorname{Re}Z' \qquad (3.9b)$$

$$\frac{\partial\left(-y\operatorname{Re}Z + \operatorname{Im}\overline{Z}\right)}{\partial x} \;=\; y\operatorname{Im}Z' - \operatorname{Re}Z \qquad (3.9c)$$

For the ellipse in Figure 3.2, the complex function and its conjugate are, respectively

$$z = x + iy = r \exp(i\theta) \tag{3.10}$$
$$\bar{z} = x - iy = r \exp(-i\theta) \tag{3.11}$$

and

$$\exp(\pm i\theta) = \cos\theta \pm i\sin\theta \tag{3.12}$$
$$y = r\sin\theta \tag{3.13}$$

Furthermore, the **Cauchy-Riemann equations** in some domain D are considered fundamental and sufficient for a complex function to be analytic in D. Letting $z = u(x,y) + iv(x,y)$, then the Cauchy-Riemann important theorem states that $\partial u/\partial x = \partial v/\partial y$ and $\partial v/\partial y = -\partial u/\partial x$ so that the function z be analytic. The Cauchy-Riemann condition is of great practical importance for determining elastic stresses. Hence,

$$\nabla^2 \operatorname{Re} Z = \nabla^2 \operatorname{Im} Z = 0 \tag{3.14}$$

which must be satisfied by an Airy's stress function. The operator ∇^2 in rectangular and polar coordinates takes the form

$$\nabla^2 = \frac{\partial^2}{\partial x^2} + \frac{\partial^2}{\partial y^2} + \frac{\partial^2}{\partial z^2} \tag{3.15a}$$
$$\nabla^2 = \frac{\partial^2}{\partial r^2} + \frac{1}{r}\frac{\partial}{\partial r} + \frac{1}{r^2}\frac{\partial^2}{\partial \theta^2} \tag{3.15b}$$

Assume that the Airy's partial derivatives given by eq. (1.9) are applicable to elastic materials. Hence,

$$\sigma_{xx} = \frac{\partial^2 \phi}{\partial y^2} + \Omega \tag{3.16}$$

$$\sigma_{yy} = \frac{\partial^2 \phi}{\partial x^2} + \Omega \tag{3.17}$$

$$\tau_{xy} = -\frac{\partial^2 \phi}{\partial x \partial y} \tag{3.18}$$

Thus,

$$\frac{\partial \phi}{\partial x} = \frac{\partial \left(\operatorname{Re}\overline{Z'}\right)}{\partial x} + \frac{\partial \left(y \operatorname{Im}\overline{Z}\right)}{\partial x} = \operatorname{Re}\overline{Z} + y \operatorname{Im} Z \tag{3.19}$$

$$\frac{\partial^2 \phi}{\partial x^2} = \frac{\partial \left(\operatorname{Re}\overline{Z}\right)}{\partial x} + \frac{\partial \left(y \operatorname{Im} Z\right)}{\partial x} = \operatorname{Re} Z + y \operatorname{Im} Z'$$

$$\frac{\partial \phi}{\partial y} = \frac{\partial \left(\operatorname{Re}\overline{Z'}\right)}{\partial y} + \frac{\partial \left(y \operatorname{Im}\overline{Z}\right)}{\partial y} = -\operatorname{Im}\overline{Z} + y \operatorname{Re} Z + \operatorname{Im}\overline{Z} = y \operatorname{Re} Z$$

$$\frac{\partial^2 \phi}{\partial y^2} = \frac{\partial \left(y \operatorname{Re} Z\right)}{\partial y} = \operatorname{Re} Z \frac{\partial \left(y\right)}{\partial y} + y \frac{\partial \left(\operatorname{Re} Z\right)}{\partial y} \operatorname{Re} Z - y \operatorname{Im} Z'$$

$$\frac{\partial \phi}{\partial x \partial y} = \frac{\partial \left(\operatorname{Re}\overline{Z}\right)}{\partial y} + \frac{\partial \left(y \operatorname{Im} Z\right)}{\partial y} = -\operatorname{Im} Z + y \operatorname{Re} Z' + \operatorname{Im} Z = y \operatorname{Re} Z'$$

Substituting eq. (3.19) into eq. (3.18) along with $\Omega = 0$ yields the Westergaard's stresses in two-dimensions

$$\begin{aligned}
\sigma_{xx} &= \operatorname{Re} Z - y \operatorname{Im} Z' \\
\sigma_{yy} &= \operatorname{Re} Z + y \operatorname{Im} Z' \qquad \text{(Westergaard's)} \\
\tau_{xy} &= -y \operatorname{Re} Z'
\end{aligned} \tag{3.20}$$

These are the stresses, eq. (3.20), that were proposed by Westergaard as the stress singularity field at the crack tip. However, additional terms must be added to the stress functions, eq. (3.20), analytic over an entire region, for an adequate representation of a stress field adjacent to the crack tip. This implies that when solving practical problems, additional boundary conditions must be imposed on the stresses. This leads to the well-known boundary value problem in which the boundary value method (BVM) is an alternative technique to the most commonly finite element method (FEM) and finite difference method (FDM). Therefore, the original Westergaard's stresses no longer give a unique solution and the analysis of the stress field in a region near the crack tip is of extreme importance.

Consider a **classical problem** in fracture mechanics in which a plate containing an elliptical crack, as shown in Figure 3.2, is subjected to biaxial stress, $\sigma_1 = \sigma_2 = \sigma$, where the Westergaard's stress function $Z(z)$ applies to this problem [1].

3.3.1   FAR-FIELD BOUNDARY CONDITIONS

The function Z is considered to be analytic because its derivative dZ/dz is defined unambiguously and the origin is located at the center of the ellipse (Figure 3.2). Let the Westergaard's complex function be defined by [1]

$$Z = \frac{z\sigma}{\sqrt{z^2 - a^2}} \qquad \text{and} \qquad Z' = 0 \tag{3.21}$$

However, the far-field boundary conditions require that $z \to \infty$ and $z \gg a$. Consequently, eq. (3.21) becomes

$$Z = \frac{Z\sigma}{\sqrt{z^2}} = \sigma \tag{3.22}$$

from which $\operatorname{Re} Z = \sigma$ and $\operatorname{Im} Z' = 0$. Substituting eq. (3.22) into (3.20) yields

$$
\begin{aligned}
\sigma_{xx} &= \operatorname{Re} Z - y \operatorname{Im} Z' = \sigma \\
\sigma_{yy} &= \operatorname{Re} Z + y \operatorname{Im} Z' = 0 \\
\tau_{xy} &= -y \operatorname{Re} Z' = 0
\end{aligned}
\tag{3.23}
$$

On the crack surface: If y = 0 and $z = x$ for $-a \le x \le +a$, then $Re\ Z = 0$ and $\sigma_{yy} = \tau_{xy} = 0$. Therefore, Z is not an analytical function because it does not have a unique derivative at a point.

3.3.2 NEAR-FIELD BOUNDARY CONDITIONS

Locate the origin at the crack tip in Figure 3.2 so that the Westergaard complex function becomes [1]

$$Z = \frac{(z+a)\,\sigma}{\sqrt{(z+a)^2 - a^2}} = \frac{(z+a)\,\sigma}{\sqrt{z^2 + 2az}} \tag{3.24}$$

The near-field boundary conditions are $z \ll a$ near the crack tip and $z = r \exp(iN\theta)$, where N is a real number. Hence, eq. (3.24) becomes

$$Z = \frac{(z+a)\,\sigma}{\sqrt{(z+a)^2 - a^2}} = \frac{a\sigma}{\sqrt{2az}} \tag{3.25a}$$

$$Z = \sigma\sqrt{\frac{a}{2}}\cdot z^{-1/2} = \sigma\sqrt{\frac{a}{2r}}\cdot\exp\left(-i\theta/2\right) \tag{3.25b}$$

$$Z = \sigma\sqrt{\frac{a}{2r}}\left(\cos\frac{\theta}{2} - i\sin\frac{\theta}{2}\right) \tag{3.25c}$$

from which the real and imaginary parts are extracted as

$$\operatorname{Re} Z = \sigma\sqrt{\frac{a}{2r}}\cos\frac{\theta}{2} \tag{3.26a}$$

$$\operatorname{Im} Z = -\sigma\sqrt{\frac{a}{2r}}\sin\frac{\theta}{2} \tag{3.26b}$$

The stresses, eq. (3.20), along the crack line, where $y = 0$ and $\theta = 0$, take the form

$$
\begin{aligned}
\sigma_{xx} &= \operatorname{Re} Z - y \operatorname{Im} Z' = \sigma \sqrt{\frac{a}{2r}} \\
\sigma_{yy} &= \operatorname{Re} Z + y \operatorname{Im} Z' = \sigma \sqrt{\frac{a}{2r}} \qquad (3.27) \\
\tau_{xy} &= -y \operatorname{Re} Z' = 0
\end{aligned}
$$

If the plastic zone ahead of the crack tip is $r \to 0$, then the stress becomes $\sigma \to \infty$. This stress defines what is referred to as "a singularity state of stress." which is in the order of $r^{-1/2}$ along the x-axis.

Substituting eq. (3.3.27) into (3.1) yields the stress intensity factor for infinite specimen dimensions (uncorrected) and finite specimen dimensions (corrected) under mode I, respectively

$$
\begin{aligned}
K_I &= \sigma \sqrt{\pi a} \qquad \text{(Uncorrected)} \qquad (3.28) \\
K_I &= \alpha \sigma \sqrt{\pi a} \qquad \text{(Corrected)} \qquad (3.29)
\end{aligned}
$$

where $\alpha = f(a/w) =$ Crack geometric correction factor
$\quad\quad w =$ Specimen width

The function $\alpha = f(a/w)$ makes the surface traction stresses vanish [4]. If $a/w \to 0$, then $\alpha = f(0) \geq 1$. Hence, eq. (3.29) reduces to (3.28). In addition, K_I has units in MPa or ksi . The K_I expression, eq. (3.28), is for an infinite (large) plate and it is a linear function of the applied stress (σ), and it increases with initial crack size (a). This is shown in Figure 3.3.
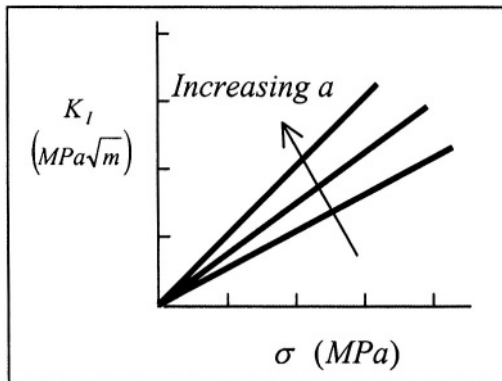
Figure 3.3 Linear behavior of $K_I = f(\sigma)$.

The onset of crack propagation is a **critical condition** so that the crack a) extends suddenly by tearing in a shear-rupture failure or b) extends suddenly at high velocity for cleavage fracture. All this means that the crack is unstable when a critical condition exists due to an applied load. In this case, the stress intensity factor reaches a critical magnitude and it is treated as a material property called fracture toughness. For sufficiently thick materials, the **plane strain fracture toughness** (K_{IC}) is a material property that measures crack resistance. Therefore, the fracture criterion by K_{IC} states that crack propagation occurs when $K_I \geq K_{IC}$, which defines a failure criterion for brittle materials.

This simply implies that the crack extends to reach a critical crack length $(a = a_c)$, defining a critical state in which the crack speed is in the magnitude of the speed of sound for most brittle materials. In fact, the LEFM theory is well documented and the ASTM E399 Standard Testing Method, Vol. 03.01, validates the K_{IC} data and assures the minimum thickness through Brown and Strawley [27] empirical equation

$$a, B \geq 2.5 \left(\frac{K_{IC}}{\sigma_{ys}} \right)^2 \qquad \text{For } a > r \qquad (3.30)$$

3.4   SPECIMEN GEOMETRIES

In general, the successful application of linear elastic fracture mechanics to structural analysis, fatigue, and stress corrosion cracking requires a known stress intensity factor equation for a particular specimen configuration. Cracks in bodies of finite size are important since cracks pose a threat to the instability and safety of an entire structure.

If mode I loading system is considered, then it is important to determine the applied stress intensity factor K_I and the plane strain fracture toughness K_{IC} for a specific geometry in order to assess the safety factor for the cracked body. In fact, mode I (opening) loading system is the most studied and evaluated mode for determining the mechanical behavior of solids having specific geometries exposed to a particular environment. Some selected and practical crack configurations are shown in Table 3.1.

3.4.1   THROUGH-THE-THICKNESS CENTER CRACK

This is a commonly encountered crack configurations under a remote applied stress as shown in Table 3.1. The geometric correction factor α expression is given in Table 3.1 and graphically shown in Figure 3.4 as per different authors cited below. For a finite width plate, the geometric correction factor is defined by
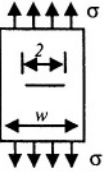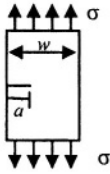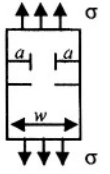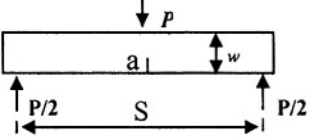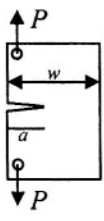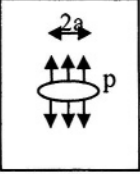
Table 3.1 Crack Configurations and related geometric correction factors for $K_I = \alpha\sigma\sqrt{\pi a}$ **and** $\sigma = P/(Bw)$

1) Through-Thickness Center Crack (CCT)

$$\alpha = \left(\sec\frac{\pi a}{w}\right)^{1/2} \approx \left(\frac{w}{\pi a}\tan\frac{\pi a}{w}\right)^{1/2} \quad for \quad 0 < a < 0.5$$

$$\alpha \approx \left[1 + 0.50(a/w)^2 + 20.46(a/w)^4 + 81.72(a/w)^6\right]^{1/2}$$

2) Single-edge Crack (SET)

$$\alpha = 1.12 - 0.23(a/w) + 10.55(a/w)^2 - 21.71(a/w)^3$$
$$+ 30.38(a/w)^4$$

3) Double-edge Crack)DET)

$$\alpha = 1.12 + 0.41(a/w) - 4.78(a/w)^2 + 15.44(a/w)^3$$

4) Three-Point Bending (SEB)

$$\alpha = \frac{XS}{\sqrt{aw}\cdot(1 + 2a/w)(1 - a/w)^{3/2}}$$

$$X = \left[1.68 - 1.82(a/w) + 1.51(a/w)^2 - 5.61(a/w)^3 + 2.28(a/w)^4 \right]$$

Table 3.1 Crack Configurations and related geometric correction factors for $K_I = \alpha\sigma\sqrt{\pi a}$ and $\sigma = P/(Bw)$ (continued)
5) Compact Tension (CT)
$\alpha = \dfrac{(2 + a/w)wX}{\sqrt{aw}\cdot(1 - a/w)^3}$ $X = \Big[\ 0.50 + 2.62(a/w) - 7.52(a/w)^2$ $\qquad\qquad + 8.30(a/w)^3 - 3.16\,(a/w)^4\Big]$
6) Internal Crack (ITT)
$K_I = P\sqrt{\pi a}$
$K_I = \sigma\sqrt{\pi a}\,\sin^2\beta$ $K_{II} = \sigma\sqrt{\pi a}\,\sin\beta\cos\beta$
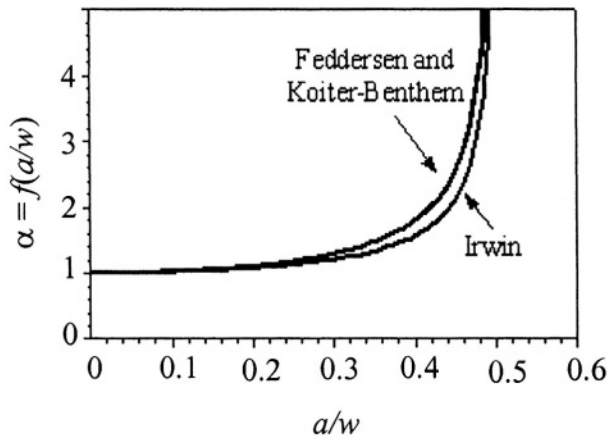
Figure 3.4 Correction factor for a central cracked plate

$$\alpha \;=\; \sqrt{\sec\left(\frac{\pi a}{w}\right)} \qquad \text{for } 0 < a \le 0.5 \qquad \text{Feddersen [12]} \qquad (3.31a)$$

$$\alpha \;=\; \sqrt{\frac{w}{\pi a}\tan\left(\frac{\pi a}{w}\right)} \qquad \text{for } 0 < a \le 0.5 \qquad \text{Irwin [13]} \qquad (3.31b)$$

$$\alpha \;=\; \frac{1 - (a/w) + 1.304\,(a/w)^2}{\sqrt{1 - 2a/w}} \quad \text{for } 0 < a \le 0.5 \text{ Koiter et al. [14]} (3.32)$$

Example 3.1 *A large plate* $(2a \ll w)$ *containing a central crack* 40-*mm long is subjected to a tension stress as shown in the figure below. If the crack growth rate is 10 mm/month and fracture is expected at 10 months from now, calculate the fracture stress. Data:* $K_{IC} = 30 \; MPa\sqrt{m}$.

Solution:
If the crack growth rate is defined by

$$\frac{da}{dt} = \frac{2a_c - 2a}{t}$$

Then

$$2a_c \;=\; 2a + t\left(\frac{da}{dt}\right)$$

$$2a_c \;=\; 40 \; mm + (10 \; month)\,(10 \; mm/month)$$

$$a_c \;=\; 70 \; mm$$

Now, the fracture stress can be calculated using eq. (3.29). A large plate implies that $a/w \to 0$ *and from Table 3.1 the geometric correction factor becomes* $\alpha = \sqrt{\sec(\pi a/w)} \to 1$. *Thus, the fracture stress is*

$$\sigma_f \;=\; \frac{K_{IC}}{\alpha\sqrt{\pi a_c}}$$

$$\sigma_f \;=\; \frac{30 MPa\sqrt{m}}{(1)\,\sqrt{\pi\,(70x10^{-3} \; m)}} = 64 \; MPa$$

Example 3.2 *A large and thick plate containing a though-the-thickness central crack is* 4-*mm long and it fractures when a tensile stress of* 7 MPa *is applied. Calculate the strain-energy release rate using a) the Griffith theory and b) the LEFM approach. Should there be a significant difference between results? Explain. Data:* $E = 62,000 \; MPa$ *and* $v = 0.20$.

Solution:
The total crack size is $2a = 4mm$. a) Using eq. (2.35) yields

$$\sigma_c = \sqrt{\frac{E'G_{IC}}{\pi a}}$$

$$G_{IC} = \frac{\pi a \sigma_f^2}{E'} = \frac{\pi \left(1 - v^2\right) a \sigma_f^2}{E}$$

$$G_{IC} = \frac{\pi \left(1 - 0.2^2\right) \left(2x10^{-3} \ m\right) \left(7 \ MPa\right)^2}{62,000 \ MPa}$$

$$G_{IC} = 4.77x10^{-6} \ MPa.m = 4.77 \ J/m^2$$

b) Using eq. (3.29) along with $\alpha = \sqrt{\sec\left(\pi a/w\right)} = 1$ and $K_I = K_{IC}$ gives

$$K_{IC} = \alpha \sigma \sqrt{\pi a}$$

$$K_{IC} = (1)(7 \ MPa) \sqrt{\pi \left(2x10^{-3} \ m\right)}$$

$$K_{IC} = 0.555 \ MPa\sqrt{m}$$

From eq. (2.34),

$$G_{IC} = \frac{K_{IC}^2}{E'} = \frac{\left(1 - v^2\right) K_{IC}^2}{E}$$

$$G_{IC} = \frac{\left(1 - 0.2^2\right) \left(0.555 \ MPa\sqrt{m}\right)^2}{62,000 \ MPa}$$

$$G_{IC} = 4.77x10^{-6} \ MPa.m = 4.77 \ J/m^2$$

These results indicate that there should not be any difference because either approach gives the same result.

3.4.2 ELLIPTICAL CRACKS

This section deals with elliptical and circular cracks. According to Irwin's analysis [13] on an infinite plate containing an embedded elliptical crack (Figure 3.5) loaded in tension, the stress intensity factor is defined by

$$K_I = \frac{\sigma \sqrt{\pi a}}{\Phi} \left[\sin^2 \lambda + \left(\frac{a}{c}\right)^2 \cos^2 \lambda\right]^{1/4} \tag{3.33}$$

which can be evaluated at a point on the perimeter of the crack. This point is located at an angle λ with respect to the direction of the applied tensile stress.
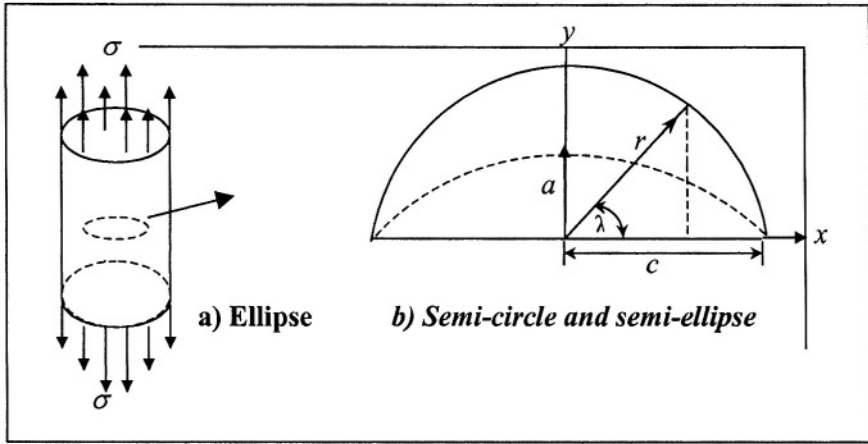
Figure 3.5 Embedded elliptical crack

In addition, the elliptical integral of the second kind is of the form

$$\Phi = \int_{o}^{\pi/2} \left[1 - \left(\frac{c^2 - a^2}{c^2} \right) \sin^2 \lambda \right]^{1/2} d\lambda \tag{3.34}$$

If $a = c$, the ellipse becomes a circle and eq. (3.33) takes the form

$$K_I = \frac{2}{\pi} \sigma \sqrt{\pi a} \tag{3.35}$$

This expression, eq. (3.35), is the equation for a circular internal crack of radius (also known as penny-shaped crack) developed by Sneddon [15]. In this case, the correction factor for a round crack is simply given by $\alpha = 2/\pi$. Actually, eq. (3.35) can also be used for a specimen containing semicircular surface flaw.

Furthermore, values of Φ can be found in mathematical tables or approximated by expanding eq. (3.34) in a Taylor's series form [6]. Hence,

$$\Phi = \frac{\pi}{2} \left[1 - \frac{1}{4} \left(\frac{c^2 - a^2}{c^2} \right) - \frac{3}{64} \left(\frac{c^2 - a^2}{c^2} \right)^2 - \ldots \right] \tag{3.36}$$

Neglecting higher terms in the series, the margin of error is not significant; and therefore, the correction factor Φ can further be approximated using the first two terms in the series given by eq. (3.36). Thus,

$$\Phi = \frac{\pi}{2} \left[1 - \frac{1}{4} \left(\frac{c^2 - a^2}{c^2} \right) \right] = \frac{\pi}{2} \left[\frac{3}{4} + \left(\frac{a}{2c} \right)^2 \right] \tag{3.37}$$

Inserting eq. (3.37) into (3.33) and evaluating the result on the perimeter of the ellipse yields

$$K_I = \frac{2\sigma\sqrt{\pi a}}{\pi\left[3/4 + (a/2c)^2\right]}\left[\sin^2\lambda + \left(\frac{a}{c}\right)^2\cos^2\lambda\right]^{1/4} \tag{3.38}$$

$$K_I = K_{\max} = \frac{2\sigma\sqrt{\pi a}}{\pi\left[3/4 + (a/2c)^2\right]} \qquad @ \lambda = \pi/2 \tag{3.39}$$

$$K_I = K_{\min} = \frac{2\sigma\sqrt{\pi a}}{\pi\left[3/4 + (a/2c)^2\right]}\sqrt{\frac{a}{c}} \qquad @ \lambda = 0 \tag{3.40}$$

The condition $\lambda = \pi/2$ is vital in evaluating elliptical crack behavior because $K_{\max}$ can be predicted for crack instability.

3.4.3   PART-THROUGH THUMBNAIL SURFACE FLAW

The stress intensity factor for a plate of finite width being subjected to a uniform and remote tensile stress (mode I) is further corrected as indicated below [21,24]

$$K_I = MM_k\sigma\sqrt{\pi a/Q}\left[\sin^2\lambda + \left(\frac{a}{c}\right)^2\cos^2\lambda\right]^{1/4} \tag{3.41}$$

$$Q = \Phi^2 - \frac{2}{3\pi}\left(\frac{\sigma}{\sigma_{ys}}\right)^2 \tag{3.42}$$

$$\sigma = \frac{Pd}{2B} \tag{3.43}$$

where M = Magnification correction factor

M_k = Front face correction factor [21,24] shown in Figure 3.6b

σ = Applied hoop stress or design stress as per Figure 3.6

Q = Shape factor for a surface flaw

P = Internal pressure (MPa)

Combining eqs. (3.37), (3.42) and (3.43) yields a convenient mathematical expression for predicting the shape factor

$$Q = \left(\frac{\pi}{2}\right)^2\left[\frac{3}{4} + \left(\frac{a}{2c}\right)^2\right]^2 - \frac{7}{33}\left(\frac{\sigma}{\sigma_{ys}}\right)^2 \tag{3.44}$$
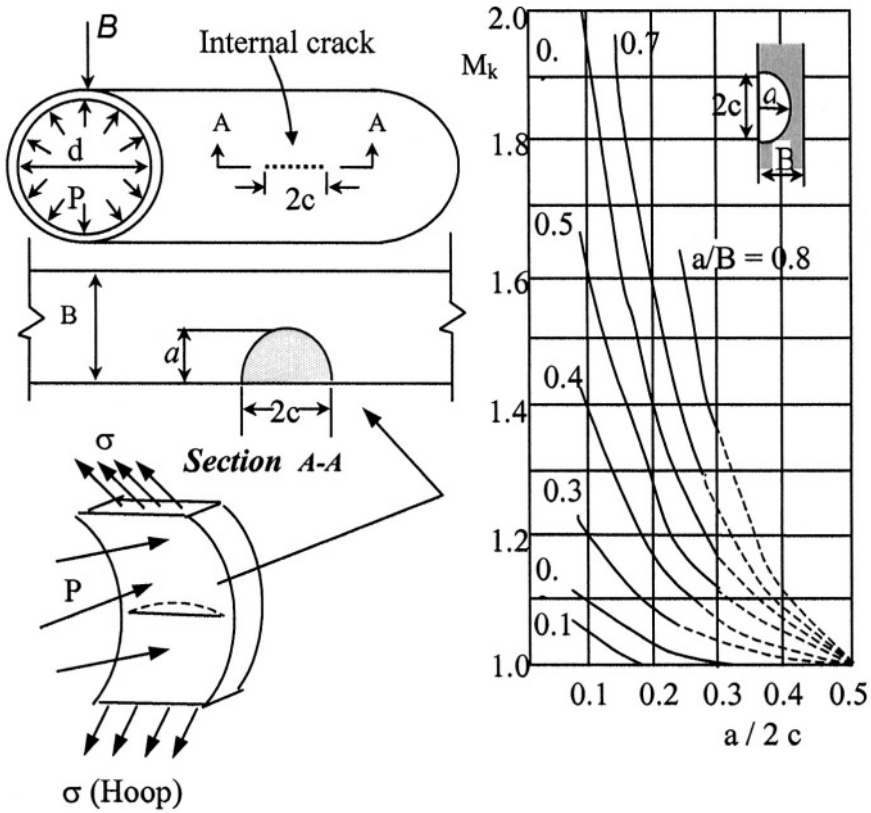
Figure 3.6 Front face correction factor M_K for a semi-elliptical surface flaw [21-22].

Manipulating eq. (3.44) and rearranging it yields an expression for predicting the elliptical axes ratio when the shape factor is known. Thus,

$$\frac{a}{2c} = \left[\frac{2}{\pi} \sqrt{Q + \frac{7}{33} \left(\frac{\sigma}{\sigma_{ys}} \right)^2} - \frac{3}{4} \right]^{1/2} \qquad (3.45)$$

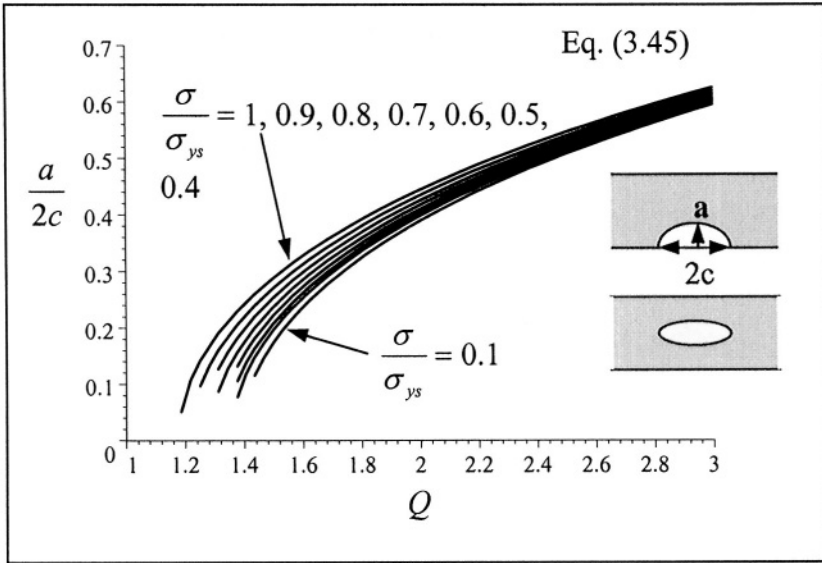Equation (3.345) can be used to plot a series of curves as shown in Figure 3.7.

Figure 3.7 Shape factor Q for internal and surface flaws.

The Magnification correction factor takes the form [21-22, 24]

$$M = 0.4 + 1.2 \left(\frac{a}{B}\right) \qquad \text{For } 0.5 \le \frac{a}{B} \le 1.0 \qquad (3.46)$$

If a back free-surface correction factor of 1.12 and plastic deformation are considered, then eq. (3.41) is further corrected as

$$K_I = 1.12 M M_k \sigma \sqrt{\pi(a+r)/Q} \qquad \text{For } \lambda = \pi/2 \qquad (3.47)$$

Example 3.3 *A steel pressure vessel (Figure 3.6) is subjected to a hoop stress of 420 MPa perpendicular to the crack depth acts as a tensile stress. The vessel has an internal semi-elliptical surface crack of dimensions a = 3 mm, 2c = 10 mm, B = 6 mm. a) Use eq. (3.42) to calculate K_I. b) Will the pressure vessel leak? Explain. Use the following data: $\sigma_{ys} = 900$ MPa and $K_{IC} = 60$ MPa .*

Solution:
a) *The following parameters are needed for calculating the stress-intensity factor. Thus,*

$$\frac{a}{2c} = 0.30, \; \frac{a}{B} = 0.50, \; \frac{\sigma}{\sigma_{ys}} = 0.60$$

$$Q = 1.7 \; from \; eq. \; (3.44) \; and \; Figure \; 3.7$$

$$M_k = 1.12 \; from \; Figure \; 3.6b$$

$$M = 1.00 \; from \; eq. \; (3.46)$$

The plastic zone size can be determined using eq. (3.1) *along* $\sigma_{yy} = \sigma_{ys}$. *This implies that a plastic zone develops as long as the material yields ahead of the crack tip. Thus,*

Collecting all correction factor gives

$$\alpha = 1.12 M M_k / \sqrt{Q} = 0.9621$$

$$K_I = \alpha \sigma \sqrt{\pi a} = 39.23 \; MPa\sqrt{m}$$

b) The pressure vessel will not leak because $K_I < K_{IC}$, *but extreme caution should be taken because* $K_I = K_{IC}/S_f = 0.79 K_{IC}$. *Thus, the safety factor is* $S_f = 60/47.56 = 1.26$. *If* $K_I = K_{IC}$, *then leakage would occur.*

3.4.4 LEAK-BEFORE-BREAK CRITERION

Designing thin-wall pressure vessels to store fluids is a common practice in engineering. By definition, a thin-wall pressure vessel requires that the plate thickness (B) be small as compared with the vessels internal diameter (d); that is, $B << d$ or $B/d \to 0$ as shown in Figure 3.6. If curved plates are welded to make pressure vessels, the welded joints become the weakest areas of the structure since weld defects can be the source of cracks during service.

Accordingly, the internal pressure P acts in the radial direction (Figure 3.6) and the total force for rupturing the vessel on a diametral plane is $P(dL)$, where dL is the projected area. Assuming that the stress across the thickness and that the cross-sectional area is $A = 2BL$, the force balance is $P(dL) - \sigma(2bL) = 0$ which gives eq. (3.43). The hoop stress is the longitudinal stress and the transverse stress is half the longitudinal one. These stress are principal stresses in designing against yielding. Normally, the design stress is the hoop stress divide by a safety factor in the range of $1 < SF < 5$.

For welded joints in pressure vessels, a welding efficient, $0.80 \leq \varepsilon \leq 1$, can be included in the hoop stress expression to account for weak welded joints [28]. Thus, eq. (3.43) becomes

$$B = \frac{Pd}{2\varepsilon\sigma} \tag{3.48}$$

Let's assume that internal surface cracks develop at welded joints or at any other area of the vessel. In such a scenario, the leak-before-break criterion

proposed by Irwin et al. [26] can be used to predict the fracture toughness of pressure vessels. This criterion allows an internal surface crack to grow through the thickness of the vessel so that $a = B$ for leakage to occur. This means that the critical crack length must be greater than the vessel thickness; that is, $a_c > B$. Assuming a semicircular through the thickness crack the effective crack length is defined as $2a = 2B$.

The fracture toughness relationship between plane stress and plane strain conditions to establish the leak-before-break criterion may be estimated using an empirical relationship developed by Irwin et al. [26]. Thus, the plane stress fracture toughness is $K_I = K_C$ and

$$K_C = K_{IC}\sqrt{1 + \frac{7}{5B^2}\left(\frac{K_{IC}}{\sigma_{ys}}\right)^4} \tag{3.49a}$$

Irwin's expression [26] for plane stress fracture toughness is derived in Chapter 5 and given here for convenience. Thus,

$$K_C^2 = \frac{\pi a \sigma^2}{1 - 0.5\left(\sigma/\sigma_{ys}\right)^2} \tag{3.49b}$$

Combining eqs. (3.48) and (3.49) along with $\sigma = \sigma_{ys}$ as the critical condition and $a = B$ yields the leak-before-break criterion for plane strain condition

$$K_{IC}^6 + 0.71B^2\sigma_{ys}^4 K_{IC}^2 - 4.49B^3\sigma_{ys}^6 = 0 \tag{3.50}$$

Use of this criterion requires that the vessel thickness meets the yielding requirement to withstand the internal pressure and the ASTM E399 thickness requirement.

Example 3.4 *A pressure vessel made of Ti-6Al-4V alloy using a welding fabrication technique is used in rocket motors as per Faires [28]. Helium (He) is used to provided pressure on the fuel and lox (liquid oxygen). The vessel internal diameter and length are 0.5 m and 0.6 m, respectively, and the internal pressure is* $28\ MPa$. *Assume a semicircular crack develops, a welding efficiency of 100% and a safety factor of 1.6 to calculate the thickness uniform thickness of the vessel. Use the resultant thickness to calculate the fracture toughness according to eq. (3.50). Select a yield strength of* $\sigma_{ys} = 900\ MPa$.

Solution:

The design stress against general yielding is

$$\sigma = \frac{\sigma_{ys}}{SF} = \frac{900\ MPa}{1.5} = 600\ MPa$$

From eq. (3.48),

$$B = \frac{Pd}{2\varepsilon\sigma} = \frac{(28 \ MPa)(0.5 \ m)}{(2)(1)(600 \ MPa)} \tag{3.48}$$

$$B = 1.17x10^{-2} \ m = 1.17 \ cm = 0.46 \ in$$

From eq.(3.50),

$$0 = K_{IC}^6 + 0.71\left(1.17x10^{-2} \ m\right)^2 (900 \ MPa)^4 K_{IC}^2 \tag{3.50}$$
$$-4.49\left(1.17x10^{-2} \ m\right)^3 (900 \ MPa)^6$$
$$K_{IC} = 119.49 \ MPa\sqrt{m}$$

From eq. (3.49a),

$$K_C = K_{IC}\sqrt{1 + \frac{7}{5B^2}\left(\frac{K_{IC}}{\sigma_{ys}}\right)^4} \tag{3.49a}$$

$$K_C = \left(119.49 \ MPa\sqrt{m}\right)\sqrt{1 + \frac{7\,(39.16)^4}{5\,(3.73x10^{-2})^2\,(900)^4}}$$

$$K_C = 121.66 \ MPa\sqrt{m}$$

In summary, select the proper heat treatment for Ti-6Al-4V alloy so that $\sigma_{ys} = 900 \ MPa$ and $K_{IC} = 119.49 \ MPa\sqrt{m}$. According to theses results, AerMet 100 meets the design requirements.

3.4.5   RADIAL CRACKS AROUND CYLINDERS

Another commonly encountered surface crack configuration under a remote applied tension, torsion or a combined loading system is shown in Figure 3.8. However, the mixed-mode interaction is of great interest in this section.

Hence, the stress intensity factors for the loading system illustrated in Figure 3.8 are

$$K_I = f(d/D)\sigma\sqrt{\pi a} \tag{3.51}$$
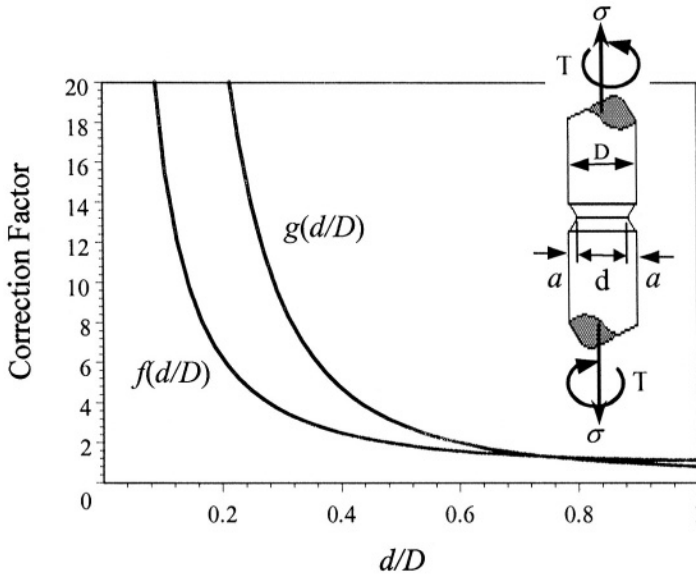$$K_{III} = g(d/D)\tau\sqrt{\pi a} \tag{3.52}$$

Figure 3.8 Radial crack around a cylinder.

For an applied torque T, the torsional shear stress becomes

$$\tau = \frac{16T}{\pi D^3} \tag{3.53}$$

The correction factors, $f(d/D)$ and $g(d/D)$, were derived by Koiter and Benthem [14] as

$$f(d/D) = \frac{1}{2}\sqrt{\frac{D}{d}}\left[\frac{D}{d} + \frac{1}{2} + \frac{3}{8}\left(\frac{d}{D}\right) - \frac{5}{14}\left(\frac{d}{D}\right)^2 + \frac{11}{15}\left(\frac{d}{D}\right)^3\right] \tag{3.54}$$

$$g(d/D) = \frac{3}{8}\sqrt{\frac{D}{d}}\left[\begin{array}{c}\left(\frac{D}{d}\right)^2 + \frac{1}{2}\left(\frac{D}{d}\right) + \frac{3}{8} + \frac{5}{16}\left(\frac{d}{D}\right) \\ -\frac{35}{128}\left(\frac{d}{D}\right)^2 + \frac{13}{62}\left(\frac{d}{D}\right)^3\end{array}\right] \tag{3.55}$$

The crack length (size) is estimated as

$$a = \frac{D - d}{2} \tag{3.56}$$

Example 3.5 *Two identical high-strength steel rods are prepared for a tension test at 106 MPa and one for torsion at 69 MPa. Calculate K_I and K_{III}. The rod dimensions are $d = 4$ mm and $D = 8$ mm. If $K_{IIIC} = \sqrt{3/4}K_{IC}$, a)*

Will the rods fracture? Explain, b) Calculate the theoretical fracture tensile and torsion stresses if fracture does not occur in part a). Use $K_{IC} = 25 \ MPa\sqrt{m}$.

Solution:

Given data: $\sigma = 106 \ MPa$ $\tau = 69 \ MPa$ $K_{IC} = 25 \ MPa\sqrt{m}$
a) The crack length and the radius ratios are, respectively
$a = (D - d)/2 = (8mm - 4mm)/2 = 2 \ mm$
$d/D = 0.50$ $D/d = 2$

From eqs. (3.54) and (3.55) or Figure 3.8,
$f(d/D) = 1.90$ *and* $g(d/D) = 2.91$

Hence, the applied stress intensity factors are calculated using eqs. (3.51) and (3.52)

$$
\begin{aligned}
K_I &= f(d/D)\,\sigma\sqrt{\pi a} = 16 MPa\sqrt{m} \\
K_{III} &= g(d/D)\,\tau\sqrt{\pi a} = 16 MPa\sqrt{m} \\
K_{IIIC} &= \sqrt{3/4} \cdot K_{IC} = 21.65 MPa\sqrt{m}
\end{aligned}
$$

Therefore, neither rod will fracture since both stress intensity factors are below their critical values; that is, $K_I < K_{IC}$ and $K_{III} < K_{IIIC}$.

b) The fracture stress are

$$
\begin{aligned}
\sigma_f &= \frac{K_{IC}}{f(d/D)\,\sqrt{\pi a}} = 166 \ MPa \\
\tau_f &= \frac{K_{IIIC}}{g(d/D)\,\sqrt{\pi a}} = 94 \ MPa
\end{aligned}
$$

3.5 FRACTURE CONTROL

Structures usually have inherent flaws or cracks introduced during 1) welding process due to welds, embedded slag, holes, porosity, lack of fusion and 2) service due to fatigue, stress corrosion cracking *(SCC),* impact damage and shrinkage.

A fracture-control practice is vital for design engineers in order to assure the integrity of particular structure. This assurance can be accomplished by a close control of

1) Design constraints   4) Maintenance
2) Fabrication   5) Nondestructive evaluation (NDE)
3) General yielding   6) Environmental effects

The pertinent details for the above elements depend on codes and procedures that are required by a particular organization. However, the suitability of a structure to brittle fracture can be evaluated using the concept of fracture mechanics, which is the main subject in this section. For instance, the elapsed time for crack-initiation and crack-propagation determines the useful life of a structure, for which the combination of an existing crack size, applied stress, and loading rate may cause the stress intensity factor reach a critical value.

In order to describe the technical aspects of a fracture control plan, consider a large plate (infinite plate) with a certain plane strain fracture toughness K_{IC} so that $K_I < K_{IC}$ for a stable crack. Thus, the typical design philosophy [8] uses eq. (3.28) or (3.29) as the general mathematical model in which $a = a_{\max}$ is the maximum allowable crack size in a component, σ is the design stress, and K_I is the applied stress intensity factor. However, the minimum detectable crack size depends on the available equipment for conducting nondestructive tests, but the critical crack size (a_c) can be predicted when the stress intensity factor reaches a critical value, which is commonly known as the plane strain fracture toughness $(K_I = K_{IC})$ for thick plates. In fact, $K_I < K_{IC}$ can be taken as the material fracture constraint; otherwise, the crack becomes unstable when it reaches a critical length, $a = a_c$, which is strongly controlled by K_{IC}. Thus, solving eqs. (3.29) for the critical crack length yields

$$a_c = \frac{1}{\pi} \left(\frac{K_{IC}}{\alpha\sigma} \right)^2 \tag{3.57}$$

This expression implies that the maximum allowable crack length depends on the magnitude of K_{IC} and the applied stress $\sigma < \sigma_{ys}$. Conclusively, crack propagation occurs when the applied stress intensity factor is equal or greater than fracture toughness, $K_I \geq K_{IC}$ for plane strain or $K_I \geq K_C$ for plane stress condition.

A typical fracture-control plan includes the following

- Plane strain fracture toughness, K_{IC}. Actually, the applied stress intensity factor must be $K_I < K_{IC}$ so that it can be used as a constraint, and the designer controls it. This design constraint assures structural integrity since crack propagation is restricted.

- Use of the following inequality $B \geq 2.5(K_{IC}/\sigma_{ys})^2$ for brittle materials assures that the thickness of designed parts do not fall below a minimum thickness

- If use of welding is necessary, then it must be used very cautiously since it can degrade the toughness of the welded material especially in the heat-affected zone (HAZ), which may become brittle as a consequence of rapid

cooling leading to smaller grains. Consequently, flaws development is detrimental to the structure or component since the local stresses may amplify at the crack tip.

- The environment in which a structure is put into service. For instance, a corrosive environment may degrade the structure by developing stress corrosion cracks (SCC).

- Limitations of the allowable crack size can be predicted by eq. (3.57)

- Use of nondestructive test (NDT) techniques. NDT techniques must be employed in order to avoid catastrophic failure by examining structural components for flaws or cracks.

The literature has a vast amount of fracture toughness data for many materials used in engineering construction. For convenience, Table 3.2 is included in this chapter to provide the reader with typical fracture toughness data for some common materials. More mechanical properties are given in Tables 9.2, 10.1 and Appendix A.

Table 3.2 Room temperature mechanical properties

Material	σ_{ys} (MPa)	σ_{ts} (MPa)	K_{IC} MPa$\sqrt{m}$	E (GPa)	%EL	%RA	Ref.
AerMet 100	1724	1965	126	207	14	65	[5]
Ti-6Al-4V	869	958	87	117	11	16	[9]
Ti-6Al-4V	1007	1034	40	130	14	29	[9]
AISI 4340	1089	1097	110	207	14	49	[22]
AISI 4147	945	1062	120	207	15	49	[22]
AISI 4340	1476	1896	81	207	10		[7]
Inconel	1172	1404	96		15	18	[16]
18Ni(250)	1290	1345	176		15	66	[9]
2014-T651	455		24				[8]
2024-T3	345		44				[8]
7075-T6	572	641	24	72	12		[17]
$Ni_{49}Fe_{29}$ $P_{14}B_6 Si_2$	800	800	12				[18]
SIC	460	460	3.7	72			[20]
Al_2O_3			4.5	380			[23]

3.6   PLANE STRESS VS. PLANE STRAIN

It is clearly shown in Figure 3.9 how fracture toughness is strongly dependent on the material thickness up to a limiting value. For a thin plate, plane stress

condition $(\sigma_Z = 0)$ governs the fracture process because the plate is too thin to sustain through-the-thickness stress.
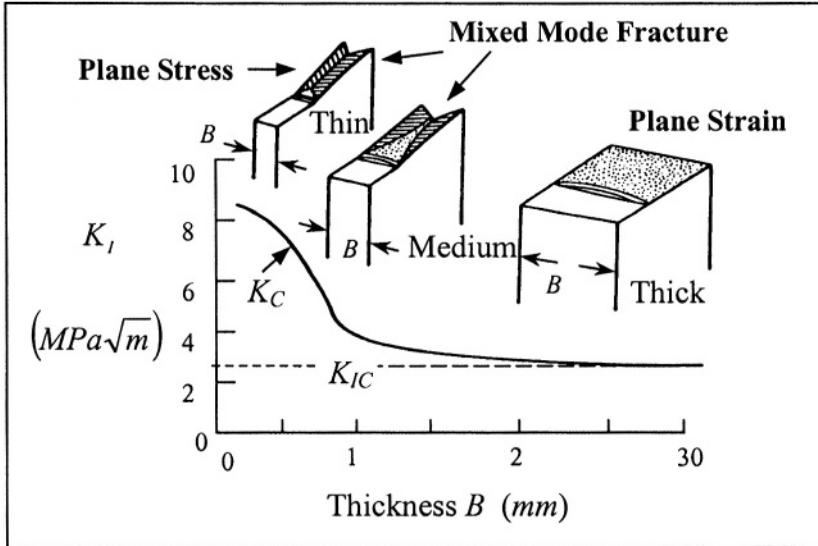

Figure 3.9 Effect of specimen thickness on fracture toughness (K_C and K_{IC}) [19].

For a thick plate, plane strain condition $(\sigma_z \neq 0)$ prevails in which K_{IC} becomes a material's property. It is this property, K_{IC}, that the designer must use to assure structural integrity. The characteristics of a fracture surface, as schematically indicated in Figure 3.9, vary between both plane stress and plane strain modes of fracture. The former fracture mode shows a slant fracture (shear lips at approximately 45°) as an indication of partial ductile fracture, and the latter exhibits a flat fracture surface as a representation of brittle fracture. Any combination of these modes of fracture leads to a mixed mode fracture surface. In addition, plane stress fracture toughness (K_C) is related to metallurgical features and specimen geometry, and plane strain fracture toughness (K_{IC}) depends only on metallurgical features and temperature.

The effect of plastic zone size (r) to plate thickness and macroscopic fracture surface appearance is also taken into account. For instance, plane stress-state is associated with a maximum toughness and slant fracture, and plane strain-state is related to a minimum toughness and flat fracture. Therefore, plane stress or plane strain condition depends on σ_{ys}.

Since the plane strain fracture toughness K_{IC} is a property for a given material, the applied stress level exhibits a dependency on the crack size. This is schematically shown in Figure 3.10 for two hypothetical materials. Notice that both K_{IC} and a_c influence the stress and the curve is shifted upwards at higher K_{IC} level. This means that ductility also has a major influence on the

stress and K_{IC}. Let curves **A** and **B** represent failure trends at two different conditions. The interpretation of Figure 3.10 indicates that there exists an initial crack size (a_o) at the yield stress loading (σ_{ys}) for material **A**. In fact, a similar assessment applies to material **B**.
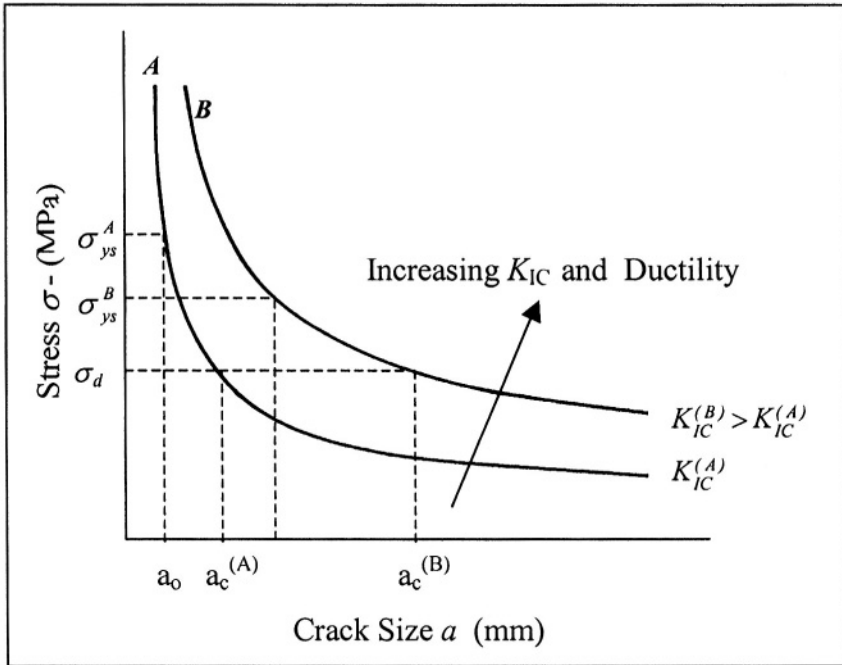

Figure 3.10 Influence of fracture on allowable stress crack size.

This fracture phenomenon proceeds in a stable manner, provided that both crack size and applied stress are within a controllable range such as $a_o < a < a_c$ and $\sigma_d < \sigma < \sigma_{ys}$. Furthermore, crack instability occurs when $a \rightarrow a_c$ and $\sigma \rightarrow \sigma_d$. This schematic representation of crack growth applies to both **A** and **B** curves, which represent the fracture behavior of two hypothetical materials.

Conclusively, the higher K_{IC} the greater a_c since the resistance to fracture is controlled by the level of the plane strain fracture toughness. Hence, for the hypothetical materials included in Figure 3.10, $a_c(B) > a_c(A)$ and $K_{IC}(B) > K_{IC}(A)$ at $\sigma = \sigma_d$. This implies that material **A** allows a smaller crack extension than material **B**. Although material **B** is the most attractive for engineering applications, its mechanical behavior can be significantly affected by changes in temperature and a corrosive environment. In addition, the solid curves represent ideal elastic behavior, but most materials exhibit plasticity due to the yielding phenomenon.

3.7 PRINCIPLE OF SUPERPOSITION

It is very common in machine parts to have a combination of stress loadings that generate a combination of stresses on the same part. Of particular interest in this section are the cases depicted in Figures 3.6 and 3.11. Each case has the same stress-field distribution described by the local stresses such as σ_x, σ_y and σ_z. Consequently, the principle of superposition requires that the total stress intensity factor (K_I) be the sum of each stress intensity factor components [6,24].
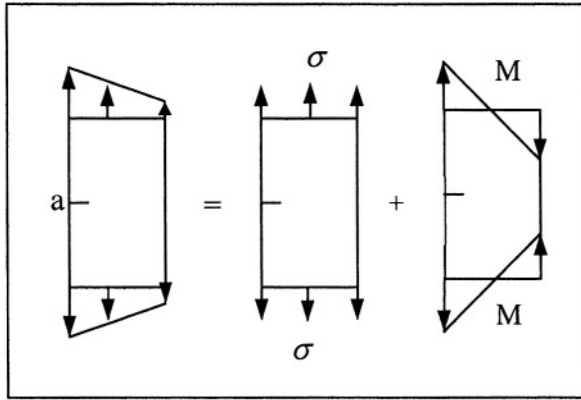
Figure 3.11 Superposition of mixed-load under mode I loading system on a single-edge cracked plate.

The individual and total stress intensity factors for the cases cited in Figures 3.6 and 3.11 are

PRESSURE VESSEL (Figure 3.6)

The total stress intensity factor along with eq. (3.43) is defined by

$$
\begin{array}{rcll}
K_I & = & K_I(\text{Hoop}) + K_I(\text{Pressure}) & (3.58) \\[2mm]
K_I & = & 1.12\sigma\sqrt{\pi a/Q} + 1.12P\sqrt{\pi a/Q} & (2) \\[2mm]
K_I & = & \dfrac{1.12Pd}{2B}\sqrt{\pi a/Q} + 1.12P\sqrt{\pi a/Q} & (b) \\[2mm]
K_I & = & \dfrac{1.12}{\sqrt{Q}}\left(\dfrac{d}{2B} + 1\right)P\sqrt{\pi a} & (c) \\[2mm]
K_I & = & \alpha P\sqrt{\pi a} & (3.59)
\end{array}
$$

where the correction factor for this combined stress loading is

$$
\alpha = \frac{1.12}{\sqrt{Q}}\left(\frac{d}{2B} + 1\right) \tag{3.60}
$$

3.7.1   SINGLE-EDGE CRACKED PLATE (Figure 3.11)

If a plate containing a single-edge cracked is subjected to both tension and bending stresses, then the total stress intensity factor
  is

$$K_I \;=\; K_I(\text{Tension}) + K_I(\text{Bending}) \tag{3.61}$$

$$K_I \;=\; 1.12\sigma\sqrt{\pi a} + \frac{6M\alpha_1}{B\,(w-a)^{3/2}} \tag{3.62}$$

$$M \;=\; FL \tag{3.63}$$

where $\alpha_1 = f\,(a/w)$ = Correction factor for bending load
  M = Bending moment *(m.MN)*
  F = Bending force
  L = Length of the plate or beam

The correction factor for a bending load can be determined from Figure 3.12 or calculated using eq. (3.62), which is a curve fitting function based on Paris and Sih [25] data for notched beams. Hence,

$$\alpha_1 = 0.83 + 0.151 \ln\left(\frac{a}{w}\right) \tag{3.64}$$
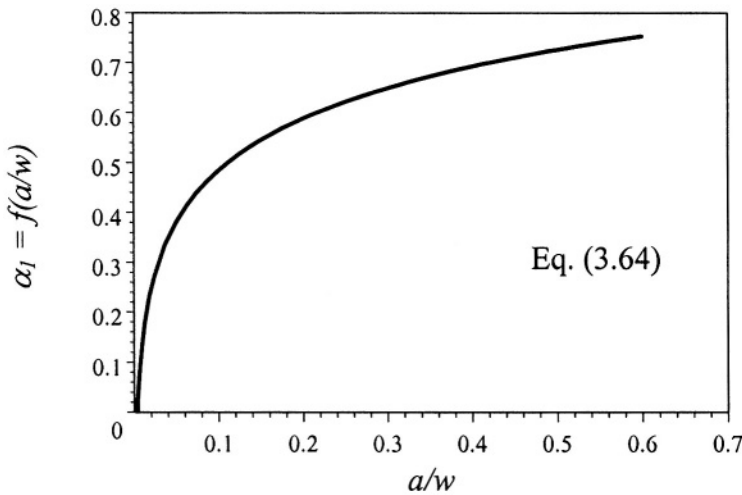
Figure 3.12 Correction factor for a notched beam under a bending moment.

Example 3.6 *A round vessel made of AISI 4147 is pressurized at 379 MPA and it has an internal semi-elliptical surface crack 5-mm deep and 10-mm long. The diameter and thickness are 0.5 m and 25 cm, respectively. In order to account for the effects of both the applied pressure and the hoop stress, calculate a) the stress intensity factor. Will the pressure vessel fracture or leak? b) Determine the maximum pressure that would cause leakage, and c) plot the correction factor vs. the shape factor.*

Solution:

Given data: $a = 5mm,\ 2c = 10\ mm,\ d = 0.5\ m,\ B = 25\ cm,\ P = 379$ *MPa*

$$a/2c = 0.50:$$

From Table 3.2,

$K_{IC} = 120\ MPa\sqrt{m}\ and\ \sigma_{ys} = 945\ MPa$

a) The hoop stress is

$$\sigma = \frac{Pd}{2B}$$

$$\sigma = \frac{(379\ MPa)\,(0.5\ m)}{(2)\,(25x10^{-2}\ m)} = 379\ MPa$$

Using eq. (3.44) yields the shape factor

$$Q = \left(\frac{\pi}{2}\right)^2\left[\frac{3}{4} + \left(\frac{a}{2c}\right)^2\right]^2 - \frac{7}{33}\left(\frac{\sigma}{\sigma_{ys}}\right)^2 \qquad (3.44)$$

$$Q = 2.43$$

Using eq. (3.59) gives the total stress-intensity factor

$$K_I = \alpha P\sqrt{\pi a} \qquad (3.59)$$

$$\alpha = \frac{1.12}{\sqrt{Q}}\left(\frac{d}{2B} + 1\right) = 1.44 \qquad (3.60)$$

$$K_I = (1.44)\,(379\ MPa)\,\sqrt{\pi\,(5x10^{-3}\ m)}$$

$$K_I = 68.40\ MPa\sqrt{m}$$

Therefore, leakage will not occur because $K_I < K_{IC} = 120\ MPa\sqrt{m}.$

c) From eq. (3.59), the maximum pressure is

$$K_{IC} = \alpha P_{\max} \sqrt{\pi a}$$

$$P_{\max} = \frac{K_{IC}}{\alpha \sqrt{\pi a}}$$

$$P_{\max} = \frac{120 \; MPa\sqrt{m}}{1.44 \sqrt{\pi \left(5x10^{-3} \; m\right)}}$$

$$P_{\max} = 665 \; MPa$$

d) Inserting the given variables into eq. (3.60) yields the following simplified expression

$$\alpha = \frac{1.12}{\sqrt{Q}} \left(\frac{d}{2B} + 1 \right)$$

$$\alpha = \frac{2.24}{\sqrt{Q}}$$

which is plotted in the figure below. Denote that the general geometric correction factor α is strongly dependent on the shape factor up to approximately $Q = 0.5$.
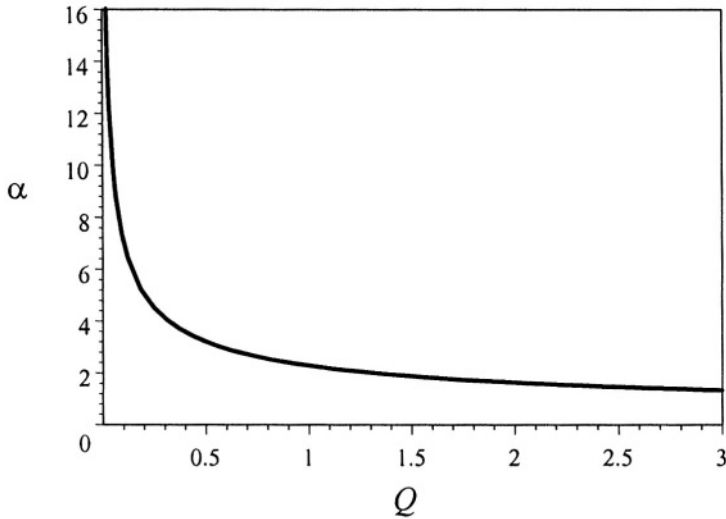
3.8 PROBLEMS

3.1 A steel strap 1-mm thick and 20-mm wide with a through-the-thickness central crack 4-mm long is loaded to failure, a) Determine the critical load if $K_{IC} = 80\ MPa\sqrt{m}$ for the strap material, b) Use an available correction factor, $\alpha = f(a/w)$, for this crack configuration and calculate the critical stress as $\sigma_c = (Fraction)\sigma_\infty$.

3.2 A steel tension bar 8-mm thick and 50-mm wide with an initial single-edge crack of 10-mm long is subjected to an uniaxial stress $\sigma = 140\ MPa$. a) Determine the stress intensity factor K_I. Is the crack stable? b) Determine the critical crack size, and c) determine the critical load. Data: $K_{IC} = 60$ $MPa\sqrt{m}$. [Solution: a) $34\ MPa$, b) $31.1\ mm$, and c) $98.84\ kN$].

3.3 A very sharp penny-shaped crack with a diameter of $22\text{-}mm$ is completely embedded in a highly brittle solid. Assume that catastrophic fracture occurs when a stress of $600\ MPa$ is applied. a) What is the fracture toughness for this solid? (Assume that this fracture toughness is for plane strain conditions). b) If a sheet 5-mm thick plate is prepared for fracture-toughness testing, Would the fracture-toughness value [(calculated in part a)] be an acceptable number according to the ASTM E399 standard? Use $\sigma_{ys} = 1342\ MPa$. c) What thickness would be required for the fracture-toughness test to be valid?

3.4 A One guitar steel string has a miniature circumferential crack of 0.009 mm deep. This implies that the radius ratio is almost unity, $d/D \simeq 1$. b) Another string has a localized miniature surface crack (single-edge crack like) of $0.009\ mm$ deep. Assume that both strings are identical with an outer diameter of $0.28\ mm$. If a load of $49\ N$ is applied to the string when being tuned, will it break? Given data: $K_{IC} = 15\ MPa\sqrt{m}$ and $\sigma_{ys} = 795\ MPa$.

3.5 A 7075-T6 aluminum alloy is loaded in tension. Initially the $10\text{-}mm$ thick, $100\text{-}mm$ wide and $500\text{-}mm$ long plate has a $4\text{-}mm$ single-edge through–the-thickness crack. a) Is this a valid test? b) Calculate the maximum allowable tension stress this plate can support. c) Is it necessary to correct K_I due to crack-tip plasticity? Why? or Why not? d) Calculate the design stress and then stress intensity factor if the safety factor is 1.5. Use the following properties: $\sigma_{ys} = 586\ MPa$ and $K_{IC} = 33\ MPa\sqrt{m}$. [Solution: a) It is a valid test because B(ASTM) < B(actual), b) $\sigma = 261\ MPa$, c) It is not necessary because $K_I \simeq K_{IC}$, and d) $\sigma_d = 174\ MPa$ and $K_{I,d} = 22\ MPa\sqrt{m}$].

3.6 A steel plate ($30\text{-}mm$ thick, $1.2\text{-}m$ wide, and $2.5\text{-}m$ long) is in tension. It is operated below its ductile-to-brittle transition temperature (with $K_{IC} = 28.3$ $MPa\sqrt{m}$). If a $65\text{-}mm$ long through the-thickness central crack is present, calculate a) the tensile stress for catastrophic failure. Compare this stress with the yield strength of 240 MPa. b) Determine the safety factor.
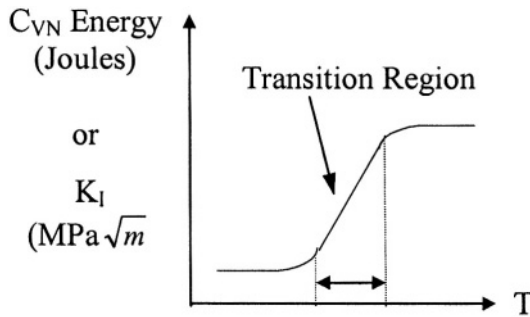
3.7 Show that the following inequality $dK_I/da > 0$ is valid for crack instability in a large plate under a remote external tension stress.

3.8 The plate below has an internal crack subjected to a pressure P on the crack surface. The stress intensity factors at points A and B are
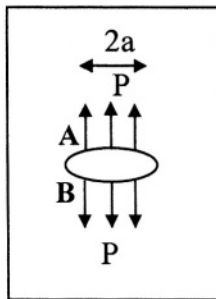
$$K_A = \int \frac{P}{\sqrt{\pi a}} \sqrt{\frac{a+x}{a-x}} \cdot dx$$

$$K_B = \int \frac{P}{\sqrt{\pi a}} \sqrt{\frac{a-x}{a+x}} \cdot dx$$

Use the principle of superposition to show that the total stress intensity factor is defined by $K_I = P\sqrt{\pi a}$.

3.9 A pressure vessel is to be designed using the **leak-before-break criterion** based on the circumferential wall stress and plane-strain fracture toughness. The design stress is restricted by the yield strength σ_{ys} and a safety factor (SF). Derive expressions for a) the critical crack size and b) the maximum allowable pressure when the crack size is equals to the vessel thickness.

3.9   REFERENCES

[1]   J. W. Dally and W.F. Riley, "Experimental Stress Analysis", 3rd ed., McGraw-Hill, Inc. New York, (1991).

[2]   G.R. Irwin, "Fracture I," S. Flugge editor, Handbuch der physik VI, Springer-Verlag, New York, (1958) 558-590.

[3]   C.E. Inglis, "Stresses in a Plate due to the Presence of Cracks and Sharp Corners", Trans. Inst. Nav. Arch., 55 (1913) 219-241.

[4]   M.A. Meyers and K.K. Chawla, "Mechanical Metallurgy Principles and Applications," Prentice-Hall, Inc., New Jersey, (1984) 161

[5]   J.M. Dahl and P.M. Novotny, Adv. Materials & Processes, 3 (1999) 23

[6]   D. Broek, "Elementary Engineering Fracture Mechanics', Fourth edition, Kluwer Academic Publisher, Boston, (1986).

[7]   R.C. Shah, ASTM STP 560, (1971) 29

[8]   R.W. Hertz berg, "Deformation and Fracture Mechanics of Engineering Materials", third edition, John Wiley & Sons, New York, (1989)

[9]   G.R. Yoder et al., ASTM STP 801, (1983) 159.

[10] H.E. Boyer And T.L. Gall, editors, Metals Handbook: Desk Edition, ASM, (1985)

[11] A.S. Kobayashi, "Fracture Mechanics", in Experimental Techniques in Fracture Mechanics, edited by A.S. Kobayashi, The Iowa State University Press, Society for experimental Stress Analysis, SESA monograph 1, (1973).

[12] C.E. Feddersen, Discussion, ASTM STP 410, (1967) 77-79.

[13] G.R. Irwin, "The Crack Extension Force for a Part-Through Crack in a Plate", Trans. ASME, J. Appl. Mech., (1962) 651 - 654.

[14] W.T. Koiter and J.P. Benthem, in "Mechanics of Fracture", Vol. 1, edited by G.C. Sih, Noordhoff, Leyden, (1973)

[15] I.N. Sneddon, "The distribution of Stress in Neighborhood of a Crack in a Elastic Solid," Proc. Royal Soc. London, A 187 (1946) 229-260

[16] R.L. Tobler, Cryogenics, Vol. 16, No. 11, (Nov. 1976) 669.

[17] T.E. Tietz and I.G. Palmer, ASM Materials Science Seminar, Advances in Power Metallurgy, (October 1981) 189

[18] J.C.M. Li, "Mechanical Properties of Amorphous Metals and Alloys," Treatise on Materials Sci. and Tech., Vol. 20, in "Ultrarapid Quenching of Liquid Alloys," Herbert Herman, ed., (1981) 326

[19] H.O. Fuchs and R.I. Stephens, "Metal Fatigue in Engineering", John Wiley, NY, 1980

[20] M.W. Barsoum, "Fundamentals of Ceramics," McGraw-Hill Co., Inc., NY, (1997) 401

[21] A.S. Kobayashi, M. Zii and L.R. Hall, Inter. J. Fracture Mechanics, (1965) 81-95

[22] J.M. Barsom and S.T. Rolfe, "Fracture and Fatigue in Structure: Application of fracture Mechanics," Third edition, American Society for Testing and Materials Philadelphia, PA, (1999).

[23] Y.M. Chiang and et al., "Physical Ceramics: Principles for Ceramic Science and Engineering," John Wiley & Sons, Inc., New York, (1997).

[24] J.M. Barsom and S.T. Rolfe, "Fracture and Fatigue Control in Structures: Application of Fracture Mechanics", Third edition, Butterworth Heinemann, Woburn, MA, (1999).

[25] C.P. Paris and G.C. Sih, "Stress Analysis of Cracks, ASTM STP 381, (1965).

[26] G.R. Irwin, J.M. Krafft, P.C. Paris, and A.A. Wells, "Basic Concepts of Crack Growth and Fracture," NRL Report 6598, Naval Research Laboratory, Washington, DC, (November 21, 1967)

[27] W.F. Brown, Jr. and J.E. Strawley, ASTM STP 410, (1966)

[28] V.M. Faires, "Design of Machine Elements," The Macmillan Company, New York, USA, (1965) 34-35

Chapter 4

ELASTIC FIELD EQUATIONS

4.1 INTRODUCTION

Linear elastic fracture mechanics (LEFM) and a quasi-static load action are considered in this chapter in order to derive the stress, strain, and displacement field equations adjacent to a crack tip. The field equations can be derived in series form using rectangular and polar coordinates. Any dynamic or local unloading is neglected in the foregoing mathematical procedures for modeling the plastic zone being as a circle with different radius r. It is intended henceforward to demonstrate that the trigonometric functions $f(\theta)$ and $g(\theta)$ have increasing terms as the radius r increases. However, the irreversible action that takes place at the crack tip suggests that a few terms in a series expansion may be needed for characterizing the crack tip field equations.

4.2 FIELD EQUATIONS: MODE I

The analytical approach used in this chapter is based on a very small plastic zone where higher-order terms in the plastic zone size (r) is neglected because the field equations are valid and exact for $r \to 0$. Consider the small plastic zone adjacent to the crack tip shown in Figure 4.1. Generalizing eq. (3.1) in series form along with $A_o = K_I/\sqrt{2\pi}$ yields the Westergaard's complex functions Z and Z' as [1]

$$Z = \sum_{m=o}^{M} A_m z^{m-1/2} \tag{4.1}$$

$$Z' = \frac{dZ}{dz} = \sum_{m=o}^{M} \left(m - \frac{1}{2} \right) A_m z^{m-3/2} \tag{4.2}$$
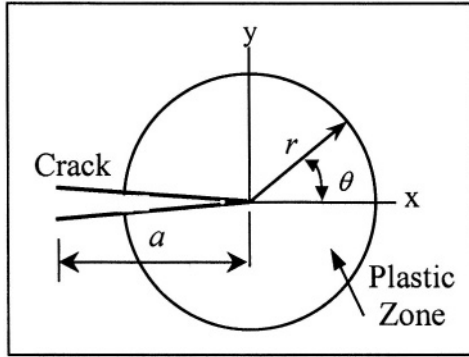
Figure 4.1 Crack tip circular regions

$$Z = \sum_{m=o}^{M} A_m r^{m-1/2} \left[\cos\left(m - \frac{1}{2}\right)\theta + i\sin\left(m - \frac{1}{2}\right)\theta \right] \tag{4.3}$$

$$Z' = \sum_{m=o}^{M} \left(m - \frac{1}{2}\right) A_m r^{m-3/2} \left[\cos\left(m - \frac{3}{2}\right)\theta + i\sin\left(m - \frac{3}{2}\right)\theta \right] \tag{4.4}$$

with N being a real number and

$$z = x + iy = re^{iN\theta} \tag{4.4}$$

$$e^{\pm iN\theta} = \cos N\theta \pm i\sin N\theta \tag{4.5}$$

$$y = r\sin\theta = 2r\sin\frac{\theta}{2}\cos\frac{\theta}{2} \tag{4.6}$$

The real and imaginary parts [consult eq. (3.9)] for the Airy's complex function defined by eq. (3.6) are

$$\mathrm{Re}\,Z = \sum_{m=o}^{M} A_m r^{m-1/2} \cos\left(m - \frac{1}{2}\right)\theta \tag{4.7}$$

$$\mathrm{Re}\,Z' = \sum_{m=o}^{M} \left(m - \frac{1}{2}\right) A_m r^{m-3/2} \cos\left(m - \frac{3}{2}\right)\theta \tag{4.8}$$

$$\mathrm{Im}\,Z = \sum_{m=o}^{M} A_m r^{m-1/2} \sin\left(m - \frac{1}{2}\right)\theta \tag{4.9}$$

$$\mathrm{Im}\,Z' = \sum_{m=o}^{M} \left(m - \frac{1}{2}\right) A_m r^{m-3/2} \sin\left(m - \frac{3}{2}\right)\theta \tag{4.10}$$

The stresses in complex form as per eq. (1.40), (3.18) or (3.20) are

$$\sigma_{xx} = \operatorname{Re} Z - y \operatorname{Im} Z'$$
$$\sigma_{yy} = \operatorname{Re} Z + y \operatorname{Im} Z' \qquad (4.11)$$
$$\tau_{xy} = -y \operatorname{Re} Z'$$

Inserting eq. (4.7) through (4.10) into (4.11) yields the stresses in series form with $0 \le m \le M$

$$
\sigma_{xx} = \sum_{m=o}^{M} A_m r^{m-1/2} \cos\left(m - \frac{1}{2}\right)\theta
$$
$$
- \sum_{m=o}^{M} 2\left(m - \frac{1}{2}\right) A_m r^{m-1/2} \sin\frac{\theta}{2} \sin\frac{\theta}{2} \sin\left(m - \frac{3}{2}\right)\theta
$$
$$
\sigma_{yy} = \sum_{m=o}^{M} A_m r^{m-1/2} \cos\left(m - \frac{1}{2}\right)\theta \qquad (4.12)
$$
$$
+ \sum_{m=o}^{M} 2\left(m - \frac{1}{2}\right) A_m r^{m-1/2} \cos\frac{\theta}{2} \sin\frac{\theta}{2} \sin\left(m - \frac{3}{2}\right)\theta
$$
$$
\tau_{xy} = -\sum_{m=o}^{M} 2\left(m - \frac{1}{2}\right) A_m r^{m-1/2} \cos\frac{\theta}{2} \sin\frac{\theta}{2} \cos\left(m - \frac{3}{2}\right)\theta
$$

Assume that a small-scale yielding phenomenon takes place in elastic solids and that the crack can be treated as a semi-infinite defect. Thus, eq. (4.1) or (4.2) indicates that the number of terms in the series and the amount of experimental data decrease when $M \to 0$ as $r \to 0$.

Let $m = 0$ in eq. (4.12) so that the first order stress field equations for mode I become

$$
\begin{bmatrix} \sigma_{xx} \\ \sigma_{yy} \\ \tau_{xy} \end{bmatrix} = \frac{K_I}{\sqrt{2\pi r}} \cos\frac{\theta}{2}
\begin{bmatrix} 1 - \sin\frac{\theta}{2}\sin\frac{3\theta}{2} \\ 1 + \sin\frac{\theta}{2}\sin\frac{3\theta}{2} \\ \sin\frac{\theta}{2}\cos\frac{3\theta}{2} \end{bmatrix} \qquad (4.13)
$$

The stress in the z-direction is of particular interest because it defines plane conditionsas defined eqs. (1.34) and (1.35). Hence, $\sigma_{zz} = 0$ for plane stress and for plane strain

$$\sigma_{zz} = v\left(\sigma_{xx} + \sigma_{yy}\right) \qquad (4.14)$$
$$\sigma_{zz} = \frac{2vK_I}{\sqrt{2\pi r}} \cos\frac{\theta}{2} \qquad (4.15)$$

Additionally, letting the angle be $\theta = 0$ implies that the crack grows along the x-axis and only one term is needed for characterizing the crack tip stress

field, which is independent of specimen size and geometry. In this case, eqs.
(4.13) and (4.15) become

$$
\begin{bmatrix}
\sigma_{xx} \\
\sigma_{yy} \\
\tau_{xy} \\
\sigma_{zz}
\end{bmatrix}
=
\begin{bmatrix}
\frac{K_I}{\sqrt{2\pi r}} \\
\frac{K_I}{\sqrt{2\pi r}} \\
0 \\
\frac{2v K_I}{\sqrt{2\pi r}}
\end{bmatrix}
\tag{4.16}
$$

Figure 4.2 depicts the trigonometric trends of the functions given in eq.
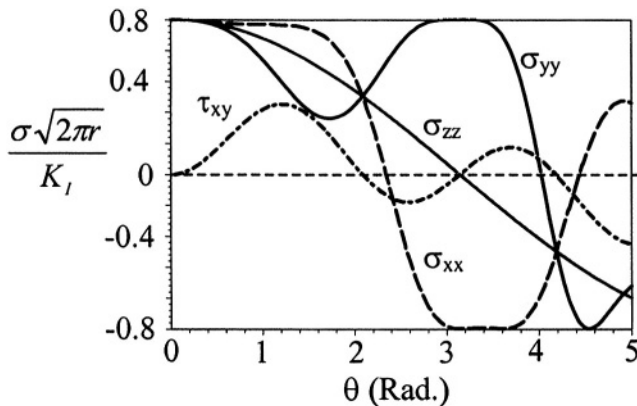(4.13) and (4.15). This is to shows the reader how these functions vary with
increasing angle θ.

Figure 4.2 Normalized stress distribution for mode I

Substituting eq. (4.13) into (1.10) and (1.11), and the resultant expressions
into (1.4) yields strain and displacement field equations

$$
\begin{bmatrix}
\epsilon_{xx} \\
\epsilon_{yy} \\
\gamma_{xy}
\end{bmatrix}
=
\frac{K_I}{\sqrt{2\pi r}} \cos\frac{\theta}{2}
\begin{bmatrix}
(1-v) - (1+v)\sin\frac{\theta}{2}\sin\frac{3\theta}{2} \\
(1-v) + (1+v)\sin\frac{\theta}{2}\cos\frac{3\theta}{2} \\
\sin\frac{\theta}{2}\cos\frac{3\theta}{2}
\end{bmatrix}
\tag{4.17}
$$

$$
\begin{bmatrix}
\mu_x \\
\mu_y \\
\mu_z
\end{bmatrix}
=
\frac{2K_I}{\sqrt{2\pi}E}
\left\{
\begin{array}{c}
\sqrt{r}\cos\frac{\theta}{2}\left[(1-v) + (1+v)\sin^2\frac{\theta}{2}\right] \\
\sqrt{r}\sin\frac{\theta}{2}\left[2 - (1+v)\right]\cos^2\frac{\theta}{2} \\
-\frac{vB}{\sqrt{r}}\cos\frac{\theta}{2}
\end{array}
\right\}
\tag{4.18}
$$

Equation (4.18) indicates that the displacement μ_z is singular since only
$\mu_x = \mu_y = 0$ and $\mu_z \rightarrow \infty$ as $r \rightarrow 0$. Therefore, μ_z is the only displacement
singularity in the order of $r^{-1/2}$ Chona [2] has shown that the circular plastic
zone in Figure 4.1 extends only a distance of 0.02a from the crack tip. Therefore,
the above field equations give an approximation to the stress intensity factor

K_I. Figure 4.3 shows the distribution of the displacements as functions of the angle θ in radians for $v = 0.3$.

$$\frac{2\mu_x K_I}{\sqrt{2\pi r}\,E}$$

$$\frac{2\mu_y K_I}{\sqrt{2\pi r}\,E}$$

$$\frac{2\mu_z K_I}{EB}\sqrt{\frac{r}{\sqrt{2\pi}}}$$
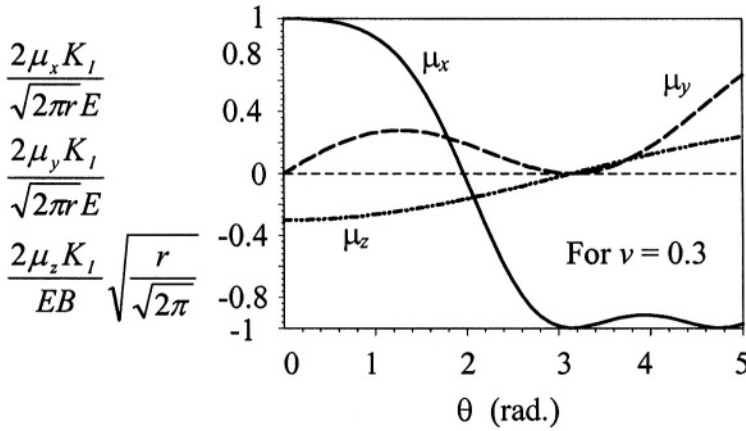
Figure 4.3 Distribution of mnormalized displacements for mode I

In addition, the thickness is defined below using x_3 as the z-axis since z is utilized as a complex function in Chapter 3

$$\int \partial x_3 = B \tag{4.19}$$

4.3   FIELD EQUATIONS: MODE II

Deriving the stress and displacement field equations in shear mode II is of particular importance for analyzing mixed-mode systems. Assuming that the crack is loaded with a remote shear stress τ interesting results can be determined. Let the Westergaard's complex functions Z, Z' and $\overline{Z}$ along with $B_o = K_{II}/\sqrt{2\pi}$ be defined by

$$Z = \sum_{m=o}^{M} B_m z^{m-1/2} \tag{4.20}$$

$$Z' = \frac{dZ}{dz} = \sum_{m=o}^{M} \left(m - \frac{1}{2}\right) B_m z^{m-3/2} \tag{4.21}$$

$$\overline{Z} = \int Z dz = \sum_{m=o}^{M} \frac{B_m z^{m+1/2}}{m + 1/2} \tag{4.22}$$

Combining eqs. (4.4) (4.5) into (4.20) through (4.22) gives

$$Z = \sum_{m=o}^{M} B_m r^{m-1/2} \left[\cos\left(m - \frac{1}{2}\right)\theta + i\sin\left(m - \frac{1}{2}\right)\theta \right] \tag{4.23}$$

$$Z' = \sum_{m=o}^{M} \left(m - \frac{1}{2}\right) B_m r^{m-\frac{3}{2}} \left[\cos\left(m - \frac{3}{2}\right)\theta + i\sin\left(m - \frac{3}{2}\right)\theta \right] \tag{4.24}$$

$$\overline{Z} = \sum_{m=o}^{M} \frac{B_m r^{m+1/2}}{m + 1/2} \left[\cos\left(m + \frac{1}{2}\right)\theta + i\sin\left(m + \frac{1}{2}\right)\theta \right] \tag{4.25}$$

From which the real and imaginary parts are

$$\operatorname{Re} Z = \sum_{m=o}^{M} B_m r^{m-1/2} \cos\left(m - \frac{1}{2}\right)\theta \tag{4.26}$$

$$\operatorname{Re} Z' = \sum_{m=o}^{M} \left(m - \frac{1}{2}\right) B_m r^{m-3/2} \cos\left(m - \frac{3}{2}\right)\theta \tag{4.27}$$

$$\operatorname{Re} \overline{Z} = \sum_{m=o}^{M} \frac{B_m r^{m+1/2}}{m + 1/2} \cos\left(m + \frac{1}{2}\right)\theta \tag{4.28}$$

$$\operatorname{Im} Z = \sum_{m=o}^{M} B_m r^{m-1/2} \sin\left(m - \frac{1}{2}\right)\theta \tag{4.29}$$

$$\operatorname{Im} Z' = \sum_{m=o}^{M} \left(m - \frac{1}{2}\right) B_m r^{m-3/2} \sin\left(m - \frac{3}{2}\right)\theta \tag{4.30}$$

$$\operatorname{Im} \overline{Z} = \sum_{m=o}^{M} \frac{B_m r^{m+1/2}}{m + 1/2} \sin\left(m + \frac{1}{2}\right)\theta \tag{4.31}$$

The Airy's stress function for the sliding shear mode can be defined by [1]

$$\phi = -y \operatorname{Re} \overline{Z} \tag{4.32}$$

According to eq. (3.18) without body forces ($\Omega = 0$) and eq. (4.32), the stress equations become

$$\sigma_{xx} = \frac{\partial^2 \phi}{\partial y^2} = y \operatorname{Re} Z' + 2\operatorname{Im} Z$$

$$\sigma_{yy} = \frac{\partial^2 \phi}{\partial x^2} = -y \operatorname{Re} Z' \tag{4.33}$$

$$\tau_{xy} = -\frac{\partial^2 \phi}{\partial x \partial y} = \operatorname{Re} Z - y \operatorname{Im} Z'$$

or

$$\sigma_{xx} = 2\sum_{m=o}^{M}\left(m-\frac{1}{2}\right)B_m r^{m-1/2}\sin\frac{\theta}{2}\cos\frac{\theta}{2}\cos\left(m-\frac{3}{2}\right)\theta$$

$$+2\sum_{m=o}^{M}B_m r^{m-1/2}\sin\left(m-\frac{1}{2}\right)\theta$$

$$\sigma_{yy} = -2\sum_{m=o}^{M}\left(m-\frac{1}{2}\right)B_m r^{m-1/2}\sin\frac{\theta}{2}\cos\frac{\theta}{2}\cos\left(m-\frac{3}{2}\right)\theta \quad (4.34)$$

$$\tau_{xy} = \sum_{m=o}^{M}B_m r^{m-1/2}\cos\left(m-\frac{1}{2}\right)\theta$$

$$-2\sum_{m=o}^{M}\left(m-\frac{1}{2}\right)B_m r^{m-1/2}\sin\frac{\theta}{2}\cos\frac{\theta}{2}\sin\left(m-\frac{3}{2}\right)\theta$$

The first terms in the series are sufficient to obtain accurate results. Thus, let $m = 0$ in eq. (4.34) along with $B_o = K_{II}/\sqrt{2\pi}$ to get

$$\sigma_{xx} = -\frac{K_{II}}{\sqrt{2\pi r}}\sin\frac{\theta}{2}\left[2+\cos\frac{\theta}{2}\cos\frac{3\theta}{2}\right]$$

$$\sigma_{yy} = \frac{K_{II}}{\sqrt{2\pi r}}\sin\frac{\theta}{2}\cos\frac{\theta}{2}\cos\frac{3\theta}{2} \quad (4.35)$$

$$\tau_{xy} = \frac{K_{II}}{\sqrt{2\pi r}}\cos\frac{\theta}{2}\left[1-\sin\frac{\theta}{2}\sin\frac{3\theta}{2}\right]$$

Substituting eq. (4.35) into (1.10) and (1.11), and the resultant expressions into (1.4) yields strains and displacements functions

$$\epsilon_{xx} = -\frac{K_{II}}{\sqrt{2\pi r}E}\sin\frac{\theta}{2}\left[2+(1+v)\cos\frac{\theta}{2}\cos\frac{3\theta}{2}\right]$$

$$\epsilon_{yy} = \frac{K_{II}}{\sqrt{2\pi r}E}\sin\frac{\theta}{2}\left[2v+(1+v)\cos\frac{\theta}{2}\cos\frac{3\theta}{2}\right] \quad (4.36)$$

$$\gamma_{xy} = \frac{2(1+v)K_{II}}{\sqrt{2\pi r}E}\cos\frac{\theta}{2}\left[1-\sin\frac{\theta}{2}\sin\frac{3\theta}{2}\right]$$

$$\mu_x = \frac{2(1+v)K_{II}}{E}\sqrt{\frac{r}{2\pi}}\sin\frac{\theta}{2}\left[\frac{2}{1+v}+\cos^2\frac{\theta}{2}\right]$$

$$\mu_y = \frac{2K_{II}}{E}\sqrt{\frac{r}{2\pi}}\cos\frac{\theta}{2}\left[(v-1)+(1+v)\sin^2\frac{\theta}{2}\right] \quad (4.37)$$

$$\mu_z = \frac{2vBK_{II}}{E}\sqrt{\frac{r}{2\pi}}\sin\frac{\theta}{2}$$

4.4   SERIES IN POLAR COORDINATES

4.4.1   MODE I AND II LOADING CASES

Consider an elastic plate containing a single-edge crack subjected to a quasi-static tension loading shown in Figure 4.4 [5-6]. In the absence of body forces, equilibrium is satisfied through the Airy stress function in polar coordinates. In a two-dimensional analysis, the stresses in polar coordinates defined in Chapter 1 are

$$
\begin{aligned}
\sigma_{rr} &= \frac{1}{r}\frac{\partial \phi}{\partial r} + \frac{1}{r^2}\frac{\partial^2 \phi}{\partial \theta^2} \\[2mm]
\sigma_{\theta\theta} &= \frac{\partial^2 \phi}{\partial \theta r^2} \\[2mm]
\tau_{r\theta} &= \frac{1}{r^2}\frac{\partial \phi}{\partial \theta} - \frac{1}{r}\frac{\partial^2 \phi}{\partial r \partial \theta}
\end{aligned}
\tag{4.38}
$$
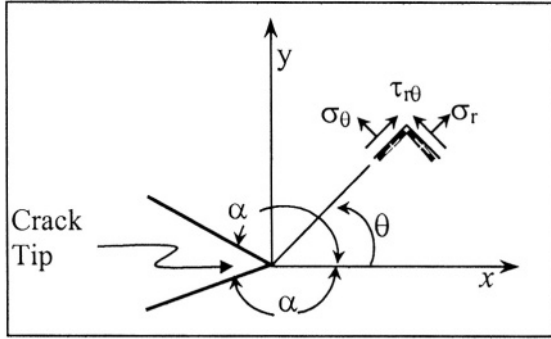
Figure 4.4 Single-edge crack

According to Figure 4.4, the boundary conditions for a single-edge crack are [5]

$$
\sigma_\theta = \tau_{r\theta} = 0 \qquad \text{for } \theta = \pm \alpha
\tag{4.39}
$$

Using the **Product Method** yields the following Airy stress function [7]

$$
\phi = r^{\lambda+1} f(\theta)
\tag{4.40}
$$

Substituting eq. (4.40) into (1.62) yields an expression in terms of the eigenvalue λ. Thus, the resultant expression is a fourth-order partial deferential homogeneous equation with $f = f(\theta)$

$$
\frac{\partial^4 f}{\partial \theta^4} + 2\left(\lambda^2 + 1\right)\frac{\partial^2 f}{\partial \theta^2} + \left(\lambda^2 - 1\right)^2 f = 0
\tag{4.41}
$$

The general solution of this high order polynomial is

$$f = C_1 \cos\left(\lambda - 1\right)\theta + C_2 \sin\left(\lambda - 1\right)\theta + C_3 \cos\left(\lambda + 1\right)\theta + C_4 \sin\left(\lambda + 1\right)\theta \quad (4.42)$$

with the following boundary conditions: $f = 0$ and $df/d\theta = 0$ for $\theta = \pm\alpha$. Using a homogeneous equation with constant coefficient technique, the following general function is used to determine the eigenvalue λ

$$f = C_i e^{r_i \theta} \quad (4.43)$$

where $C_i = $ Constants
$\quad\quad r_i = $ Roots

Hence, eq. (4.43) gives

$$\frac{\partial f}{\partial \theta} = C_i r_i e^{r\theta}$$

$$\frac{\partial^2 f}{\partial \theta^2} = C_i r_i^2 e^{r\theta} \quad (4.44)$$

$$\frac{\partial^3 f}{\partial \theta^3} = C_i r_i^3 e^{r\theta}$$

$$\frac{\partial^4 f}{\partial \theta^4} = C_i r_i^4 e^{r\theta}$$

Substituting these derivatives into eq. (4.42) and (4.43) into(4.41) yields a fourth order polynomial

$$r^4 + 2\left(\lambda^2 + 1\right) r^2 + \left(\lambda^2 - 1\right)^2 = 0 \quad (4.45)$$

The solution of eq. (4.44) is gives four roots defined by

$$\begin{array}{rcl} r_1 & = & i\left(\lambda - 1\right) \\ r_2 & = & -i\left(\lambda - 1\right) \\ r_3 & = & i\left(\lambda + 1\right) \\ r_4 & = & -i\left(\lambda + 1\right) \end{array} \quad (4.46)$$

which satisfies eq. (4.44) since each root yields $\lambda = \lambda$. In addition, the symmetric and antisymmetric parts of eq. (4.42) for mode I and II are, respectively [5]

$$\begin{bmatrix} \cos\left(\lambda - 1\right)\alpha & \cos\left(\lambda + 1\right)\alpha \\ \left(\lambda - 1\right)\sin\left(\lambda - 1\right)\alpha & \left(+ - 1\right)\sin\left(\lambda + 1\right)\alpha \end{bmatrix} \begin{bmatrix} C_1 \\ C_2 \end{bmatrix} = \begin{bmatrix} 0 \\ 0 \end{bmatrix} \quad (4.47)$$

$$\begin{bmatrix} \sin\left(\lambda - 1\right)\alpha & \sin\left(\lambda + 1\right)\alpha \\ \left(\lambda - 1\right)\cos\left(\lambda - 1\right)\alpha & \left(+ - 1\right)\cos\left(\lambda + 1\right)\alpha \end{bmatrix} \begin{bmatrix} C_2 \\ C_4 \end{bmatrix} = \begin{bmatrix} 0 \\ 0 \end{bmatrix} \quad (4.48)$$

Setting the determinants of eqs. (4.47) and (4.48) to zero along with the trigonometric function $2 \sin A \cos B = \sin (A + B) \sin (A - B)$ yields

$$\sin (2\lambda\alpha) \pm \lambda \sin (2\alpha) = 0 \tag{4.49}$$

If $\alpha = \pi$, then $\sin (2\pi) = \sin (360°) = 0$ and the solution of eq. (4.49) is a characteristic equation of the form

$$\sin (2\lambda\alpha) = 0 \tag{4.50}$$

which has only real roots for $\lambda = n/2$ where $n = 1, 2, 3, 4, ...$ The constants in eq. (4.47) and (4.48) take the form [5]

$$
\begin{array}{lll}
C_{3n} = -\frac{n-2}{n+2} C_{1n} & C_{4n} = -C_{2n} & \text{For } n = 1, 3, 5, 7.... \\
C_{3n} = -C_{1n} & C_{4n} = -\frac{n-2}{n+2} C_{2n} & \text{For } n = 2, 4, 6, 8....
\end{array}
\tag{4.51}
$$

Substituting eqs. (4.51) into (4.42) and the resulting expression for $f = f(\theta)$ is substituted back into (4.40) yields the Airy stress function power series form along with $\lambda = n/2$ and $\alpha = \theta$

$$
\phi = \sum_{n=1,3...}^{N} r^{1+n/2} \left\{
\begin{array}{l}
C_{1n} \left[\cos \left(\frac{n}{2} - 1 \right) \theta - \frac{n-2}{n+2} \cos \left(\frac{n}{2} + 1 \right) \theta \right] \\
+ C_{2n} \left[\sin \left(\frac{n}{2} - 1 \right) \theta - \sin \left(\frac{n}{2} + 1 \right) \theta \right]
\end{array}
\right\}
\tag{4.52}
$$

$$
+ \sum_{n=2,4...}^{N} r^{1+n/2} \left\{
\begin{array}{l}
C_{1n} \left[\cos \left(\frac{n}{2} - 1 \right) \theta - \cos \left(\frac{n}{2} + 1 \right) \theta \right] \\
+ C_{2n} \left[\sin \left(\frac{n}{2} - 1 \right) \theta - \frac{n-2}{n+2} \sin \left(\frac{n}{2} + 1 \right) \theta \right]
\end{array}
\right\}
$$

Substituting eq. (4.52) into (4.38) yields the elastic stresses for mode I

$$
\sigma_{rr} = \sum_{n=1,3,...}^{N} \frac{1}{4} r^{n/2-1} \left\{
\begin{array}{l}
C_{1n} \left[\begin{array}{l} n(6-n) \cos \left(\frac{n}{2} - 1 \right) \theta \\ -n(2-n) \cos \left(\frac{n}{2} + 1 \right) \theta \end{array} \right] \\
+ C_{2n} \left[\begin{array}{l} n(6-n) \sin \left(\frac{n}{2} - 1 \right) \theta \\ -n(2+n) \sin \left(\frac{n}{2} + 1 \right) \theta \end{array} \right]
\end{array}
\right\}
\tag{4.53}
$$

$$
+ \sum_{n=2,4,...}^{N} \frac{1}{4} r^{n/2-1} \left\{
\begin{array}{l}
C_{1n} \left[\begin{array}{l} n(6-n) \cos \left(\frac{n}{2} - 1 \right) \theta \\ -n(2+n) \cos \left(\frac{n}{2} + 1 \right) \theta \end{array} \right] \\
+ C_{2n} \left[\begin{array}{l} n(6-n) \sin \left(\frac{n}{2} - 1 \right) \theta \\ -n(2-n) \sin \left(\frac{n}{2} + 1 \right) \theta \end{array} \right]
\end{array}
\right\}
$$

$$
\sigma_{\theta\theta} = \sum_{n=1,3,...}^{N} \frac{1}{4} r^{n/2-1} \left\{
\begin{array}{l}
C_{1n} \left[\begin{array}{l} n(2+n) \cos \left(\frac{n}{2} - 1 \right) \theta \\ -n(2-n) \cos \left(\frac{n}{2} + 1 \right) \theta \end{array} \right] \\
+ C_{2n} \left[\begin{array}{l} n(2+n) \sin \left(\frac{n}{2} - 1 \right) \theta \\ -n(2+n) \sin \left(\frac{n}{2} + 1 \right) \theta \end{array} \right]
\end{array}
\right\}
\tag{4.54}
$$

$$
+ \sum_{n=2,4,...}^{N} \frac{1}{4} r^{n/2-1} \left\{
\begin{array}{l}
C_{1n} \left[\begin{array}{l} n(2+n) \cos \left(\frac{n}{2} - 1 \right) \theta \\ -n(2+n) \cos \left(\frac{n}{2} + 1 \right) \theta \end{array} \right] \\
+ C_{2n} \left[\begin{array}{l} n(2+n) \sin \left(\frac{n}{2} - 1 \right) \theta \\ -n(2-n) \sin \left(\frac{n}{2} + 1 \right) \theta \end{array} \right]
\end{array}
\right\}
$$

$$
\tau_{r\theta} = \sum_{n=1,3,\ldots}^{N} \frac{1}{4} r^{n/2-1} \left\{ C_{1n} \begin{bmatrix} n(2-n)\sin\left(\frac{n}{2}-1\right)\theta \\ +n(2-n)\sin\left(\frac{n}{2}+1\right)\theta \end{bmatrix} \\ +C_{2n} \begin{bmatrix} n(2-n)\cos\left(\frac{n}{2}-1\right)\theta \\ -n(2+n)\cos\left(\frac{n}{2}+1\right)\theta \end{bmatrix} \right\} \tag{4.55}
$$

$$
\sum_{n=2,4,\ldots}^{N} \frac{1}{4} r^{n/2-1} \left\{ C_{1n} \begin{bmatrix} n(n-2)\sin\left(\frac{n}{2}-1\right)\theta \\ -n(n+2)\sin\left(\frac{n}{2}+1\right)\theta \end{bmatrix} \\ +C_{2n} \begin{bmatrix} n(2-n)\cos\left(\frac{n}{2}-1\right)\theta \\ +n(n-2)\cos\left(\frac{n}{2}+1\right)\theta \end{bmatrix} \right\}
$$

with

$$
C_{11} = \frac{K_I}{\sqrt{2\pi}} \tag{4.56}
$$

$$
C_{21} = \frac{K_{II}}{\sqrt{2\pi}} \tag{4.57}
$$

Simplifying eqs. (4.53) through (4.57) with $n = 1$ gives the dominant stresses adjacent to the crack tip for $r \to 0$. This means that a single term in the series is sufficient to determine the stress field equations. Thus,

$$
\begin{aligned}
\sigma_{rr} &= \frac{K_I}{4\sqrt{2\pi r}} \left(5\cos\frac{\theta}{2} - \cos\frac{3\theta}{2} \right) \\
\sigma_{\theta\theta} &= \frac{K_I}{4\sqrt{2\pi r}} \left(3\cos\frac{\theta}{2} + \cos\frac{3\theta}{2} \right) \qquad \text{For mode I} \\
\tau_{r\theta} &= \frac{K_I}{4\sqrt{2\pi r}} \left(\sin\frac{\theta}{2} + \sin\frac{3\theta}{2} \right)
\end{aligned} \tag{4.58}
$$

and

$$
\begin{aligned}
\sigma_{rr} &= \frac{K_{II}}{4\sqrt{2\pi r}} \left(-5\sin\frac{\theta}{2} + 3\sin\frac{3\theta}{2} \right) \\
\sigma_{\theta\theta} &= \frac{K_{II}}{4\sqrt{2\pi r}} \left(-3\sin\frac{\theta}{2} - 3\sin\frac{3\theta}{2} \right) \qquad \text{For mode II} \\
\tau_{r\theta} &= \frac{K_{II}}{4\sqrt{2\pi r}} \left(\cos\frac{\theta}{2} + 3\cos\frac{3\theta}{2} \right)
\end{aligned} \tag{4.59}
$$

For convenience, the distribution of normalized stresses per eq. (4.58) is
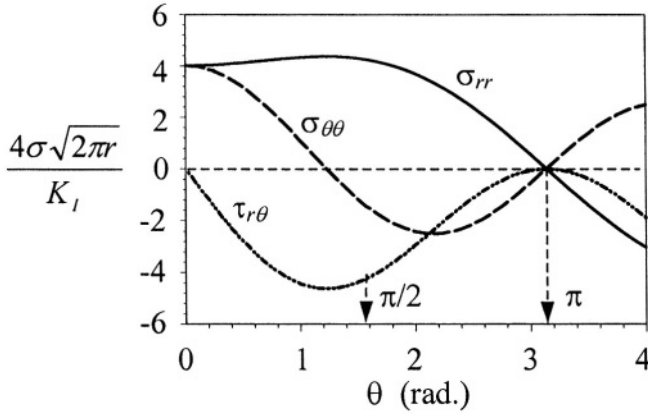
Figure 4.5 Distribution of normalized polar stresses for mode I

Consider a single-edge crack model shown in Figure 4.6 and related radial and circumferential displacement μ_r and μ_θ, respectively. The strains are defined by

$$
\begin{aligned}
\epsilon_r &= \frac{\partial \mu_r}{\partial r} \\[2mm]
\epsilon_\theta &= \frac{\mu_r}{r} + \frac{1}{r}\frac{\partial \mu_\theta}{\partial \theta} \\[2mm]
\gamma_{r\theta} &= \frac{1}{r}\frac{\partial \mu_r}{\partial r} + \frac{\partial \mu_\theta}{\partial r} - \frac{\mu_\theta}{r}
\end{aligned}
\tag{4.60}
$$
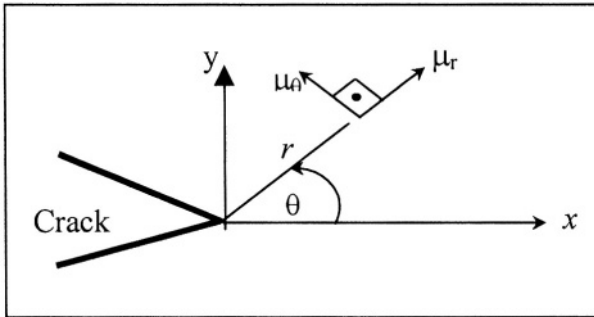
Figure 4.6 Polar displacements at a single-edge crack

For convenience, Hooke's law for plane conditions gives the following strain expressions

$$\begin{aligned} E\epsilon_r &= \sigma_r - v\sigma_\theta \\ E\epsilon_\theta &= \sigma_\theta - v\sigma_r \qquad \text{For plane stress} \\ G\gamma_{r\theta} &= \tau_{r\theta} \end{aligned} \qquad (4.61)$$

$$\begin{aligned} 2G\epsilon_r &= (1-v)\,\sigma_r - v\sigma_\theta \\ 2G\epsilon_\theta &= (1-v)\,\sigma_\theta - v\sigma_r \qquad \text{For plane strain} \\ G\gamma_{r\theta} &= \tau_{r\theta} \end{aligned} \qquad (4.62)$$

Substitute eqs. (4.58) and (4.59) into (4.61) and (4.62), and solve for ϵ_r and ϵ_θ. Then, substitute these strains into eq. (4.60) and integrate the strains to get the displacement expressions. Thus,

$$\mu_r = \frac{K_I}{4G}\sqrt{\frac{r}{2\pi}}\left[(2\kappa-1)\cos\frac{\theta}{2}-\cos\frac{3\theta}{2}\right] \qquad \text{For mode I} \qquad (4.63)$$

$$\mu_\theta = \frac{K_I}{4G}\sqrt{\frac{r}{2\pi}}\left[-(2\kappa-1)\sin\frac{\theta}{2}+\sin\frac{3\theta}{2}\right] \qquad \text{For mode I}$$

and

$$\mu_r = \frac{K_{II}}{4G}\sqrt{\frac{r}{2\pi}}\left[-(2\kappa-1)\sin\frac{\theta}{2}+3\sin\frac{3\theta}{2}\right] \qquad \text{For mode II} \qquad (4.64)$$

$$\mu_\theta = \frac{K_{II}}{4G}\sqrt{\frac{r}{2\pi}}\left[-(2\kappa-1)\cos\frac{\theta}{2}+3\cos\frac{3\theta}{2}\right] \qquad \text{For mode II}$$

where the constant κ is defined by

$$\kappa = \frac{3-v}{1+v} \qquad \text{For plane stress} \qquad (4.65)$$

$$\kappa = 3-4v \qquad \text{For plane strain} \qquad (4.66)$$

4.4.2 MODE III LOADING CASE

Consider a solid body bounded by two intersecting planes as indicated in Figure 4.7 where the stresses and strains are independent of the coordinate x_3 since $\mu_x = \mu_y = 0$ and $\sigma_{xx} = \sigma_{yy} = \sigma_{zz} = \tau_{xy} = 0$, but $\tau_{xz} \neq 0$, $\tau_{yz} \neq 0$, and $\mu_z \neq 0$. In polar coordinates, $\tau_{rz} \neq 0$ and $\tau_{\theta z} \neq 0$. Figure 4.7 shows the antiplane stress components and Figure 4.8 depicts cracks under mode III action by torsion.
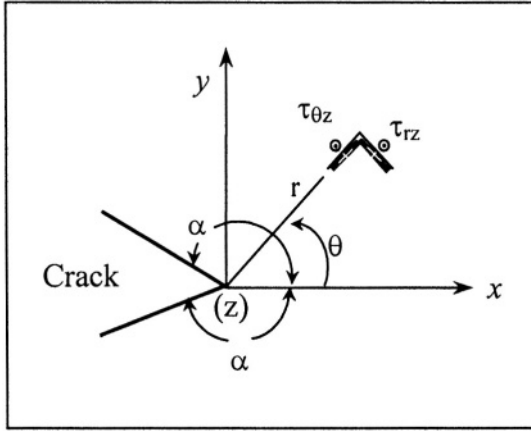
Figure 4.7 Antiplane stress components [5].
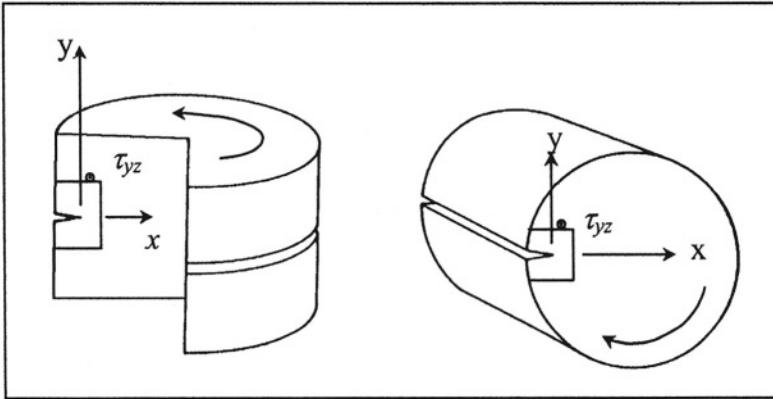
Figure 4.8 Mode III action by torsion [5].

Hooke's law in polar coordinates (Figure 4.7) gives the shear stresses as

$$\tau_{rz} = G\gamma_{rz} = G\frac{\partial \mu_z}{\partial r} \qquad (4.67)$$

$$\tau_{\theta z} = G\gamma_{\theta z} = \frac{G}{r}\frac{\partial \mu_z}{\partial \theta}$$

The equilibrium equation, the bipotential equation and the boundary condition for μ_z are, respectively

$$\frac{\partial\left(r\tau_{rz}\right)}{\partial r} + \frac{\partial\tau_{\theta z}}{\partial \theta} = 0 \tag{4.68}$$

$$\nabla^2 \mu_z = \frac{\partial^2 \mu_z}{\partial r^2} + \frac{1}{r}\frac{\partial \mu_z}{\partial r} + \frac{1}{r^2}\frac{\partial^2 \mu_z}{\partial \theta^2} = 0 \tag{4.69}$$

$$\tau_{\theta z} = \frac{\partial \mu_z}{\partial \theta} = 0 \qquad \text{For } \theta = \pm\alpha \tag{4.70}$$

Now assume that the out-of-plane displacement is defined by [5]

$$\mu_z = r^\lambda f\left(\theta\right) \tag{4.71}$$

Letting $f = f\left(\theta\right)$ and taking the derivatives needed in eq. (4.69), and simplifying the resultant expression yields the governing second order differential equation

$$\frac{\partial^2 f}{\partial \theta^2} + \lambda^2 f = 0 \tag{4.72}$$

The solution of eq. (4.72) can be determined by letting the function g be defined by

$$f = De^{r\theta} \tag{4.73}$$

Thus, eq. (4.72) yields

$$r^2 + \lambda^2 = 0 \tag{4.74}$$

$$r = -i\lambda \tag{4.75}$$

Inserting eq. (4.75) into (4.73) gives the characteristic equation as the solution of eq. (4.72) needed for determining the antisymmetric displacement μ_z when $\theta = 0$

$$f = De^{i\lambda\theta} = D\sin\lambda\theta \tag{4.76}$$

Differentiating eq. (4.76) generates the boundary condition expression, which in turn is the characteristic equation

$$\frac{df}{d\theta} = D\lambda\cos\lambda\theta = 0 \qquad \text{For } \theta = \pm\alpha \tag{4.77}$$

$$\cos\lambda\theta = 0 \tag{4.78}$$

Let $\alpha = \pi$ in eq. (4.78) in order to simulate a crack in a solid body (Figure 4.5) under mode III loading. Consequently, the eigenvalues λ take the form

$$\lambda = \frac{n}{2} \qquad \text{For } n = 1, 3, 5, 7, ... \tag{4.79}$$

Clearly, eq. (4.78) becomes

$$\cos \lambda \pi = 0 \tag{4.80}$$

$$\cos \frac{\pi}{2} = \cos \frac{3\pi}{2} = \cos \frac{5\pi}{2} = \cos \frac{7\pi}{2} = ... = 0 \tag{4.81}$$

Consequently, the antisymmetric displacement along the crack line and the respective shear stresses defined by eqs. (4.71) and (4.67), respectively, become

$$\mu_z = D_n r^{n/2} \sin \frac{n\theta}{2} \tag{4.82}$$

$$\tau_{rz} = G \frac{\partial \mu_z}{\partial r} = \frac{nG}{2} D_n r^{n/2-1} \sin \frac{n\theta}{2} \tag{4.83}$$

$$\tau_{\theta z} = \frac{G}{r} \frac{\partial \mu_z}{\partial \theta} = \frac{nG}{2} D_n r^{n/2-1} \cos \frac{n\theta}{2} \tag{4.84}$$

The normalized shear stress distribution is depicted in Figure 4.9. Notice that these stresses, eqs. (4.83) and (4.84), have an opposite distribution because the trigonometric terms in the equations
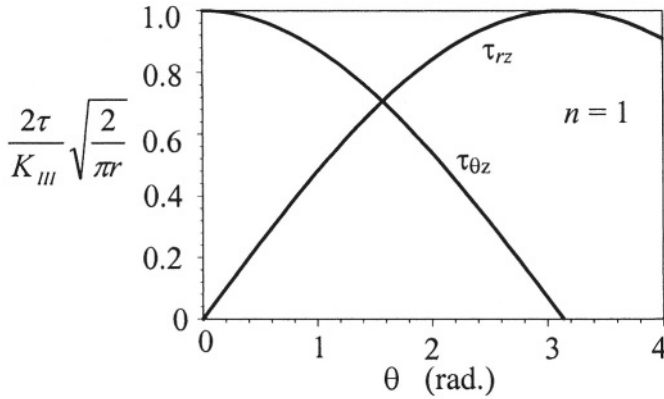
Figure 4.9 Distribution of normalized shear stresses for mode III and n = 1

The constant D_n for $n = 1$ becomes [5]

$$D_1 = \frac{K_{III}}{G} \sqrt{\frac{2}{\pi}} \tag{4.85}$$

The parameter D_1 in eqs. (4.82) through (4.84) corresponds to the dominant term in the series. So far the mechanics framework for including higher order terms in the stress series has been described for a purely linear-elastic stress field at the crack tip. This analytical treatment allows a small plastic zone (r) and predicts the shear stress field. Furthermore, K_{III} is the antiplane stress intensity factor. Recall that G is the shear modulus of elasticity defined by eq. (1.9).

However, the only nonzero stress is $\tau_{\theta z}$ at $\theta = 0$. Thus,

$$\tau_{\theta z} = \frac{K_{III}}{\sqrt{2\pi r}} \qquad \text{For } \theta = 0 \qquad (4.86)$$

$$\tau_{rz} = 0 \qquad \text{For } \theta = 0 \qquad (4.87)$$

$$\mu_z = \frac{2K_{III}}{G}\sqrt{\frac{r}{2\pi}} \qquad \text{For } \theta = \pi \qquad (4.88)$$

Thus far, the reader should have a clear understanding of the complexity of fracture mechanics. For instance, the field equations being derived are for elastic materials so that the linear elastic fracture mechanics (LEFM) approach can easily be applied to crack-related problems. This is a subject well documented in the literature.

All the stress, strain and displacement field equations have the plastic zone size (r) in common. This implies that LEFM allows some degree of plasticity adjacent to the crack tip. However, the constraint is that the plastic zone size must be much smaller than the crack length; that is, $r << a$, otherwise, LEFM would not be valid in solving fracture mechanics problems. If $r \geq a$, then the plastic fracture mechanics (PFM) approach becomes very useful. This subject will be dealt with in a later chapter.

4.5   HIGHER ORDER STRESS FIELD

The assume that the damage ahead of the crack tip is characterized by second order local stresses, which are dependent of specimen size and geometry as opposed to the first order terms. Consequently, the stress field are no longer singular as $r \to 0$ and the second order term in the series of expansion is known in the literature as the T-stress for elastic behavior which accounts for effects of stress biaxiality. Several T-stress solutions are available in the literature [8-14].

For elastic-plastic and fully plastic materials, the second order term is also known as the J-Q approach [8]. In particular, O'Dowd and Shih [15-16] can be consulted for obtaining details of the J-Q theory which describes the fundamentals that provide quantitative measures of the crack tip deformation. Nevertheless, the term Q accounts for plasticity in the triaxiality state crack tip stress field.

Considering a mixed mode fracture process and the effects of the T-stress in cracked bodies, the asymptotic stress state at the crack tip can be determined by

adding eqs. (4.13) and (4.35) and T-stress. Thus, for mode I and II interaction the stresses are

$$
\begin{bmatrix} \sigma_{xx} & \tau_{xy} \\ \tau_{xy} & \sigma_{yy} \end{bmatrix} = \frac{K_I}{\sqrt{2\pi r}} \begin{bmatrix} f_x(\theta) & f_{xy}(\theta) \\ f_{xy}(\theta) & f_y(\theta) \end{bmatrix}
$$
$$
+ \frac{K_{II}}{\sqrt{2\pi r}} \begin{bmatrix} g_x(\theta) & g_{xy}(\theta) \\ g_{xy}(\theta) & g_{xy}(\theta) \end{bmatrix} + \begin{bmatrix} T_x & 0 \\ 0 & 0 \end{bmatrix}
\tag{4.89}
$$

With regard to the T-stress theory, Larsson and Carlsson [17] and Sherry et al. [18] defined T_x as the non-singular stress that acts in the direction parallel to the crack plane and it is given as [19]

$$
T_x = \sigma_{xx} - \frac{K_I}{\sqrt{2\pi r}} f_x(\theta)
\tag{4.90}
$$

For $\theta = 0$, the stress state eq. (4.89) becomes

$$
\begin{bmatrix} \sigma_{xx} & \tau_{xy} \\ \tau_{xy} & \sigma_{yy} \end{bmatrix} = \frac{K_I}{\sqrt{2\pi r}} \begin{bmatrix} 1 & 0 \\ 0 & 1 \end{bmatrix} + \frac{K_{II}}{\sqrt{2\pi r}} \begin{bmatrix} 0 & 1 \\ 1 & 0 \end{bmatrix}
$$
$$
+ \begin{bmatrix} T_x & 0 \\ 0 & 0 \end{bmatrix}
\tag{4.91}
$$

and for pure mode I loading, $K_{II} = 0$, T-stress becomes

$$
\begin{aligned}
T_x &= \sigma_{xx} - \frac{K_I}{\sqrt{2\pi r}} \\
T_x &= \sigma_{xx} - \sigma_{yy}
\end{aligned}
\tag{4.92}
$$

In fact, this equation is the modified σ_{xx} stress function in eq. (4.13). Moreover, Leevers and Radon [20] defined T_x to be independent of the stress intensity factor as

$$
T_x = \beta\sigma
\tag{4.93}
$$

where σ = Remote applied stress (MPa)

Similarly, for pure mode II, the T-stress is [14]

$$
T_x = \sigma_{xx} + \frac{K_{II}}{\sqrt{2\pi r}}
\tag{4.94}
$$
$$
T_x = \sigma_{xx} + \tau_{xy}
\tag{4.95}
$$

In addition, β in eq. (4.93) is the dimensionless stress biaxiality ratio given as [20]

$$\beta = \frac{T_x \sqrt{\pi a}}{K_I} \tag{4.96}$$

For convenience, the geometric correction factors and biaxiality. ratios for some common specimen configurations are

- Single-edge cracked plate (SET) in tension (Table 3.1) with $L/w \geq 1.5$ and $x = a/w$ [12]:

$$\frac{T_x}{\sigma} = \frac{1}{(1-x)^2} \left[\begin{array}{c} -0.526 + 0.641x + 0.2049x^2 \\ +0.755x^3 - 0.7974x^4 + 0.1966x^5 \end{array} \right] \tag{4.97}$$

$$\beta = \frac{1}{\sqrt{1-x}} \left[\begin{array}{c} -0.469 + 0.1414x + 1.433x^2 + 0.0777x^3 \\ -1.6195x^4 + 0.859x^5 \end{array} \right] \tag{4.98}$$

- Double-edge cracked plate (DET) in tension (Table 3.1) with $L/w \geq 1.5$ and $x = a/w$ [12]:

$$\frac{T_x}{\sigma} = -0.526 - 0.0438x + 0.0444x^2 + 0.12194x^3 \tag{4.99}$$

$$\beta = -0.469 - 0.071x + 0.1196x^2 + 0.2801x^3 \tag{4.100}$$

- Double-edge cracked plate (DET) in tension (Table 3.1) with $L/w = 1$ and $x = a/w$ [12]:

$$\frac{T_x}{\sigma} = -0.526 + 0.1804x - 2.7241x^2 + 9.5966x^3 - 6.3883x^4 \tag{4.101}$$

$$\beta = -0.469 + 0.1229x - 1.2256x^2 + 6.0628x^3 - 4.4983x^4 \tag{4.102}$$

- Double cantilever beam (DCB) in tension (Figure 6.5) [12]:

$$T_x = \frac{\beta K_I}{\sqrt{\pi a}} = P \sqrt{\frac{12}{\pi a h}} \left[\frac{a/h + 0.68}{0.681 (h/a) + 0.0685} \right] \tag{4.103}$$

$$\beta = \frac{1}{0.681 (h/a) + 0.685} \qquad \text{For } h/a < 1.5 \tag{4.104}$$

$$K_I = P \sqrt{\frac{12}{h}} (a/h + 0.68) \tag{4.105}$$

where $P =$ Load per unit length (MN/m)

- Compact tension (CT) specimen in tension (Table 3.1) with $L/w = 0.6$ and $a/w < 1$ [18]:

$$\frac{T_x}{\sigma} = 6.063 - 78.987x + 380.46x^2 - 661.70x^3 + 428.45x^4 \tag{4.106}$$

The significance of the T-stress can be explained by plotting, say, eq. (4.101) along with eq. (4.102) as shown in Figure 4.10 for a double-edge cracked plate (DET) (Table 3.1) with $L/w = 1$ and $x = a/w$ [12]. For $T_x/\sigma < 0$, the local crack tip stresses are below the limits predicted by the small-scale yielding since the T_x is in the compressive state stabilizing the crack path [8]. The opposite occurs for $T_x/\sigma > 0$, leading to a high degree of triaxiality in the crack tip stresses since T_x is the tensile state [21]. From Figure 4.10, the transition for this particular specimen configuration occurs at approximately $a/w = 0.70$. Similarly, the dimensionless stress biaxiality ratio also exhibits nearly equal trend as the T_x/σ curve.
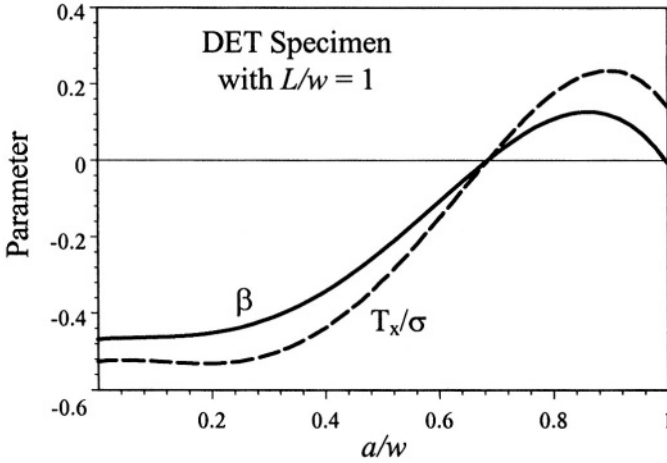
Figure 4.10 Normalized T-stress as a function of normalized crack length for a double-edge specimen loaded in tension.

According to Williams [7], the T-stress can be derived using an Airy's stress function in polar coordinates for a cracked body having the coordinates origin at the crack tip. This equation can also be found in a compendium of the T-stress solutions reported by Fett [12]. Thus, the symmetric Airy's stress part for mode I loading is

$$\phi_s = \sigma w^2 \sum_{m=0}^{\infty} \left(\frac{r}{w}\right)^{m+3/2} A_m \left[\cos\left(m + \frac{1}{2}\right)\theta - \frac{m + \frac{3}{2}}{m - \frac{1}{2}} \cos\left(m - \frac{1}{2}\right)\theta\right]$$

$$+ \sigma w^2 \sum_{m=0}^{\infty} \left(\frac{r}{w}\right)^{m+2} B_m \left[\cos\left(m + 2\right)\theta - \cos m\theta\right] \tag{4.107}$$

and the antisymmetric part for mode II becomes

$$\phi_a = \sigma w^2 \sum_{m=0}^{\infty} \left(\frac{r}{w}\right)^{m+3/2} C_m \left[\sin\left(m + \frac{1}{2}\right)\theta - \sin\left(m - \frac{1}{2}\right)\theta\right] \quad (4.108)$$

$$+ \sigma w^2 \sum_{m=0}^{\infty} \left(\frac{r}{w}\right)^{m+2} D_m \left[\sin\left(m + 3\right)\theta - \frac{m+3}{m+1}\sin\left(m + 1\right)\theta\right]$$

where w is the characteristic dimension. According to Fett [12], eq. (4.107) can be used to determine the T-stress as

$$T_x = -4\sigma B_o - \sigma_x^{(o)} \quad (4.109)$$

Here, $\sigma_x^{(o)}$ is the stress contribution in the uncracked body. Further details on this topic can be found elsewhere [12,19,21].

4.6 REFERENCES

[1] J. W. Dally and W.F. Riley, "Experimental Stress Analysis," Third Edition, McGraw-Hill, Inc. New York, (1991)

[2] R. Chona, "Non-singular stress effects in fracture test specimens: A Photoelastic study," M.S. thesis, University of Maryland, College Park, (August 1985)

[3] G.R. Irwin, Proc. SESA, Vol. XVI, No. 1 (1958) 93-96

[4] R.J. Sanford, "A critical re-examination of the Westergaard Method for Solving Opening-Mode Crack problems," Mech. Res., Vol. 6, No. 5, (1979) 289-294

[5] K. Hellan, "Introduction to Fracture Mechanics," McGraw-Hill Book company, New York, (1984)

[6] M.H. Aliabadi and D.P. Rooke, "Numerical Fracture Mechanics," Computational Mechanics Publications, Kluwer Academic Publishers, Boston, (1992) Chapter 2.

[7] M.L. Williams, "On The Stress Distribution At The Base Of A Stationary Crack," J. Appl. Mech., 24 (1957) 109-114

[8] T.L. Becker Jr., R.M. Cannon and R.O. Ritchie, "Finite Crack Kinking and T-stresses in Functionally Graded Materials," Inter. Journal of Solids and Structures, 38 (2001) 5545-5563

[9] T. Fett, "Stress Intensity Factors and T-stress For Single and Double-Edge Cracked Circular Disks Under Mixed Boundary Conditions," Eng. Fract. Mech., Vol. 69, No. 1, (2002) 69-83

[10] T. Fett, D. Munz and G. Thun "Fracture Toughness Testing on Bars Under Opposite Cylinder Loading," ASME, Inter. Gas Turbine and Institute, Turbo Expo IGTI, Vol. 4A, (2002) 97-102

[11] T. Fett, "Stress Intensity Factors and T-stress For Internally Cracked Circular Disks Under Various Boundary Conditions," Eng. Fract. Mech., Vol. 68, No. 9, (2001) 1119-1136

[12] T. Fett, "A Compendium of T-stress Solutions," Forschungszentrum Karlsruhe, Technik and Umwelt, Wissenschaftliche Berichte, FZKA 6057, www.ubka.uni-karlsruhe.de, (1998) 1-72

[13] T. Fett, "Stress Intensity Factors and T-stress for Cracked Circular Disks," Forschungszentrum Karlsruhe, Technik and Umwelt, Wissenschaftliche Berichte, FZKA 6484, www.ubka.uni-karlsruhe.de, (2000) 1-68

[14] B. Chen, "The Effect of the T-stress on Crack Path Selection in Adhesively Bonded Joints," Inter. Journal of Adhesion and Adhesives, Vol 21, No. 5, (2001) 357-368

[15] N.P. O'Dowd and C.F. Shih, "Family of Crack-Tip Fields Characterized by a Triaxiality Parameter: I Structure of Fields," J. Mechanics and Physics of Solids, Vol. 39, (1991) 989-1015

[16] N.P. O'Dowd and C.F. Shih, "Family of Crack-Tip Fields Characterized by a Triaxiality Parameter: II Fracture Applications," J, Mechanics and Physics of Solids, Vol. 40, (1992) 939-963

[17] S.G. Larsson and A.J. Carlsson, "Influence of Non-Singular Stress Terms and Specimen Geometry on Small-Scale Yielding at Crack Tips in Elastic-Plastic Materials," J. Mechanics and Physics of Solids, Vol. 21, (1973) 263-277

[18] A.H. Sherry, C.C. France and L. Edwards, "Compendium of T-Stress Solutions for Two and Three Dimensional Cracked Geometries," The Inter. Journal, Vol. 18, (1995) 141-155

[19] A. Saxena, "Nonlinear Fracture Mechanics for Engineers," CRC Press LLC, New York, (1998) 126,.221

[20] P.S. Leevers and J.C. Radon, "Inherent Biaxiality. in Various Fracture Specimen Geometries," Inter. Journal, Vol. 19, (1982) 311-325

[21] M.T. Kirk, R.H. Dodds Jr,.and T.L. Anderson, "An Application Technique for Predicting Size Effects on Cleavage Fracture Toughness (J_c) Using Elastic T-stress," in Fracture Mechanics, Vol. 24, ASTM STP 1207, (1994) 62-86

Chapter 5

CRACK TIP PLASTICITY

5.1 INTRODUCTION

In this chapter, a few models of the configuration or the shape of the crack tip plasticity are included. It is essential to have a thorough knowledge of the shape and size of the plastic zone in order to compare theoretical and experimental results for plane stress and plane strain conditions. Furthermore, the formation of the plastic zone depends on the material properties, specimen or structural element configuration, and loading conditions.

Most solid materials develop plastic strains when the yield strength is exceeded in the region near a crack tip. Thus, the amount of plastic deformation is restricted by the surrounding material, which remains elastic during loading.

Theoretically, linear elastic stress analysis of sharp cracks predicts infinite stresses at the crack tip. In fact, inelastic deformation, such as plasticity in metals and crazing in polymers, leads to relaxation of crack tip stresses caused by the yielding phenomenon at the crack tip. As a result, a plastic zone is formed containing microstructural defects such dislocations and voids. Consequently, the local stresses are limited to the yield strength of the material. This implies that the elastic stress analysis becomes increasingly inaccurate as the inelastic region at the crack tip becomes sufficiently large and linear elastic fracture mechanics (LEFM) is no longer useful for predicting the field equations.

The size of the plastic zone can be estimated when moderate crack tip yielding occurs. Thus, the introduction of the plastic zone size as a correction parameter that accounts for plasticity effects adjacent to the crack tip is vital in determining the effective stress intensity factor (K_e) or a corrected stress intensity factor. The plastic zone is also determined for plane conditions; that is, plane strain for maximum constraint on relatively thick components and plane stress for variable constraint due to thickness effects of thin solid bodies. Moreover, the plastic zone develops in most common in materials subjected to an increase in the tensile stress that causes local yielding at the crack tip.

5.2   CRACK TIP STRESS STATE

The stress field equations derived in Chapter 4 predict that the crack tip stresses reach infinite values (stress singularity) as the plastic zone size (r) approaches zero; that is, $\sigma_{ij} \to \infty$ as $r \to 0$. However, most engineering metallic materials are subjected to an irreversible plastic deformation. If plastic deformation occurs, then the elastic stresses are limited by yielding since stress singularity cannot occur, but stress relaxation takes place within the plastic zone. This plastic deformation occurs in a small region and it is called the crack-tip plastic zone. A small plastic zone, $(r << a)$ is referred to as small-scale yielding.

On the other hand, a large-scale yielding corresponds to a large plastic zone, which occurs in ductile materials in which $r >> a$. This suggests that the stress intensity factors within and outside the boundary of the plastic zone are different in magnitude so that $K_I(plastic) > K_I(elastic)$. In fact, $K_I(plastic)$ must be defined in terms of plastic stresses and displacements in order to characterize crack growth, and subsequently ductile fracture. As a consequence of plastic deformation ahead of the crack tip, the linear elastic fracture mechanics (LEFM) theory is limited to $r << a$; otherwise, elastic-plastic fracture mechanics (EPFM) theory controls the fracture process due to a large plastic zone size $(r \geq a)$. This argument implies that r may be determined in order to set an approximate limit for both LEFM and EPFM theories.

Figure 5.1 shows schematic plastic zones for plane stress (thin plate) and plane strain (thick plate) conditions. Some requirements for plane conditions were introduced in Chapter 1; but they are included henceforth from a different prospective. Thus,

PLANE STRAIN:
1. Large thickness *B,* and $\epsilon_z \simeq 0$ in an internal region and $\sigma_z = v\left(\sigma_x + \sigma_y\right)$. This means that the material is constrained in the z-direction due to a sufficiently large thickness and the absence of strain in this axis. In fact, the stress in the z-direction develops due to the Poisson's effect as explicitly included in the equation that defines σ_z.

2. Yielding is suppressed due to the kinematics constrain from the surrounding elastic material.

3. Plastic deformation is associated with the hinge mechanism (internal necking) Figure 5.1a)

4. The plastic zone size is small in the midsection of the plate (Figure 5.1a). This condition implies that the plastic zone must be smaller than the crack length

PLANE STRESS:
1. The thickness B is small, $\sigma_z = 0$ and $\epsilon_z \neq 0$ on the surface (external region) and through the whole thickness. This means that the stresses normal to the free surface are absent and therefore, $\sigma_z = 0$ through the thickness. Consequently, a biaxial state of stress results.

2. If $\sigma_y \geq \sigma_x > 0$ (Tresca Criterion), then yielding occurs by a cumulative slip mechanism (Figure 5.1b)
3. The height of the yielded zone is limited due to the slip mechanism.
4. The total motion has a necking effect in front of the crack as it opens

a) Plastic Zone

Slip surfaces

c) Hinge Mechanism In
Thick Plates

Plane Strain
Mode I

b) Surface

Plane Stress
Mode I

Notch

Critical
Zone

Smooth
Specimen

d) Hinge Mechanism In
Thin Plates
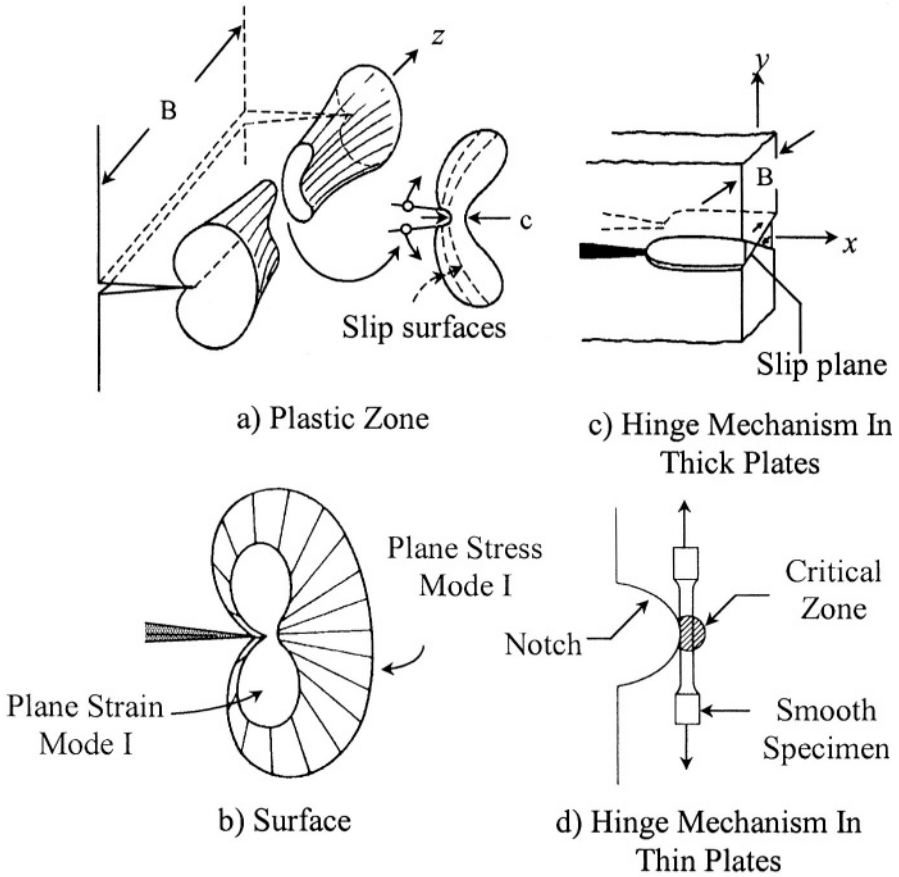
Figure 5.1 Yielding mechanisms of a plate [1-3]

Consider the circular plastic zone shown in Figure 5.2. To study the size of the plastic zone, consider Mode I loading and assume that crack growth occurs along its plane so that $\theta = 0$ and $y = 0$ along the crack line (x-axis). For convenience, eqs. (3.27) and (3.29) are included in this chapter as a starting point for determining the plastic zone size equation. Thus,

$$\sigma_y = \sigma\sqrt{\frac{a}{2r}} \qquad\qquad (5.1)$$

$$K_I = \sigma\sqrt{\pi a} \qquad\qquad (5.2)$$

Setting $\sigma_y = \sigma_{ys}$ in eq. (35.1) means that plasticity exists adjacent to the crack tip. Notice that the double subscript in this local stress has being changed to one just for convenience. Combining these equations yields the plastic zone size as

$$r = \frac{a}{2}\left(\frac{\sigma}{\sigma_{ys}}\right)^2 \tag{5.3}$$

where σ = Applied stress (MPa)
σ_{ys} = Yield strength (MPa)
a = Crack length (m)

It has been reported that [2,12] that yielding at the crack tip causes the crack behave as if it is larger than the actual size and, therefore, the tensile stress reaches a finite value. This indicates that the plastic zone represents an area that strain hardens and the internal tensile stress (σ_y) is limited to the ultimate tensile stress (σ_u). Furthermore, the stress σ_y produces plastic work when $\sigma_{ys} \leq \sigma_y \leq \sigma_u$ due to an external applied stress σ and it is transferred into strain energy density for plastic deformation to occur. This implies that the plastic zone size reaches a maximum magnitude when $\sigma_y = \sigma_u$ and, consequently, the effective crack size $a_e = a + r$ becomes the new actual size, which extends through the plastic zone due to initiation and coalescence of voids. This may repeat and continue until the actual crack reaches a critical value at the onset of crack propagation for fracture or separation. Unfortunately, the use of the plastic zone size in practical applications is limited to elastic solids that may undergo very little plastic deformation.

5.3   IRWIN'S APPROXIMATION

Irwin [2,12] has shown that the effect on the plastic zone is to artificially extend the crack by a distance r_1 (Figure 5.2) known as Irwin's plastic zone correction. The elastic stress distribution shown in Figure 5.2 indicates that $\sigma_y \rightarrow \infty$ as $r \rightarrow 0$. Actually, σ_y is limited to σ_{ys} as shown by the elastic-plastic stress distribution. This means that $\sigma_y \rightarrow \infty$ occurs mathematically, not physically. In order to account for the changes due to the artificial crack extension or virtual crack length and to visualize the plastic zone as a cylinder, the crack length a can be replaced by a_e in eq. (5.3).

Moreover, the virtual crack length defined by a_e is referred to as the effective crack length in the literature. The conditions of equilibrium for an immobile crack tip include internal and external forces per unit length [5,24]. In such a case, the areas related to the shedding loads P_s and P_{ys} due to yielding, as indicated in Figure 5.2, are equal; that is $AP_s = AP_{ys}$ when the plastic zone size is $r << a$. Mathematically, these loads are the equilibrium forces per unit length defined by [1]
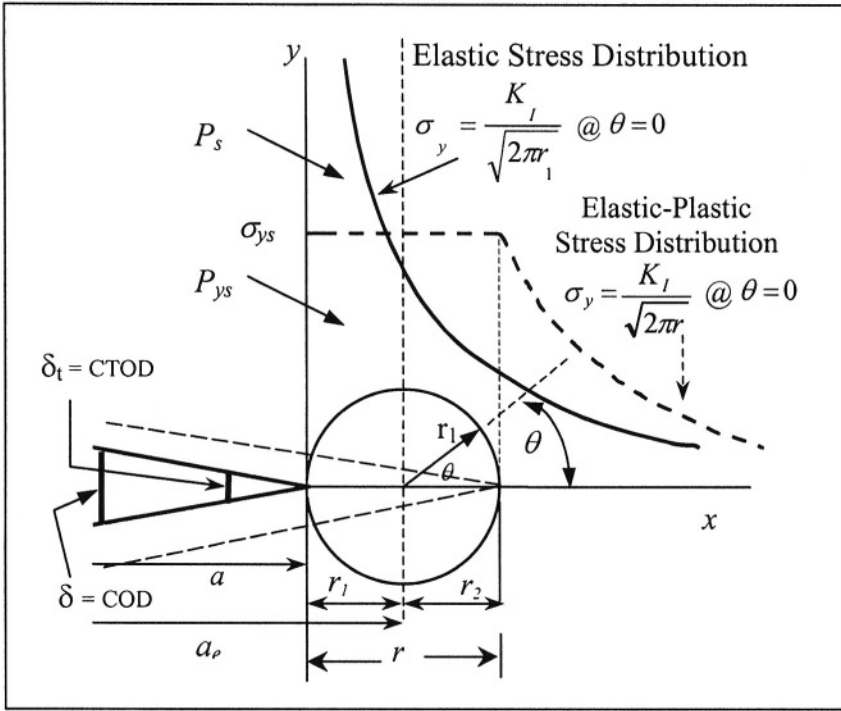
Figure 5.2 Crack tip plastic zone model

$$P_s = B \int_o^{r_1} (\sigma - \lambda \sigma_{ys}) \, dx \qquad (5.4)$$

$$P_{ys} = B \int_o^{r_2} \lambda \sigma_{ys} dx \qquad (5.5)$$

where B = Thickness
$\quad \lambda = 1$ for plane stress
$\quad \lambda = \sqrt{3}$ =Irwin's yielding factor for plane strain [12]

For equilibrium conditions, the force balance $\sum (P_s + P_{ys}) = 0$ leads to the determination of the of the plastic zone size Hence,

$$\int_o^{r_1} (\sigma - \lambda \sigma_{ys}) \, dx - \int_o^{r_2} \lambda \sigma_{ys} dx = 0 \qquad (5.6)$$

Inserting eq. (3.1) into (5.6) and integrating yields

$$\int_o^{r_1} \left(\frac{K_I}{\sqrt{2\pi x}} - \lambda\sigma_{ys} \right) dx - \int_o^{r_2} \lambda\sigma_{ys} dx \;\; = \;\; 0 \tag{5.7}$$

$$\frac{2r_1 K_I}{\sqrt{2\pi r_1}} - \lambda\sigma_{ys}(r_1 + r_2) \;\; = \;\; 0 \tag{5.8}$$

$$2r_1\sigma_y - \lambda\sigma_{ys}(r_1 + r_2) \;\; = \;\; 0 \tag{5.9}$$

When yielding occurs, the boundary between the elastic and the plastic is estimated is limited to the yield strength as by a yield criterion. Thus, the elastic stress can be defined by

$$\sigma_y = \lambda\sigma_{ys} \tag{5.10}$$

Inserting eq. (5.10) into (5.9) gives $2r_1 = r_1 + r_2$ which implies that $r_1 = r_2$ and from Figure 5.2, $r = r_1 + r_2$. Hence, $a_e = a + r$ is the virtual crack length proposed by Irwin [1,12]. Obviously, eq. (3.29) provides the effective stress intensity factor

$$K_I = \alpha\sigma\sqrt{\pi(a+r)} = \alpha\sigma\sqrt{\pi a_e} \tag{5.11}$$

This K_I equation is the corrected stress intensity factor due to finite specimen size and plasticity. Now, inserting eqs. (5.3) into (5.11) yields

$$K_I = \alpha\sigma\sqrt{\pi a \left[1 + \frac{1}{2} \left(\frac{\sigma}{\sigma_{ys}} \right)^2 \right]} \tag{5.12}$$

Furthermore, the plastic zone size for plane conditions can easily be determined by combining eqs. (3.1) and (5.10). Thus,

$$r = \frac{1}{2\pi} \left(\frac{K_I}{\lambda\sigma_{ys}} \right)^2 = \frac{a}{2} \left(\frac{\sigma}{\lambda\sigma_{ys}} \right)^2 \tag{5.13}$$

In plane strain condition, yielding is suppressed by the triaxial state of stress and the plastic zone size is smaller than that for plane stress as predicted by the λ parameter in eq. (5.13).

The same reasoning can be used for mode III. Thus, the plastic zone becomes [7]

$$r = \frac{1}{2\pi} \left(\frac{K_{III}}{\tau_{ys}} \right)^2 \tag{5.14}$$

The application of Irwin's approximation seems reasonable for solving practical engineering problems. For instance, the pressure vessel containing a semi-elliptical crack shown in Figure 3.6 may be corrected for plasticity.

5.4   DUGDALE'S APPROXIMATION

Dugdale [15] proposed a strip yield model for the plastic zone under plane stress conditions. Consider Figure 5.3 which shows the plastic zones in the form of narrow strips extending a distance r each, and carrying the yield stress σ_{ys}. The phenomenon of crack closure is caused by internal stresses since they tend to close the crack in the region where $a < x < c$.
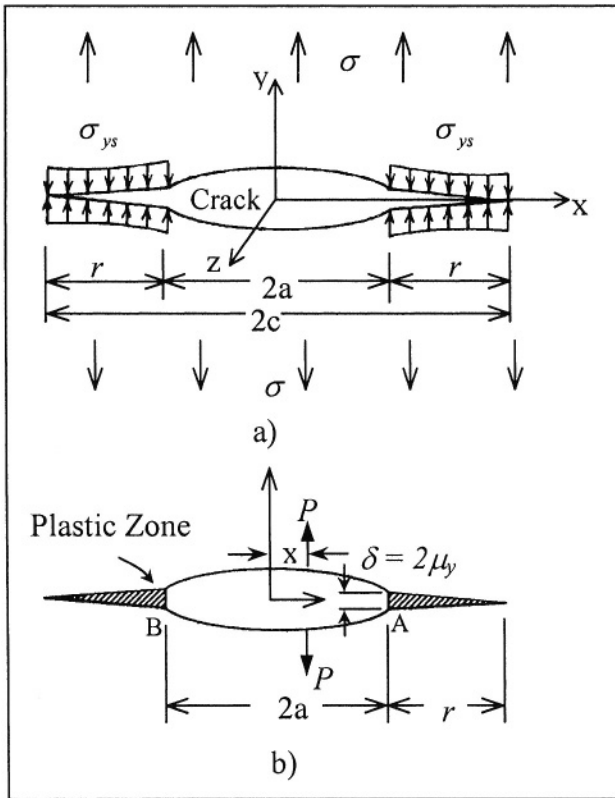
Figure 5.3. Dugdale plastic zone strip model for non-strain hardening solids under plane stress conditions: a) Dugdale crack and b) wedge crack [6].

Furthermore, assume that stress singularities disappear when the following equality is true $K_\sigma = -K_I$, where K_σ is the applied stress intensity factor and K_I is due to yielding ahead of the crack tip [6]. Hence, the stress intensity factors due to wedge internal forces are defined by

$$K_A \;=\; \int_a^{a+r} \frac{P}{\sqrt{\pi a}} \sqrt{\frac{a+x}{a-x}}\, dx \qquad (5.15)$$

$$K_B \;=\; \int_a^{a+r} \frac{P}{\sqrt{\pi a}} \sqrt{\frac{a-x}{a+x}}\, dx \qquad (5.16)$$

According to the principle of superposition, the total stress intensity factor is $K_I = K_A + K_B$ so that

$$K_I \;=\; \frac{P}{\sqrt{\pi a}} \int_a^{a+r} \left(\sqrt{\frac{a+x}{a-x}} + \sqrt{\frac{a-x}{a+x}} \right) dx \qquad (a)$$

$$K_I \;=\; \frac{P}{\sqrt{\pi a}} \int_a^{a+r} \frac{2a\, dx}{\sqrt{a^2 = x^2}} \qquad (b)$$

$$K_I \;=\; 2P \sqrt{\frac{a}{\pi}} \int_a^{a+r} \frac{dx}{\sqrt{a^2 = x^2}} \qquad (c)$$

$$K_I \;=\; -2P \sqrt{\frac{a}{\pi}} \arccos \frac{x}{a} \qquad (5.17)$$

The plastic zone correction can be accomplished by replacing the crack length a for the virtual crack length $(a+r)$, and P for σ_{ys}. Thus, the stress intensity factor are

$$K_I \;=\; -\frac{2\sigma_{ys}}{\pi} \sqrt{\pi\,(a+r)} \arccos \frac{x}{a+r} \qquad (5.18)$$

$$K_\sigma \;=\; \sigma \sqrt{\pi\,(a+r)} \qquad (5.19)$$

But, $K_\sigma = -K_I$ and the simplified equation takes the form

$$\frac{\pi\sigma}{2\sigma_{ys}} = \arccos \frac{x}{a+r} \qquad (5.20)$$

Let $y = \pi\sigma/2\sigma_{ys}$ so that

$$\frac{x}{a+r} \;=\; \cos y \qquad (5.21)$$

$$r \;=\; a\,(\sec y - 1) \qquad (5.22)$$

Expanding the trigonometric function eq. (5.22) yields

$$\sec y = 1 + \frac{y^2}{2!} + \frac{y^4}{4!} + \frac{y^6}{6!} + \ldots \simeq .1 + \frac{y^2}{2} \qquad (5.23)$$

Neglecting the higher order terms eq. (5.22) becomes

$$r = \frac{ay^2}{2} = \frac{a}{2}\left(\frac{\pi\sigma}{2\sigma_{ys}} \right)^2 \qquad (5.24)$$

Substituting eq. (5.24) into (5.11) gives the corrected stress intensity factor due plasticity at the crack tip and crack geometry

$$K_I = \alpha\sigma\sqrt{\pi a\left[1 + \frac{1}{2}\left(\frac{\pi\sigma}{2\sigma_{ys}}\right)^2\right]} \tag{5.25}$$

Expression (5.25) is similar to Irwin's expression, eq. (5.12). In addition, if $r \ll a$, plasticity corrections are not necessary. If $r > a$, linear elastic fracture mechanics (LEFM) is a doubtful approach for solving engineering problems using brittle or elastic solids and therefore, the most attractive approach is the elastic-plastic fracture mechanics (EPFM), which will be dealt with in a later chapter.

Comparing Irwin's and Dugdale's approximation schemes can easily be done by combining eqs. (5.13) and (5.24) for plane stress conditions .Thus,

$$r\,[Irwin] = \frac{8}{\pi^2}r\,[Dugdale] = 0.81r\,[Dugdale] \tag{5.26}$$

Figure 5.4 compares the normalized stress intensity factors as per Irwin's and Dugdale's approximations. The curves significantly differ as $\sigma/\sigma_{ys} \rightarrow 1$; however, similarities occur at $0 < \sigma/\sigma_{ys} \lesssim 0.2$. This strongly suggests that both Irwin's and Dugdale's approximation methods should be used very carefully at large stress rations because of their differences in normalized stress intensity factor.
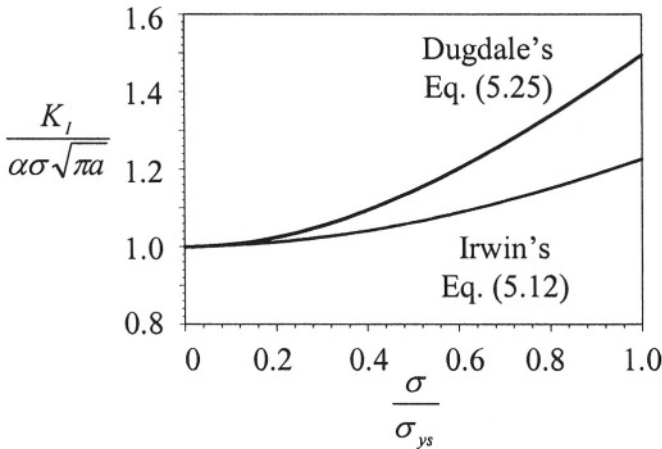
Figure 5.4 Normalized stress intensity factor as a functio of stress ration

5.5   CRACK OPENING DISPLACEMENT

So far, the characterization of cracked brittle materials has been restricted to the linear elastic fracture criterion, which treats localized plasticity, if formed ahead of the crack tip, as a small deformed area at a small-scale yielding. Otherwise, this criterion invalidates the applicability of analytical solutions associated with a material resistance to crack growth at a large-scale yielding. In the latter case, therefore, the physical sense of K_{IC}, acting as the controlling fracture critical parameter is lost, to a great extent, in spite of that K_{IC} may be applicable when $\sigma < \sigma_{ys}$.

The aforementioned restriction is fundamentally and quantitatively governed by nonlinear fracture mechanics through models, such as the crack tip opening displacement (δ_t-model) and the J-integral (J-model). The latter model treats the presence of large deformations as an integral part of analytical formulations that comprehensively describe the state of plastic stresses and strains [19-20]. Moreover, linear elastic fracture mechanics (ELFM) restricts the use of the elastic-plastic materials due to the formation of large plastic zones and nonlinear plastic behavior. Furthermore, the crack tip opening displacement ($\delta_t = CTOD$) is a measure of fracture toughness of solid materials that undergo ductile-to-brittle transition [26] and elastic-plastic or fully plastic behavior as in large structures (ships, pressure vessels). Subsequently, the critical stress and crack size might be predicted using this technique, provided that a critical value of $CTOD$ ($\delta_t = \delta_c$) is known. Wells [29-30] first proposed this as a fracture criterion by $CTOD$ ($\delta_t \geq \delta_c$). The meaningful magnitude of dc is simply a measure of fracture toughness of ductile and thin materials.

According to the ASTM E1290 Standard [26], δ_c is used when the K_{IC} requirements are not met. Figure 5.3 shows the Dugdale's model [15] for a central crack containing yielding as confined and localized narrow plastic zones in a thin sheet. This model, as depicted in Figure 5.3 simply shows the effect of yielding on the crack length. Thus, the virtual crack size (artificial or effective crack size) is $a_e = a + r$, but the plastic zone (r) restrains crack growth (also referred to as crack extension) as the applied stress (σ) is increased. Consequently, the plastic zone reaches a critical size ($r \to r_c$) and crack growth occurs since localized plasticity imparts an increase in dislocation density, formation of voids, and void coalescence, which act as micro-cracks within the plastic zone volume ahead of the main crack tip.

Conclusively, the use of a plastic correction approach is an appropriate mathematical tool for reflecting the suitability to include crystal lattice defects, as part of fracture at a microscopic scale, as an indirect form of adhered plasticity to the crack tips. Thus, the plastic zone correction appears to be suitable for correcting the crack opening displacement ($COD = \delta$). Indeed, there exists a choice of plastic zone model, Irwin's and Dugdale's for correcting the parameter δ for thin sheets and elastic-plastic materials. According to the models shown in Figure 5.2 and 5.3, δ corresponds to the upper and lower relative displacement of the crack edges. If measurements of the crack opening displacement are made close enough to the crack tip, then $\delta \to \delta_t$. From Figure 5.3b, δ_t is defined as

twice the crack tip displacement in the y-direction. Hence,

$$\delta_t = 2\mu_y \tag{5.27}$$

According to crack configuration shown in Figure 5.3b, the crack opening displacement can be defined by [23,44]

$$\delta \;\; = \;\; \frac{4\sigma}{E}\sqrt{a^2 - x^2}...........(\text{Uncorrected}) \tag{5.28}$$

$$\delta \;\; = \;\; \frac{4\sigma}{E}\sqrt{(a+r)^2 - x^2} \quad (\text{Corrected}) \tag{5.29}$$

If $x = a$, then $\delta = \delta_t$

$$\delta_t = \frac{4\sigma}{E}\sqrt{(a+r)^2 - a^2} \simeq \frac{4\sigma}{E}\sqrt{2ar} \tag{5.30}$$

Inserting eq. (5.13) and (5.24) independently into (5.30) under plane stress condition yields the crack tip opening displacement as

$$\delta_t \;\; = \;\; \frac{4a\sigma^2}{E\sigma_{ys}} = \frac{4K_I^2}{\pi\lambda E\sigma_{ys}} \quad (\text{Irwin}) \tag{5.31}$$

$$\delta_t \;\; = \;\; \frac{2\pi a\sigma^2}{E\sigma_{ys}} = \frac{2K_I^2}{E\sigma_{ys}} \quad (\text{Dugdale}) \tag{5.32}$$

These two equations can be related as

$$\delta_t^{Irwin} = \frac{2}{\pi}\delta_t^{Dugdale} \tag{5.33}$$

Alternatively, Burdekin [30] and Rice [14] independently developed δ_t mathematical models based on Dugdale's work [15] and the definition of eq. (5.27) for plane stress and plane strain conditions, respectively. Hence,

$$\delta_t \;\; = \;\; \frac{8a\sigma_{ys}}{\pi E}\log\left[\sec\left(\frac{\pi\sigma}{2\sigma_{ys}}\right)\right] \quad (\text{Burdekin}) \tag{5.34}$$

$$\delta_t \;\; = \;\; \frac{2(\kappa+1)(1+v)a\sigma_{ys}}{\pi E}\log\left[\sec\left(\frac{\pi\sigma}{2\sigma_{ys}}\right)\right] \quad (\text{Rice}) \tag{5.35}$$

and from eqs. (4.47) and (4.48)

$$\kappa \;\; = \;\; \frac{3-v}{1+v} \quad \text{For plane stress} \tag{5.36}$$

$$\kappa \;\; = \;\; 3-4v \quad \text{For plane strain} \tag{5.37}$$

Expanding the logarithmic function as yields

$$\log\left[\sec y\right] \;=\; \frac{1}{2}y^2 + \frac{1}{12}y^4 + \frac{1}{45}y^6 + \dots \simeq \frac{1}{2}y^2 \qquad (5.38)$$

$$\log\left[\sec\left(\frac{\pi\sigma}{2\sigma_{ys}}\right)\right] \;\simeq\; \frac{1}{2}\left(\frac{\pi\sigma}{2\sigma_{ys}}\right)^2 \qquad (5.39)$$

Thus, eqs. (5.34) and (5.35) become

$$\delta_t \;=\; \frac{\pi a \sigma^2}{E\sigma_{ys}} = \frac{K_I^2}{E\sigma_{ys}} \qquad \text{(Burdekin)} \quad (5.40)$$

$$\delta_t \;=\; \frac{(\kappa+1)\,(1+v)\,a\sigma^2}{4E\sigma_{ys}} = \frac{(\kappa+1)\,(1+v)\,K_I^2}{4\pi E\sigma_{ys}} \qquad \text{(Rice)} \quad (5.41)$$

The preceding procedure provides a selection of mathematical models, which define the crack tip opening displacement (δ_t). In fact, the applicability of these models for characterizing fracture of thin sheets is of great importance since the dimensional requirements are not too strict as in the K_I-criterion for thick materials.

Figure 5.5 shows the relationship of $\delta_t = f(K_I)$ as per the above models for plane stress and plane strain conditions. Notice that the δ_t curves do not agree with each other due to different assumptions used by each cited author to develop a δ_t-model. However, Burdekin's model, eq. (5.40), agrees with the work done by Broek and Vlieger [31], Robinson and Tetelman [32] and Bowles [33]. The choice of model for evaluating the crack tip opening displacement or the stress intensity factor is a confusing matter.
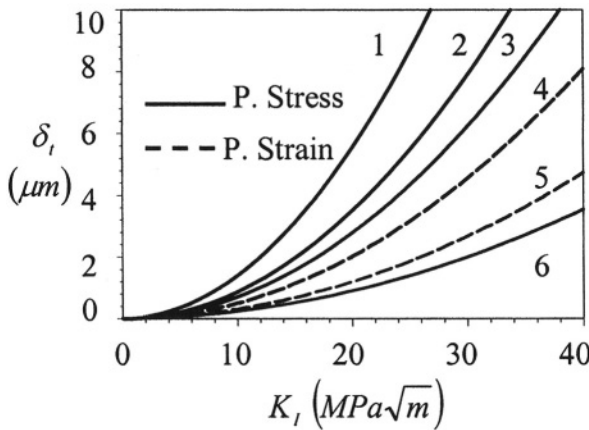
Figure 5.5 Comparison of crack tip opening displacement for a material having $E = 207\ MPa$, $\sigma_{ys} = 700\ MPa$, $K_{IC} = 60\ MPa\sqrt{m}$ **and** $v = 1/3$. **Legend: Irwin: Curve 2 &4, Dugdale: Curve1, Burdekin: Curve 3 and Rice: Curve 5 & 6.**

Considerable work has been confined to the δ_t-**model** since it has the advantage of measuring fracture toughness for elastic materials and it is very sensitive to variations in temperature, loading rate, specimen thickness, and thermo-mechanical processing [34].

In general, the δ_c-**criterion** should be confined to the yielding phenomenon in a microscopic scale, but the mathematical formulation is very complicated. For instance, yielding in the vicinity of a crack tip is related to complex dislocation networks, such as the dislocation pile-up. In this regard, reference should be made to the classical work of Eshelby et al. [7], Stroh [8], Puttick [9], Rogers [10], Gurland et al. [11], and a review paper written by Low [13], who analyzed and studied several dislocation models for the nucleation of cracks. Therefore, the physical interpretation of the yielding phenomenon herein is confined to a macroscopic scale.

Returning to the δ_t–**model,** crack tip plastic deformation in a thin sheet is not restricted to lateral contraction which causes localized thinning at the crack tip. Thereby, crack tip blunting causes an extensive increase in the crack tip radius (ρ) in the order of sheet thickness *(B),* and thus, the plastic zone size (r) may be estimated as $r \simeq B \simeq \rho$ [15,27].

Additionally, δ_t can be related to the strain-energy release rate (G_I) through eq. (3.5). For instance, combining eq. (3.5) and (5.40) at $G_I = G_C$ yields

$$G_C = \delta_c \sigma_{ys} \tag{5.42}$$

For plane stress condition at fracture, the strain energy release rate can be estimated as [28]

$$G_C = \epsilon_f \rho \sigma_{ys} \tag{5.43}$$

Combining eqs. (5.42) and (5.43) gives

$$\delta_c \simeq B\epsilon_f \tag{5.44}$$

where $\epsilon_f =$ Fracture strain

5.6 THE SHAPE OF THE PLASTIC ZONE

So far, the extent of plastic zone has been considered along the *x*-axis with $\theta = 0$ since it has been modeled as a circle. However, a more accurate procedure follows when $\theta \neq 0$ so that yielding is examined in a small area modeled according to a particular yielding criterion, which is responsible for the theoretical shape of the plastic zone. This fact implies that crack-tip plasticity occurs and the stresses in the zone are limited to yielding phenomenon. Therefore, the stresses are truncated to the yield stress of the material being examined and stress singularity phenomenon is simply a theoretical matter. Moreover, the Von Mises criterion and Tresca Yielding Criterion may be used to derive expressions for the plastic zone size, which in turn gives the plastic zone shape.

5.6.1   VON MISES YIELDING CRITERION

This criterion is deduced from the Maximum Distortion Energy Theory in which the state of stress is referred to as the principal stress directions and the principal stresses defined by the following common mathematical equations

$$(\sigma_1 - \sigma_2)^2 + (\sigma_2 - \sigma_3)^2 + (\sigma_3 - \sigma_1)^2 = 2\sigma_{ys}^2 \qquad (5.45)$$

and

$$\sigma_1, \sigma_2 = \frac{\sigma_{xx} + \sigma_{yy}}{2} \pm \sqrt{\left(\frac{\sigma_{xx} - \sigma_{yy}}{2}\right)^2 \tau_{xy}^2} \qquad (5.46)$$

Substituting eq. (4.13) into (5.46) yields the principal stresses defined by

$$\sigma_1 \;\; = \;\; \frac{K_I}{\sqrt{2\pi r}} \cos\frac{\theta}{2}\left(1 + \sin\frac{\theta}{2}\right) \qquad (5.47)$$

$$\sigma_2 \;\; = \;\; \frac{K_I}{\sqrt{2\pi r}} \cos\frac{\theta}{2}\left(1 - \sin\frac{\theta}{2}\right) \qquad (5.48)$$

$$\sigma_3 \;\; = \;\; 0 \qquad\qquad \text{For plane stress} \qquad (5.49)$$

$$\sigma_3 \;\; = \;\; \frac{2v K_I}{\sqrt{2\pi r}} \cos\frac{\theta}{2} \quad \text{For plane strain} \qquad (5.50)$$

Substituting eq. (5.47) through (5.50) into (5.45) and manipulating the resultant expressions yields the Von Mises yielding criterion

$$\frac{K_I^2}{2\pi r}\left[\frac{3}{2}\sin^2\theta + h\left(1 + \cos\theta\right)\right] = 2\sigma_{ys}^2 \qquad (5.51)$$

from which the plastic zone size takes the following analytical form

$$r = \frac{1}{4\pi}\left(\frac{K_I}{\sigma_{ys}}\right)^2\left[\frac{3}{2}\sin^2\theta + h\left(1 + \cos\theta\right)\right] \qquad (5.52)$$

where $h = 1$ for plane stress
       $h = (1 - 2v)^2$ for plane strain

Letting $\theta = 0$ in eq. (5.52) gives the plastic zone size along the x-axis as

$$r = \frac{h}{2\pi}\left(\frac{K_I}{\sigma_{ys}}\right)^2 = \frac{ha}{2}\left(\frac{\sigma}{\sigma_{ys}}\right)^2 \qquad (5.53)$$

This equation resembles eqs. (5.3) and (5.13) for plane stress condition.

5.6.2 TRESCA YIELDING CRITERION

This criterion is based on the Maximum Shear Stress Theory, which predicts that yielding occurs when the maximum shear stress reaches half value of the yield stress in a uniaxial-tension test. This is known as the Tresca Yielding Criterion. Thus,

$$\tau_{\max} = \frac{1}{2}\sigma_{ys} \tag{5.54}$$

According to Mohr's circle theory, the maximum shear stress is

$$\tau_{\max} = \frac{1}{2}\left(\sigma_1 - \sigma_3\right) \tag{5.55}$$

Henceforward, is algebraically the largest and s3 algebraically the smallest principal-stress components. Combining eqs. (5.54) and (5.55) yields the maximum shear stress or Tresca yielding criterion

$$\sigma_1 - \sigma_3 = \sigma_{ys} \tag{5.56}$$

Now, the plane conditions may be set using eq. (5.56)

$$
\begin{array}{rclll}
\sigma_1 & = & \sigma_{ys} & \text{For plane stress} & (5.57) \\
\sigma_1 - \sigma_3 & = & \sigma_{ys} & \text{For plane strain} & (5.56) \\
\sigma_1 - \sigma_2 & = & \sigma_{ys} & \text{For plane strain} & (5.58)
\end{array}
$$

Substituting the stresses given in eq. (5.47) through (5.50) into (5.57) through (5.58) yields

$$r = \frac{1}{2\pi}\left(\frac{K_I}{\sigma_{ys}}\right)^2\left[\cos\frac{\theta}{2}\left(1 + \sin\frac{\theta}{2}\right)\right] \qquad \text{For plane stress} \qquad (5.59)$$

$$r = \frac{1}{2\pi}\left(\frac{K_I}{\sigma_{ys}}\right)^2\cos^2\frac{\theta}{2} \qquad\qquad \text{For plane strain} \qquad (5.60)$$

The shapes of the normalized plastic zone as per eqs.(5.52), (5.59) and (5.60) are shown in Figure 5.6. Notice that both Von Mises and Tresca plastic zone shapes are different, but the plane strain shape is smaller than the plane stress shape in both cases.

Conclusively, the Tresca criterion at $\theta = 0$ does not recognized either the plane stress or the plane strain conditions since the plastic zone size has the same analytical definition. In addition, McClintock and Irwin [16] used the Von Mises yielding criterion to determine the plastic zone shapes for mode II and III loading. Figure 5.7 shows these authors' analyses. Nevertheless, the preceding analytical and theoretical results were limited to the yield stress. This analytical procedure led to an error on the plastic zone size expressions due to the exclusion of the extra load that a material has to carry outside the plastic zone boundaries.
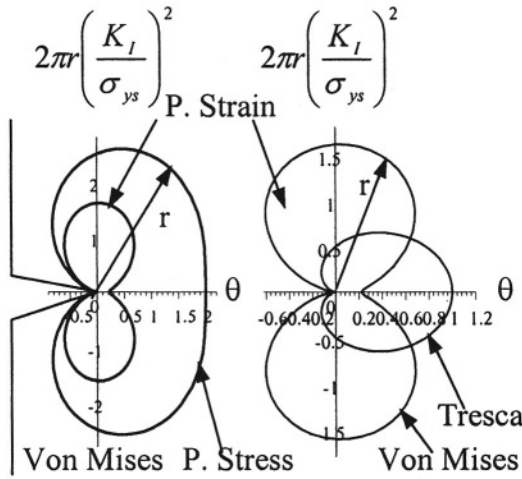
Figure 5.6 Plastic zone shapes according to Von Mises and Tresca yield criteria

Figures 5.8 and 5.9 illustrate experimental results obtainable by using relaxation methods. For instance, Figure 5.9 compares experimental and theoretical normalized results from several authors [12,17,19-21]. The data scatter in this figure is due to different theoretical procedures used by these authors.
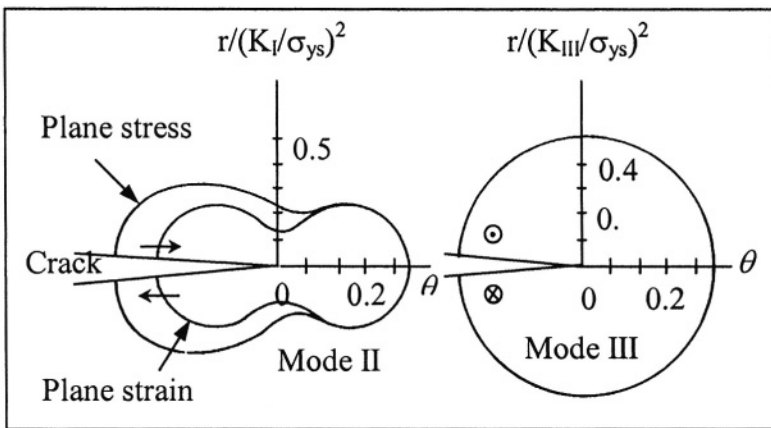
Figure 5.7 Plastic zone shapes for mode II and III [16]
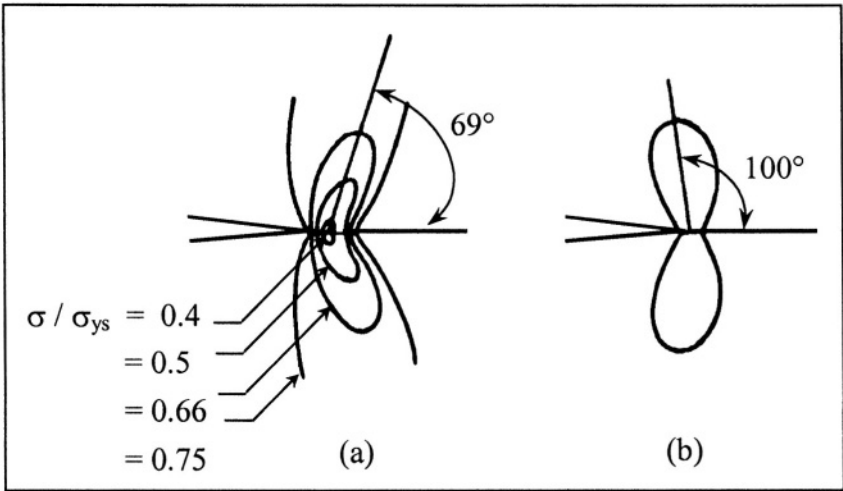
Figure 5.8 Plastic zones in mode I [4]. a) Tuba [17] and b) Rice and
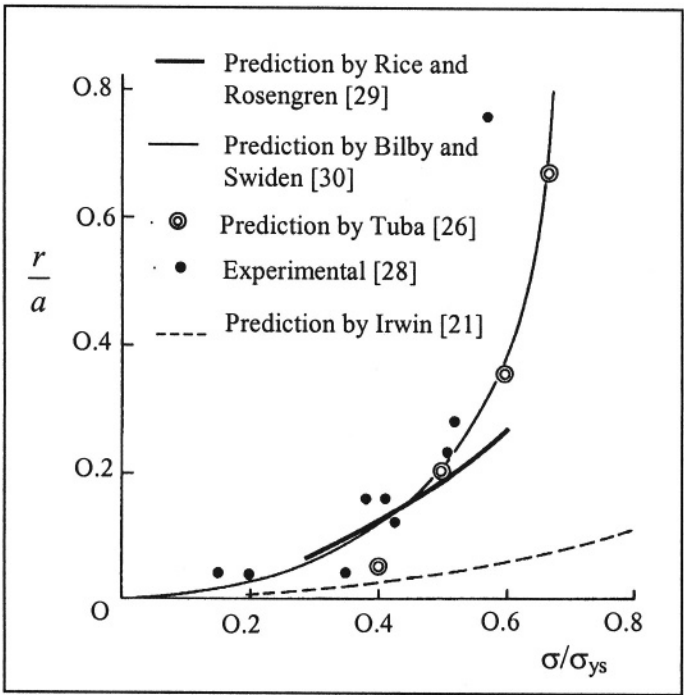
Figure 5.9 Effects of normalized stress on the normalized plastic zone size [28]

Predictions by Tuba [17] and Bilby and Swiden [21] fit the Hahn and Rosen-field [19] experimental data to an extent. Measurements of the plastic zone can

be accomplished by using techniques like

1. Surface Replicas	4. Photoelastic Coatings
2. Moiré Patterns	5. Etching
3. X-Ray Diffraction	. Microhardness

However, difficulties do arise when analyzing the outcome of experiments because the elastic and plastic strains cannot easily be distinguished, and the measurements are usually restricted to specimen surfaces. These difficulties may be avoided, to an extent, by using the Hahn-Rosengren etching technique [20,22], requires a proper polycrystalline material and an etching solution so that dislocations and slip band would be etched in all grains. This way the area of plastic yielding can be delineated with fewer difficulties. However, Hahn and Rosenfield [28] affirmed that the above theoretical mathematical approaches do not provide satisfactory description of the plastic zone shape. Therefore, none of the existing theories appear to suitable for predicting the plastic zone shape and size at $\theta = 0$. Figure 5.10 shows real plastic zone shape obtained by using the Hahn and Rosenfield etching technique [22].

Additionally, Theocaris and Andrianopoulos [25] used the Von Mises Yielding Criterion and the Strain Energy Density Factor Criterion for developing the plastic zone shapes under mixed-mode I and II conditions. These theoretical results can be depicted in Figure 5.11, in which the plastic zone shape for the Von Mises yielding criterion is larger than the one for the Strain Energy Density Factor *(S)*. Furthermore, these shapes get enlarged and rotated as the inclined angle β increases.
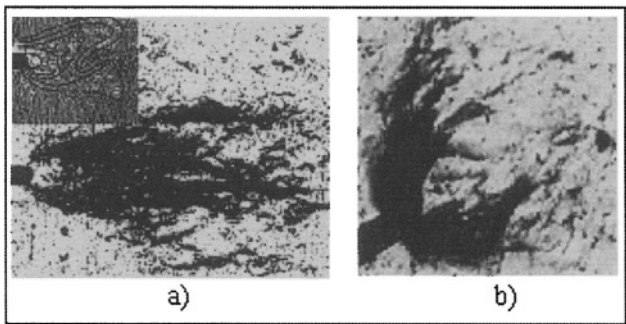
Figure 5.10 a) Interference pattern with strain contours (top left corner) and the corresponding plastic zone revealed by etching a 3Si-steel specimen with a thickness of 0.4 mm [22], and b) shape region of high shear in plane stress plastic zone of an Al-Cu-Mg alloy [23].
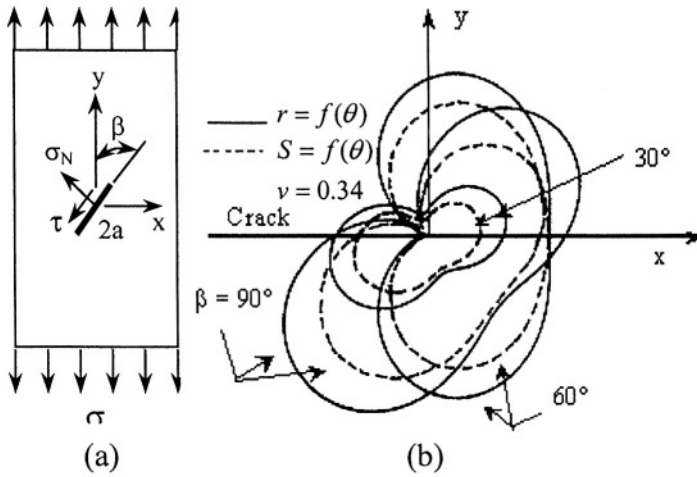
Figure 5.11 Mixed-mode I and II interaction. a) Through the thickness

---

Example 5.1 *If the critical strain-energy release rate and the yield strength of a* 13-*mm thick steel plate are* **32** kJ/m^2 *and* **1,500** MPa, *respectively, determine a) the validity of the fracture mechanics bending test for the plate containing a single-edge crack of* 8-*mm long at fracture, b) the fracture stress if the plate is* 130-*mm wide and* 1-*m long c) the critical crack tip opening displacement, d) the displacement, e) the plastic zone size, and f) interpret the results with regard to plane strain condition. Use a Poisson's ratio of* 1/3 *and assume that elastic modulus of the steel* **207** GPa.

Solution:

Given data:
$G_{IC} = 32x10^{-3} \, MPa.m, \, \sigma_{ys} = 1,500 \, MPa, \, B_o = 13 \, mm$
$E = 207,000 \, MPa, \, v = 1/3$
a) Using eq. (3.5) yields the critical stress intensity factor

$$G_{IC} = \frac{K_{IC}^2}{E'} = \frac{(1-v^2) \, K_{IC}^2}{E} \tag{3.5}$$

$$K_{IC} = \sqrt{\frac{EG_{IC}}{(1-v^2)}} = \sqrt{\frac{(207,000 \, MPa)(32x10^{-3}MPa.m)}{1-1/9}}$$

$$K_{IC} = 86.33 \, MPa\sqrt{m}$$

The minimum allowable thickness can be computed using eq. (3.30). Thus,

$$B \geq 2.5 \left(\frac{K_{IC}}{\sigma_{ys}} \right)^2 \tag{3.30}$$

$$B_{\min} = 2.5 \left(\frac{K_{IC}}{\sigma_{ys}} \right)^2 = 2.5 \left(\frac{86.33 \ MPa\sqrt{m}}{1,500MPa} \right)^2$$

$$B_{\min} = 8.28 \ mm$$

Therefore, the test is valid because the actual specimen thickness is greater than the ASTM minimum thickness; that is, $B_o > B_{\min} = 8.28 \ mm$.

b) The fracture stress is determined from eq. (3.29) along with $\alpha = 1.12$ *since* $a/w \simeq 0$ *(Consult Table 3.1).*

$$K_{IC} = \alpha \sigma_f \sqrt{\pi a} \tag{3.29}$$

$$\sigma_f = \frac{K_{IC}}{\alpha \sqrt{\pi a}} = \frac{86.33 \ MPa\sqrt{m}}{(1.12) \sqrt{\pi \left(5x10^{-3} \ m \right)}}$$

$$\sigma_f = 486.21 \ MPa < \sigma_{ys}$$

c) The crack tip opening displacement is calculated using Rice's equation with $\kappa = 3 - 4v = 5/3$ *and* $(\kappa + 1)(1 + v) = 32/9$

$$\delta_{ct} = \frac{(\kappa + 1)(1 + v) K_{IC}^2}{4\pi E \sigma_{ys}} \tag{5.41}$$

$$\delta_{ct} = \frac{32}{36\pi} \frac{(86.33 \ MPa\sqrt{m})^2}{(207,000 \ MPa)(1,500 \ MPa)}$$

$$\delta_{ct} = 6.79 \ \mu m$$

d) The displacement is

$$\delta_t = 2\mu_y = (2)(6.79 \ \mu m) = 13.58 \ \mu m \tag{5.27}$$

e) The plastic zone can be calculated using eq. (5.53) along with $h = (1 - 2v)^2 = 1/9$

$$r = \frac{h}{2\pi} \left(\frac{K_{IC}}{\sigma_{ys}} \right)^2 = \frac{1}{18\pi} \left(\frac{86.33 \ MPa\sqrt{m}}{1,500 \ MPa} \right)^2 \tag{5.53}$$

$$r = 0.059 \ mm$$

f) The above results suggests that the plate met the ASTM E399 thickness requirements because $B_o > B_{\min}$ *and behaved in a brittle manner because both the plastic zone size and the crack tip opening displacement are very small.*

Example 5.2 *A thin steel plate having a 8 mm through the thickness single-edge crack size is designed to hold a* **60 kN** *static tension load. The steel properties are* K_{IC} = 60 $MPa\sqrt{m}$, σ_{ys} = 600 MPa, *and* v = 0.30. *The plate is L = 4-m long, 60-mm wide and 3-mm thick. Assume that the steel plate is part of a structure that operates at room temperature and controlled environment, and that the nominal applied stress is a von Mises stress. Determine the the safety factor* (S_F) *based on a) yielding and b) on fracture mechanics. Calculate c) the von Mises plastic zone size and the critical crack length.*

Solution:

Calculate the nominal stress:

$$\sigma = \frac{P}{A} = \frac{P}{Bw} = \frac{50,000 \ N}{(3x10^{-3} \ m)(60x10^{-3} \ m)}$$
$$\sigma \simeq 278 \ MPa$$

a) Safety factor based on yielding:

$$S_F = \frac{\sigma_{ys}}{\sigma} = \frac{600 \ MPa}{278 \ MPa}$$
$$S_F \simeq 2.16$$

which is a reasonable safety factor for designing against yielding.
b) Safety factor based on fracture mechanics requires the used of Table 3.1 for calculating the geometric correction factor. For a/w = 8/60 = 0.13, *the geometric correction factor is*

$$\alpha = 1.12 - 0.23\left(\frac{a}{w}\right) + 10.55\left(\frac{a}{w}\right)^2 - 21.71\left(\frac{a}{w}\right)^3 + 30.38\left(\frac{a}{w}\right)^4$$
$$\alpha = 1.12 - 0.23\,(0.13) + 10.55\,(0.13)^2 - 21.71\,(0.13)^3 + 30.38\,(0.13)^4$$
$$\alpha = 1.23$$

From eq. (3.29),

$$K_I = \alpha\sigma\sqrt{\pi a} \qquad\qquad (3.29)$$
$$K_I = (1.23)\,(278 \ MPa)\,\sqrt{\pi\,(8x10^{-3} \ m)}$$
$$K_I \simeq 54 \ MPa\sqrt{m}$$

Thus,

$$S_F = \frac{K_{IC}}{K_I} = \frac{70 \ MPa\sqrt{m}}{54 \ MPa\sqrt{m}}$$
$$S_F \simeq 1.30$$

This safety factor is actually very low for designing against fracture. There-fore, crack propagation or sudden fracture will occur at a $(70 - 54)/54 \simeq 0.30$ *or 30% overload.*

c) Using eq. (5.52) along the crack plane $(\theta 0)$ *the plastic zone size becomes*

$$r = \frac{h}{2\pi}\left(\frac{K_I}{\sigma_{ys}}\right)^2 \tag{5.52}$$

$$r = \frac{(1-2v)^2}{2\pi}\left(\frac{K_I}{\sigma_{ys}}\right)^2 \tag{5.1}$$

$$r = \frac{(1-0.6)^2}{2\pi}\left(\frac{54\ MPa\sqrt{m}}{600\ MPa}\right)^2 \tag{5.2}$$

$$r = 0.21\ mm \tag{5.3}$$

d) the critical is

$$K_I = \alpha\sigma\sqrt{\pi a}$$

$$a_a = \frac{1}{\pi}\left(\frac{K_{IC}}{\alpha\sigma}\right)^2 = \frac{1}{\pi}\left[\frac{70\ MPa\sqrt{m}}{(1.23)(278\ MPa)}\right]^2$$

$$a_a = 13.34\ mm$$

5.7   PROBLEMS

5.1   Use the inequality $K_{IC} \geq K_I$ as a criterion for crack instability where K_I is defined by Irwin's plastic zone corrected expression for a finite size, to determine if a steel pressure vessel is susceptible to explode under $\sigma = 200$ MPa hoop stress. The vessel contains an internal circular crack perpendicular to the hoop stress. If the properties of the steel are $K_{IC} = 60\ MPa\sqrt{m}$ and $\sigma_{ys} = 700\ MPa$, and the crack size is $a = 20\ mm$, a) determine the ASTM E399 thickness requirement and the minimum thickness to be used to prevent explosion, b) Will crack propagation occur at $200\ MPa$? c) Plot $B = f(\sigma/\sigma_{ys})$ for $a = 10, 20$, and $30\ mm$, and d) Will the pressure vessel explode when the crack size is $30\ mm$? Why? or Why not?, and e) When will the pressure vessel explode? [**Solution:** a) $B_{min} = 8.28\ mm$, b) No, it will not because $K_I < K_{IC}$, c) Plot, d) No and e) it explodes when $a_c = 67.91\ mm$].

5.2   A project was carried out to measure the elastic-strain energy release rate as a function of normalized stress (σ/σ_{ys}) of large plates made out a hypo-thetical brittle solid. All specimens had a single-edge crack of $3\text{-}mm$ long. Plot the given data and do regression analysis on this data set. Determine a) the

maximum allowable σ/σ_{ys} ratio for $G_{IC} = 30\ kPa.m$ and b) K_{IC} in $MPa\sqrt{m}$. Given data: $v = 0.3$, $\sigma_{ys} = 900\ MPa$, $E = 207\ GPa$,

σ/σ_{ys}	0	0.10	0.20	0.30	0.40	0.50	0.60	0.70	0.80	0.90
G_{IC}	0	0.40	1.70	1.90	7.00	12.00	19.00	26.00	36.00	48.00

5.3 Calculate the critical crack length of problem 5.2. [Solution: $a_c = 3\ mm$].

5.4 A large brittle plate containing a central crack 4-mm long is subjected to a tensile stress of $800\ MPa$. The material has $K_{IC} = 80\ MPa\sqrt{m}$, $\sigma_{ys} = 1200\ MPa$ and $v = 0.30$. Calculate a) the applied K_I, b) the plastic zone size using the Von Mises yield criterion and prove that $r = r_{max}$ when $\theta = \theta_o$. Consider all calculations for plane stress and plane strain conditions, and c) draw the entire plastic zone contour where the crack tip is the origin of the coordinates.

5.5 Use the data given in Example 3.3 for a pressure vessel containing a semi-elliptical crack (Figure 3.6) to calculate Irwin's and Dugdale's a) plastic zones, b) using Kabayashi's finite size correction factor and plasticity correction factor. c) Compare results and determine the percent error against each case. d) Is it necessary to include a plastic correction factor? Explain. [Solution: a) $r\ (Irwin) = 0.54\ mm$, and $r\ (Dugdale) = 1.33\ mm$, b) $K_I\ (Irwin) = 5.63\ MPa\sqrt{m}$ and $K_I\ (Dugdale) = 6.22\ MPa\sqrt{m}$].

5.6 A 50-mm thick pressure vessel is to support a hoop stress of $300\ MPa$ at room temperature under no action of corrosive agents. Assume that a semi-elliptical crack (Figure 3.6) is likely to develop on the inner surface with the major axis $2c = 40\ mm$ and semi-minor axis $a = 10\ mm$. A 300-M steel, which is normally used for airplane landing gear, is to be considered. Will crack propagation occur at $300\ MPa$ hoop stress? Make sure you include the Irwin's plastic zone correction in your calculations. Is it necessary to do such a plastic correction? Use the data below and select the suitable tempered steel.

300-M Steel	σ_{ys}	K_{IC}
	(MPa)	$(MPa\sqrt{m})$
650° Temper	1070	152
300° Temper	1740	65

5.7 If localized plasticity is to be considered, explain the physical meaning of the following inequality $\pi a \sigma^2/E > \delta_t \sigma_{ys}$.

5.8 Show that $r = \delta_t/(2\pi\epsilon_{ys})$ where r is the plastic zone size due to dislocation networks within the plastic zone area ahead of the crack tip.

5.9 Show that $\delta_t/\epsilon_{ys} = (K_I/\sigma_{ys})^2$ and give a reasonable interpretation of this equality.

5.10 A large strong plate containing a through-the-thickness central crack of $2a_c = 20\ mm$ has $E = 207\ MPa$, $\sigma_{ys} = 1,275\ MPa$ and $\delta_c = 9.47\ \mu m$ at service temperature. Determine a) the plane strain fracture toughness, b) the design stress intensity factor for a safety factor (S_F) of 2, c) the critical fracture stress, and d) the design service stress.

5.11 Predict δ_t for a glass using $\delta = \left(4\sigma\sqrt{a^2 - x^2}\right)/E$.

5.12 Derive an expression for δ_t using a Von Mises material. Compare it with that for a Tresca material under plane strain conditions.

5.13 A material has $E = 70\ MPa$, $\sigma_{ys} = 500\ MPa$ and $v = 1/3$. It has to be used as a plate in a large structure. Non-destructive evaluation detects a central crack of 50-mm long. If the displacement at fracture is $0.007\ mm$ and the plate width is three times the thickness, calculate a) the crack tip opening displacement, b) the plane strain fracture toughness, c) the plane strain-energy release rate, d) the plate thickness and e) What's the safety factor being indirectly included in this elastic-plastic fracture mechanics approach? Assume plane strain conditions as per eq. (5.31) and a fracture load of $200\ kN$. [Solution: a) $\delta_c = 0.014\ mm$, b) $K_{IC} = 41.61\ MPa\sqrt{m}$, c) $\sigma_c = 148.48MPa$, d) $B = 21.19\ mm$ and e) $S_F = 5.43$].

5.14 Repeat problem 5.13 using eq. (5.41). Compare results.

5.15 A hypothetical large metallic plate containing a 10-mm central crack is 30-mm wide and 5-mm thick and mechanically loaded in tension. This plate has $E = 69\ MPa$, $\sigma_{ys} = 500\ MPa$, $v = 1/3$ and $\epsilon = 0.3\%$ for plane stress strain. Determine a) δ_t, b) G_I and c) σ as per Irwin, Dugdale, Burdekin and Rice equations. Compare results. {Solution: a) $\delta_t = 0.015\ mm$, b) $G_I = 7.5\ kJ/m^2$ and c) $\sigma\,(\text{Irwin}) = 161\ MPa$, $\sigma\,(\text{Dugdale}) = 128\ MPa$, $\sigma\,(\text{Burdekin}) = 182\ MPa$, $\sigma\,(\text{Rice}) = 322\ MPa$].

5.16 Determine a) the critical crack tip opening displacement (δ_c), b) the plastic zone size (r) and c) the fracture stress (σ_f) for a large aluminum alloy plate containing a central crack of 5-mm long. Use the following available data and assume plane strain conditions: $K_{IC} = 25\ MPa\sqrt{m}$, $\sigma_{ys} = 500\ MPa$ and $E = 70\ MPa$.

5.17 Show that $\delta \simeq \delta_t\sqrt{1 + (E/8a\sigma)^2\,\delta_t^2}$ for plane stress conditions. Schematically, plot $\delta = f\,(\delta)$ for various a and fixed a values.

5.8   REFERENCES

[1]   W.W. Dally and W.F. Riley, "Experimental Stress Analysis," Third Edition, McGraw-Hill, Inc. New York, (1991)

[2]   G.R. Irwin, "Fracture I," in S. Flugge (ed.), Handbuch der Physik VI, Springer-Verlag, New York, (1958)

[3]   S.P. Timoshenko and J.N. Goodier, "Theory of Elasticity," third edition, McGraw-Hill Co., New York, (1970) 142

[4]   J.R. Rice, Proc. 1st Inter. Conf. On Fracture, Sendai, 1965, Edited by T. Yokobori, et al., Japanese Society for strength and Fracture of Materials, Tokyo, Vol. I, (1966) 283

[5]   H.M. Westergaard, "Bearing Pressures and Cracks," J. Appl. Mech., G1 (1939) A49 - A53

[6]   D. Broek, "Elementary Engineering Fracture Mechanics," Fourth edition, Kluwer Academic Publisher, Boston, (1986)

[7]   K. Hellan, "Introduction to Fracture Mechanics," McGraw-Hill Book company, New York, (1984)

[8]   R.W. Hertzberg, "Deformation and Fracture Mechanics of Engineering Materials," Third edition, John Wiley & Sons, New York, (1989)

[9]   G.R. Irwin, Proc. SESA, Vol. XVI, No. 1 (1958) 93-96

[10] M.H. Aliabadi and D.P. Rooke, "Numerical Fracture Mechanics," Computational Mechanics Publications, Kluwer Academic Publishers, Boston, (1992) Chapter 2.

[11] J.D. Eshelby, Proc. Roy. Soc., Series A 241, (1957) 376

[12] A.N. Stroh, Adv. Physics, 6(1957) 418.

[13] K.E. Puttick, Phil. Mag., 4 (1959) 964.

[14] H.C. Rogers, Trans. Met. Soc. AIME, 218 (1960) 498

[15] J. Gurland and J. Plateau, ASM Trans. Quart., 56 (1963) 442

[16] R. Chona, "Non-singular Stress Effects in Fracture Test Specimens - A Photoelastic Study," M.S. Thesis, University of Maryland, College Park, (August 1985)

[17] R.J. Sanford, "A critical Re - Examination of the Westergaard Method for Solving Opening Mode Crack Problems," Mech. Res., Vol. 6, No. 5, (1979) 289-294

[18] M.L. Williams, J. Appl. Mech., 24 (1957) 109 - 114

[19] H.O. Fuchs and R.I. Stephens, "Metal Fatigue in Engineering," John Wiley & Sons, New York, 1980

[20] J.A. Collins, "Failure of Materials in Mechanical Design: Analysis, Prediction, Prevention," John Wiley & Sons, New York, (1981)

[21] G.R. Irwin, "Plastic Zone near a Crack and Fracture Toughness," Proc. 7th Sagamore conference, (1960) IV-63

[22] J.R. Low, Progr. Mater. Sci., 12 (1) (1963)

[23] J.R. Rice, in "Fracture an Advanced Treatise," edited by H. Liebowitz, Academic Press, New York, Vol. II, (1968) 191

[24] D.S. Dugdale, "Yielding of Steel Sheets Containing Slits," J. Mech. Phys. Sol. 8(1960) 100-108

[25] F.A. McClintock and G.R. Irwin, "Plasticity Aspects of Fracture Mechanics," ASTM STP 381, (1965) 84-113

[26] I.S. Tuba, "A method of Elastic-Plastic Plane Stress and Plane Strain Analysis," J. Strain Analysis, 1 (1966) 115-122

[27] J.H. Underwood and D.P. Kendall, "Measurement of Plastic Strain Distribution in the Region of a Crack Tip," Exp. Mechanics (1969) 296-304

[28] G.T. Hahn and A.R. Rosenfield, "Plastic Flow in the Locale on Notches and Cracks in Fe-3Si Steel under Condition Approaching Plane Strain," Report to ship structure committee (1968)

[29] J.R. Rice and G.F. Rosengren, "Plane Strain Deformation near a Crack Tip in a Power-Law Hardening Material", J. Mech. Phys. Sol., 16 (1968) 1

[30] B.A. Bilby and K.H. Swiden, "Representation of Plasticity at Notches by Linear Dislocation Arrays", Proc. Royal Soc. A285 (19650 22-30

[31] G.T. Hahn and A.R. Rosenfield, "Local Yielding and Extension of a Crack Under Plane Stress," Acta Metallurgica, 13 (March 1965) 293-306

[32] D. Broek, "A Study on Ductile Fracture," Nat. Aerospace Inst. Amsterdam, Report TR 71021 (1971)

[33] V.Z. Parton and E.M. Morozov, "Mechanics of Elastic-Plastic Fracture," second edition, Hemisphere publishing corporation, New York, (1989)

[34] P.S. Theocaris and N.P. Andrianopoulos, "The Mises Elastic-Plastic Boundary as the Core Region in Fracture Criteria," Engineering Fracture Mechanics, 16 (3) (1982) 425-432

[35] ASTYME1290, standard method for crack-tip opening Displacement (CTOD) Fracture Toughens Measurement, (1998) 846

[36] A.R. Rosenfield, et al., Proc. 1st International Conference on Fracture, Sendai, Edited by T. Yokobori, et al. (1965) 223

[37] T.H. Courtney, "Mechanical Behavior of Materials," McGraw-Hill Co., New York, (1990)

[38] A.A. wells, British Welding Research Association Rep., M13 (1963)

[39] F.M. Burdekin, and D.E. Stone, J. Strain Analysis, 1 (1966) 145

[40] D. Broek and h. Vlieger, National Aerospace Lab. TR 74032, (1974)

[41] J.N. Robinson and A.S. Tetelman, Un. Cal. Los Angeles Report Eng. 7360 (1973)

[42] C.Q. Bowles, Army Mat. And Mech. Research Center, Watertown, Massachusetts,
Report AMMRC Cr 70-23, (1970)

[43] J.F. Lancaster, "Metallurgy of Welding," Fifth ed., Chapman & Hall, New York, (1993)

[44] M.A. Meyers and K.K. Chawla, "Mechanical Behavior of Materials," Prentice Hall, Upper Saddle River, New Jersey, (1999) 358

Chapter 6

THE ENERGY PRINCIPLE

6.1 INTRODUCTION

In this chapter, the elastic behavior of solids containing cracks is examined using the energy principal approach, which includes all forms of energy since loading develops mechanical work, energy absorption around the crack tip, and energy dissipation as heat. Williams [1] and Broek [2] undertook this energy approach as the primary form of energy (mechanical work) being considered. If work is done, then crack growth occurs and elastic energy is released. With the exception of pure brittle solids, engineering materials undergo some form of plastic deformation at the crack tip due to an applied external stress. Such plastic deformation is an irreversible process and the material undergoes a plastic flow process.

In a general sense, plastic flow is referred to as a permanent and non-recoverable deformation in most common solid materials. On the other hand, viscous flow describes the mechanical behavior of plastics, such as non-crystalline polymers, and it is temperature and time dependent. The term viscoelasticity is also used to indicate viscous flow.

6.2 ENERGY RELEASE RATE

The focus of this section is to determine the energy balance and the crack driving force for a slow crack growth event due to the action of an external quasi-static load. The crack may be embedded, on the surface or through-the-thickness. Consider a body with a boundary contour Γ as shown in Figure 6.1 subjected to an energy input increment (dU) due to an external loading [1,7]. Assume that the solid body is elastic and its elastic mechanical behavior can be characterized by a linear load-displacement relationship, $P = f(\mu)$, as depicted in Figure 6.2

for which the slope is $0 < dP/da < \infty$ [7]. The slope is referred to as the stiffness and the inverse of stiffness is called the compliance.
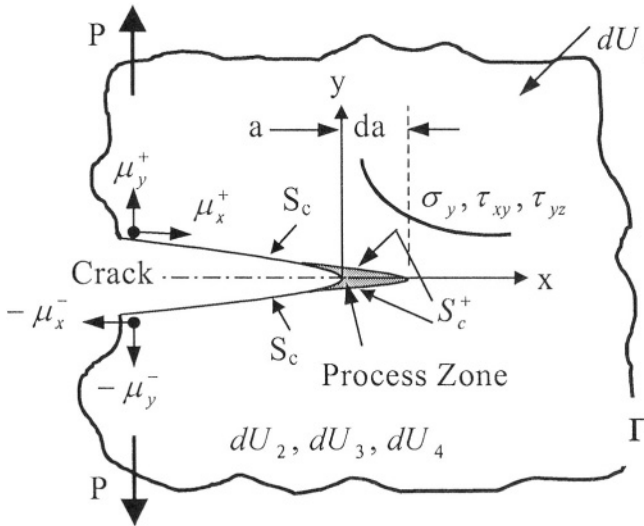
Figure 6.1 Cracked body with energy changes
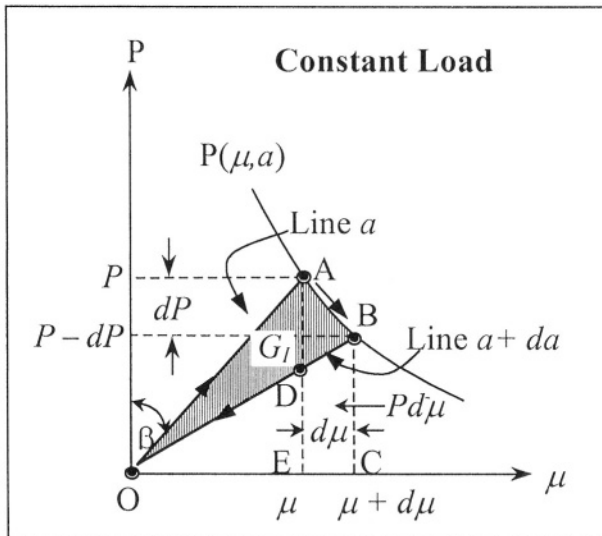
Figure 6.2 Load vs. displacement for a growing crack

From Figure 6.1, the shaded area represents a very small process zone surrounded by an elastic continuum, S_c and S_c^+ are the exiting and new crack

surface [7]. The energy change in a loaded plate occurs due to the displacements arising from the fracture area change $dA = d\partial a$ for a constant thickness B and variable crack length a. Thus, the input energy change (dU_1) is divided into the change in dissipated energy (dU_2) as heat which arises due to the irreversible process during plastic or viscous flow, the change in stored energy or total potential elastic energy (dU_3), and the change in kinetic energy (dU_4) of the system. For an isothermal case, dU_2 is transferred across the contour Γ of the system and for an adiabatic case, dU_2 is not transferred and the system temperature rises. Consequently, the conservation of energy change due to the displacements arising from the fracture area change dA can be defined as

$$\frac{dU_1}{dA} - \frac{dU_2}{dA} = \frac{dU_3}{dA} + \frac{dU_4}{dA} \tag{6.1}$$

For a growing crack, dU_2/dA is the energy dissipated in propagating fracture over an increment of area dA which is referred to as the fracture resistance R. On the other hand, $dU_1/dA - dU_2/dA$ can be defined as the net energy input. Another important definition is the energy release rate G_i, where $i = I, II, III$ or a combination of loading modes described in Figure 3.1. Thus,

$$G_i = \frac{dU_1}{dA} - \frac{dU_3}{dA} = \frac{dU_1}{Bda} - \frac{dU_3}{Bda} \tag{6.2}$$

Combining eqs. (6.1) and (6.2) along with $R = dU_2/dA$ and $U_4 = 0$ for a stationary body, the energy release rate criterion for crack tip instability is

$$G_{iC} \geq R \tag{6.3}$$

If the cracked plate shown in Figure 6.1 is subjected to an external load P and the crack growth very slow, then the load-points undergo a relative displacement $d\mu$ perpendicular to the crack plane and the crack length extends an amount da. Consequently, the work done responsible for such an increment in displacement and crack length is defined by

$$\frac{dU_1}{da} = P\frac{d\mu}{da} \tag{6.4}$$

6.3 LINEAR COMPLIANCE

Consider mode I (tension) loading and the linear behavior shown in Figure 6.2. The stored energy due to tension loading can be defined as the area under the curve

$$U_3 = \frac{1}{2}P\mu \tag{6.5}$$

from which

$$\frac{dU_3}{da} = \frac{P\,d\mu}{2\,da} + \frac{\mu\,dP}{2\,da} \tag{6.6}$$

Inserting eqs. (6.4) and (6.6) into (6.2) gives

$$G_I = \frac{1}{2B}\left(P\frac{d\mu}{da} - \mu\frac{dP}{da}\right) \tag{6.7}$$

For essentially elastic response, the linear compliance is the inverse of the slope of Figure 6.2, from which the displacement takes the form

$$\mu = PC \tag{6.8}$$

Thus,

$$\frac{d\mu}{da} = P\frac{dC}{da} + C\frac{dp}{da} \tag{6.9}$$

Substituting eqs. (6.8) and (6.9) into (6.7) yields the crack driving force as

$$G_I = \frac{P^2}{2B}\frac{dC}{da} \tag{6.10}$$

$$G_I = \frac{1}{2B}\left(\frac{\mu}{C}\right)^2\frac{dC}{da} \tag{6.11}$$

$$G_I = \frac{U_3}{BC}\frac{dC}{da} \tag{6.12}$$

Equation (6.7) can also be derived using the segments and areas in Figure 6.2. For instance,

- OA = Initial loading line

- AB = Unloading line since $P_1 \rightarrow P_1 - dP$ as $\mu \rightarrow \mu + d\mu$. Consequently, the crack area changes from A to $A + dA$ or the crack grows from a to $a + da$. This leads to.

- Area OAE =Stored energy at fracture = $P\mu/2$

- Area OBC = Stored energy after fracture = $(P - dP)(\mu + d\mu)/2$

- Area $ABCE$ = Work done = $Pd\mu$

- Area OAB = OAE+$ABCE$–OBC = Release of elastic energy = $G_I dA$ = $G_I B da$. Thus,

$$OAB = \frac{1}{2}P\mu + Pd\mu - \frac{1}{2}(P - dP)(\mu + d\mu)$$

$$G_I = \frac{1}{2B}\left(P\frac{d\mu}{da} - \mu\frac{dP}{da}\right) \tag{6.7}$$

This concludes the interpretation of Figure 6.2.

6.4 NONLINEAR CRACK GROWTH

The possible load lines for a nonlinear behavior is shown in Figure 6.3 [1,6-7].The analysis is carried out using a nonlinear compliance expression of the form [1]

$$\mu = (PC_n)^{1/n} \tag{6.13}$$

where $n =$ Strain hardening exponent

The strain energy release rate is defined by [1]

$$G_I = \frac{1}{B}\left[P\frac{d\mu}{da} - \frac{d}{da}\left(\frac{p\mu}{1+n}\right)\right] \tag{6.14}$$

$$G_I = \frac{1}{(1+n)B}\left(nP\frac{d\mu}{da} - \mu\frac{dP}{da}\right) \tag{6.15}$$
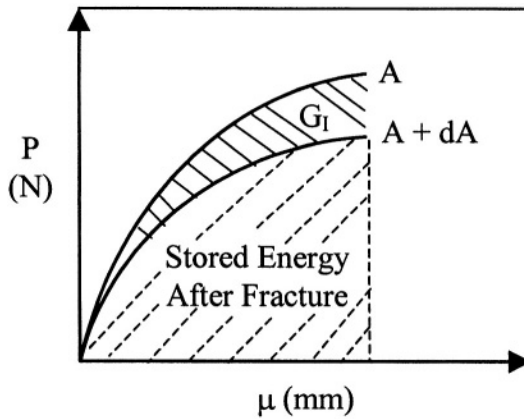
Figure 6.3 Possible load trajectory for a growing crack in a nonlinear elastic-plastic material

Combining eqs. (6.13) and (6.15) yields

$$G_I = \frac{1}{(1+n)B}P^{(1+n)/n}C_n^{(1-n)/n}\frac{dC_n}{da} \tag{6.16}$$

$$G_I = \frac{1}{(1+n)B}\frac{\mu^{1+n}}{C_n^2}\frac{dC_n}{da} \tag{6.17}$$

$$G_I = \frac{U_3}{BC_n}\frac{dC_n}{da} \tag{6.18}$$

A remarkable observation is that if $n = 1$, then eq. (6.16) yields eq. (6.10).

6.5   TRACTION FORCES

Consider two-dimensional problems in Cartesian system x, y, z, where $z = x_3$ has a unit length an it is treated here as a coordinate. Assume that the path of the crack tip is along x-axis and that the origin is at the crack tip (Figure 6.1) for a pure elastic state under quasi-static loading. This implies that the crack area along with a unit length in the x_3-axis becomes $\Delta A = \Delta a x_3 \rightarrow \Delta a$ By definition, the traction excerpted through S_c^+ from the continuum on the process zone is $-\overrightarrow{T} = \{T_i\}$, where i denotes the type of stress per stressing mode I, II or III.

According to Hellan [7], the magnitude of the traction forces on the upper and lower crack sides are $T_i = -\sigma_{yi}$ and $T_i = +\sigma_{yi}$ or $T_i = -\sigma_{yi} (+\sigma_{yi})$, respectively. The corresponding displacements are $\mu_i = \mu_i^+$ and $\mu_i = \mu_i^-$ or $\mu_i = \mu_i^+ (\mu_i^-)$. Moreover, the dominant stresses along the crack line can be determined at $\theta = 0$ and the displacements along the crack sides at $\theta = \pm\pi$. This implies that the crack tip is located at $(x, y) = (\geq 0, 0)$ for the principle stresses and $(x, y) = (\leq 0, 0)$ for the displacements.

Accordingly, the translation of the fields at the crack front leads to $\Delta a \rightarrow 0$, which is required to determine the limit of the crack driving force. This can clearly be appreciated by considering a two-dimensional analysis of a pure elastic solid body subjected to a quasi-static loading as depicted in Figure 6.1. Thus, the strain energy release rate on the elastic continuum over the crack surface S_c^+ can be defined by [7]

$$G_i = \lim_{\Delta A \rightarrow 0} \int_{S_c^+} \left(\int_{(a)}^{(b)} T_i d\mu_i \right) ds \qquad \text{For } \Delta A \rightarrow 0 \qquad (6.19)$$

$$G_i = \lim_{\Delta a \rightarrow 0} \int_o^{\Delta a} \left[\int_{(a)}^{(b)} \sigma_{yi} d \left(\mu_i^+ - \mu_i^- \right) \right] dx \qquad (6.20)$$

$$G_i = \frac{1}{2\Delta a} \int_o^{\Delta a} \sigma_{yi}^{(a)} \left(\mu_i^+ - \mu_i^- \right)^{(b)} dx \qquad (6.21)$$

where ds = Differential surface area
$d\mu_i$ = Displacement increments at ds
ΔA = Change in crack area
(a) = Representation of a stage for plastic process
(b) = Representation of a stage for crack extension

In order to solve eq. (6.21), the stresses and the displacements for the three modes of loading (as depicted in Figure 3.1) being derived in Chapter 4 can be defined in a general form by replacing the plastic zone size r for x in the stress equations for each stress mode and r for $\Delta a - x$ in the displacement equations when crack extension occurs.

For the symmetric mode I at $y = 0$ and $\mu_y^\pm = -\mu_\theta$,

$$\sigma_{yy} = \sigma_\theta = \frac{K_I}{\sqrt{2\pi r}} \qquad\qquad \text{For } x \geq 0;\ \theta = 0 \quad (6.22)$$

$$\mu_y^\pm = \pm\frac{(\kappa + 1)(1 + v)K_I}{E}\sqrt{-\frac{x}{2\pi}} \quad \text{For } x \leq 0;\ \theta = \pm\pi (6.23)$$

$$\sigma_{yy}\left(\mu_y^+ - \mu_y^-\right) = \frac{(\kappa + 1)(1 + v)K_I^2}{\pi E}\sqrt{\frac{\Delta a - x}{2\pi}} \qquad\qquad (6.24)$$

For the antisymmetric mode II at $y = 0$ and $\mu_x^\pm = -\mu_r$,

$$\tau_{xy} = \tau_{r\theta} = \frac{K_{II}}{\sqrt{2\pi x}} \qquad\qquad \text{For } x \geq 0;\ \theta = 0 \quad (6.25)$$

$$\mu_x^\pm = \pm\frac{(\kappa + 1)(1 + v)K_{II}}{E}\sqrt{-\frac{x}{2\pi}} \quad \text{For } x \leq 0;\ \theta = \pm\pi (6.26)$$

$$\tau_{xy}\left(\mu_x^+ - \mu_x^-\right) = \frac{(\kappa + 1)(1 + v)K_{II}^2}{\pi E}\sqrt{\frac{\Delta a - x}{2\pi}} \qquad\qquad (6.27)$$

For the antisymmetric mode III at $y = 0$,

$$\tau_{yz} = \tau_{z\theta} = \frac{K_{III}}{\sqrt{2\pi x}} \qquad\qquad \text{For } x \geq 0;\ \theta = 0 \quad (6.28)$$

$$\mu_z^\pm = \pm\frac{4(1 + v)K_{III}}{E}\sqrt{-\frac{x}{2\pi}} \qquad \text{For } x \leq 0;\ \theta = \pm\pi (6.29)$$

$$\tau_{yz}\left(\mu_z^+ - \mu_z^-\right) = \frac{4(1 + v)K_{III}^2}{\pi E}\sqrt{\frac{\Delta a - x}{2\pi}} \qquad\qquad (6.30)$$

From Chapter 4, the constant κ is defined by

$$\kappa = \frac{3 - v}{1 + v} \qquad \text{For plane stress} \qquad (4.31)$$

$$\kappa = 3 - 4v \qquad \text{For plane strain} \qquad (4.32)$$

Substituting eqs. (6.24), (6.27) and (6.30) into (6.21) yields the crack driving force for a mixed-mode interaction

$$G_i = \frac{1}{2\Delta a}\int_o^{\Delta a}\left[\sigma_{yy}\left(\mu_y^+ - \mu_y^-\right) + \tau_{xy}\left(\mu_x^+ - \mu_x^-\right) + \tau_{yz}\left(\mu_z^+ - \mu_z^-\right)\right]dx \text{(a)}$$

$$G_i = \frac{2(1 + v)}{\pi\Delta aE}\left[\frac{\kappa + 1}{4}\left(K_I^2 + K_{II}^2\right) + K_{III}^2\right]\int_o^{\Delta a}\sqrt{\frac{\Delta a - x}{x}}\,dx \qquad \text{(b)}$$

The integral can be solved by letting $x = \Delta a \sin^2 \alpha$ for $0 \le \alpha \le \pi/2$ so that $dx = 2\Delta a \sin \alpha \cos \alpha \cdot d\alpha$. Thus,

$$
\int_o^{\pi/2} \sqrt{\frac{\Delta a - x}{2\pi}}\, dx = 2\Delta a \int_o^{\pi/2} \cos^2 \alpha \cdot d\alpha
$$

$$
= \Delta a \left[\frac{\alpha}{2} + \frac{\sin 2\alpha}{4} \right]_0^{\pi/2} \tag{c}
$$

$$
= \frac{\pi \Delta a}{2}
$$

and

$$
G_i = \frac{(1+v)}{E} \left[\frac{\kappa+1}{4} \left(K_I^2 + K_{II}^2 \right) + K_{III}^2 \right] \tag{6.33}
$$

Algebraic manipulation of eq. (6.33) along with eqs. (6.31) and (6.32) gives G_i for crack motion on its tangent plane

$$
G_i = \frac{K_I^2}{E'} + \frac{K_{II}^2}{E'} + \frac{(1+v)\,K_{III}^2}{E} \tag{6.34}
$$

where $E' = E$ for plane stress
$\qquad E' = E/\left(1 - v^2\right)$ for plane strain

For convenience, the effect of Poisson's ratio on the energy release rate for mode I loading is shown in Figure 6.4.
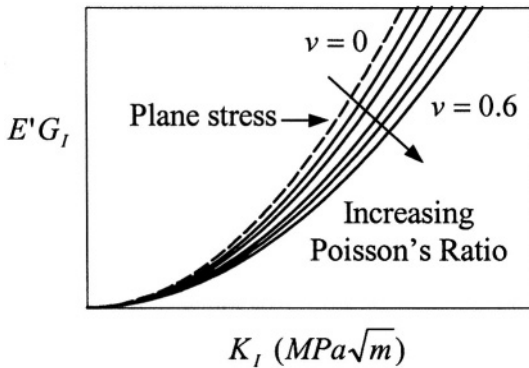
Figure 6.4 Variation of the energy release rate $E'G_I = f(K_I)$

6.6   LOAD AND DISPLACEMENT CONTROL

Assume that the slender $(a \gg h)$ double cantilever beam (DCB) shown in Figure 6.4 is loaded in tension with no rotation at the end of the beam. If the displacement and linear compliance equations are[1,7,16]

$$\mu \;=\; \frac{2Pa^3}{3E'I} \tag{6.35}$$

$$C \;=\; \frac{\mu}{P} = \frac{2a^3}{3E'I} \tag{6.36}$$

where a = Crack length
$\quad\quad I$ = Moment of inertia = $Bh^3/12$

$$P = \sigma A_o = \sigma Bh$$

$$M = Pa$$
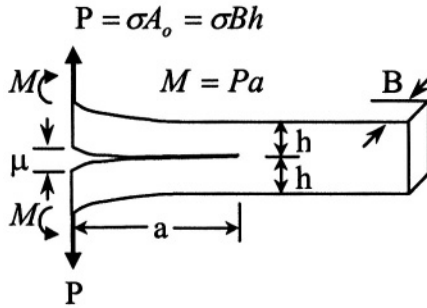
Figure 6.5 Slender double cantilever beam (DCB) with a $\gg$ h

For constant load, the compliance, displacement and load gradient and are, respectively

$$\frac{dC}{da} \;=\; \frac{2a^2}{E'I} \tag{6.37}$$

$$\frac{d\mu}{da} \;=\; \frac{2Pa^2}{E'I} \tag{6.38}$$

$$\frac{dP}{da} \;=\; 0 \tag{6.39}$$

Substituting eqs. (6.38) and (6.39) into (6.7) gives

$$G_I \;=\; \frac{P}{2B}\frac{d\mu}{da} \tag{6.40}$$

$$G_I \;=\; \frac{P^2 a^2}{BE'I} \qquad \text{For } P = \text{Constant} \tag{6.41}$$

If eq. (6.10) is used instead of (6.7) yields the same result. Thus,

$$G_I = \frac{P^2}{2B}\frac{dC}{da} = \frac{P^2 a^2}{BE'I} \qquad \text{For } P = \text{Constant} \qquad (6.42)$$

As a result, $G_I \propto a^2$ (proportional) which implies that G_I increases rapidly as a increases. Crack propagation occurs when $G_I = G_{IC}$ and $a = a_c$. In addition, crack instability occurs under load-control if $dP/da < 0$ when $G_I \propto a^2$. This is clearly demonstrated by solving eq. (6.42) for P and deriving the load gradient

$$P = \frac{\sqrt{G_I BE'I}}{a} \qquad (6.43)$$

$$\frac{dP}{da} = -\frac{\sqrt{G_I BE'I}}{a^2} < 0 \qquad (6.44)$$

Consider the slender DCB under **constant displacement.** In this case, the load and load gradient expressions are

$$P = \frac{\mu}{C} = \frac{3\mu E'I}{2a^3} \qquad (6.45)$$

$$\frac{dP}{da} = -\frac{9\mu E'I}{2a^4} \qquad (6.46)$$

$$\frac{d\mu}{da} = 0 \qquad (6.47)$$

Insert eqs. (6.46) and (6.47) into (6.7) to get

$$G_I = -\frac{\mu}{2B}\frac{dP}{da} = \frac{9\mu^2 E'I}{4Ba^4} \qquad \text{For } \mu = \text{Constant} \qquad (6.48)$$

This result suggests that $G_I \propto a^{-4}$ and G_I decreases as a increases. Therefore, crack stability occurs if $d\mu/da > 0$ and $dG_I/da < 0$ when $G_I \propto a^2$; that is,

$$\mu = \frac{2a^2}{3}\sqrt{\frac{4G_I B}{9E'I}} \qquad (6.49)$$

$$\frac{d\mu}{da} = \frac{4a}{3}\sqrt{\frac{4G_I B}{9E'I}} > 0 \qquad (6.50)$$

$$\frac{dG_I}{da} = -\frac{9\mu^2 E'I}{Ba^3} < 0 \qquad (6.51)$$

The theoretical trend of the behavior of the strain-energy release rate as per eqs. (6.42) and (6.48).are shown in Figures 6.5 and 6.6, respectively.
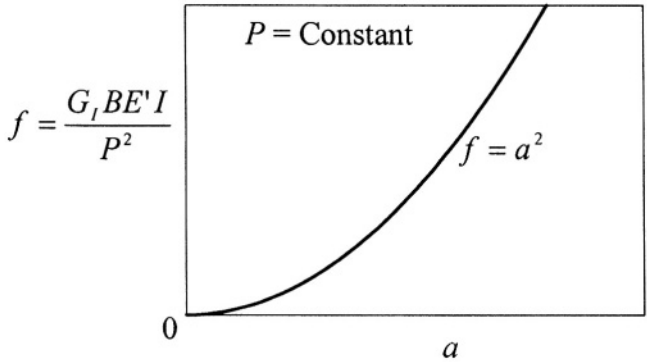
Figure 6.6 Normalized crack driving force as a function of crack length under load-control sytem
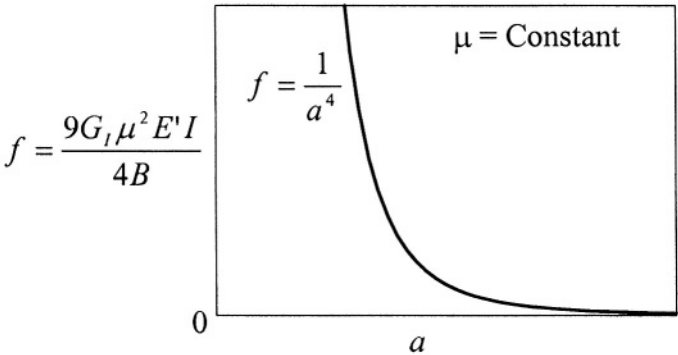
Figure 6.7 Normalized crack driving force as a function of crack length under displacement-control sytem

Example 6.1 *Suppose that three specimens made of 7075-T651 Al-alloy (E = 70 GPa, σ_{ys} = 850 MPa and n = 0.30) have identical dimensions were loaded in tension and the following data shown below was obtained at room temperature. The specimens exhibited linear behavior.*

No.	a (mm)	B (mm)	P (kN)	μ_y (mm)	Fracture
1	25.00	25	145		Yes
2	25.00	25	100	0.2500	No
3	25.50	25	100	0.2525	No

Determine the plane strain fracture   toughness K_{IC}.

Solution:

Calculate the compliance for spec specimens 2 and 3.   Thus,

$$C_2 \ = \ \frac{\mu_{y2}}{P_2} = \frac{0.2500x10^{-3} \ m}{100x10^3 \ N} = 2.500x10^{-9} \ m/N$$

$$C_3 \ = \ \frac{\mu_{y3}}{P_3} = \frac{0.2525x10^{-3} \ m}{100x10^3 \ N} = 2.525x10^{-9} \ m/N$$

$$\frac{dC}{da} \ \simeq \ \frac{C_3 - C_2}{a_3 - a_2} = \frac{2.525x10^{-9} \ m/N - 2.500x10^{-9} \ m/N}{(25.50 - 25.00) \, x10^3}$$

$$\frac{dC}{da} \ \simeq \ 5.00x10^{-8} \ N^{-1}$$

From eq.   (6.42),

$$G_{IC} \ = \ \frac{P_f^2}{2B} \frac{dC}{da} \tag{6.42}$$

$$G_{IC} \ = \ \frac{\left(145x10^3 \ N\right)^2 \left(5.00x10^{-8} \ N^{-1}\right)}{2\left(25x10^{-3} \ m\right)} =$$

$$G_{IC} \ = \ 21,025 \ N/m \simeq 0.021025 \ MN$$

From eq.   (6.34) fro pure mode I $\left(K_{II} = 0$ and $K_{III} = 0\right)$,

$$G_{IC} \ = \ \frac{K_{IC}^2}{E'} = \frac{\left(1 - v^2\right) K_{IC}^2}{E} \tag{6.34}$$

$$K_{IC} \ = \ \sqrt{\frac{G_{IC}E}{\left(1 - v^2\right)}}$$

$$K_{IC} \ = \ \sqrt{\frac{\left(0.021025 \ MN/m\right)\left(70x10^3 \ MN/m^2\right)}{1 - 0.30^2}}$$

$$K_{IC} \ = \ 40.22 \ MPa\sqrt{m}$$

*According to the ASTM E399 standard thickness requirement, the validity
of this result can be verified using eq.   (3.30)*

$$B_{ASTM} \geq 2.5 \left(\frac{K_{IC}}{\sigma_{ys}}\right)^2 = 5.60 \ mm$$

*Therefore, the result is valid since the given thickness is higher than the
calculate one; that is, $B > B_{ASTM}$.*

6.7   CRACK RESISTANCE CURVES

For plane stress conditions, the Griffith energy criterion for crack growth $(R = G_i)$ was modified by Irwin [10] when he proposed that crack instability should occur when

$$\frac{dG_i}{da} = \frac{dR}{da} \tag{6.52}$$

The shape of the **R-curve** is horizontal for pure brittle materials since the surface energy is an invariant material property and R is independent of crack size. [2,20]. For pure mode I, the Griffith instability criterion, R-curve, is shown in Figure 6.8 as a dashed horizontal line for which $R = G_{IC}$. [17]. The characterization of this fracture criterion anticipates that R increases when the plastic zone, at a small-scale yielding, increases and strain hardens. However, local material separation should occur due to void initiation and coalescence at high strains and stresses. In this case, the plastic zone must reach a critical size for crack growth to occur since sufficient energy must be available; otherwise, the crack would be stationary. Hence, both G_I and R increase with increasing stress level and subsequently, unstable crack growth occurs when the crack adheres a critical condition, shown in Figure 6.8 as a stability point, at which G_I, a, σ, and K_I acquire critical values.
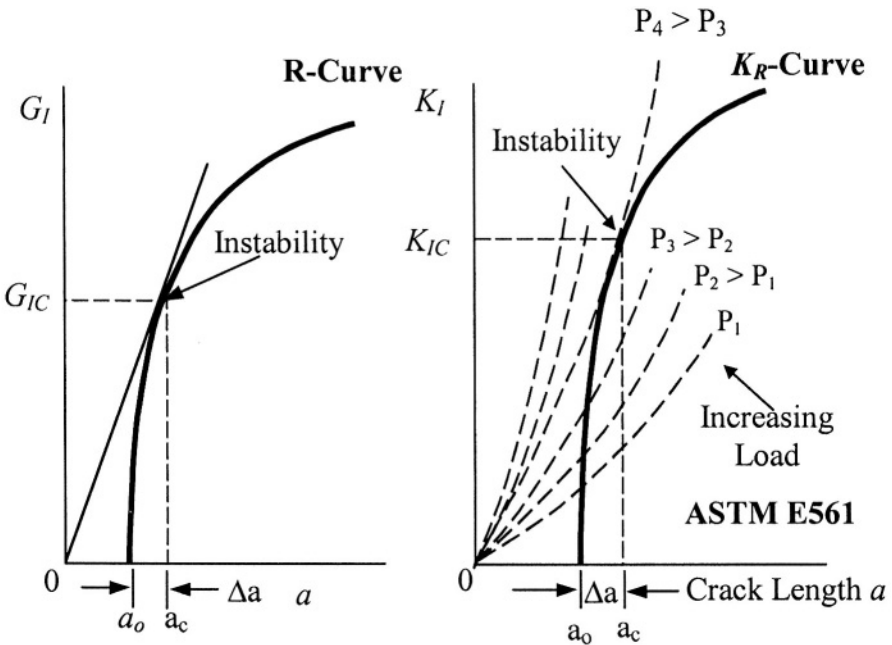
Figure 6.8 The R-curve showing the instability point

Accordingly, the ASTM E561 Standard Practice includes the R-curve to provide a toughness diagram in the form of applied $K_I = f(\Delta a)$ so that crack instability (onset of unstable fracture process) occurs when $K_I = K_{IC}$ and $a = ac$ for a specific applied load P_4 (Figure 6.8). This implies that the resistance to fracture of a metallic solid containing an initial crack size (a_c) may be characterized by an R-curve, provided that crack growth or extension develops slowly and stably.

Furthermore, the R-curve can be constructed by drawing secant lines on a load-displacement curve as shown in Figure 6.9a [17]. The slope of the secant lines as a measure of the compliance C and the crack lengths a_i are determined. Subsequently, follow the sequence in Figure 6.9.
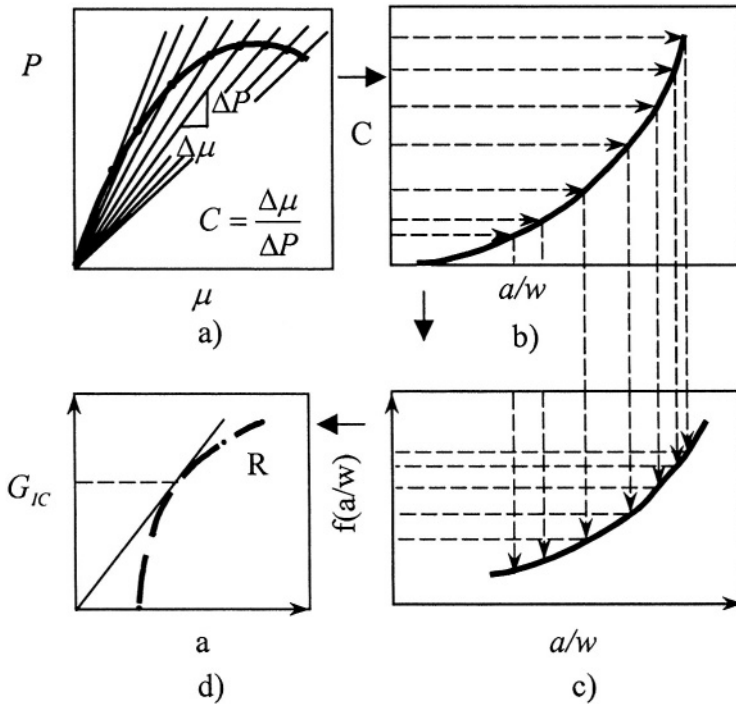
Figure 6.9 Determination of the R-curve

Plot the compliance C as a function a/w, where $a = a_o + \Delta a + r$ is the effective crack length. This is depicted in Figure 6.9b. The, plot the calibration curve as a polynomial $\alpha = f(a/w)$ (Figure 6.9c). Finally, calculate K_I and G_I and plot them as functions of crack length a. The resultant plot is the R-curve schematically shown in Figure 6.9d for G_I. The point of intersection between the secant line and the R-curve defines the critical strain energy release rate (G_{IC}), which in turn is related to the critical stress intensity factor or plane strain fracture toughness (K_{IC}).

6.8   THE J-INTEGRAL

Consider the two-dimensional crack being surrounded by two arbitrary counterclockwise contours Γ_1 and Γ_2 shown in Figure 6.10. If a small-scale yielding prevails, then the quantities K_I, K_{II}, K_{III} and G_i defined in Chapter 4 can describe the stress state near the crack tip when the field is elastic with a relatively small plastic zone $r \ll a$; otherwise, Ki and G_i do not describe of the elastic-plastic behavior of tough materials containing large plastic zones $r \geq a$ (large-scale yielding) as in tough materials. Nevertheless, the need to characterize tough solid prevails since many engineering materials are of this category.

In order to determine an energy quantity that describes the elastic-plastic behavior of tough materials, Rice [9] introduced a contour integral or line integral that encloses the crack front shown in Figure 6.10 originally by Eshelby [15] as

$$J = \int_{\Gamma} \left(W \, dy - \vec{T} \frac{\partial \vec{\mu}}{\partial x} \, ds \right) \tag{6.53}$$
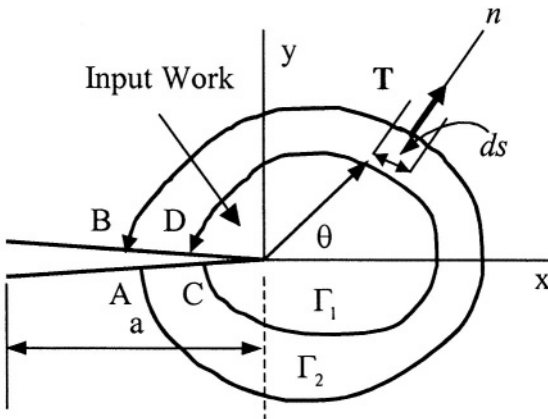
Figure 6.10 J-integral contours around the crack surfaces

where J = Effective energy release rate $(MPa.m$ or $MN/m)$
W = Elastic strain energy density or plastic loading work (J/m^3)
$\vec{\mu}$ = Displacement vector at ds
ds = Differential element along the contour
n = Outward unit normal to Γ
$\vec{T} (\partial \vec{\mu} / \partial x) \, ds$ = Input work
s = Arc length
$\vec{T}$ = Tension vector (traction forces) on the body bounded by Γ
Γ = Arbitrary counterclockwise contour

The term J in eq. (6.53) is a line of surface integral defined around a contour Γ It characterizes the stress-strain field around the crack front and therefore, it must be the energy release to the crack tip during crack growth. Due to this fact, the J-integral is used as failure criterion and it is a measure of the fracture toughness at the onset of slow crack growth for elastic and elastic-plastic metallic materials. The inherent characteristics of the J-integral exhibits a) remarkable path, contour size and shape independence, and b) an invariability in magnitude when the contour lies either inside or outside the plastic zone [18]. The former characteristic indicates that the J-integral vanishes ($J = 0$) around an arbitrary closed contour as shown by Parton and Morozov [19] using Green's formula.

The interpretation of the J-integral includes the following observations:

- The J-integral vanishes along the closed contours Γ_1 and Γ_2 because the traction forces ($\overrightarrow{T} = 0$) along the crack lower and upper surfaces are zero and $dy = 0$ along AC and BD. Thus, eq. (6.53) becomes $J_{\Gamma_1} - J_{\Gamma_2} = 0$. Therefore, the J-integral is path independent and it is a measure of the straining at the crack tip that accounts for significant plastic deformation at the onset of crack initiation. The contour path can be defined arbitrarily for computational advantages [7], as it will be shown in a later section, since J is conserved. This means that the contour Γ can conveniently be defined along the plastic zone boundary so that the Von Mises plastic zone size, eq. (3.52), can define the contour shape as shown in Figure 5.6.

- The crack line can be included in the contour Γ_1 or Γ_2 without contributing to the value of J. For this reason, points A and B or C and D do not need to coincide.

- The J-integral along a contour around the crack is the change in potential energy (elastic energy) for a virtual crack extension da. Thus, the J-integral can be defined by

$$J = -\frac{U_3}{da} \tag{6.54}$$

- Remarkably, the J-integral can be evaluated along remote paths, where small crack-tip yielding does not interfere.

With regard to eq. (6.53), the work input and the strain energy density are defined as

$$\overrightarrow{T} \;\; = \;\; \sigma_{ij} n \qquad (i,j) = 1,2,3 \tag{6.55}$$

$$W \;\; = \;\; \int \sigma_{ij} d\epsilon_{ij} \tag{6.56}$$

In general, the elastic stresses needed in eq. (6.56) are defined in matrix form

$$\sigma_{ij} = \begin{bmatrix} \sigma_{xx} & \tau_{xy} & \tau_{xz} \\ \tau_{yx} & \sigma_{yy} & \tau_{yz} \\ \tau_{zx} & \tau_{zy} & \sigma_{zz} \end{bmatrix} \tag{6.57}$$

The train energy density can be expressed as

$$W = \frac{1}{E'} \left[\begin{array}{c} \frac{1}{2} \left(\sigma_{xx}^2 + \sigma_{yy}^2 + \sigma_{zz}^2 \right) - v \left(\sigma_{xx}\sigma_{yy} + \sigma_{yy}\sigma_{zz} + \sigma_{zz}\sigma_{xx} \right) \\ + \left(1 + v \right) \left(\tau_{xy}^2 + \tau_{yz}^2 + \tau_{zx}^2 \right) \end{array} \right] \tag{6.58}$$

Recall that plane stress condition requires that $\sigma_{zz} = \tau_{zx} = \tau_{zy} = 0$ and $E' = E$. Consequently, eq. (6.58) reduces to

$$W = \frac{1}{2E} \left[\sigma_{xx}^2 + \sigma_{yy}^2 - 2v\sigma_{xx}\sigma_{yy} + 2 \left(1 + v \right) \tau_{xy}^2 \right] \tag{6.59}$$

For pure tension loading, W becomes

$$W = \frac{\sigma_{yy}^2}{2E} \tag{6.60}$$

However, the elastic mixed-mode interaction described by eq. (6.34) can be used to predict the J-integral, provided that $r \ll a$. This means that $J_i = G_i$ so that

$$J_i = \frac{K_I^2}{E'} + \frac{K_{II}^2}{E'} + \frac{(1 + v) K_{III}^2}{E} \tag{6.61}$$

6.8.1   FRACTURE CRITERION

The J-integral is used as a critical parameter for determining the onset of stable crack growth and predicting fracture toughness. The fracture criterion by J_{IC} for the initiation of stable crack growth is established when the applied J-integral reaches a critical value. This is indicated below for elastic and elastic-plastic materials

$$
\begin{aligned}
J_i &= J_c = G_C & &\text{For elastic-plastic behavior} & &(6.62) \\
J_i &= J_c \neq G_C & &\text{For elastic-plastic behavior} & &(6.63) \\
J_I &= J_{IC} = G_{IC} & &\text{For elastic behavior under mode I loading} & &(6.64) \\
J_I &= J_{IC} \neq G_{IC} & &\text{For elastic-plastic behavior for mode I} & &(6.65)
\end{aligned}
$$

Similar fracture criteria can be used for mode II and III loading systems. In general, J_{IC} may be used as a brittle or ductile fracture toughness criterion for characterizing a material behavior that does not meet the requirements of G_{IC} or K_{IC} fracture criterion. In addition, the measurement of K_{IC} is described by the ASTM E399 Standard Testing Method, Vol. 03.01.

For a large-scale yielding case, the J-integral becomes the controlling factor in characterizing plastic behavior of ductile materials containing stationary cracks since J is the available energy per unit crack extension at the crack tip.

With regard to elastic-plastic mechanical behavior, crack blunting may occur at the crack tip and the fracture criterion used for determining the onset of crack instability depends on the amount of plasticity ahead of the crack tip. Fortunately, the J-integral can be used when $r << a$ or $r \geq a$. The latter case is treated in Chapter 7 in great details.

6.8.2   CRACK OPENING DISPLACEMENT

Using the Dugdale's model, the crack tip opening displacement *(CTOD)* δ_t indicated in Figures 5.3 can be related to the J integral, provided that the path of integration is arbitrarily chosen in the elastic regime and the contour curve Γ is taken around the yield strip or plastic zone boundary.

According to Hella's analysis [7] for thin plates and Tresca properties, the Dugdale's model (Figure 5.3) can be used as the path contour Γ needed to solve the J-integral. That is, the arbitrary contour depicted in Figure 6.10 can be shrunk to a shape similar to the Dugdale's yield strip, which is shown in Figure 6.11 for convenience.
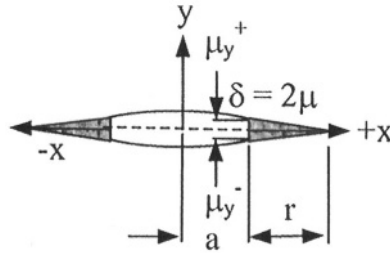
Figure 6.11 Dugdale's yield strip for COD measurements

Let $x = a$ at the lower crack side before localized yield occurs and $x = a + r$ at the upper crack side after yielding be the limits of the J-integral under pure tension loading (mode I). As a result, $dy = 0$ along the crack plane and the traction force becomes $T = \sigma_{yy} = \sigma_{ys}$. Thus, the J-integral becomes [7]

$$J_I \;=\; -\int_\Gamma \vec{T}\frac{\partial \vec{\mu}}{\partial x}\, ds = -\int_a^{a+r} \sigma_{ys}\frac{\partial}{\partial x}\left(\mu_y^+ - \mu_y^-\right) dx \qquad \text{(a)}$$

$$J_I \;=\; \int_a^{\delta_t} \sigma_{ys}\, d\left(\mu_y^+ - \mu_y^-\right) = \sigma_{ys}\delta_t \qquad (6.66)$$

Here, μ_y^+ and μ_y^- are the upper and lower displacements. Denote that this expression resembles eq. (5.42) when $J_I = G_I$ for small-scale yielding under plane stress.

6.8.3 J-INTEGRAL MEASUREMENTS

Most practical fracture mechanics applications are base on mode I loading. However, mode II and III may be important in certain engineering situation. In fact, mixed-fracture in a complex theory and will be dealt with in details in Chapter 7.

The J-integral measurement is valid if unloading does not occur. For instance, the region $J\Delta A$ in Figure 6.12 represents the area between the loading curves for crack areas A and $A + \Delta A$ as $A \to 0$. Figure 6.12 is the nonlinear equivalent of Figure 6.2. The J-integral can be determined from a load-displacement diagram shown in Figure 6.12, from which the critical value of the J-integral (fracture toughness) can be determined at the onset of slow crack growth [7-8]. Some experimental results for a $Ni - Cr - Mo - V$ steel alloy are depicted in Figure 6.13 [6,11].

In addition, eq. (6.54) can be redefined as

$$J = -\frac{1}{B} \int_o^\mu \left(\frac{U_3}{da}\right)_\mu d\mu = \frac{1}{B} \int_o^P \left(\frac{U_3}{da}\right)_P dP \qquad (6.67)$$
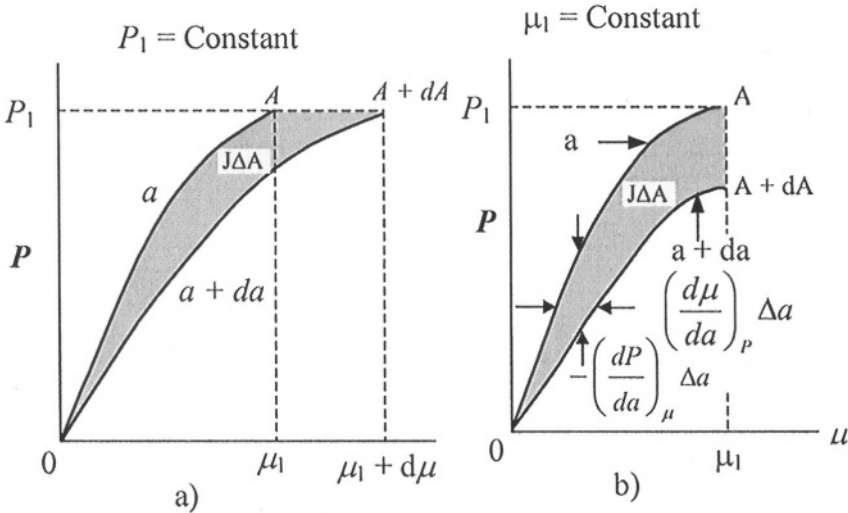
Figure 6.12 J-integral at a) fixed displacement and at b) fixed load
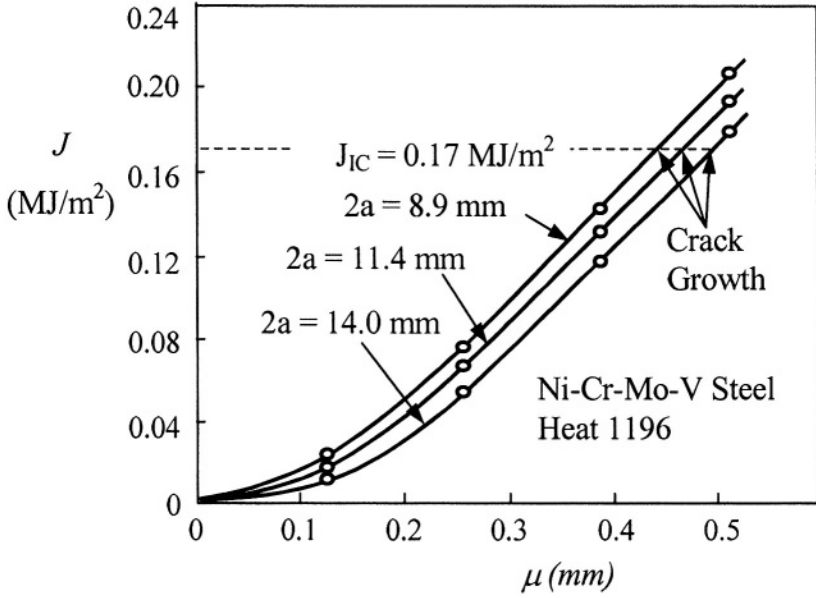
Figure 6.13 J-integral vs. displacement [6,11]

6.9   TEARING MODULUS

Those materials (ductile) that exhibit appreciable plasticity at fracture usually show slow and stable crack growth before fracture. Stable crack growth starts at J_{IC}, but further increase of the applied stress is required to maintain the crack growing. The resistance curve in these materials is the J_R-curve, which is equivalent to the R-curve discussed previously. The crack driving force is J_I instead of G_I [8]. The criteria for stable crack growth are

$$\frac{dJ}{da} < \frac{dJ_R}{da} \qquad \text{For stable crack growth} \qquad (6.68)$$

$$\frac{dJ}{da} \geq \frac{dJ_R}{da} \qquad \text{For unstable crack growth} \qquad (6.69)$$

Paris et al. [12] have proposed a dimensionless tearing modulus (T_R) defined by multiplying eq. (6.69) by E/σ_{ys}^2 so that

$$\frac{E}{\sigma_{ys}^2}\frac{dJ}{da} = \frac{E}{\sigma_{ys}^2}\frac{dJ_R}{da} \qquad (6.70)$$

$$T_R = \frac{E}{\sigma_{ys}^2}\frac{dJ}{da} \qquad (6.71)$$

In fact, T_R is nothing but the crack resistance for crack growth. Here, dJ/da is the slope of the $J - \Delta a$ resistance curve in the stable crack growth regimen and fracture toughness is denoted by J_{IC} as indicated in Figure 6.14 [14]. In fact, Hutchinson-Paris [13] devised a procedure to validate the J-controlled crack growth by stating that 1) the elastic unloading region in the fracture process zone requires that $\Delta a << r$ and 2) J must increase rapidly with crack extension so that the region of non-proportionality is small so that $dJ/da >> J/r$.
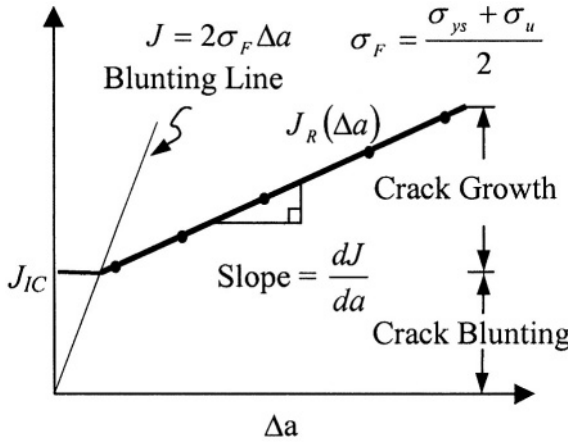
Figure 6.14 Schematic J-resistance curve

The J-integral can also be used as defined in the ASTM E813 Standard Practice. That is,

$$J = \frac{2A}{bB} \tag{6.72}$$

where A = Area under the load-displacement curve (Joules)
   $b = w - a$ = Ligament in plates (mm)

_____

Example 6.2 *a) Show that J-integral vanishes in the square counterclockwise contour a-b-c-d shown in Figure 6.E2. The square contour has four segments such as* $\Gamma = ab - bc - cd - da$. *b) Determine the strain energy density W and the J-integral under plane stress and plane strain conditions, for a steel plate having* $w = 50.80$ mm, , $\sigma = \sigma_{ys} = 700$ MPa, $v = 1/3$ *and* $E = 207$ GPa.
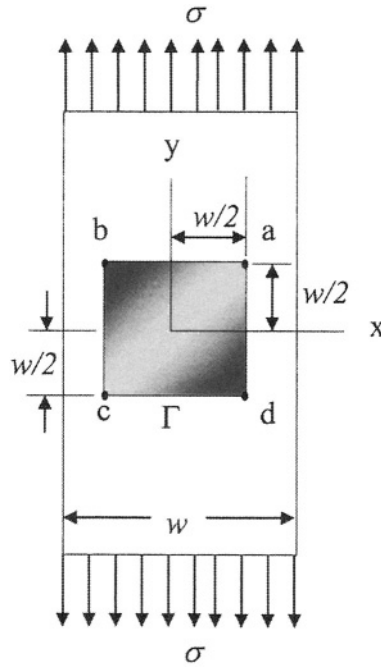
Figure 6.E2

Solution:

Use only half of the entire contour due to symmetry. The present stress and displacement fields shown in the given figure leads to and $E' = E$.

$$\sigma_{yy} \;=\; \sigma \qquad\qquad\qquad\qquad\text{Applied}$$

$$\sigma_{xx} \;=\; \sigma_{zz} = \tau_{zx} = \tau_{zy} = 0 \quad\text{For plane stress}$$

$$\sigma_{zz} \;=\; v\left(\sigma_{xx} + \sigma_{yy}\right) = v\sigma \quad\text{For planer strain}$$

$$W \;=\; \int \sigma_{ij} d\epsilon_{ij} = \frac{\sigma^2}{2E'}$$

$$\vec{\mu} \;=\; \frac{\sigma}{E}\,\vec{y} \qquad\qquad\qquad\text{Over the contour}$$

$$\vec{T_i} \;=\; \sigma_{ij}\,\vec{n} = \sigma_{yy} n$$

a) For plane stress condition,

$$J_{ab} = \int_a^b \left(W dy - T_i \frac{\partial \mu}{\partial x} dx \right) = 0 \ \text{ since } dy = 0, \ \partial \mu / dx = 0, \ ds = dx \quad (6.53)$$

$$J_{bc} = \int_b^c \left(W dy - T_i \frac{\partial \mu}{\partial x} dy \right) = \int_b^c W dy = \frac{\sigma^2 (c - b)}{2E} \ \text{ since } T_i = 0, \ ds = dy$$

$$J_{cd} = \int_c^d \left(W dy - T_i \frac{\partial \mu}{\partial x} dx \right) = 0 \ \text{ since } dy = 0, \ \partial \mu / dx = 0, \ ds = dx$$

$$J_{da} = \int_b^c \left(W dy - T_i \frac{\partial \mu}{\partial x} dy \right) = \int_b^c W dy = \frac{\sigma^2 (a - d)}{2E} \ \text{ since } T_i = 0, \ ds = dy$$

Thus,

$$J_{bc} = \frac{\sigma^2 (-w/2 - w/2)}{2E} = -\frac{w\sigma^2}{2E}$$

$$J_{da} = \frac{\sigma^2 (-w/2 + w/2)}{2E} = \frac{w\sigma^2}{2E}$$

and

$$J_\Gamma = \sum J_i = J_{ab} + J_{bc} + J_{cd} + J_{da}$$

$$J_\Gamma = 0 - \frac{w\sigma^2}{2E} + 0 + \frac{w\sigma^2}{2E} = 0$$

Therefore, the J-integral vanishes. If $w = 50.80 \ mm$, , $\sigma = \sigma_{ys} = 700$ *MPa, v = 1/3 and* $E = 207 \ GPa$, *then*

$$W = \frac{\sigma^2}{2E} = \frac{(700 \ MPa)^2}{(2)(207,000 \ MPa)} = 1.18 \ MPa = 1.18 \ MJ/m^3$$

$$J_{da} = -J_{bc} = \frac{w\sigma^2}{2E} = W w = \left(1.18 \ MJ/m^3 \right) \left(50.80 x 10^{-3} \ m \right)$$

$$J_{da} = -J_{bc} \simeq 60 \ kPa.m = 60 \ kJ/m^2$$

b) For plane strain,

$$\sigma_{zz} = v\sigma = (1/3)(700 \ MPa) = 233.33 \ MPa$$

$$W = \frac{\sigma^2}{2E'} = \frac{\left(1 - v^2 \right) \sigma^2}{2E}$$

Using a similar approach for the determining the total J-integral yields

$$J_\Gamma = \sum J_i = J_{ab} + J_{bc} + J_{cd} + J_{da}$$

$$J_\Gamma = 0 - \frac{w \left(1 - v^2 \right) \sigma^2}{2E} + 0 + \frac{w \left(1 - v^2 \right) \sigma^2}{2E} = 0$$

Therefore, the J-integral vanishes. If $w = 50.80\ mm,\ ,\ \sigma = \sigma_{ys} = 700$ *M Pa,* $v = 1/3$ *and* $E = 207\ GPa,$ *then*

$$W = \frac{(1-v^2)\,\sigma^2}{2E} = \frac{(1-1/9)\,(700\ MPa)^2}{(2)\,(207,000\ MPa)} = 1.05\ MPa = 1.05\ MJ/m^3$$

$$J_{da} = -J_{bc} = \frac{w\,(1-v^2)\,\sigma^2}{2E} = Ww = (1.05\ MJ/m^3)\,(50.80x10^{-3}\ m)$$

$$J_{da} = -J_{bc} \simeq 53.34\ kPa.m = 53.34\ kJ/m^2$$

6.10   PROBLEMS

6.1 Use Dugdale's model for a fully developed plane stress yielding confined to a narrow plastic zone. Yielding is localized to a narrow size roughly equal to the sheet thickness *(B)*. This is a fully elastic case in which the plastic strain may be defines as $\epsilon = \delta_t/B$. If the J-integral is by $dJ = \sigma d\delta$, where δ_t is the crack tip opening displacement. Show that

$$\delta_t = \frac{\pi \alpha^2 a \sigma^2}{E \sigma_{ys}}$$

6.2 The crack tip opening displacement (δ_t) for perfectly plastic solution to the Dugdale model was derive by Rice in 1966 [21] as defined by eq. (5.35). Show that the path-independent J-integral is defined by

$$J = \frac{(\kappa + 1)\,(1 + v)\,\pi a \sigma^2}{E}$$

6.3 A bending test specimen made out of carbon steel showed a load-displacement behavior

A = Area =10 Joules
E = 207 GPa
σ_{ys} = 1,500 MPa
B = 25 mm
b = 25 mm
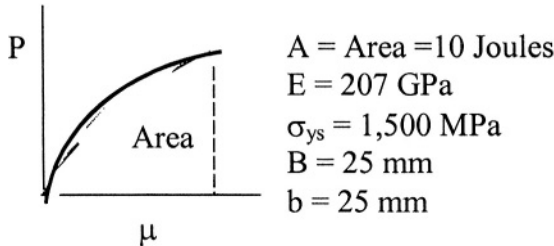
If the area under the curve the $P = f(\mu)$ is 10 joules at the onset of crack growth, determine a) the fracture toughness in terms of J_{IC} as per ASTM E813 Standard, b) K_{IC} and its validity as per ASTM E399 testing method, and c) δ_{tc} using eq. (5.31) with $\lambda = 3$, d) the fracture strain, e) the displacement and f) the plastic zone size. Explain the meaning of the results. [Solution: a) $J_{IC} = 32$ $kPa.m$, b) $K_{IC} = 81.39\ MPa\sqrt{m}$, c) $\delta_{tc} = 0.016\ mm$, d) $\epsilon_f = 0.064\%$, e) 0.008 mm and f) $r = 0.16\ mm$].

6.4   If $J_I = \sigma_{ys}\delta_t$ is used to determine the fracture toughness, will δ_t be a path-independent entity? Explain.

6.5   Assume hat crack growth occurs when $J_I \leq J_{IC}$. If a well-developed plastic flow occurs, will this inequality be valid? Explain.

6.11   REFERENCES

[1]   J.G. Williams,"Fracture Mechanics of Polymers," Ellis Horwood Limited, Halsted Press: a Division of John Wiley & Sons, New York, (1984).

[2]   D. Broek, "Elementary Engineering Fracture Mechanics," Fourth edition, Kluwer Academic Publisher, Boston, (1986).

[3]   C.E. Inglis, "Stresses in a Plate due to the Presence of Cracks and Sharp Corners," Trans. Inst. Nav. Arch., 55 (1913) 219-241.

[4]   A.A. Griffith, Phil. Trans. Royal Soc., 221 (1921) 163-167

[5]   H.M. Westergaard, "Bearing Pressures and Cracks," J. Appl. Mech., G1 (1939) A49-A53

[6]   D. Broek, "Elementary Engineering Fracture Mechanics," Fourth edition, Kluwer Academic Publisher, Boston, (1986)

[7]   K. Hellan, "Introduction to Fracture Mechanics", McGraw-Hill Book, New York, (1984)

[8]   R.W. Hertzberg, "Deformation and Fracture Mechanics of Engineering Materials," third edition, John Wiley & Sons, New York, (1989)

[9]   J.R. Rice, J. Appl. Mech. 35 (1968) 379-386

[10] G.R. Irwin, ASTM Bulletin, (Jan. 1960) 29

[11] J.D. Landes and J.A. Begley, ASTM STP 514, (1972) 24-39

[12] P. C. Paris, H. Tada, A. Zahoor and H. Ernst, "Instability of the Tearing Model of Elastic-Plastic Crack Growth," ASTM STP 668, (1979) 5.36.

[13] J.E.W. Hutchinson and P.C. Paris, in Elastic -Plastic Fracture, ASTM STP 668, (1979) 37.

[14] S. Surch and A.K. Vasudevan, "On the Relationship between Crack Initiation Toughness and Crack Growth," Math. Sci. Eng., "79 (1986) 183-190.

[15] J.D. Eshelby, "Calculation of Energy Release Rate," in Prospects of Fracture Mechanics, G.C. Sih, H.C. Von Elst, and D. Broek, Noordhoff, Growingen, (1974) 69-84.

[16] D.K. Felbeck and A.G. Atkins, "Strength and Fracture of Engineering Solids," Second Edition, Prentice-Hall, Inc., Upper Saddle River, N.J. (1996) 430-443

[17] ASTM 351-94, Annual Book of ASTM Standards, Vol. 03.01

[18] E.M. Morozov and G.P. Nikishkov, "Finite Element Method in Fracture Mechanics," Nauka, Moscow, (1980), reference cited in [19].

[19] V.Z. Parton and E.M. Morozov, "Mechanics of Elastic-Plastic Fracture," second edition, Hemisphere publishing corporation, New York, (1989)

[20] T.L. Anderson, "Fracture Mechanics: Fundamentals and Applications," CRC Press, Inc., Boston, (1991) 58.

Chapter 7

PLASTIC FRACTURE MECHANICS

7.1 INTRODUCTION

This chapter describes the stress-strain fields at a crack tip for materials that will obey the Ramberg-Osgood nonlinear stress-strain relation. These materials are considered to be strain hardenable , specially under tension loading. A two-dimensional field equations are characterized for ductile or low-strength materials, which can be strain hardened at a large scale yielding. In fact, hardening in a polycrystalline material is due to plastic deformation, in which dislocation motion is the primary phenomenon for this irreversible process. However, dislocation-imperfection interactions impede the mobility of dislocations leading to strain hardening. For instance, the dislocation distribution within a plastic zone is normally a complex and mixed phenomenon.

The mechanism of fracture is related to plastic deformation at the crack tip where high stresses and strains are developed. Therefore, the use of a dislocation model for determining stresses and strains would be an ideal mathematical approach for predicting crack instability. Instead, for a cracked elastic-plastic material subjected to an external load, the onset of plastic flow occurs at the crack tip and the flow criterion that predicts the onset of crack instability is usually the J-integral, which is limited to a stationary crack in a strain hardening material.

7.2 J-CONTROLLED CRACK GROWTH

Hutchinson [1] and Rice and Rosengren [2] in separate publications in 1968 showed that the J-integral characterizes the stress and strain fields at the crack tip in nonlinear elastic materials. Their work is referred to as the HRR theory, which is as an extension of linear fracture mechanics that account for a

large-scale yielding phenomenon and related microscopic fracture mechanisms, such as void formation and void coalescence within the plastic zone. Subsequently, the pertinent mathematical relationships have become known as the HRR field equations applicable near the crack tip within the J-dominated region as schematically illustrated in Figure 7. 1a [6-7].

Since the J-integral is path-independent, a circular path of radius r is convenient for deriving the field equations. Therefore, the nonlinear fracture mechanics approach can be used for analyzing rate-independent materials under monotonic loading [4]. Particularly, the J-integral and the Ramberg-Osgood semi-empirical uniaxial stress-strain relationship are widely used for characterizing crack growth at a large-scale yielding. Therefore, nonlinear fracture mechanics has a semi empirical foundation.
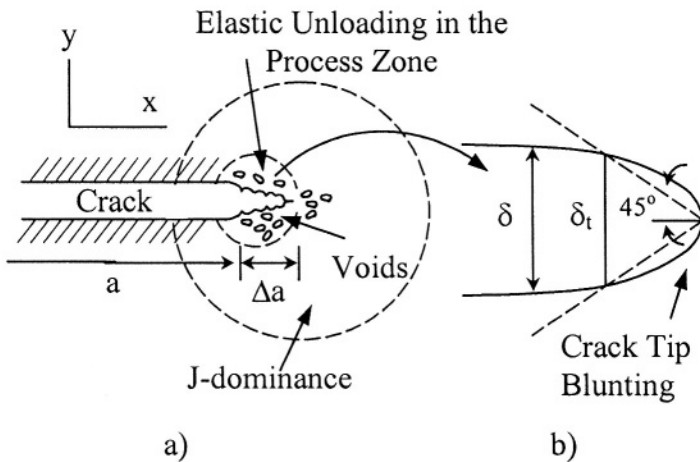
Figure 7.1 Schematic process zone within the J-dominant region

Furthermore, the crack growth model shown in Figure 7.1 indicates that the J-dominated region, where microscopic separation occurs, is within a relatively large plastic zone. One particular characteristic of a cracked ductile and strain hardenable material is the occurrence of crack blunting (Figure 7.1b) before appreciable crack growth takes place under monotonic loading. Despite that the J-integral does not model elastic unloading, the J-controlled crack growth requires that the region of elastic unloading and distinct non-proportional loading be contained with the J-dominated region of the deformation theory [7].

The conditions for J-controlled crack growth require that the amount of crack growth be related to the plastic zone size r, the J-integral, and the crack tip opening displacement δ_r. For crack extension, $\Delta a < r$, $J/(dJ/da) < r$ and $r > \delta_t$. In fact, the inequality $\Delta a < r$ assures that crack advance and unloading take place within the J-dominance zone. The plastic zone size (r) is some reaction of the unbroken ligament b and the tearing modulus dJ/da.

7.3   HRR FIELD EQUATIONS

The analysis given below is for a study on strain-hardening plasticity reported by Hutchinson [1] and Rice and Rosengren [2]. These authors defined the J-Integral as the crack driving force for characterizing plastic solids containing cracks. For instance, Hutchinson's analysis [1] is also found elsewhere [3,8].

Figure 7.2 schematically shows the stages of a ductile fracture process for load control systems.
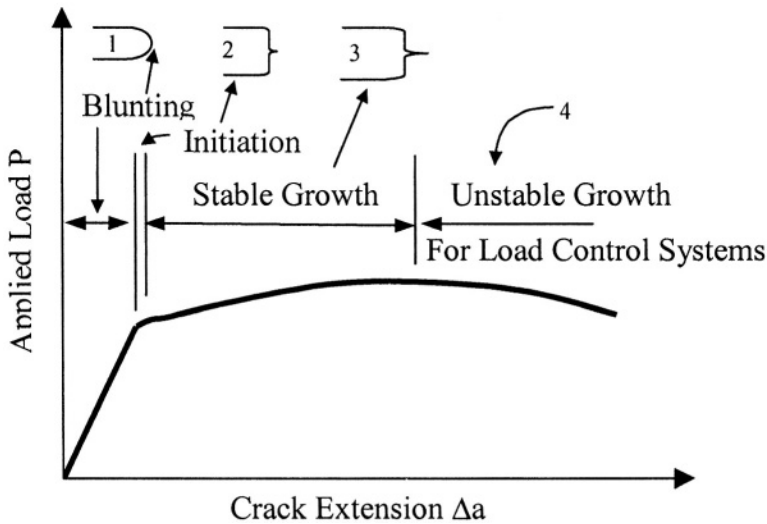
Figure 7.2 Schematic crack growth behavior of ductile materials [8]

It should be pointed out that Begley et al. [9,18] proposed the use of the J-integral [4] as the crack driving force for characterizing the onset of crack growth (crack extension) at a large-scale yielding. Crack growth may be stable if the concentration of the HRR field on the crack tip region, during deformation, is continuous, irreversible, and maintained, to an extent, a plastic level. This means that the J-integral and the crack tip opening displacement characterize plastic fracture at the crack tip region, where the *HRR* fields are located. Hence, fracture toughness is defined at the onset of stable crack growth for a J-controlled situation [11-12].

According to the multiaxial stress J_2-deformation theory of plasticity, the nonlinear multiaxial strains (ϵ_{ij}), the first deviatory stress (S_{ij}), and the effective stress (σ_e) for incompressible materials under tension are, respectively

$$J_2 = \frac{1}{2} S_{ij} S_{ij} \tag{7.1}$$

$$\epsilon_{ij} = \frac{3\epsilon_o S_{ij}}{2\sigma_e} \left(\frac{\sigma_e}{\sigma_o} \right) \tag{7.2}$$

$$S_{ij} = \sigma_{ij} - \frac{1}{3} \delta_{ij} \sigma_{kk} \tag{7.3}$$

$$\sigma_e = \sqrt{\frac{3}{2} S_{ij} S_{ij}} \tag{7.4}$$

In fact, the deformation theory of plasticity is basically a nonlinear elasticity [2]. The effective stress for plane stress is

$$\sigma_e = \sqrt{\sigma_r^2 + \sigma_\theta^2 - \sigma_r \sigma_\theta + 3\tau_{r\theta}^2} \qquad \text{For plane stress} \tag{7.5}$$

and the effective stress and the strains for plane strain are [1]

$$\sigma_e = \sqrt{\frac{3}{4} (\sigma_r - \sigma_\theta)^2 + 3\tau_{r\theta}^2} \qquad \text{For plane strain} \tag{7.6}$$

$$\epsilon_r = \sigma_r - v\sigma_\theta + \alpha' \left(\sigma_r - \frac{1}{2}\sigma_\theta \right) \sigma_e^{n-1} \tag{7.7}$$

$$\epsilon_\theta = \sigma_\theta - v\sigma_r + \alpha' \left(\sigma_\theta - \frac{1}{2}\sigma_r \right) \sigma_e^{n-1} \tag{7.8}$$

$$\gamma_{r\theta} = (1+v)\tau_{r\theta} + \frac{3}{2}\alpha'\tau_{r\theta}\sigma_e^{n-1} \tag{7.9}$$

where α' = Constant
n = Strain hardening exponent
ϵ_o = Yield strain or reference strain
σ_o = Yield strength or reference stress (MPa)

With regard to the strain hardening exponent n, low-strength (ductile) materials have greater hardening exponents than high-strength ones. As a result, large tensile stresses at the crack front in ductile materials cause nucleation of voids and void coalescence as the source for crack nucleation. Consequently, the effects of yielding and strain hardening at the crack front is a major concern in fracture mechanics. The phenomena of yielding and strain hardening is schematically shown in Figure 7.3 for quasi-static loading
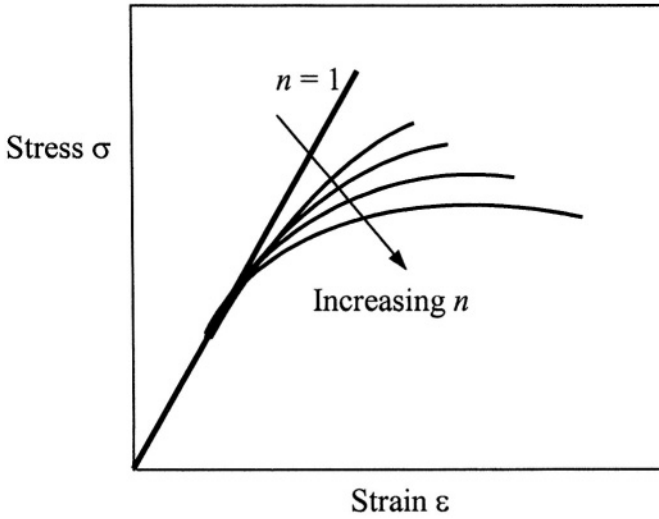
Figure 7.3 Schematic stress-strain curves showing the effect of strain hardening

Further, the hydrostatic stress and the Kronecker delta are, respectively

$$\sigma_{kk} = \sigma_{xx} + \sigma_{yy} + \sigma_{zz} \tag{7.10}$$

$$\delta_{ij} = \begin{bmatrix} 1 & 0 & 0 \\ 0 & 1 & 0 \\ 0 & 0 & 1 \end{bmatrix} \tag{7.11}$$

For an elastic-plastic behavior and a circular plastic zone with radius r, the Airy stress function defined by eq. (1.60) can be used here for deriving the plastic stresses at the crack front [3]. Thus,

$$\phi = r^{\lambda+1} f(\theta) \tag{7.12}$$

The polar stresses are defined by eq. (1.58), but they are included in this chapter for convenience. Hence,

$$
\begin{aligned}
\sigma_r &= \frac{1}{r}\frac{\partial \phi}{\partial r} + \frac{1}{r^2}\frac{\partial^2 \phi}{\partial \theta^2} \\
\sigma_\theta &= \frac{\partial^2 \phi}{\partial r^2} \\
\tau_{r\theta} &= \frac{1}{r^2}\frac{\partial \phi}{\partial \theta} - \frac{1}{r}\frac{\partial^2 \phi}{\partial r \partial \theta} = -\frac{\partial}{\partial r}\left(\frac{1}{r}\frac{\partial \phi}{\partial \theta}\right)
\end{aligned} \tag{7.13}
$$

The boundary conditions can be set as

$$\sigma_\theta \quad = \quad \tau_{r\theta} = 0 \qquad\qquad \text{For } \theta = \pm\alpha \qquad\qquad (7.14)$$

$$f \quad = \quad f(\theta) = \frac{df}{d\theta} = 0 \quad \text{For } \theta = \pm\alpha \qquad (7.15)$$

The strain compatibility equation that must be satisfied is of the form

$$\frac{\partial^2 \epsilon_\theta}{\partial r^2} + \frac{2}{r}\frac{\partial \epsilon_\theta}{\partial r} - \frac{1}{r}\frac{\partial^2 \gamma_{r\theta}}{\partial r\partial\theta} - \frac{1}{r^2}\frac{\partial \gamma_{r\theta}}{\partial \theta} + \frac{1}{r^2}\frac{\partial^2 \epsilon_r}{\partial \theta^2} - \frac{1}{r}\frac{\partial \epsilon_r}{\partial r} = 0 \qquad (7.16)$$

Inserting the partial derivatives of the Airy's stress function, eq. (7.12), into (7.13) yields

$$\sigma_r \quad = \quad r^{\lambda-1}\left[(\lambda+1)f + \frac{d^2 f}{d\theta^2}\right] = r^{\lambda-1}\tilde{\sigma}_r$$

$$\sigma_\theta \quad = \quad r^{\lambda-1}\lambda(\lambda+1)f = r^{\lambda-1}\tilde{\sigma}_\theta \qquad\qquad (7.15)$$

$$\tau_{r\theta} \quad = \quad r^{\lambda-1}\lambda f = r^{\lambda-1}\tilde{\tau}_{r\theta}$$

Thus, the equivalent stress as defined by eq. (7.5) and (7.6), respectively, become

$$\sigma_e \quad = \quad r^{\lambda-1}\sqrt{\tilde{\sigma}_r^2 + \tilde{\sigma}_\theta^2 - \tilde{\sigma}_r\tilde{\sigma}_\theta + 3\tilde{\tau}_{r\theta}^2} \qquad \text{For plane stress} \qquad (7.16)$$

$$\sigma_e \quad = \quad r^{\lambda-1}\sqrt{\frac{3}{4}(\tilde{\sigma}_r - \tilde{\sigma}_\theta)^2 + 3\tilde{\tau}_{r\theta}^2} \qquad\qquad \text{For plane strain} \qquad (7.17)$$

One can observe that these stresses depend on r. The J-integral defined by eq. (6.53) along with $y = r\sin\theta$, eq. (4.6), $dy = r\cos\theta d\theta$ and $ds = rd\theta$ can be written as [2]

$$\frac{J}{r} = \int_{-\pi}^{\pi}\left[W(r,\theta)\cos\theta - \overrightarrow{T}(r,\theta)\frac{\partial\overrightarrow{\mu}(r,\theta)}{\partial x}\right]d\theta \qquad (7.18)$$

The remaining analytical procedure for deriving the trigonometric functions for the field equations is lengthy and complicated. Therefore, only relevant results are included as reported in the literature. Important papers on the subject are cited accordingly.

The essential mathematical approach for deriving the *HRR* field equations is a well-developed method, and yet, a sophisticated technique for assessing the plastic J-integral [1-2]. Essentially, a rigorous computational skill is required to explicitly characterize the crack behavior in the elastic-plastic regime, which is a complex nonlinearity manifested through the strain-hardening phenomenon at the crack tip region, where the J-controlled crack growth is characterized.

A ductile crack behavior, as opposed to brittle crack behavior, exhibits a significant crack tip blunting before the onset of crack growth (crack extension), complicating the applicability of the aforementioned mathematical technique [8]. Therefore, the resultant *HRR* field equations or *HRR* singularities near the crack tip for a stationary crack, as reported by Hutchinson [7] are

$$\sigma_{ij} = [\sigma_r, \sigma_\theta, \tau_{r\theta}] = \sigma_{ys} \left(\frac{J}{\alpha' \sigma_{ys} \epsilon_{ys} I_n r} \right)^{1/(n+1)} . \tilde{\sigma}_{ij} \qquad (7.19)$$

$$\epsilon_{ij} = [\epsilon_r, \epsilon_\theta, \gamma_{r\theta}] = \alpha' \epsilon_{ys} \left(\frac{J}{\alpha' \sigma_{ys} \epsilon_{ys} I_n r} \right)^{n/(n+1)} . \tilde{\epsilon}_{ij} \qquad (7.20)$$

$$\mu_{ij} = [\mu_r, \mu_\theta, \mu_z] = \frac{J}{I_n \sigma_{ys}} \left(\frac{\alpha' \sigma_{ys} \epsilon_{ys} I_n r}{J} \right)^{1/(n+1)} . \tilde{\mu}_{ij} \qquad (7.21)$$

where $\tilde{\sigma}_{ij} = [\tilde{\sigma}_r, \tilde{\sigma}_\theta, \tilde{\tau}_{r\theta}]$
$\tilde{\epsilon}_{ij} = [\tilde{\epsilon}_r, \tilde{\epsilon}_\theta, \tilde{\gamma}_{r\theta}]$
$\tilde{\mu}_{ij} = [\tilde{\mu}_r, \tilde{\mu}_\theta, \tilde{\mu}_z]$

Mathematically, for a power-law hardening material, field equations at the crack tip have singularities in the order shown below [2]

$$\begin{aligned} \sigma_{ij} &\propto r^{-1/(n+1)} \\ \epsilon_{ij} &\propto r^{-n/(n+1)} \\ \mu_{ij} &\propto r^{-1/(n+1)} \end{aligned} \qquad (7.22)$$

Figure 7.4 shows the numerical distribution of dimensionless stress $\tilde{\sigma}_{ij}(n, \theta) = [\tilde{\sigma}_r, \tilde{\sigma}_\theta, \tilde{\tau}_{r\theta}]$ and strain $\tilde{\epsilon}_{ij}(n, \theta) = [\tilde{\epsilon}_r, \tilde{\epsilon}_\theta, \tilde{\gamma}_{r\theta}]$ functions [1] and Table 7.1 gives the numerical results for the constant $I_n = f(n)$. Furthermore, the interpretation of the strain-hardening exponent (n) is based on the type of mechanical behavior of the solid material being tested and the size of the plastic zone in terms of the crack length, such as $r \leq 0.02a$ for the J-controlled condition [23]. For fully linear elasticity, the strain hardening is $n = 1$ and the field equations have a singularity in the order of $\sigma_{ij} \propto r^{-1/2}$, $\epsilon_{ij} \propto r^{-1/2}$ and $\mu_{ij} \propto r^{-1/2}$ which is exactly the order as determined in Chapter 4. Conversely, $n = \infty$ for fully nonlinear plasticity so that $\sigma_{ij} \geq \sigma_{ys}$.

Furthermore, dividing eq. (7.21) by (7,20) yields the plastic zone size as

$$r = \frac{\mu_{ij}}{\epsilon_{ij}} \frac{\tilde{\mu}_{ij}}{\tilde{\epsilon}_{ij}} \qquad (7.23)$$
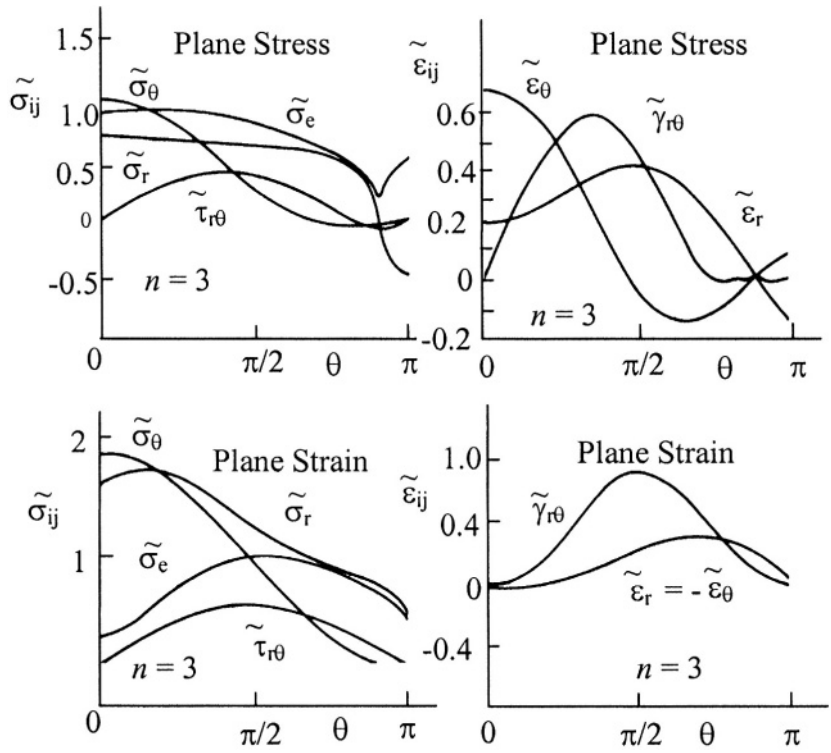
Figure 7.4 Distribution of stresses and strains in a hardening material [1]

Table 7.1 Values of I_n at $\sigma_e = 1$ [1]

n	1		3	5	9	13	∞
Plane Stress	2π		3.86	3.41	3.03	2.87	2.8
$I_n = 8.956 - 3.338n + 0.731n^2 - 0.068n^3$							
Plane Strain	$2\pi(1-v^2)$		5.51	5.01	4.60	4.40	4.3
$I_n = 5.188 + 0.611n - 0.240n^2 + 0.027n^3$							

Thus, eq. (7.19) becomes

$$J = \alpha' I_n \sigma_{ys} \mu_{ij} \left(\frac{\epsilon_{ys}}{\epsilon_{ij}}\right) \left(\frac{\sigma_{ys}}{\sigma_{ij}}\right)^{n+1} \cdot \frac{\tilde{\mu}_{ij}\tilde{\sigma}_{ij}}{\tilde{\epsilon}_{ij}} \tag{7.24}$$

It is clear from eq. (7.24) that the plastic J-integral can be regarded as a measure of the intensity of the field parameters at the crack tip and accounts for a large-scale yielding tied to the small-strain theory. Therefore, J characterizes the crack tip field parameters.

Most efforts to assess the J-dominance, modeled in Figure 7.1 as a circular region, have been focused on plane strain condition under mode I loading [7]. Both the stress intensity factor K_I and J_I are indirect fracture toughness that characterize local field parameters, but K_I is strictly used for a small-scale yielding and J_I for small-scale and large-scale yielding cases. The complete assessment of the fracture process includes fracture mechanisms because fracture toughness is a measure of fracture ductility of a material having a particular crack configuration within its geometrical shape. The concept of fracture ductility, as reported by Liu [25], depends on hydrostatic tensile stresses during deformation, during which the tearing modulus is a measure of the increase in fracture ductility.

The preceding rigorous and complex mathematical treatment in plastic fracture mechanics can now be simplified for practical purposes. Since most characterization of cracked materials is confined to a axial tension loading, it can be assumed that crack growth takes place along the crack plane. Thus, stress, strain, and displacement analyses are simplified to an extent.

For a loaded stationary crack in tension, the field equations become

$$\sigma = \sigma_{ys} \left(\frac{J}{\alpha' \sigma_{ys} \epsilon_{ys} I_n r} \right)^{1/(n+1)} \tag{7.25}$$

$$\epsilon = \alpha' \epsilon_{ys} \left(\frac{J}{\alpha' \sigma_{ys} \epsilon_{ys} I_n r} \right)^{n/(n+1)} \tag{7.26}$$

$$\mu = \frac{J}{I_n \sigma_{ys}} \left(\frac{\alpha' \sigma_{ys} \epsilon_{ys} I_n r}{J} \right)^{1/(n+1)} \tag{7.27}$$

and eqs. (7.24) and (7.23) become, respectively

$$J = \alpha' I_n \sigma_{ys} \mu_y \left(\frac{\epsilon_{ys}}{\epsilon_y} \right) \left(\frac{\sigma_{ys}}{\sigma_y} \right)^{n+1} \tag{7.28}$$

$$r = \frac{\mu}{\epsilon} \tag{7.29}$$

For instance, combining eqs. (7.25) and (7.26) for a axial tension loading yields the widely used Ramberg-Osgood relationship for plastic flow in axial tension loading. The resultant expression is compared with the Hollomon equation for the same purpose. Thus,

$$\epsilon = \alpha' \epsilon_{ys} \left(\frac{\sigma}{\sigma_{ys}} \right)^n \qquad \text{For } \sigma \geq \sigma_{ys} \quad \text{(Ramberg-Osgood)} \tag{7.30}$$

$$\epsilon = \left(\frac{\sigma}{k} \right)^m \qquad \text{For } \sigma \geq \sigma_{ys} \quad \text{(Hollomon)} \tag{7.31}$$

or

$$\sigma \; = \; \sigma_{ys} \left(\frac{\epsilon}{\alpha' \epsilon_{ys}} \right)^{1/n} \qquad \text{For } \sigma \geq \sigma_{ys} \; \text{(Ramberg-Osgood)} \qquad (7.32)$$

$$\sigma \; = \; k \epsilon^{1/m} \qquad \qquad \text{For } \sigma \geq \sigma_{ys} \; \text{(Hollomon)} \qquad (7.33)$$

Denote that both exponents in eqs. (7.30) and (7.31) or (7.32) and (7.33) have the same meaning, but differ in magnitude since $1 < n < \infty$ and $0 < m < 1$. Typically, $3 < n < 6$ for high hardening and $n \leq 20$ for low hardening. [7]. The k term in eq. (7.30) is called the strength coefficient in the literature. Both Ramberg-Osgood and Hollomon equations are used to predict the plastic uniaxial stress-strain relationship schematically depicted in Figure 7.3. These power-law relations indicate that the contributions to the strains that depend linearly on the stress are simply negligible.

For a axial tension loading, the equivalent stress, eq. (7.5) or (7.6), is simply defined by

$$\sigma_e = \psi \sigma \qquad (7.34)$$

where $\psi = 1$ for plane stress
$\qquad \psi = \sqrt{3}/2$ for plane strain
$\qquad \alpha' = $ Constant

From eq. (7.25), the plastic zone size becomes

$$r = \frac{J}{\alpha' \sigma_{ys} \epsilon_{ys} I_n} \left(\frac{\sigma_{ys}}{\sigma} \right)^{n+1} \qquad \text{For } \sigma \geq \sigma_{ys} \qquad (7.35)$$

Example 7.1 *Calculate the maximum plastic zone size for compact tension [CT] specimen made of ASTM A533B steel at a strain of 0.1. Use the data reported by Kumar [8]. The steel obeys the Ramberg-Osgood stress-strain relation.*

$$\sigma_{ys} = 414 \; MPa \qquad n = 9.71 \qquad a_o = 117 \; mm$$
$$E = 207 \; GPa \qquad \alpha' = 1.12 \qquad a_c = 121 \; mm$$
$$T = 93^{\circ}C \qquad w = 203 \; mm \qquad \mu = 4.7 \; mm$$
$$\sigma =? \qquad B = 0.5w \qquad J_{IC} = 1.00 \; m.MPa$$

Solution:

The yield strain is calculated using Hooke's law. Thus,

$$\epsilon_{ys} = \frac{\sigma_{ys}}{E} = \frac{414 MPa}{207,000 \; MPa} = 0.002$$

From eq. (7.32), the stress-strain curve is plotted below to verify that the given 0.1 strain corresponds to a an applied tress greater than the yield strength.

$$\sigma = \sigma_{ys} \left(\frac{\epsilon}{\alpha' \epsilon_{ys}} \right)^{1/n} = 776.05 \epsilon^{0.103}$$
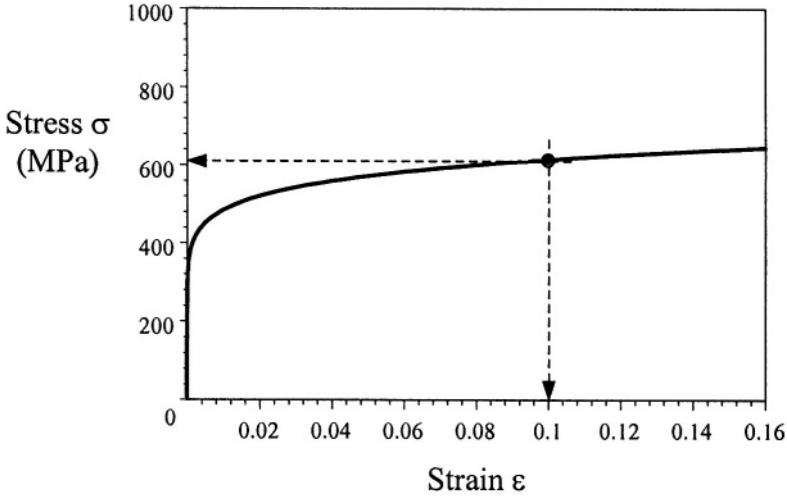
Figure E7.1

If $\epsilon = 0.1$, then $\sigma = 612.21\ MPa > \sigma_{ys}$. Thus, the requirement that $\sigma > \sigma_{ys}$ has been met. Using eq. (7.35) yields

$$r = \frac{J}{\alpha' \sigma_{ys} \epsilon_{ys} I_n} \left(\frac{\sigma_{ys}}{\sigma} \right)^{n+1} \tag{7.35}$$

$$r = \frac{(1.00\ MPa.m)}{(1.12)(414\ MPa)(0.002)(4.64)} \left(\frac{414\ MPa}{612.21\ MPa} \right)^{10.71}$$

$$r = 3.52\ mm$$

7.4 SEMI-EMPIRICAL APPROACH

Characterization of the J-integral, the crack opening displacement $(\delta = COD)$, and the load-line displacement (μ) have numerically been established in an engineering approach, as an approximation scheme, for elastic [13-15] and fully

plastic [4-5,16,18] fracture analyses. Explicitly, the elastic analysis has been carried out using the stress intensity factor (K_I), which is related to the J-integral for mode I. Conversely, the fully plastic analysis is strictly based on the Ramberg-Osgood and the Hollomon stress-strain power laws. The elastic-plastic analysis can be defined in a general form as the sum of the elastic and plastic parts

$$J = J_e(a_e) + J_p(a, n) \tag{7.36}$$
$$\delta = \delta_e(a_e) + \delta_p(a, n) \tag{7.37}$$
$$\mu = \mu_e(a_e) + \mu_p(a, n) \tag{7.38}$$

where a_e = Effective crack length
a = original crack length

It can be anticipated that for a fully plastic fracture, $J \simeq J_p$ since plasticity governs the fracture process for a slow moving stable crack, as oppose to an elastic fracture, in which crack motion can reach velocities nearly the speed of sound. Therefore, the plastic J-integral (J_p) is higher than the elastic J-integral (J_e) component at a sufficiently developed plasticity ahead of the crack tip. This is shown in Figure 7.5 for elastic-plastic estimation procedures [8].
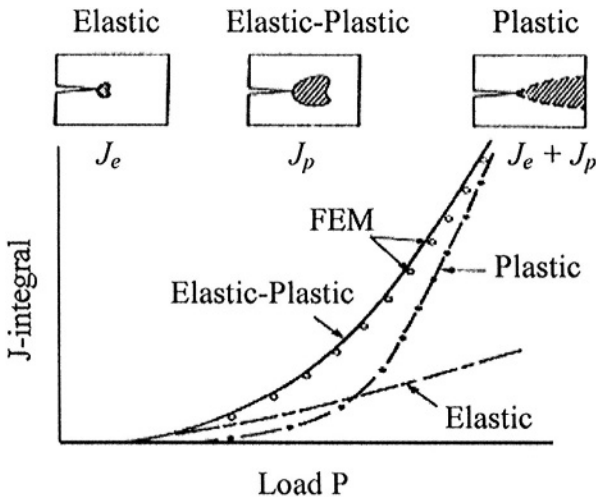
Figure 7.5 Schematic elastic-plastic fracture behavior [8]

7.4.1   NEAR-FIELD J-INTEGRAL

Consider the single-edge notched *(SEN)* specimen shown in Figure 7.6 containing Γ_1 and Γ_2 as the near-field and far-field contours for predicting the J-integral. The specimen edges constitute the contour Γ_2. Use of half of the entire contour due to symmetry is a practical assumption.

Kang and Kobayashi [5] developed a J-estimation procedure for two dimensional states of stress and strains. Consider the near-field J-Integral and a strain-hardening material that obeys the Ramberg-Osgood relation defined by eq. (7.30) in order to solve the integral for the plastic strain energy density, which is needed in the J-integral equation. Thus,
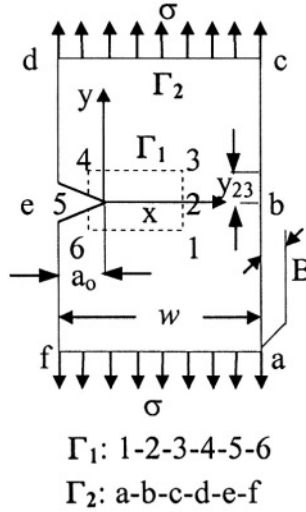
Γ_1: 1-2-3-4-5-6
Γ_2: a-b-c-d-e-f

**Figure 7.6 SEN specimen having two contours: near-field Γ_1:
1-2-3-4-5-6 and far-field Γ_2: a-b-c-d-e-f**

$$W_p = \int \sigma d\epsilon = \int \sigma_{ys} \left(\frac{\epsilon}{\alpha'\epsilon_{ys}}\right)^{1/n} d\epsilon \qquad (7.39)$$

$$W_p = \left(\frac{n}{n+1}\right) \frac{\sigma_{ys}}{(\alpha'\epsilon_{ys})^{1/n}} \epsilon^{(n+1)/n} \qquad (7.40)$$

Substituting eq. (7.30) back into (7.40) along with Hooke's law yields the most practical expression for the plastic strain energy density

$$W_p = \frac{\alpha'\sigma_{ys}^2}{E} \left(\frac{n}{n+1}\right) \left(\frac{\sigma}{\sigma_{ys}}\right)^{n+1} \qquad (7.41)$$

Let's evaluate the plastic J-integral on each segment of the upper half of contour Γ_1. Hence,

$$J_p = \int_{23}\left(W\,dy - T_i\frac{\partial\mu}{\partial x}dx\right) + \int_{45}\left(W\,dy - T_i\frac{\partial\mu}{\partial x}dx\right) \tag{7.42}$$
$$+ \int_{34}\left(W\,dy - T_i\frac{\partial\mu}{\partial x}dx\right) + \int_{52}\left(W\,dy - T_i\frac{\partial\mu}{\partial x}dx\right)$$

where $T_{23} = T_{45} = 0$, $ds = dy$ and $y_{23} = y_{45}$
$dy_{34} = dy_{52} = 0$ and $d\mu_{34} = d\mu_{52} = 0$

Thus,

$$J_p = \int_{23}W_p\,dy + \int_{45}W_p\,dy = 2\int_0^{y_{23}}W_p\,dy = 2W_p y_{23} \tag{7.43}$$

Substituting eq. (7.41) into (7.43) yields

$$J_p = \frac{2\alpha'\sigma_{ys}^2}{E}\left(\frac{n}{n+1}\right)\left(\frac{\sigma}{\sigma_{ys}}\right)^{n+1}y_{23} \tag{7.44}$$

For pure tension loading, the elastic J-integral is defined by eq. (6.61) as

$$J_I = \frac{K_I^2}{E'} = \frac{\pi a \sigma^2}{E'} \tag{7.45}$$

Finally, the total J-integral becomes

$$J = \frac{\pi a \sigma^2}{E'} + \frac{2\alpha'\sigma_{ys}^2}{E}\left(\frac{n}{n+1}\right)\left(\frac{\sigma}{\sigma_{ys}}\right)^{n+1}y_{23} \tag{7.46}$$

Similarly, the contour Γ_2 for the far-field condition yields

$$J = \frac{\pi a \sigma^2}{E'} + \frac{2\alpha'\sigma_{ys}^2}{E}\left(\frac{n}{n+1}\right)\left(\frac{\sigma}{\sigma_{ys}}\right)^{n+1}y_{bc} \tag{7.47}$$

The only difference between eqs. (7.46) and (7.47) is the height of the upper vertical segments; that is, $y_{bc} > y_{23}$. Conclusively, the elastic and plastic J-integrals are generalized as $J_e = f(a,\sigma)$ and $J_p = f(n,\sigma)$. An example can make this procedure sufficiently clear how to determine the J-integral.

Example 7.2 a) *Calculate the total J-integral (J_I) for a* 2024 *Al-alloy plate under plane stress conditions (Figure 7.6). b) Determine if the elastic J-integral contributes significantly to the total value. c) What does the plastic strain energy density W measure? d) Plot the plastic stress-strain and $J = (\sigma)$. Use the following data to carry out all calculations: $a = 1.40\ mm$, $w = 19\ mm$, $B = 0.8\ mm$, $\sigma_{ys} = 64\ MPa$, $E = 72,300\ MPa$, $\alpha' = 0.35$, $n = 5$, $P = 1.01\ kN$ (load) and $y_{23} = w/3$.*

Solution:

a) *The following calculations are self-contained. Thus,*

$$\epsilon_{ys} = \frac{\sigma_{ys}}{E} = \frac{64}{72,300} = 8.852 \times 10^{-4} \qquad A = wB = 15.20x10^{-6} \ m^2$$

$$\sigma = \frac{P}{A} = \frac{1.01x10^{-3} \ MN}{15.20x10^{-6} \ m^2} = 66.45 \ MPa > \sigma_{ys}$$

$$y_{23} = \frac{w}{3} = \frac{19 \ mm}{3} = 6.33 \ mm$$

From eq.(7.41),

$$W_p = \frac{\alpha'\sigma_{ys}^2}{E} \left(\frac{n}{n+1}\right) \left(\frac{\sigma}{\sigma_{ys}}\right)^{n+1} \tag{7.41}$$

$$W_p = \frac{(0.35)(64 \ MPa)^2}{72,300 \ MPa} \left(\frac{5}{6}\right) \left(\frac{66.45}{64}\right)^6 = 2.070 \ 1 \times 10^{-2} \ MPa$$

$$W_p = 20.70 \ kPa = 20.70 \ kJ/m^3$$

From eq.(7.44),

$$J_p = 2Wy_{23} = (2)(20.70 \ kJ/m^3) \left(\frac{19}{3}x10^{-3} \ m\right)$$

$$J_p = 262.20 \ N/m$$

From eq. (7.45),

$$J_e = \frac{K_I^2}{E} = \frac{\pi a \sigma^2}{E} = \frac{\pi (1.40x10^{-3} \ m)(66.45 \ MPa)^2}{72,300 \ MPa} \tag{7.45}$$

$$J_e = 2.6861 \times 10^{-4} \ MPa.m = 268.61 \ N/m$$

The total J-integral is

$$J_I = J_e + J_p = 268.61 \ N/m + 262.20 \ N/m = 530.81 \ N/m$$

b) *Therefore, the contribution of the elastic J-integral very significant in the current problem because $J_p = 0.9761J_e$ which means that J_e contributes $(100)(530.81 - 268.61)/268.1 \simeq 97.80\%$ to J_I.*

c) *The meaning of the W_p is clearly stated in Chapter 1. It measures the plastic fracture toughness as the area under the stress-strain curve.*

d) *The required stress-strain curve can be determined using eq. (7.30). Thus,*

$$\sigma = \sigma_{ys} \left(\frac{\epsilon}{\alpha'\epsilon_{ys}}\right)^{1/n} = (322.08 \ MPa) \sqrt[5]{\epsilon}$$
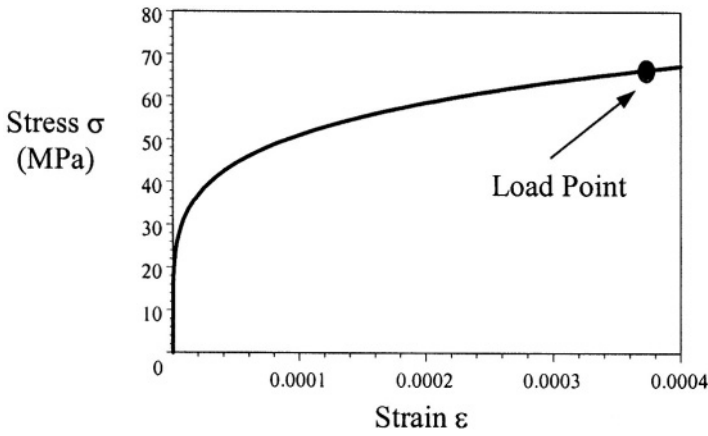
The J-integral plot along with the load point is based on the following equation:

$$J_I = \frac{\pi a \sigma^2}{E} + \frac{2\alpha' \sigma_{ys}^2}{E}\left(\frac{n}{n+1}\right)\left(\frac{\sigma}{\sigma_{ys}}\right)^{n+1} y_{23}$$

$$J_I = 6.083\,3 \times 10^{-2}\sigma^2 + 3.045\,7 \times 10^{-9}\sigma^6 \quad \text{in } N/m$$

The trend of the $J = f(\sigma)$ in this example resembles the trend shown in Figure 7.5.
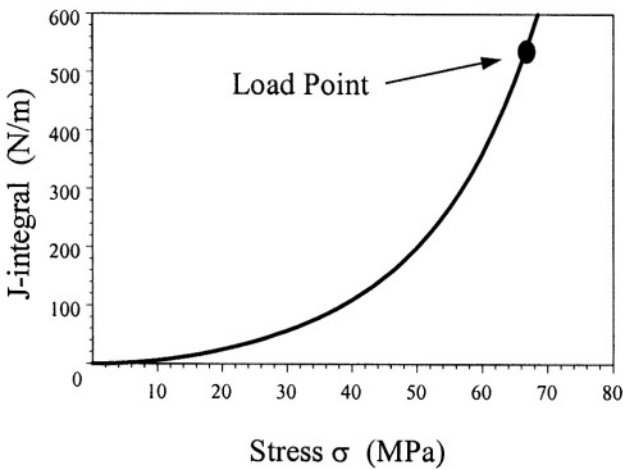
7.4.2   FAR-FIELD J-INTEGRAL

Consider the single-edge notched (SEN) specimen with Γ_2 contour as large as the specimen shown in Figure 7.6 for characterizing the far-field J-integral using only half of the entire contour due to symmetry. The present stress field requires that $\sigma_y = \sigma$ and $\sigma_x = \tau_{xy} = 0$ for the assumed contour a-b–c-d-e-f with segments ab-bc-cd-de-ef and fa. Thus, the far-field J-integral evaluation can be treated as a reasonable approximation for the near-field. For an axial tension loading, Kang and Kobayashi [5] using Moiré interferometry evaluated the J-integral as the sum of the vertical and horizontal parts of half the contour due to symmetry. Thus, the J-integral for the traction free vertical edges of the segments bc and de becomes

$$J_v = \int_{bc} W\,dy + \int_{de} W\,dy \tag{7.48}$$

$$J_v \simeq \sum (W_i \Delta y_i)_{bc} + \sum (W_i \Delta y_i)_{de}$$

and that for the horizontal part along with $\sigma_x = \tau_{xy} = 0$ and $\mu_x = 0$ on the crack line is

$$J_h = \int_{cd} T_y \frac{\partial \mu}{\partial x}\,dx = \int_{cd} \sigma_y \frac{\partial \mu}{\partial x}\,dx \tag{7.49}$$

$$J_h \simeq \sum \left[\left(\sigma_y \frac{\Delta \mu_y}{\Delta x}_i \right) \Delta x_i \right]_{cd}$$

The total J-integral due to symmetry becomes

$$J_I = 2\,(J_v + J_h) \tag{7.50}$$

7.5   ENGINEERING APPROACH

Kumar et al. [8] developed another approximation scheme for characterizing simple specimen configurations. Assume that a material obeys the Ramberg-Osgood power law, eq. (7.30) and that the plastic field is controlled by the J-integral for limited crack growth. It is also assumed that unloading does not occur behind the crack tip during the irreversible plastic deformation [11] and that the onset of unstable crack growth (crack propagation) occurs at the maximum load carrying capability of the component. The measurement of the J-integral is carried out by determining the displacement from the deformation properties of the Ramberg-Osgood material [21]

The simplified methodology for predicting fracture of structural components is based on eqs. (7.36) through (7.38) along with modified (7.30) and $\sigma_{ys} = \sigma_o$

and $\epsilon_{ys} = \epsilon_o$. The general field equations for elastic-plastic fracture analysis are defined as [8]

$$
\begin{aligned}
J &= \frac{P^2}{E'} f_1 + \alpha' \sigma_o \epsilon_o \lambda_1 h_1 \left(\frac{P}{P_o} \right)^{n+1} \\
\delta &= \frac{P}{E'} f_2 + \alpha' a \epsilon_o h_2 \left(\frac{P}{P_o} \right)^n \\
\mu &= \frac{P}{E'} f_3 + \alpha' a \epsilon_o h_3 \left(\frac{P}{P_o} \right)^n
\end{aligned}
\tag{7.51}
$$

where P = Load per unit thickness (MN/m)
$\quad\quad P_o$ = Limit load per unit thickness (MN/m)
$\quad\quad h_1, h_2, h_3$ = Constant tabulated in Ref. [8]
$\quad\quad f_1, f_2, f_3$ = Constant tabulated in Ref. [13]

The constants λ_1 and P_o are defined in Table 7.2, and a_e is Irwin's effective crack length defined by

$$
a_e = a_o + \overline{w} r
\tag{7.52}
$$

with

$$
\overline{w} = \frac{1}{1 + (P/P_o)^2}
\tag{7.53}
$$

$$
r = \left(\frac{1}{\pi\beta} \right) \left(\frac{n-1}{n+1} \right) \left(\frac{K_I(a_e)}{\sigma_o} \right)^2
\tag{7.54}
$$

where β = 2 for plane stress
$\quad\quad \beta$ = 6 for plane strain

The above field equations are strongly dependent on increasing load raised to the power n. Therefore, the plastic part of these equations are dominant in strain hardenable and incompressible materials. Despite that these equations represent approximations, they can provide satisfactorily accurate results of the J-integral, strains and displacements in appropriate engineering applications.

Table 7.2 Crack Configurations and related geometric correction factors for J_p, δ_p and μ_p.
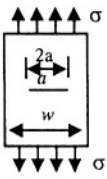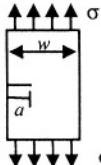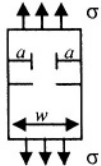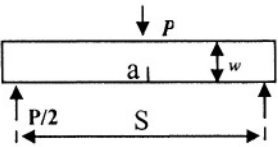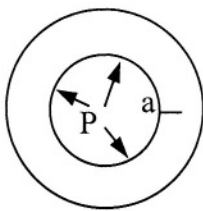
1) Through-Thickness Center Crack (CCT)

$$\sigma = P/2w$$
$$\lambda_1 = a(1-a/w) \quad and \quad \lambda_2 = a$$
$$P_o = 4(w-a)\sigma_o/\sqrt{3} \quad For\ plane\ strain$$
$$P_o = 2(w-a)\sigma_o \quad\quad For\ plane\ stress$$

2) Single-edge Crack (SET)

$$\sigma = P/w$$
$$\lambda_1 = (w-a)(a/w) \quad and \quad \lambda_2 = a$$
$$P_o = 1.455x(w-a)\sigma_o \quad For\ plane\ strain$$
$$P_o = 1.072x(w-a)\sigma_o \quad For\ plane\ stress$$
$$x = \left[1+(a/(w-a))^2\right]^{1/2} - a/(w-a)$$

3) Double-edge Crack (DET)

$$\sigma = P/w \qquad \lambda_1 = \lambda_2 = w-a$$
$$P_o = w[0.72+1.82(1-a/w)]\sigma_o \ (plane\ strain)$$
$$P_o = (4w/\sqrt{3})(1-a/w)\sigma_o \ (plane\ stress)$$

4) Three-Point Bending (SEB)

$$\sigma = P/w; \quad \lambda_1 = w(1-a/w); \quad \lambda_2 = a$$
$$P_o = 0.728\sigma_o(w-a/w)^2/S \quad (P.\ strain)$$
$$P_o = 0.728\sigma_o(w-a/w)^2/S \quad (P.\ stress)$$

5) Internally pressurized cylinder (IPC)

$$\sigma = \frac{PR}{B} \quad where \quad R = Internal\ radius$$
$$\lambda_1 = (B-a)(B/w) \quad and \quad \lambda_2 = a$$
$$P_o = \frac{2(B-a)\sigma_o}{\sqrt{3}(R_i+a)}$$

Figure 7.7 shows a crack driving force diagram for an axially cracked and internally pressurized cylinder made of ASTM A533B steel [22]. This diagram represents a complete history of deformation and crack growth. Thus, the onset of crack growth can be predicted when $J = J_R$ at the intercept of J_R-P_{fixed}. This intercept is the instability point where

$$
\begin{aligned}
J_{IC} &\simeq 10 \, in.kips/in^2 \simeq 21kJ/m^2 \\
P &\simeq 5.5 \, kips = 24.47 \, kN \\
a_c &\simeq 2.6 \, in = 6.60 \, cm \\
a_o &\simeq 2.25 \, in = 5.72 \, cm \\
\Delta a &= 0.88 \, cm
\end{aligned}
$$
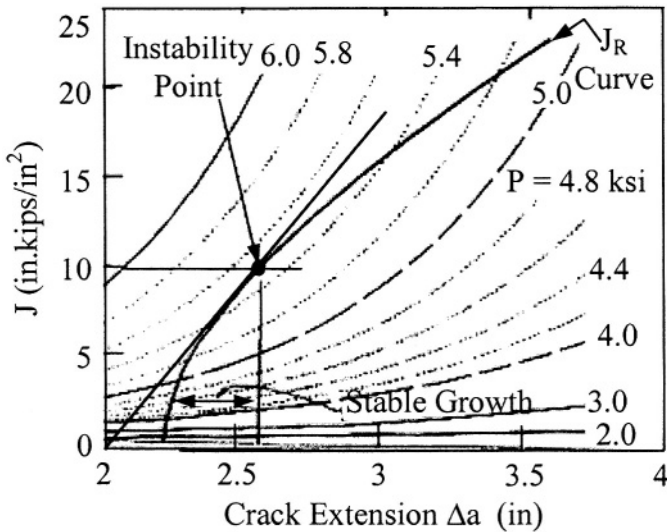
Figure 7.7 Experimental J-integral diagram for an axially cracked internally pressurized cylinder masde of ASTM A533B steel [22]

Furthermore, careful attention to the data in Figure 7.7 indicates stable crack growth is $\Delta a = 0.88 \, mm$ for the monotonic load-controlled system. This amount of crack growth is considered very small prior to crack propagation. If the load is $P > P_c$, then the crack becomes unstable and grows very rapidly.

Additionally, He and Hutchinson [23] derived principles associated with upper and lower bounds on the J-integral for a finite crack in an infinite plane (central crack case) and edge-crack in a semi-infinite plane. These principles are based on the complementary potential energy and potential energy theories. The resultant J-integral equation [23] is also given in Refs. [21,24]. Thus,

$$J_p = \frac{3\pi a \epsilon_e \sigma_e \sqrt{n}}{4} \left(\frac{\sigma}{\sigma_e} \right)^2 \tag{7.55}$$

Let eq. (7.30) be an equivalent expression so that

$$\epsilon_e = \alpha' \epsilon_o \left(\frac{\sigma_e}{\sigma_o} \right)^n \tag{7.56}$$

Substituting eqs. (7.34) and (7.56) into (7.55) yields the upper bound J-integral for plane conditions

$$J_p = \frac{3\pi a \sqrt{n}}{4\psi^{1-n}} \alpha' \epsilon_o \sigma \left(\frac{\sigma}{\sigma_o} \right)^n \qquad \text{(Upper bound)} \tag{7.57}$$

He and Hutchinson [23,24] also derived an upper bound form of the J-integral as defined below

$$J_p = \pi a h \sqrt{n} \epsilon_e \sigma_e \tag{7.58}$$

where $h = 1$ for a central crack
$h = 1.26$ for an edge crack

Similarly, substitute eqs. (7.34) and (7.56) into (7.58) to get

$$J_p = \pi a h \psi \alpha' \sqrt{n} \epsilon_o \sigma \left(\frac{\psi \sigma}{\sigma_o} \right)^n \qquad \text{(Upper bound)} \tag{7.59}$$

It should be mention that both eqs. (7.57) and (7.59) should give similar results. An example in the next section will prove this statement.

7.5.1 THE CONSTANT h_1

The constant h_1 in eq. (7.51) can be derived for the specimen configurations illustrated in Table 7.2. This can be done very easily by equating eqs. (7.51) and (7.57) and using the definitions of λ_1 and P_o. The resultant expression are

$$h_1 = \frac{3\pi a \sqrt{n}}{4\psi \lambda_1} \left(\frac{\sigma}{P} \right)^{n+1} \left(\frac{\sigma_o}{P_o} \right)^{n+1} \tag{7.60}$$

For the central cracked plate given in Table 7.2,

$$h_1 = \frac{3\pi 2^n \sqrt{n}}{4\psi \left(\sqrt{3} \right)^{n+1}} \left(1 - \frac{a}{w} \right)^n \qquad \text{For a CCT Specimen} \tag{7.61}$$

where ψ is defined in eq. (7.34).

Example 7.3 *The application of the above procedure can be made clear by analyzing the example given below. a) Calculate the total J-integral* $(J = Je + Jp)$ *for a center-crack plate made out of* 2024 *Al-alloy under plane conditions. Assume that the material obeys the Ramberg-Osgood relation. Use the following data:* $a = 1.40\ mm$, $w = 19\ mm$, $B = 0.8\ mm$, $\sigma_o = 64\ MPa$, $E = 72,300\ MPa$, $\alpha' = 0.35$, $n = 5$, $\nu = 0.3$ *and* $\sigma = 80\ MPa$. *b) Plot* J_I *vs.* σ *for plane strain conditions. Explain.*

Solution:

a) The solution requires the following parameters

$$\frac{a}{w} = 0.0737 \qquad \left(1 - \frac{a}{w}\right) = 0.9263, \qquad \epsilon_o = \frac{\sigma_o}{E} = 0.0009$$

From eq. (3.29) and Table 3.1, the applied stress intensity factor is

$$
\begin{aligned}
K_I &= \alpha\sigma\sqrt{\pi a} &\text{(3.29)}\\
\alpha &= \left[1 + 0.5\left(\frac{a}{w}\right)^2 + 20.46\left(\frac{a}{w}\right)^4 + 81.72\left(\frac{a}{w}\right)^6\right]^{1/2} \simeq 1\\
K_I &= (80\ MPa)\sqrt{\pi\left(1.40x10^{-3}\ m\right)} = 3.31\ MPa\sqrt{m}
\end{aligned}
$$

and from eq. (6.61) for pure tension loading, the elastic J-integral becomes

$$J_e = \frac{K_I^2}{E'} = \frac{\left(1 - \nu^2\right)K_I^2}{E} = 41.66x10^{-6}\ MPa.m = 0.042\ kJ/m^2 \qquad \text{(6.61)}$$

Let's determine J_p *using eq. (7.51) and Table 7.2*

$$J_p = \alpha'\sigma_o\epsilon_o\lambda_1 h_1\left(\frac{P}{P_o}\right)^{n+1} \qquad \text{(7.51)}$$

The constant h_1 *along with* $\psi = \sqrt{3}/2$ *and* $n = 5$ *is*

$$
\begin{aligned}
h_1 &= \frac{3\pi 2^n\sqrt{n}}{4\psi\left(\sqrt{3}\right)^{n+1}}\left(1 - \frac{a}{w}\right)^n &\text{(7.61)}\\
h_1 &= \frac{3\pi\left(2\right)^5\sqrt{5}}{2\left(\sqrt{3}\right)^{5+2}}\left(1 - 0.0737\right)^5 = 4.92
\end{aligned}
$$

The calculated value of h_1 *is close to the value tabulated by Kumar and Shih* [8].

The other parameters are

$$\lambda_1 = a\left(1 - \frac{a}{w}\right) = (1.40x10^{-3}\ m)(1 - 0.0737) = 1.30 \times 10^{-3}\ m$$

$$P = 2w\sigma = 2\left(19x10^{-3}\ m\right)(80\ MPa) = 3.04\ MPa.m$$

$$P_o = \frac{4(w - a)\sigma_o}{\sqrt{3}} = \frac{4\left(19x10^{-3}\ m - 1.4x10^{-3}\ m\right)(64\ MPa)}{\sqrt{3}}$$

$$P_o = 2.601\,3\ MPa.m$$

Thus,

$$J_p = (0.35)(64\ MPa)(0.0009)\left(1.30x10^{-3}\ m\right)(4.92)\left(\frac{3.04\ MPa.m}{2.601\,3\ MPa.m}\right)^6$$

$$J_p = 3.30 \times 10^{-4}\ MPa.m = 0.33\ kJ/m^2$$

The plastic J-integral is now calculated using eq. (7.57) for comparison purposes. Thus,

$$J_p = \frac{3\pi a\sqrt{n}}{4\psi^{1-n}}\alpha'\epsilon_o\sigma\left(\frac{\sigma}{\sigma_o}\right)^n \quad \text{(Upper bound)} \tag{7.57}$$

$$J_p = \frac{3\pi\left(1.40x10^{-3}\ m\right)\sqrt{5}}{4\left(\sqrt{3}/2\right)^{-4}}(0.35)(0.0009)(80\ MPa)\left(\frac{80\ MPa}{64\ MPa}\right)^5$$

$$J_p = 3.20x10^{-4}\ MPa.m = 0.32\ kJ/m^2$$

$$J_p = \pi ah\psi\alpha'\sqrt{n}\epsilon_o\sigma\left(\frac{\psi\sigma}{\sigma_o}\right)^n \quad \text{(Lower bound)} \tag{7.59}$$

$$J_p = \pi\left(1.4x10^{-3}\ m\right)(1)\left(\frac{\sqrt{3}}{2}\right)(0.35)\sqrt{5}(0.0009)(80\ MPa)\left(\frac{\sqrt{3}x80\ MPa}{2x64\ MPa}\right)^5$$

$$J_p = 3.20x10^{-4}MPa.m = 0.32\ kJ/m^2$$

Denote that eqs. (7.51), (7.57) and (7.59) yield similar results. The former gives approximately 3% higher value than the later equation.

The total j-integral value is basically due to the contribution of the plastic part because $J_p = 0.32\ kJ/m^2 > J_e = 0.042\ kJ/m^2$. *In other words, the elastic contribution is slightly less than 12%. Nevertheless, the total value is*

$$J_I = J_e + J_p = 0.042\ kJ/m^2 + 0.32\ kJ/m^2 = 0.362\ kJ/m^2$$

b) The second part of the problem requires the determination of a function $J_I = f(\sigma)$ *with the stress* σ *in MPa. From part a),*

$$J_I = 5.5358 \times 10^{-5}\sigma^2 + 1.2172 \times 10^{-12}\sigma^6 \quad \text{in } kJ/m^2$$

The required plot for plane strain condition is shown below
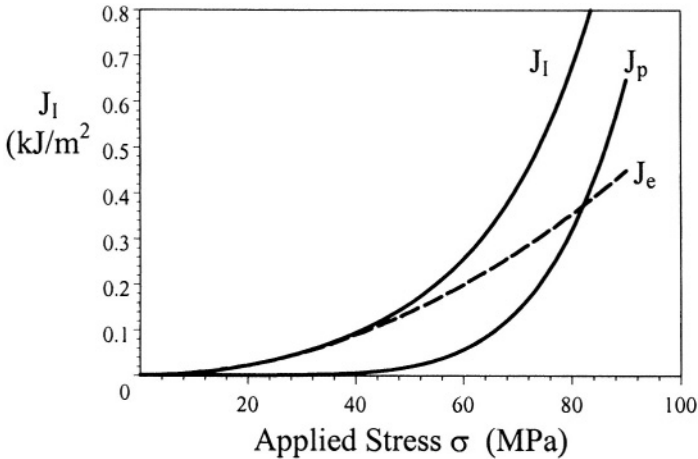
This plot indicates that the elastic contribution is significant up to approximately 44 MPa since both J_I and J_e coincide. Beyond this point the plastic contribution becomes apparent.

7.6   PROBLEMS

7.1 a) the J-integral (J), b) the crack opening displacement (δ), c) load line displacement (μ) and dJ/da for a ductile AISI 304 stainless steel plate-containing a central crack of 114 mm. What does dJ/da mean? Assume plane strain conditions and that the stainless steel obeys the Ramberg-Osgood relation at room temperature. Explain the results. Given data: $\sigma_{ys} = 207\ MPa$, $E = 206,850\ MPa$, $v = 0.3$, $\alpha' = 1.69$, $n = 5.42$, $a/w = 1/4$, $J_{IC} = 6.48\ MJ/m^2$, $\sigma = 276\ MPa$, $h_1 = 3.29$, $h_2 = 2.70$ and $h_3 = 1.75$. [Solution: a) $J_I = 269.22\ MJ/m^2$, $\delta = 115.53\ mm$, $\mu = 74.88\ mm$ and $dJ/da = -7,005\ MJ/m^3$].
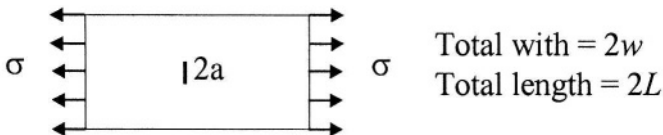
7.2 A single-edge cracked plate made out of ASTM A533B steel is loaded in tension at 93°C. Plot the given uniaxial stress-strain data and perform a regression analysis based on the Ramberg-Osgood equation. Determine the elastic-plastic J-integral. Will the crack grow in a stable manner? Why? or Why

not? Assume plane strain conditions and necessary assumptions. Let $v = 0.30$, $E = 207\ GPa$, $L = 3w$, $w = 400\ mm$, $J_{IC} = 1.20\ m.MPa$, and $B = 150\ mm$.

$\epsilon\ (x10^{-3})$	0	1.00	2.24	2.30	5.00	7.50	10	20	40
$\sigma\ (MPa)$	0	381	414	415	450	469	483	519	557

7.3 Repeat problem 7.2 using the Hollomon equation, $\sigma = K\epsilon^m$, for the plastic region. Curve fitting should be performed using this equation for obtaining K and m. Assume plane strain conditions and make the necessary assumptions. Compare the results from Problem 7.2. What can you conclude from these results? [Solution: a) $J = 15.70\ m.MPa$].

7.4 Calculate a) the load-line displacement (μ) and b) the crack opening displacement (δ) which corresponds to a point J_R-μ_{fixed} for $J_{IC} = 1.20\ m.MPa$. Use the following uniaxial data: $E = 206,850\ MPa$, $n = 0.3$, $h_1 = 0.523$, $h_2 = 1.93$, $h_3 = 3.42$, $B = 150\ mm$, $w = 400\ mm$, $L = 1.20\ m$.

7.5 Determine the strain hardening exponent for a steel with $\sigma_{ys} = 400\ MPa$, $E = 207\ GPa$. Assume that it obeys the Hollomon equation, $\sigma = K\epsilon^m$, with $K = 700\ MPa$. Consider the maximum plastic stress in your calculations. [Solution: $n = 0.0895$].

7.6 a) Derive an expression for the J-integral ratio, $J_p/J_e = f(\sigma/\sigma_o)$, using Rice model. b) Plot the resultant expression for a remote stress ratio range $0 \leq \sigma/\sigma_0 \leq 1$. Explain the resultant plot.

7.7 REFERENCES

[1]   J.W. Hutchinson, "Singular Behavior at the End of a Tensile Crack in a Hardening Material," Journal Mech. Phys. Solids, 16(1968) 13-31

[2]   J.R. Rice and G.F. Rosengren, "Plane Strain Deformation near a Crack Tip in a Power-Law Hardening Material," Journal Mech. Phys. Sol., 16 (1968) 1

[3]   K. Hellan, "Introduction to Fracture Mechanics," McGraw-Hill Book company, New York, (1984)

[4]   J.R. Rice, "A path Independent Integral and the Approximate Analysis of Strain Concentrations by Notches and Cracks," J. Applied Mech. 35 (1968) 379-386

[5]   B.S.J. Kang and A.S. Kobayashi, "J-Estimation Procedure based on Moiré Interferometry Data," Report UWA/DME/TR-87/58, Office of Naval Research (ONR), (August 1987)

[6]   J.W. Dally and W.F. Riley, "Experimental Stress Analysis," third edition, McGraw-Hill, Inc. New York, (1991)

[7]   J.W. Hutchinson, "Fundamentals of the Phenomenological Theory of Nonlinear Fracture Mechanics," J. Appl. Mech. 50(1983) 1042-1051

[8] V. Kumar, M.D. German, and C.F. Shih, "An Engineering Approach for Elastic-Plastic Fracture Analysis," General Electric Company, Report Project 1237-1, (July 1981)

[9]   J.A. Begley and J.D. Landes, American Society for Testing Materials (ASTM), STP 514, (1972)

[10] J.R. Rice, "Mathematical Analysis in the Mechanics of Fracture," in Fracture edited by H. Liebowitz, Vol. II, Academic Press, New York, (1968) 191.

[11] J.W. Hutchinson and P.C. Paris, American Society for Testing Materials (ASTM), STP 668, (1979) 37.

[12] C.F. Shih et al., ASTM STP 668, (1979) 65

[13] H. Tada et al., "The Stress Analysis of Cracks Handbook," Del Research Corporation, Hellertown, PA, (1973)

[14] D.P. Rooke and J.C. Cartwright, "Compendium of Stress Intensity Factors," Her Majesty's Stationary Office, London, UK, (1976)

[15] G.C. Sih, "Handbook of Stress Intensity Factors," Inst. of Fracture and Solid Mechanics, Lehigh University, (1973)

[16] V. Kumar and C.F. Shih, "Fully Plastic Crack Solutions, Estimates Scheme and Stability Analyses for Compact Specimens," American Society for Testing Materials (ASTM), STP 700, (1980) 406

[17] P.S. Timoshenko and J.N. Goodier, "Theory of Elasticity," McGraw-Hill Co., third edition, (1970)

[18] J.A. Begley et al., ASTM STP 560, (1974) 155.

[19] C.F. Shih, "Tables of Hutchinson-Rice-Rosengren Singular Field Quantities," Division of Engineering, Brown University, Province, RI, USA, (June 1983)

[20] M.S. Dadhah and A.S. Kobayashi, "Further Studies of the HRR Fields of a Moving Crack: an Experimental Analysis," Office of the Chief of Naval Research, Contract N00014-85-0187, Technical Report No. UWA/DME/TR-88/61, (1988)

[21] A. Saxena, "Nonlinear Fracture Mechanics for Engineers," CRC Press LLC, New York, (1998) 126.

[22] V. Kumar, M. D. German, and C. F. Shih, "Elastic-Plastic and Fully Plastic Analysis of Crack Initiation, Stable Growth, and Instability in Flawed Cylinders," in Elastic-Plastic Fracture: Second Symposium, ASTM STP 803, Vol. I, (1983) 306-353

[23] M.Y. He and J.W. Hutchinson, "The Penny-Shaped Crack and the Plane Strain Crack in an Infinite Body of Power-Law Material," Trans. ASME, J. Applied Mechanics, Vol. 48, (1981) 830-840

[24] M.Y. He and J.W. Hutchinson, "Bounds for Fully Plastic Crack Problems for Infinite Bodies," ASTM STP 803, Vol. I, (1983) 277-290

[25] H.W. Liu, "On The Fundamentals Basis of Fracture Mechanics," Eng. Fracture Mech. Vol. 17, No. 5, (1983) 425-438

Chapter 8

MIXED-MODE FRACTURE MECHANICS

8.1   INTRODUCTION

Practical structures are not only subjected to tension, but also experience shear and torsion loading leading to a mixed-mode interaction. Correspondingly, the stress state ahead of a crack is frequently based on mixed-mode I and II or I and III type of interactions, which designate the amplitude of the crack-tip stresses because of skew-symmetric loading. Problems of this type are encountered in multi-phase materials such as welded structures, adhesive joints, composite materials, plain and reinforced concrete structures, bridges, aircrafts and so forth. A mixed mode interaction can also arise when crack branching occurs; that is, when a crack changes direction in which the classical energy balance of Griffith can no longer be carried out in a simple manner since cracking is not collinear as it has been assumed in previous chapters.

In addition, cracks may develop in the skin of aircraft fuselages and can be subjected to mixed-mode fracture conditions. In general, crack initiation and growth must be correlated with the governing stress intensity factors in a complex state of stress. This means that the crack tip fields are inherently three dimensional with varying distribution through the thickness of the solid component. Therefore, the field equations must be determined for a better understanding of mixed-mode fracture mechanics [1-7]. For instance, cracks loaded in tension and shear may exhibit crack branching or kinking can be characterized using traditional singular and high-order terms in the stress field. The mixed-mode analysis of branched cracks requires the determinations of stress intensity factors for the original and branched crack parts in terms of the stress field surrounding the crack tip [1-28]. Therefore, an optimal kink angle and the T-stress can be determined based on far-field boundary conditions in a homogeneous or heterogeneous materials.

8.2   ELASTIC STATE OF STRESSES

Using the linear superposition of stresses in rectangular or polar coordinates the elastic state of stress at the crack tip are obtainable very easily. For a mixed mode I-II shown in Figure 8.1a, the total stress in Cartesian coordinates are the sum of the stresses of each loading mode component derived in Chapter 4.

$$\sigma_{xx} = \frac{K_I}{\sqrt{2\pi r}} \cos\frac{\theta}{2}\left[1 - \sin\frac{\theta}{2}\sin\frac{3\theta}{2}\right] - \frac{K_{II}}{\sqrt{2\pi r}}\sin\frac{\theta}{2}\left[2 + \cos\frac{\theta}{2}\cos\frac{3\theta}{2}\right]$$

$$\sigma_{yy} = \frac{K_I}{\sqrt{2\pi r}} \cos\frac{\theta}{2}\left[1 + \sin\frac{\theta}{2}\sin\frac{3\theta}{2}\right] + \frac{K_{II}}{\sqrt{2\pi r}}\sin\frac{\theta}{2}\cos\frac{\theta}{2}\cos\frac{3\theta}{2} \qquad (8.1)$$

$$\tau_{xy} = \frac{K_I}{\sqrt{2\pi r}} \cos\frac{\theta}{2}\sin\frac{\theta}{2}\cos\frac{3\theta}{2} + \frac{K_{II}}{\sqrt{2\pi r}}\cos\frac{\theta}{2}\left[1 - \sin\frac{\theta}{2}\sin\frac{3\theta}{2}\right]$$
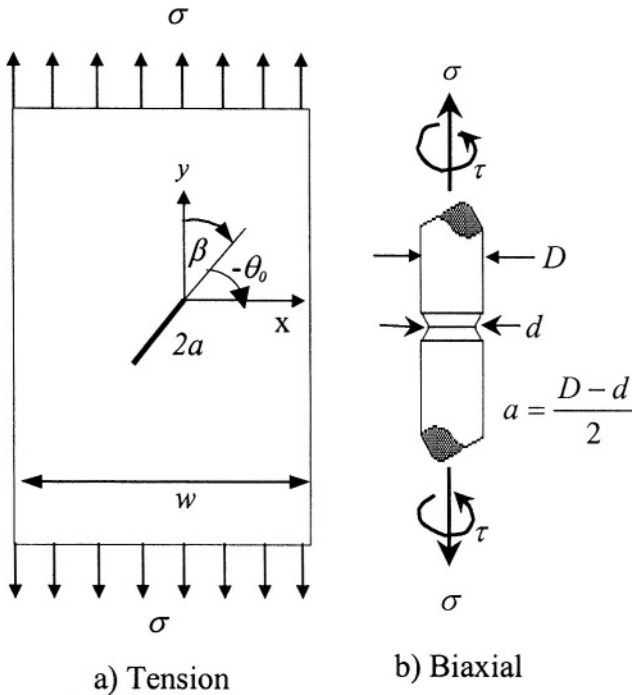
Figure 8.1 Mixed mode interactions

The displacements are the sum of eqs. (4.18) and (4.37)

$$\mu_x = \frac{2K_I}{E}\sqrt{\frac{r}{2\pi}}\cos\frac{\theta}{2}\left[(1-v)+(1+v)\sin^2\frac{\theta}{2}\right]$$

$$+\frac{2(1+v)K_{II}}{E}\sqrt{\frac{r}{2\pi}}\sin\frac{\theta}{2}\left[\frac{2}{1+v}+\cos^2\frac{\theta}{2}\right]$$

$$\mu_y = \frac{2K_I}{E}\sqrt{\frac{r}{2\pi}}\sin\frac{\theta}{2}\left[2-(1+v)\right]\cos^2\frac{\theta}{2} \qquad (8.2)$$

$$+\frac{2K_{II}}{E}\sqrt{\frac{r}{2\pi}}\cos\frac{\theta}{2}\left[(v-1)+(1+v)\sin^2\frac{\theta}{2}\right]$$

$$\mu_z = -\frac{2vBK_I}{E}\sqrt{\frac{r}{2\pi}}\cos\frac{\theta}{2}+\frac{2vBK_{II}}{E}\sqrt{\frac{r}{2\pi}}\sin\frac{\theta}{2}$$

For polar coordinates, eqs. (4.58) and (4.59) yield

$$\sigma_{rr} = \frac{K_I}{4\sqrt{2\pi r}}\left(5\cos\frac{\theta}{2}-\cos\frac{3\theta}{2}\right)+\frac{K_{II}}{4\sqrt{2\pi r}}\left(-5\sin\frac{\theta}{2}+3\sin\frac{3\theta}{2}\right)$$

$$\sigma_{\theta\theta} = \frac{K_I}{4\sqrt{2\pi r}}\left(3\cos\frac{\theta}{2}+\cos\frac{3\theta}{2}\right)+\frac{K_{II}}{4\sqrt{2\pi r}}\left(-3\sin\frac{\theta}{2}-3\sin\frac{3\theta}{2}\right) \quad (8.3)$$

$$\tau_{r\theta} = \frac{K_I}{4\sqrt{2\pi r}}\left(\sin\frac{\theta}{2}+\sin\frac{3\theta}{2}\right)+\frac{K_{II}}{4\sqrt{2\pi r}}\left(\cos\frac{\theta}{2}+3\cos\frac{3\theta}{2}\right)$$

Rearranging eq. (8.3) yields [1]

$$\sigma_{rr} = \frac{2}{\sqrt{2\pi r}}\left[K_I(3-\cos\theta)\cos\frac{\theta}{2}+K_{II}(3\cos\theta-1)\right]$$

$$\sigma_{\theta\theta} = \frac{2}{\sqrt{2\pi r}}\left[K_I(1+\cos\theta)\cos\frac{\theta}{2}+3K_{II}\sin\theta\cos\frac{\theta}{2}\right] \qquad (8.4)$$

$$\tau_{r\theta} = \frac{2}{\sqrt{2\pi r}}\left[K_I\sin\theta\cos\frac{\theta}{2}+K_{II}(3\cos\theta-1)\cos\frac{\theta}{2}\right]$$

and the displacements are obtained from eqs. (4.63) and (4.64)

$$\mu_r = \frac{K_I}{4G}\sqrt{\frac{r}{2\pi}}\left[(2\kappa-1)\cos\frac{\theta}{2}-\cos\frac{3\theta}{2}\right]$$

$$+\frac{K_{II}}{4G}\sqrt{\frac{r}{2\pi}}\left[-(2\kappa-1)\sin\frac{\theta}{2}+3\sin\frac{3\theta}{2}\right]$$

$$\mu_\theta = \frac{K_I}{4G}\sqrt{\frac{r}{2\pi}}\left[-(2\kappa-1)\sin\frac{\theta}{2}+\sin\frac{3\theta}{2}\right] \qquad (8.5)$$

$$+\frac{K_{II}}{4G}\sqrt{\frac{r}{2\pi}}\left[-(2\kappa-1)\cos\frac{\theta}{2}+3\cos\frac{3\theta}{2}\right]$$

$$\mu_z = -\frac{2vBK_I}{E}\sqrt{\frac{r}{2\pi}}\cos\frac{\theta}{2}+\frac{2vBK_{II}}{E}\sqrt{\frac{r}{2\pi}}\sin\frac{\theta}{2}$$

where

$$\kappa = \frac{3-v}{1+v} \qquad \text{For plane stress} \tag{8.6}$$

$$\kappa = 3-4v \qquad \text{For plane strain} \tag{8.7}$$

From Chapter, the stresses and displacements for the specimen configuration shown in Figure 8.1b are

$$\sigma_r = \frac{2K_I}{\sqrt{2\pi r}}(3-\cos\theta)\cos\frac{\theta}{2} + \frac{K_{III}}{2}\sqrt{\frac{2}{\pi r}}\sin\frac{\theta}{2}$$

$$\sigma_\theta = \frac{2K_I}{\sqrt{2\pi r}}(1+\cos\theta)\cos\frac{\theta}{2} + \frac{K_{III}}{2}\sqrt{\frac{2}{\pi r}}\cos\frac{\theta}{2} \tag{8.8}$$

$$\mu_z = -\frac{2vBK_I}{E}\sqrt{\frac{r}{2\pi}}\cos\frac{\theta}{2} + \frac{K_{III}}{G}\sqrt{\frac{2r}{\pi}}\sin\frac{\theta}{2}$$

$$\mu_z = \frac{K_{III}}{G}\sqrt{\frac{2r}{\pi}}\sin\frac{n\theta}{2}$$

$$\tau_{rz} = \frac{K_{III}}{2}\sqrt{\frac{2}{\pi r}}\sin\frac{n\theta}{2} \tag{8.9}$$

$$\tau_{\theta z} = \frac{K_{III}}{2}\sqrt{\frac{2}{\pi r}}\cos\frac{n\theta}{2}$$

8.3   STRAIN ENERGY RELEASE RATE

8.3.1   MODE I AND II

The main objective in this section is to develop a fracture criterion based on the strain energy release rate for mixed I and II interaction. Assume that the basic three mode interact on a elastic component and the elastic J-integral and the elastic strain energy release rate are equal. Thus, eq. (6.61) is applicable for crack motion on its tangent plane

$$J_i = G_i = G_I + G_{II} + G_{III} \tag{8.10}$$

$$G_I = \frac{K_I^2}{E'} + \frac{K_{II}^2}{E'} + \frac{(1+v)\,K_{III}^2}{E} \tag{8.11}$$

where $E' = E$ for plane stress
$\qquad E' = E/\left(1-v^2\right)$ for plane strain

For pure mode I loading at fracture, the fracture toughness expression is

$$G_{IC} = G_I = \frac{K_{IC}^2}{E'} \qquad (8.12)$$

Substituting eq. (8.12) into (8.11) gives the fracture criterion equation which is named as the G-Criterion

$$K_{IC}^2 = K_I^2 + K_{II}^2 + \frac{E'(1+v)K_{III}^2}{E} \qquad (\text{G-Criterion}) \qquad (8.13)$$

This equation indicates that any combination of the stress intensity factors may give the value for fracture toughness K_{IC}. Now, consider the mixed mode I-II configuration shown in Figure 8.1a. The stress components and the stress intensity factors become

$$\begin{aligned} \sigma_{xx} &= \sigma \cos^2 \beta \\ \sigma_{yy} &= \sigma \sin^2 \beta \\ \tau_{xy} &= \sigma \sin \beta \cos \beta \end{aligned} \qquad (8.14)$$

and

$$\begin{aligned} K_I &= \sigma_{yy}\sqrt{\pi a} = \sigma\sqrt{\pi a}\sin^2 \beta & (8.15) \\ K_{II} &= \tau_{xy}\sqrt{\pi a} = \sigma\sqrt{\pi a}\sin \beta \cos \beta & (8.16) \end{aligned}$$

Thus, eq. (8.13) reduces to

$$K_{IC}^2 = K_I^2 + K_{II}^2 \qquad (\text{Circle}) \qquad (8.17)$$

This fracture criterion is named so because eq. (8.17) is the equation of a circle for a constant radius K_{IC}. Now, inserting eq. (8.14) into (8.17) yields the plane strain fracture toughness as a function of the fracture or critical stress and inclined angle

$$K_{IC} = \sigma_f \sqrt{\pi a}\sin \beta \qquad (\text{Circle}) \qquad (8.18)$$

Figure 8.2 shows how the fracture stress varies with increasing incline angle at a fixed crack length and various levels of fracture toughness. .
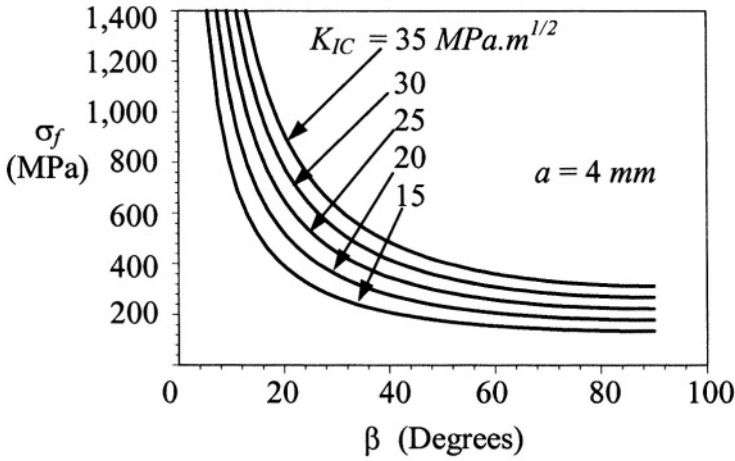
Figure 8.2 Variation of fracture stress for a fixed crack length and varying fracture toughness

Example 8.1 *A large steel plate is has a* **8-mm** *long inclined central crack at* 20°. *If the applied stress is* **200** *MPa, determine whether or not the plate will fracture. The fracture toughness of the steel is* $K_{IC} = 30$ *MPa*$\sqrt{m}$.

Solution:

From eqs. (8.15) and (8.16),

$$K_I \;=\; \sigma\sqrt{\pi a}\sin^2\beta = (200 MPa)\left(\sqrt{4\pi x10^{-3}\ m}\right)\sin^2(20)$$

$$K_I \;=\; 7.67\ MPa\sqrt{m}$$

$$K_{II} \;=\; \sigma\sqrt{\pi a}\sin\beta\cos\beta = (200 MPa)\left(\sqrt{4\pi x10^{-3}\ m}\right)\sin(20)\cos(20)$$

$$K_{II} \;=\; 7.21\ MPa\sqrt{m}$$

Thus,

$$\sqrt{K_I^2 + K_{II}^2} = 10.53\ MPa\sqrt{m} < K_{IC}$$

The fracture stress should be calculated using eq. (8.18)

$$\sigma_f = \frac{K_{IC}}{\sqrt{\pi a}\sin\beta} = \frac{30 MPa\sqrt{m}}{\left(\sqrt{4\pi x10^{-3}\ m}\right)\sin(20)} = 782.46\ MPa$$

Therefore, *the plate will not fracture because* $K_{IC} > 10.53\ MPa\sqrt{m}$ *and* $\sigma < \sigma_f$ *for a fixed crack length.*

8.3.2 FRACTURE ANGLE

Assume that the incline crack shown in Figure 8.1a changes direction under the influence of an applied tension stress and that crack propagation occurs along the x-axis (tangent plane). Take this fracture angle as negative angle since it rotates clockwise. Thus,

$$\theta_o = \frac{\pi}{2} - \beta \tag{8.19}$$

Using the trigonometric function $\sin \beta = \sin (\pi/2 - \theta_o) = \cos \theta_o$ in eq. (8.18) and arranging the resultant expression yield the plane-strain fracture toughness as a function of the fracture angle θ_o. Hence,

$$K_{IC} = \sigma_f \sqrt{\pi a} \cos \theta_o \tag{8.20}$$

This expression indicates that fracture occurs when $K_I = K_{IC}$ at a fracture angle $\theta = \theta_o$ for pure mode I loading. Conversely, $K_{II} = K_{IIC}$ for pure mode II. Some materials may obey this particular criterion and the mixed-mode evaluation is very simple. The fact remains that K_{IIC} vanishes when crack growth changes direction along the x-axis as depicted in Figure 8.1a. Thus, the crack fracture angle can be predicted to be $\theta_o > (\pi/2 - \beta)$. It is clear that the relationship between the fracture and incline angles is linear.

If the circular fracture criterion does not explain some data, then one approach is to use the elliptical fracture condition with $K_{IC} = \sqrt{2/3}K_{IIC}$ as a practical definition [4]. Thus, the mixed-mode equation is

$$\left(\frac{K_I}{K_{IC}}\right)^2 + \left(\frac{K_{II}}{K_{IIC}}\right)^2 = 1 \quad \text{(Ellipse)} \tag{8.21}$$

$$K_I^2 + \frac{2}{3}K_{II}^2 = K_{IC}^2 \quad \text{(Ellipse)} \tag{8.22}$$

Figure 8.3 shows the trend of eqs. (8.17) and (8.21) for a quarter of an ellipse. The elliptical fracture criterion is based on the assumption that the crack propagates in a self-similar manner (extension along the plane of the original crack). Previously, Xu [21-22] used this method in a three-dimensional approach. In practice, crack extension in a combined loading system takes place under an angle θ_o with respect to the original crack plane. This leads to other fracture theories.

Substituting eq. (8.14) into (8.22) gives

$$K_{IC} = \sigma_f \sqrt{\frac{\pi a}{3} (3 - \cos^2 \beta)} . \sin \beta \quad \text{(Ellipse)} \tag{8.23}$$
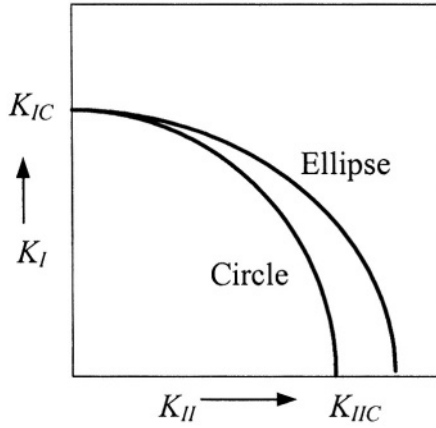
Figure 8.3 Locus of the circle and ellipse criteria

Example 8.2 *A brittle steel plate containing a 6-mm long inclined central crack (Figure 8.1a) is loaded in tension. Use both the circular and the elliptical fracture criteria to determine a) the fracture stress when $\beta = \pi/4$ and $\pi/3$ b) β and θ_o when the fracture stress is $\sigma_f^{(c)}$ (circle) $= \sigma_f^{(e)}$. Given data: $K_{IC} = 40$ $MPa\sqrt{m}$, $E = 206,850$ MPa and $n = 0.30$.*

Solution:

a) This part of the problem is for $\sigma_f^{(c)}$ (circle) $\neq \sigma_f^{(e)}$ (ellipse). Thus, eqs. (8.18) and (8.23) yield, respectively

$$\sigma_f^{(c)} = \frac{K_{IC}}{\sqrt{\pi a}\sin\beta} = \frac{40\ MPa\sqrt{m}}{\sqrt{\pi\,(3x10^{-3}\ m)}.\sin(\pi/4)}$$

$$\sigma_f^{(c)} = 582.69\ MPa$$

and

$$\sigma_f^{(e)} = \sqrt{\frac{3}{\pi a\,(3 - \cos^2\beta)}}\frac{K_{IC}}{\sin\beta}$$

$$\sigma_f^{(e)} = \sqrt{\frac{3}{\pi\,(3x10^{-3}\ m)\,(3 - \cos^2(\pi/4))}}\frac{(40\ MPa\sqrt{m})}{\sin(\pi/4)}$$

$$\sigma_f^{(e)} = 638.31\ MPa > \sigma_f^{(c)}$$

and

$$\sigma_f^{(e)} = \sqrt{\frac{3}{\pi\,(3x10^{-3}\,m)\,(3-\cos^2{(\pi/3)})}} \frac{(40\,MPa\sqrt{m})}{\sin{(\pi/3)}}$$

$$\sigma_f^{(e)} = 496.92\,MPa > \sigma_f^{(c)}$$

Therefore, the fracture stress decreases as the incline angle decreases

b) For $\sigma_f^{(c)}$ (circle) $\neq \sigma_f^{(e)}$,

$$\frac{K_{IC}}{\sqrt{\pi a}\sin\beta} = \sqrt{\frac{3}{\pi a\,(3-\cos^2\beta)}} \frac{K_{IC}}{\sin\beta}$$

$$\cos\beta = 3-3 = 0$$

$$\beta = \frac{\pi}{2} = 90^o$$

Therefore, $\beta = \pi/2$ implies that the crack should be located along the x-axis and the fracture angle should be zero because crack motion should occur on its tangent plane. This is known in the literature as a self-similar crack growth. This can be proven by using eq. (8.19). Thus, $\theta_o = \pi/2 - \beta = 0$

8.3.3 MODE I AND III

consider the crack configuration for a solid cylinder shown in Figure 8.1b. For a mixed mode I-III, the cylinder is subjected to a biaxial loading and eq. (8.13) reduces to

$$K_{IC}^2 = K_I^2 + \frac{E'\,(1+v)\,K_{III}^2}{E} \tag{8.24}$$

$$K_{IC}^2 = K_I^2 + \frac{K_{III}^2}{1-v} \qquad \text{For plane strain} \tag{8.25}$$

$$K_C^2 = K_I^2 + (1+v)\,K_{III}^2 \qquad \text{For plane stress} \tag{8.26}$$

Denote that K_{IC} is changed to K_C for plane stress. These expressions indicate that crack growth occurs in a self-similar manner or crack motion manifests itself along its tangent plane. This is in accord with the basis for deriving eq. (8.13). Therefore, the crack fracture angle is $\theta_o = 0$.

When the fracture crack angle of an incline crack is defined by the inequality $\theta_o > (\pi/2 - \beta)$, where the crack incline angle is $\beta \neq \pi/2$, both Circular and Elliptical Criteria may be invalid and therefore, different mixed mode fracture criteria should be considered in order to obtain reliable and accurate results.

8.4   PRINCIPLE STRESS CRITERION

This mixed-mode fracture criterion, σ_θ-criterion, has been shown [3,5,6] to be equivalent to the mixed-mode strain energy release rate criterion. This fracture criterion postulates that crack growth takes place in a direction perpendicular to the maximum principal stress. Hence, the fracture criterion requires that the maximum principal stress be a tension stress for opening the crack along its plane. This criterion also requires that

$$\left.\frac{\partial\sigma_\theta}{\partial\theta}\right|_{\theta=\theta_o} = 0 \quad \text{and} \quad \frac{\partial^2\sigma_\theta}{\partial\theta^2} < 0 \quad \text{For } \sigma_\theta > 0 \tag{8.27}$$

Consider the tension loading that produces a mixed-mode I and II interaction as shown in Figure 8.1a and that the stress σ_θ in eq. (8.4) is a principal stress if $\partial\sigma_\theta/\partial\theta = \tau_{r\theta} = 0$. Setting $\tau_{r\theta} = 0$ in eq. (8.4) and using eq. (8.15) and (8.16) yield

$$K_I \sin\theta_o + K_{II}\,(3\cos\theta_o - 1) \;=\; 0 \tag{8.28}$$
$$\sin\theta_o + (3\cos\theta_o - 1)\cot\beta \;=\; 0 \quad \text{For } \beta \neq 0 \tag{8.29}$$

Using the trigonometric function $\sin\theta_o = \sqrt{(1 - \cos 2\theta_o)/2}$ and $x = K_I/K_{II}$ in eq. (8.28) and solving for θ_o yields

$$\theta_o = -\arccos\frac{1}{3}\left[1 - \frac{x\left(x - 3\sqrt{(x^2 + 8)}\right)}{x^2 + 9}\right] \quad \text{For } \theta_o < \frac{\pi}{2} \tag{8.29}$$

This equation is of practical interest since the fracture angle can be estimated knowing $x = K_I/K_{II}$ value. This fracture angle may be considered as a kink angle in a mixed-mode fracture process in a homogeneous material. For pure mode II loading, the tension stress intensity factor vanishes ($K_I = 0$) and consequently, eq. (8.28) yields the fracture angle as

$$-\cos\theta_o = \frac{1}{3} \quad \text{or} \quad \theta_o = -70.53 \tag{8.30}$$

The maximum principle stress is defined, after manipulating the trigonometric functions in eq. (8.4), by

$$\sigma_1 = \sigma_\theta\,(\theta = \theta_o) = \frac{1}{\sqrt{2\pi r}}\cos^2\frac{\theta_o}{2}\left[K_I\cos\frac{\theta_o}{2} - 3K_{II}\sin\frac{\theta_o}{2}\right] \tag{8.31}$$

For pure mode I loading at fracture with $K_I = K_{IC}$, eq. (8.31) becomes

$$\sigma_1 = \frac{K_{IC}}{\sqrt{2\pi r}} \tag{8.32}$$

Equating eqs. (8.31) and (8.32) yields the fracture criterion as a trigonometric function

$$K_{IC} = K_I \cos^3 \frac{\theta_o}{2} - 3K_{II} \sin \frac{\theta_o}{2} \cos^2 \frac{\theta_o}{2} \qquad (\sigma_\theta\text{-Criterion}) \qquad (8.33)$$

Furthermore, the fracture toughness ratio can be determined by substituting the fracture angle $\theta_o = -70.53$ into eq. (8.33) for pure mode II at fracture. Thus, $K_{II} = K_{IIC}$ and

$$K_{IIC} = \sqrt{\frac{3}{4}} K_{IC} \simeq \frac{13}{15} K_{IC} \simeq 1.15 K_{IC} \qquad (\sigma_\theta\text{-Criterion}) \qquad (8.34)$$

For convenience, squaring eq. (8.33), manipulating and simplifying the trigonometric identities yields

$$K_{IC}^2 = b_{11} K_I^2 - 2b_{12} K_I K_{II} + b_{22} K_{II}^2 \qquad (\sigma_\theta\text{-Criterion}) \qquad (8.35)$$

with

$$b_{11} = \frac{1}{8}(1 + \cos\theta_o)^3 \qquad b_{12} = \frac{3}{8}\sin\theta_o (1 + \cos\theta_o)^2 \qquad (8.36)$$

$$b_{22} = \frac{9}{8}\sin^2\theta_o (1 + \cos\theta_o)$$

The distribution of each constant b_{ij} is shown in Figure 8.4. Denote the three intercepting points where the constants are equal. For instance,

$$
\begin{aligned}
K_{IC}^2 &= b\left(11 K_I^2 + K_{II}^2\right) - 2b_{12} K_I K_{II} & \text{For } b_{11} = b_{22} & \qquad (a) \\
K_{IC}^2 &= b_{11} K_I^2 - 2b_{22}\left(K_I K_{II} + K_{II}^2\right) & \text{For } b_{12} = b_{22} & \qquad (b) \\
K_{IC}^2 &= b_{11} K_I \left(K_I - 2b_{12} K_{II}\right) + b_{22} K_{II}^2 & \text{For } b_{11} = b_{12} & \qquad (c)
\end{aligned}
$$
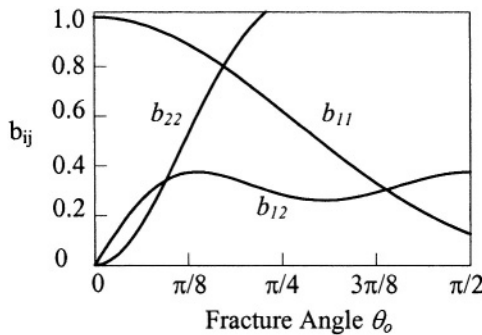
Figure 8.4 Distribution of b_{ij} as functions of fracture angle θ_o

8.5   STRAIN-ENERGY DENSITY FACTOR

Sih [2] proposed this criterion using the strain energy density factor *(S)* for a two-dimensional stress field. This criterion states that the initial crack growth takes place in the direction along which the strain-energy-density factor reaches a minimum stationary value so that

$$\frac{\partial S}{\partial \theta} \;=\; 0 \qquad \text{For } \theta = \theta_o \tag{8.37}$$

$$\frac{\partial^2 S}{\partial \theta^2} \;>\; 0 \qquad \text{For } -\pi < \theta_o < \pi \tag{8.38}$$

This theory can predict crack propagation in an arbitrary direction it states that crack propagation occurs when $S = S_c$ at $\theta = \theta_o$ where S_c is the critical strain energy density factor and θ_o is the fracture angle.

The development of S-criterion is achieved by inserting the previously derived stresses and displacements into the strain energy density equations (with unit thickness). This criterion is related to the work done by the an external load, which is the stored strain energy density in solids. Thus, eq. (6.58) in rectangular and polar coordinates becomes

$$\frac{dW}{dV} \;=\; \frac{1}{2E}\left(\sigma_{xx}^2 + \sigma_{yy}^2 + \sigma_{zz}^2\right) \tag{8.39}$$

$$-\frac{v}{E}\left(\sigma_{xx}\sigma_{yy} + \sigma_{yy}\sigma_{zz} + \sigma_{zz}\sigma_{xx}\right)$$

$$+\frac{1}{E}\left(1+v\right)\left(\tau_{xy}^2 + \tau_{yz}^2 + \tau_{zx}^2\right)$$

$$\frac{dW}{dA} \;=\; \frac{1}{2}\left[\sigma_r\frac{\partial \mu_r}{\partial r} + \sigma_\theta\left(\frac{\mu_r}{r} + \frac{1}{r}\frac{\partial \mu_\theta}{\partial \theta}\right)\right] \tag{8.40}$$

$$+\frac{1}{2}\tau_{r\theta}\left(\frac{1}{r}\frac{\partial \mu_r}{\partial \theta} + \frac{1}{r}\frac{\partial \mu_\theta}{\partial r} - \frac{\mu_\theta}{r}\right)$$

Here, V is the volume and $A = rd\theta dr$ is the inner area (region) of the plastic zone model shown Figure 8.5 [2]. This region should not have its sides coincide with the free crack surface which corresponds to the trivial case when $S = 0$.

The strain energy density factor is derived by combining eqs. (8.5) and (8.40). Thus,

$$S = r\frac{dW}{dA} = a_{11}K_I^2 + 2a_{12}K_I K_{II} + a_{22}K_{II}^2 \tag{8.41}$$

where a_{ij} = constants
$\qquad G = E/\left[2\left(1+v\right)\right]$ = Modulus elasticity in shear
$\qquad E$ = Modulus elasticity in tension
$\qquad v$ = Poisson's ratio
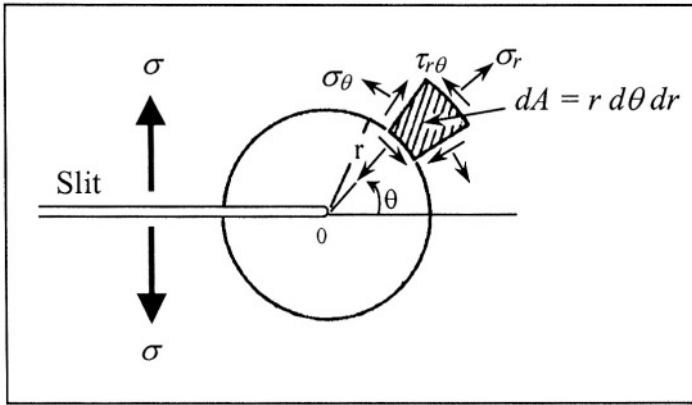
Figure 8.5 Stress field of an element at the circular plastic zone boundary in polar coordinates [2]

The constants a_{ij} are

$$a_{11} = \frac{1}{16G} \left[(1 + \cos\theta)(\kappa - \cos\theta) \right]$$

$$a_{12} = \frac{1}{16G} \sin\theta \left[2\cos\theta - (\kappa - 1) \right] \tag{8.42}$$

$$a_{22} = \frac{1}{16G} \left[(\kappa + 1)(1 - \cos\theta) + (1 + \cos\theta)(3\cos\theta - 1) \right]$$

Figure 8.6 shows the distribution of the constants a_{ij} as a function of θ for Poisson's ratio of $v = 0.3$ and modulus of elasticity of $E = 70\ GPa$ under plane strain condition.
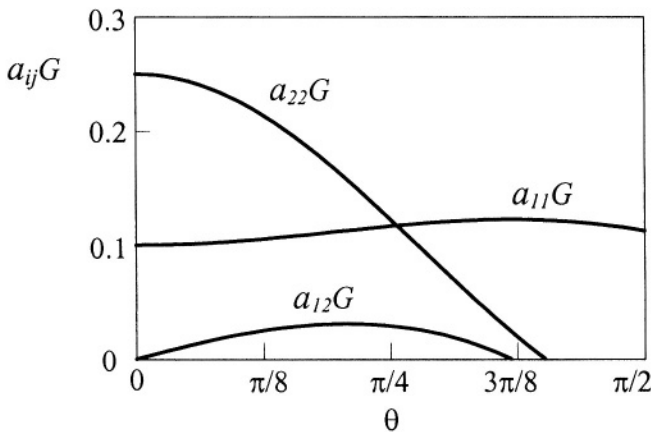
Figure 8.6 Distribution of a_{ij} for a material having $v = 0.3$ under plane strain condition

For pure mode II, $K_I = 0$ and eq. (8.41) yields

$$S_{II} = a_{22} K_{II}^2 \tag{8.43}$$

Letting $\partial S / \partial \theta = 0$ at $\theta = -\theta_o$ yields

$$\cos \theta_o \;\; = \;\; \frac{\kappa - 1}{6} \tag{8.44}$$

$$\theta_o \;\; = \;\; -\arccos \frac{\kappa - 1}{6} \tag{8.45}$$

and eq. (8.43) becomes

$$S_{IIC} = S_{\min - II} = \frac{1}{192G} \left[14\kappa - \kappa^2 - 1 \right] K_{IIC}^2 \tag{8.46}$$

For instance, if Poisson's ratio is $v = 0.3$, then the fracture angle under plane conditions become

$$\theta_o \;\; = \;\; -\arccos \frac{1 - v}{3} = -76.51^\circ \quad \text{For plane stress} \tag{8.47}$$

$$\theta_o \;\; = \;\; -\arccos \frac{1 - 2v}{3} = -82.34^\circ \quad \text{For plane strain} \tag{8.48}$$

On the other hand, if $K_{II} = 0$ in eq. (8.41), then

$$S_I = a_{11} K_I^2 \tag{8.49}$$

Letting $\partial S / \partial \theta = 0$ in eq. (8.49) at $\theta = -\theta_o$ gives

$$\cos \theta_o = \frac{\kappa - 1}{2} \tag{8.50}$$

and

$$S_{IC} = S_{\min - I} = \frac{(\kappa + 1)(\kappa - 1)}{32G} K_{IC}^2 \tag{8.51}$$

Let $\partial S / \partial \theta = 0$ at $\theta = -\theta_o$ in eq. (41) for $K_I > 0$ and $K_{II} > 0$ so that

$$\begin{aligned}
0 \;\; = \;\; & \left[(1 + \cos \theta_o) \sin \theta_o - (\sin \theta_o)(\kappa - \cos \theta_o) \right] K_I^2 \\
& + 2 \left[(\cos \theta_o (2 \cos \theta_o - \kappa + 1))(2 \cos \theta_o - \kappa + 1 - 2\theta_o \sin \theta_o) \right] K_I K_{II} \\
& + \left[(\kappa + 1) \sin \theta_o - (\sin \theta_o)(3 \cos \theta_o - 1) - 3(1 + \cos \theta_o) \sin \theta_o \right] K_{II}^2
\end{aligned} \tag{8.52}$$

or

$$
\begin{aligned}
0 \;=\; & \left[(1 + \cos\theta_o)\sin\theta_o - (\sin\theta_o)(\kappa - \cos\theta_o)\right] \hspace{2cm} (8.53) \\[4pt]
& + 2\left[(\cos\theta_o\,(2\cos\theta_o - \kappa + 1))\,(2\cos\theta_o - \kappa + 1 - 2\theta_o\sin\theta_o)\right]\left(\frac{K_{II}}{K_I}\right) \\[6pt]
& + \left[(\kappa + 1)\sin\theta_o - (\sin\theta_o)(3\cos\theta_o - 1) - 3(1 + \cos\theta_o)\sin\theta_o\right]\left(\frac{K_{II}}{K_I}\right)^2
\end{aligned}
$$

This equation can be used to determined θ_o knowing K_{II}/K_I values. The S-criterion for a mixed-mode I and II can be determined by inserting eq. (8.51) into (8.41). Thus,

$$
K_{IC}^2 = \frac{4E}{(\kappa + 1)(\kappa - 1)(1 + v)}\left[a_{11}K_I^2 + 2a_{12}K_I K_{II} + a_{22}K_{II}^2\right]_{\theta=\theta_o} \quad (8.54)
$$

Inserting eq. (8.50) into (8.54) along with a_{22} yields the fracture toughness for mode II

$$
K_{IIC} = \sqrt{\frac{24(\kappa - 1)}{4a_{22}E}}.K_{IC} \hspace{3cm} (8.55)
$$

$$
a_{22} = \frac{(1 + v)(k + 1)^2}{32E} \hspace{3cm} (8.56)
$$

$$
K_{IIC} = \sqrt{\frac{8(\kappa - 1)}{(\kappa + 1)^2}}.K_{IC} \hspace{3cm} (8.57)
$$

For plane strain with $v = 1/3$ and $\kappa = 3 - 4v$, eq. (8.57) yields exactly the same result as predicted by the principle stress theory given by eq. (8.34).

The numerical results of eq. (8.54) along with other criteria for negative values of θ_o (tension) and positive applied stress are shown in Figure 8.7 [4] In addition, notice the remarkable agreement between experimental and theoretical results for Plexiglas given in Table 8.1 [2]. This illustrates the usefulness of these criteria for predicting the fracture angle in elastic solids. Figure 8.8 shows the relationship between the fracture and inclined angles for tension loading [2].

Figure 8.7 Some mixed mode I and II fracture criteria [4]

Table 8.1 Experimental and theoretical values of the fracture angle for Plexiglas plates with a crack length a = 25.4 mm (Dimensions: 228.60-mm x 4570.20-mm x 4.76-mm) [2].

β	30°	40°	50°	60°	70°	80°
θ_o (Exp.)	-62.4°	-55.6	-51.6°	-43.1°	-30.7°	-17.3°
σ_θ-Criterion	-60.2°	-55.7	-50.2°	-43.2°	-33.2°	-19.3°
S-Criterion	-63.5_o	-56.7	-49.5°	-41.5°	-31.8°	-18.5°
G-Criterion	-60	-50	-40	-30	-20	-10
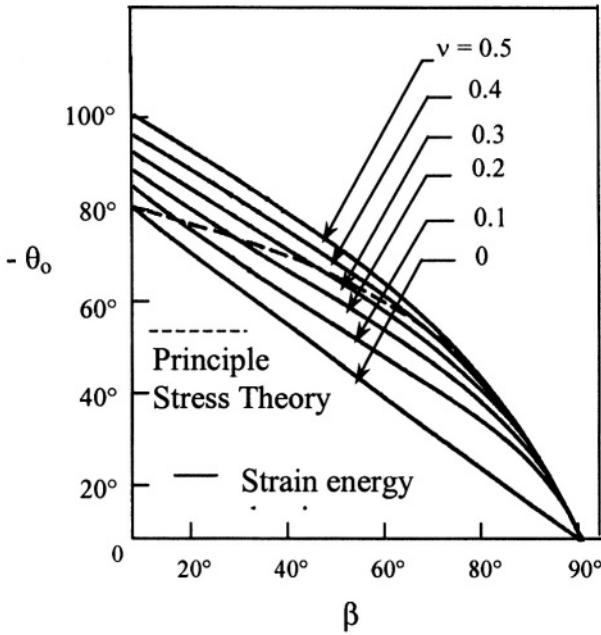
Figure 8.8 Theoretical results for an inclined central crack loaded in tension [2]

Example 8.3 *A large 2024 Al-alloy plate containing a central crack inclined at β is subjected to a combined mode I-II loading. The plate fractures at a tensile stress of $\sigma_{yy} = 138\ MPa$ and a shear stress of $\tau_{xy} = 103\ MPa$. Use the Maximum Principal Stress Criterion (σ_θ-criterion) and the Strain Energy Density Factor (S) Criterion (S-criterion) to calculate the fracture angle θ_o, the incline angle β, and the plane-strain fracture toughness K_{IC} and K_{IIC}. Use the following data: crack length $2a = 76\ mm$, $v = 1/3$ and $E = 72,300\ MPa$.*

Solution:

a) *Maximum principle stress criterion:*
If $\sigma_{yy} = 138\ MPa$, $\tau_{xy} = 103\ MPa$, $a = 38\ mm$, and $\beta = 85°$, the stress intensity factors are

$$K_I = \sigma_{yy}\sqrt{\pi a} = (138\ MPa)\sqrt{\pi\,(38x10^{-3}\ m)} = 47.68\ MPa\sqrt{m}$$

$$K_{II} = \tau_{xy}\sqrt{\pi a} = (103\ MPa)\sqrt{\pi\,(38x10^{-3}\ m)} = 35.59\ MPa\sqrt{m}$$

$$x = \frac{K_I}{K_{II}} = \frac{4}{3}$$

From eq. (8.29),

$$\theta_o = -\arccos\frac{1}{3}\left[1 - \frac{x\left(x - 3\sqrt{(x^2 + 8)}\right)}{x^2 + 9}\right] \qquad For\ \theta_o < \frac{\pi}{2} \qquad (8.29)$$

$$\theta_o = -\left(\frac{180}{\pi}\right)\arccos\left(\frac{1}{3}\right)\left[1 - \frac{(4/3)\left(4/3 - 3\sqrt{\left[(4/3)^2 + 8\right]}\right)}{(4/3)^2 + 9}\right]$$

$$\theta_o = -48.30^o$$

The crack is incline at

$$\frac{K_I}{K_{II}} \approx \frac{\sigma\sqrt{\pi a}\sin^2\beta}{\sigma\sqrt{\pi a}\sin\beta\cos\beta} = \tan\beta$$

$$\beta = \arctan\left(\frac{K_I}{K_{II}}\right) = \arctan\left(\frac{3}{4}\right) = 36.87^o$$

Inserting the value of θ_o, K_I and K_{II} into eq. (8.33) yields

$$K_{IC} = \cos^3\frac{\theta_o}{2}K_I - 3\sin\frac{\theta_o}{2}\cos^2\frac{\theta_o}{2}K_{II} \qquad (8.33)$$

$$K_{IC} = \cos^3\left(\frac{-48.30^o}{2}\right)(47.68\ MPa\sqrt{m})$$

$$-3\sin\left(\frac{-48.30^o}{2}\right)\cos^2\left(\frac{-48.30^o}{2}\right)(35.59\ MPa\sqrt{m})$$

$$K_{IC} = 72.60\ MPa\sqrt{m}$$

From eq. (8.34),

$$K_{IIC} = \sqrt{\frac{3}{4}}K_{IC} = 62.78\ MPa\sqrt{m} \qquad (8.34)$$

b) *Strain energy density factor criterion:*
For plane strain condition,

$$\kappa = 3 - 4v = 3 - 4/3 = 5/3$$

Using eq. (8.53) and an iteration procedure, the fracture angle becomes

$$0 = [(1 + \cos\theta_o)\sin\theta_o - (\sin\theta_o)(\kappa - \cos\theta_o)] \tag{8.53}$$

$$+2[(\cos\theta_o(2\cos\theta_o - \kappa + 1))(2\cos\theta_o - \kappa + 1 - 2\theta_o\sin\theta_o)]\left(\frac{3}{4}\right)$$

$$+[(\kappa + 1)\sin\theta_o - (\sin\theta_o)(3\cos\theta_o - 1) - 3(1 + \cos\theta_o)\sin\theta_o]\left(\frac{3}{4}\right)^2$$

$$\theta_o = -48.82°$$

From eq. (8.42) and (8.54),

$$a_{11} = \frac{1+v}{8E}[(1 + \cos\theta)(\kappa - \cos\theta)] = 3.8545 \times 10^{-6} \ MPa^{-1}$$

$$a_{12} = \frac{1+v}{8E}\sin\theta[2\cos\theta - (\kappa - 1)] = -1.2128 \times 10^{-6} \ MPa^{-1} \tag{8.42}$$

$$a_{22} = \frac{1+v}{8E}[(\kappa + 1)(1 - \cos\theta) + (1 + \cos\theta)(3\cos\theta - 1)]$$

$$a_{22} = 5.8282 \times 10^{-6} \ MPa^{-1}$$

and

$$K_{IC} = \sqrt{\frac{4E}{(\kappa - 1)(1 + v)}[a_{11}K_I^2 + 2a_{12}K_IK_{II} + a_{22}K_{II}^2]} \tag{8.54}$$

$$K_{IC} = 62.56 \ MPa\sqrt{m}$$

Finally, the fracture toughness for mode II and the critical strain energy density factor are

$$K_{IIC} = \sqrt{\frac{3}{4}}\left(62.56 \ MPa\sqrt{m}\right) = 54.18 \ MPa\sqrt{m} \tag{8.34}$$

and

$$S_c = a_{11}K_{IC}^2 + 2a_{12}K_{IC}K_{IIC} + a_{22}K_{IIC}^2 \tag{8.41}$$

$$S_c = \left(3.8545 \times 10^{-6} \ MPa^{-1}\right)\left(62.56 \ MPa\sqrt{m}\right)^2$$

$$-2\left(1.2128 \times 10^{-6} \ MPa^{-1}\right)\left(62.56 \ MPa\sqrt{m}\right)\left(54.18 \ MPa\sqrt{m}\right)$$

$$+\left(5.8282 \times 10^{-6} \ MPa^{-1}\right)\left(54.18 \ MPa\sqrt{m}\right)^2$$

$$S_c = 23.97 \ kPa.m = 23.97 \ kJ/m^2 \quad \text{(Critical)}$$

Therefore, crack propagation takes place when $S_c = 23.97 \ kJ/m^2$ at $\theta_o = -48.82°$.

8.6   CRACK BRANCHING

It is recognized that the tensile cracks in solids can significantly branch due to mechanical, microstructural or environmental effects. Changes in crack path are normally induced by [7-12]

- 1) Multiaxial far field stresses

- 2) Interaction of the crack tip with microstructural defects

- 3) Sudden changes in load

- 4) The embrittlement effect of an aggressive environment

Figure 8.9 illustrates some examples of severely branched cracks in ductile materials during different conditions, which can be found in the cited references. The effects of crack branching can be rationalized based on the stress intensity factors for the small-branched cracks shown in Figure 8.10. However, numerous solutions for kinked and forked cracks have been proposed, but there have been considerable disagreements.

The stress intensity factors K_1 and K_2 for kinked and forked cracks are smaller than the nominal K_I and K_{II}. Based on the projected length of the crack, K_1 and K_2 are meaningful if the plastic zone is smaller than the zone of dominance of the K_I and K_{II} singular fields.

The stress intensity factor solutions for kinked and forked elastic cracks under mixed mode I-II loading are based on the models shown in Figure 8.10 [7,13-16]. Thus,

$$
\begin{aligned}
K_1 &= a_{11}\left(\alpha\right) K_I + a_{12}\left(\alpha\right) K_{II} \\
K_2 &= a_{21}\left(\alpha\right) K_I + a_{22}\left(\alpha\right) K_{II}
\end{aligned}
\qquad (8.58)
$$

where $a_{ij}\left(\alpha\right)$ are defined as

$$
\begin{aligned}
a_{11}\left(\alpha\right) &= \frac{1}{4}\left(3\cos\frac{\alpha}{2} + \cos\frac{3\alpha}{2}\right) \\
a_{12}\left(\alpha\right) &= -\frac{3}{4}\left(\sin\frac{\alpha}{2} + \sin\frac{3\alpha}{2}\right) \\
a_{21}\left(\alpha\right) &= \frac{1}{4}\left(\sin\frac{\alpha}{2} + \sin\frac{3\alpha}{2}\right) \\
a_{22}\left(\alpha\right) &= \frac{1}{4}\left(\cos\frac{\alpha}{2} + 3\cos\frac{3\alpha}{2}\right)
\end{aligned}
\qquad (4.59)
$$
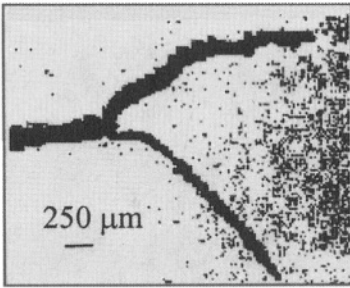
a) Ref. [8]
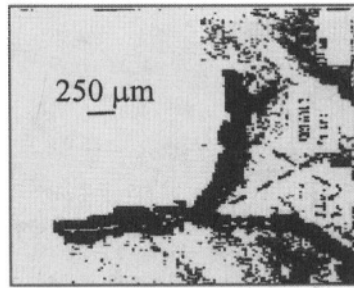
b) Ref. [8]
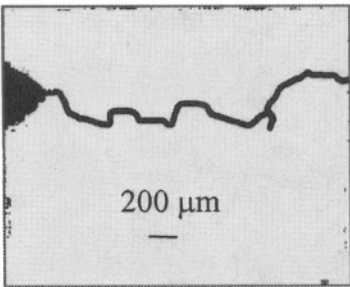
c) Ref. [9]
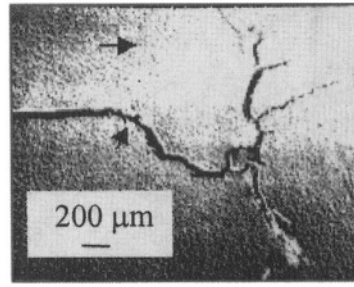
d) Ref. [10]
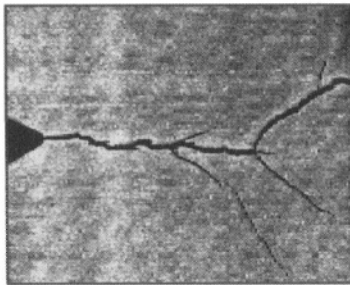
e) Ref. [11]
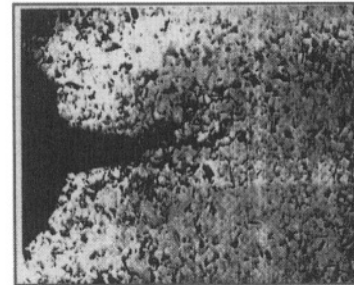
f) Ref.[12]

Figure 8.9 a), b) and c) Mode I crack branching in an Al-2.9Cu-2.1Li-0.12Zr alloy, d) kinking of a fatigue crack in 2020-T651 Al-alloy, e) stress corrosion crack branching in 9Ni-4Co-0.45C martensitic steel, and f) creep crack branching in copper.

a) Kinked crack

b) Forked cracks
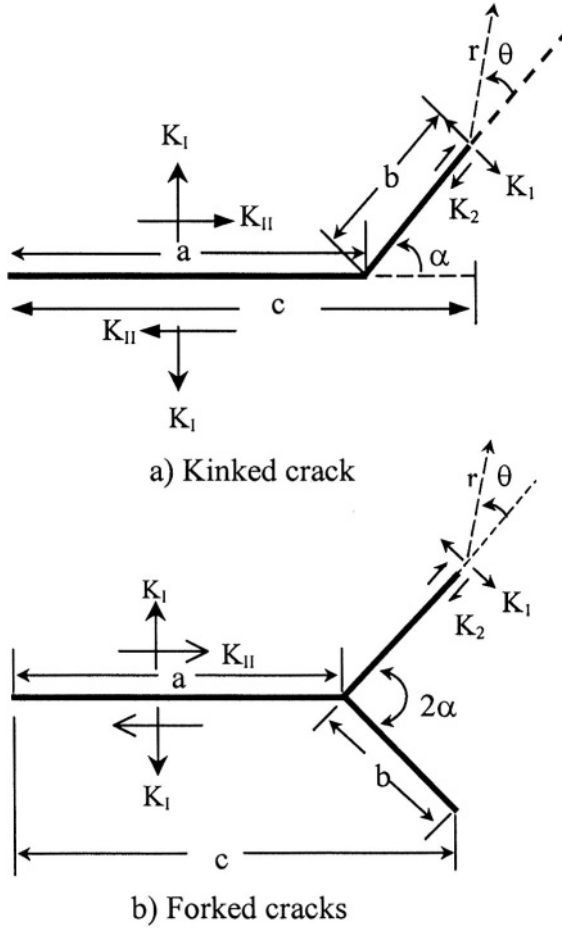
Figure 8.10 Nomenclature for mode I-II crack branching [7]

These coefficients are the solutions for an infinitesimal kink or branch crack $b/a \to 0$. A simple analysis of these equations imply that if $a = 0$, then the stress intensity factors for crack kinking become equal to the nominal counterparts; that is, $K_1 = K_I$ and $K_2 = K_{II}$. The profiles for $a_{ij}(\alpha)$ and normalized stress intensity factors for the branched crack are depicted in Figure 8.11.

The strain-energy release rate for crack extension in a self-similar manner (in the plane of the original crack plane) was derived previously as eq. (6.34). For an infinitesimally small crack branched out, the strain energy release rate, eq. (6.34), is now defined in terms of the stress intensity factor for the kinked crack tip

$$G(\alpha)_i = \frac{K_1^2}{E'} + \frac{K_2^2}{E'} + \frac{(1+v)\,K_3^2}{E} \qquad (8.60)$$
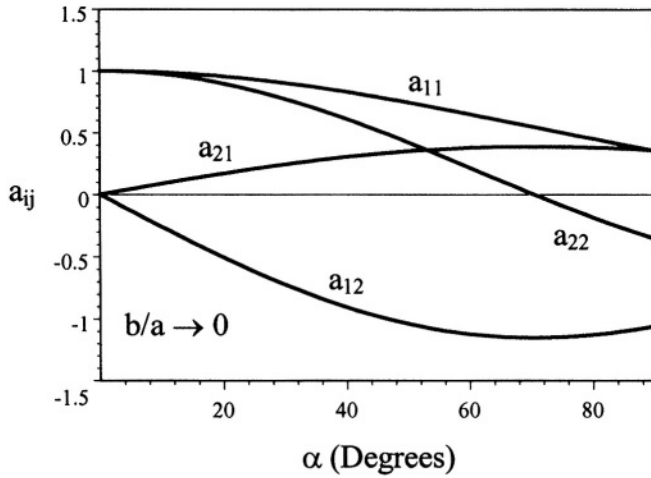
Figure 8.11 Variation of constants a_{ij} with kink angle

The stress intensity factor K_1 and K_2 derived by Hussain et al. [17] and K_3 by Sih [18] are

$$K_1 = \left(\frac{4}{3+\cos^2\alpha}\right)\left(\frac{\pi-a}{\pi+a}\right)^{\alpha/2\pi}\left(K_I\cos\alpha + \frac{3}{2}K_{II}\sin\alpha\right)$$

$$K_2 = \left(\frac{4}{3+\cos^2\alpha}\right)\left(\frac{\pi-a}{\pi+a}\right)^{\alpha/2\pi}\left(-\frac{1}{2}K_I\sin\alpha + K_{II}\cos\alpha\right) \quad (8.61)$$

$$K_2 = \left(\frac{\pi-a}{\pi+a}\right)^{\alpha/2\pi}K_{III}$$

Substituting eq. (8.61) into (8.60) yields an expression for the strain energy release rate

$$G(\alpha)_i = \frac{4\lambda}{(3+\cos^2\alpha)^2 E'}\left[\begin{array}{c}(1+3\cos^2\alpha)K_I^2 + (4\sin 2\alpha)K_IK_{II} \\ + (9-5\cos^2\alpha)K_{II}^2\end{array}\right]$$

$$+\frac{\lambda(1+v)K_{III}^2}{E} \quad (8.62)$$

$$\lambda = \left(\frac{\pi-a}{\pi+a}\right)^{\alpha/\pi} \quad (8.62a)$$

The hypothesis states that crack extension takes place in a direction of maximum strain energy release rate $G(\alpha)_{\mathbf{max}}$ and that crack branching occurs at a fracture angle $\alpha = \alpha_o$. Hence,

$$\frac{\partial G(\alpha)}{\partial \alpha} = 0 \quad \text{and} \quad \frac{\partial^2 G(\alpha)}{\partial \alpha^2} < 0 \quad \text{for } \alpha = \alpha_o \tag{8.63}$$

Crack propagation takes place when $G(\alpha)_i = G(\alpha)_c$. For pure mode I at fracture, eq. (8.62) becomes

$$G(\alpha)_{IC} = \frac{K_{IC}^2}{E'} \tag{8.64}$$

Letting $G(\alpha)_{IC} = G(\alpha)_i$ in eq. (8.62) yields the fracture criterion

$$K_{IC}^2 = \frac{4\lambda}{(3 + \cos^2 \alpha)^2} \left[\begin{array}{c} (1 + 3\cos^2 \alpha) K_I^2 + (4\sin 2\alpha) K_I K_{II} \\ + (9 - 5\cos^2 \alpha) K_{II}^2 \end{array} \right] \tag{8.65}$$
$$+ \frac{E'\lambda(1 + v) K_{III}^2}{E}$$

Denote that if $\alpha = 0$ in eqs. (8.62) and (8.65), the former reduces to eq. (6.34) and the latter becomes eq. (8.13).

Furthermore, the above mathematical treatment of mixed-mode fracture mechanics problems has been based on the stress field surrounding the crack tip where stress singularities exists as $r \to 0$. Including the influence of the T-stress (T_x) in the mixed mode I and II process, the generalized stress based on Williams [23] K-field solution for unkinked crack is defined as [24]

$$\sigma = \frac{K_I f_I(\theta) + K_{II} f_{II}(\theta)}{\sqrt{2\pi r}} + T_x \tag{8.66}$$

Recall from Chapter 4 that T_x is a second order term in the series expansion of the stress field and it is non-singular, but specimen size and geometry dependent. As pointed out by Becker et al. [24], T_x represents the strength in the crack x-direction. For mode I loading, $T_x < 0$ and $K_{II} = 0$ for stabilizing the crack. Conversely, crack branching may occur when $T_x > 0$ and $K_{II} > 0$ at angle α as indicated in Figure 8.10. Further theoretical or numerical details on crack kinking can be found elsewhere [25-28].

8.7 PROBLEMS

[**8.1**] A large plate (2024-0 Al-alloy) containing a central crack is subjected to a combined mode I-II loading. The internal stresses are $\sigma_{sy} = 138 \ MPa$ and $\tau_{xy} = 103 \ MPa$. Use the maximum principal stress criterion (σ_θ-criterion) to calculate the fracture toughness (K_{IC} and K_{IIC}). Data: crack length $2a = 76 \ mm$, $v = 1/3$ and $E = 72{,}300 \ MPa$. [Solution: $K_{IC} = 72.5 \ MPa\sqrt{m}$ and $K_{IIC} = 62.77 \ MPa\sqrt{m}$].

[**8.2**] Repeat problem 8.1 using the strain energy density factor criterion (*S*-criterion).

[**8.3**] Determine a) the applied tensile stress and b) the safety factor for a loaded plate containing a $76\text{-}mm$ central crack inclined at 53.25°. The strain energy release rate mode I is $9.642\ kJ/m^2$. Data: $E = 207\ GPa$, $\sigma_{ys} = 958\ MPa$ and $v = 0.35$. [Solution: $\sigma = 201.38\ MPa$ and $SF = 4.46$].

[**8.4**] Calculate the critical stress (fracture stress) for the problem described in problem 8.3 according to the σ_θ-criterion. Will crack propagation take place?

[**8.5**] Repeat problem 8.4 using the *S*-criterion with [Solution: $\sigma_c = 204\ MPa$].

[**8.6**] Show that the stress intensity factor is $K_I = \left(\sqrt{8/11}\right) K_{IC}$ when $K_I = 2K_{III}$ and the Poisson's ration is $v = 1/3$.

8.8 REFERENCES

[1]   G.C. Sih and H. Liebowitz, "Mathematical Fundamental of Fracture," Academic Press, New York, (1968) 67-190

[2]   G.C. Sih, Inter. J. Fracture, 10(3) (1974) 305 - 321.

[3]   G.C. Sih, P.C. Paris and F. Erdogan, Inter. J. Fracture Mech., 29(1962) 306-312

[4]   R.W. Hertzberg, "Deformation and Fracture Mechanics of Engineering Materials," Third edition, John Wiley & Sons, New York, (1989)

[5]   F. Erdogan and G.C. Sih, "On The Crack Extension in Plates Under Plane Loading and Transverse Shear," J. Basic Eng., 85(1963) 519-527

[6]   R.J. Nuismer, Inter. Journal of Fracture, 11(1975) 245-250

[7]   S. Suresh and C.F. Shin, Inter J. Fracture, 30 (1986) 237-259

[8]   A.K. Vasudevan and S. Suresh, Mat. Sci. Eng. 72 (1985) 37-49

[9]   S. Suresh, Met. Trans. 16A (1985) 249-260

[10] C.H. Wu, J. Applied Mechanics, 45 (1978) 553-558

[11] C.S. Carter, Eng. Fract. Mech. 3(1971) 1-13

[12] D.R. Hayhurst, P.R. Brown and C.J. Morrison, Philosophical Transactions Royal Society London, A 311 (1984) 131-158

[13] Z. Yishu, Eng. Fracture Mech. Vol. 26, No. 5 (1987) 683-689

[14] B. Cottrell and J.R. Rice, Inter. J. Fracture 16 (1980) 155-169

[15] B.A. Bilby, G.E. Cardew and I.C. Howard, in fracture 1977, ed. by D.M.R. Taplin, Vol. 3, University of Waterloo Press (1977) 197-200

[16] H. Kitagawa, R. Yuki and T. Ohira, Eng. Fract. Mech. 7(1975) 515-529

[17] M.A. Hussain, S.L. Pu and J. Underwood, ASTM STP 560, (1973) 2-28.

[18] G.C. Sih, J. Appl. Mech. 32 (1965) 51-58

[19] K. Palaniswamy, Ph.D. Thesis, California Institute of Technology, (1972)

[20] B.C. Hoskin, D.G. Graff and P.J. Foden, Aer. Res. Lab., Melbourne, Report S.M. 305 (1965)

[21] Y. Xu, B. Moran, and T. Belytschko, Trans. ASME, J. Applied Mechanics, Vol. 65, (Sept. 1998) 557-565

[22] Y. Xu, Engineering Fracture Mechanics, Vol. 59, 2 (1999)

[23] M.L. Williams, "On The Stress Distribution At The Base Of A Stationary Crack," J. Appl. Mech., 24 (1957) 109-114

[24] T.L. Becker Jr., R.M. Cannon and R.O. Ritchie, "Finite Crack Kinking and T-stresses in Functionally Graded Materials," Inter. Journal of Solids and Structures, 38 (2001) 5545-5563

[25] B. Cotterell, "Notes on the Paths and Instability of Cracks," Inter. Journal of Fracture, 2 (1966) 526-533

[26] M.Y. He and J.W. Hutchinson, "Kinking of a Crack out of an Interface," J. Applied Mechanics, 56 (1989) 270-278

[27] M.Y. He, A. Bartlett, A. Evans and J.W. Hutchinson, "Kinking of a Crack out of an Interface: Role of Plane Stress," J. Am. Ceram. Soc., 74 (1991) 767-771

[28] K. Palaniswamy and W.G. Knauss, "On the Problem of Crack Extension in Brittle Solids under general loading," in S. Namat-Nassar editor, Mechanics Today, Pergamon Press, New York, Vol. 4 (1978)

Chapter 9

FATIGUE CRACK GROWTH

9.1   INTRODUCTION

Fatigue in materials subjected to repeated cyclic loading can be defined as a progressive failure due to crack initiation (stage I), crack growth (stage II), and crack propagation (stage III) or instability stage. For instance, crack initiation of crack-free solids may be characterized by fatigue crack nuclei due to dislocation motion, which generates slip bands at the surface having slip steps in the order of $0.1\ \mu m$ in height [1-2] or slip may occur at matrix-inclusion interfaces. These steps produce surface intrusions and extrusions as schematically indicate below for stages I and II. These intrusions caused by reversed slip due to load reversal are the source for crack initiation, which may consume most of the solid life before crack growth. This crack initiation may occur along the slip direction due to a local maximum shear stress. After the consumption of many cycles, the crack may change in direction when the maximum principal normal stress (in the vicinity of the crack tip) governs crack growth. In this stage II some materials show striations and beach marks as common surface features of fatigue fracture.

In general, fatigue is a form of failure caused by fluctuating or cyclic loads over a short or prolong period of time. Therefore, fatigue is a time-dependent failure mechanism related to microstructural features. The fluctuating loading condition is not a continuous failure process as opposed to cyclic loading. The former is manifested in bridges, aircrafts and machine components, while the latter requires a continuous constant or variable stress amplitude until fracture occurs. It is also important for the reader to know that fatigue failure or fracture can occur at a maximum stress below the static yield strength of a particular material. Obviously, temperature effects must be considered in fatigue failure characterization. From an engineering point of view, predicting fatigue life is major a requirement.

9.2   CYCLIC STRESS HISTORY

Figure 9.1 shows schematic cyclic-stress fluctuating curves with constant stress amplitude (symmetrical) and random loading as function of time. These schematic curves represent cyclic stress histories from which the number of cycles are accounted for fatigue life (N).
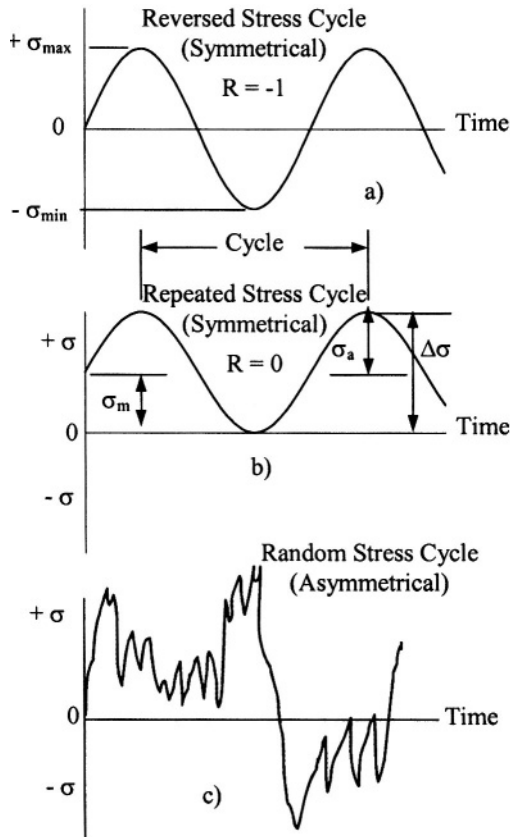
Figure 9.1 Schematic stress cycle histories

The stress history or stress spectrum can be

- 1) Axial due to tension-compression applied stresses

- 2) Flexural due to bending applied stress

- 3) Torsion due to twisting

The common stress parameters extracted from the constant amplitude (symmetrical) curves are the mean stress (σ_m), alternating stress (σ_a), the stress ratio and the stress amplitude (A_s)

$$\sigma_m = \frac{\sigma_{\max} + \sigma_{\min}}{2} \tag{9.1}$$

$$\sigma_a = \frac{\Delta\sigma}{2} = \frac{\sigma_{\max} - \sigma_{\min}}{2} \tag{9.2}$$

$$R = \frac{\sigma_{\min}}{\sigma_{\max}} = \frac{K_{\min}}{K_{\max}} \tag{9.3}$$

$$A_s = \frac{\sigma_a}{\sigma_m} \tag{9.4}$$

These stress parameters can be varied while conducting fatigue tests for characterizing materials having specific geometries, weldments or microstructural features. In fact, varying stress ratio is the most common parameter in determining the fatigue behavior of crack-free and cracked specimens. For crack-free specimens, the number of cycles to initiate a fatigue crack is known as the fatigue-crack initiation life (N_i), which can have a very large magnitude representing most of the usual life of a component. The remaining fatigue life (N_p) is related to stable fatigue crack growth till the crack reaches a critical length and consequently, crack propagation occurs very rapidly without any warning. As a result, a component can have a fatigue life defined by the total number of cycles, $N = N_i + N_p$, consumed during testing or service. Conversely, a pre-existing crack reduces fatigue life because $N_i = 0$ and $N = N_p$.

Despite that fatigue represents a cumulative damage in structural components, it is the fluctuating or cyclic local stresses and strains imparted by an external or nominal loading mode that are the primary factors for localized crack initiation and growth. Therefore, fatigue life can be prolonged if the nominal fluctuating or cyclic stress level is reduced or eliminated, the microstructure is homogeneous, dimensional changes are not severe enough or if the environment is not significantly corrosive.

For crack-free or notched specimens, the usual characterization of fatigue behavior is through a stress-cycle curve, commonly known as a S-N diagram. Figure 9.2 shows two S-N curves for different materials.

Figure 9.2 illustration with labels: Average S-N Curves @ R, Data scatter, Applied Stress (vertical axis), Fatigue Limit, Ferrous and Titanium Alloys, S_L, S_f, Fatigue Strength @ N, Nonferrous Alloys, N, $N_L \geq 10^6$, Cycles To Failure N
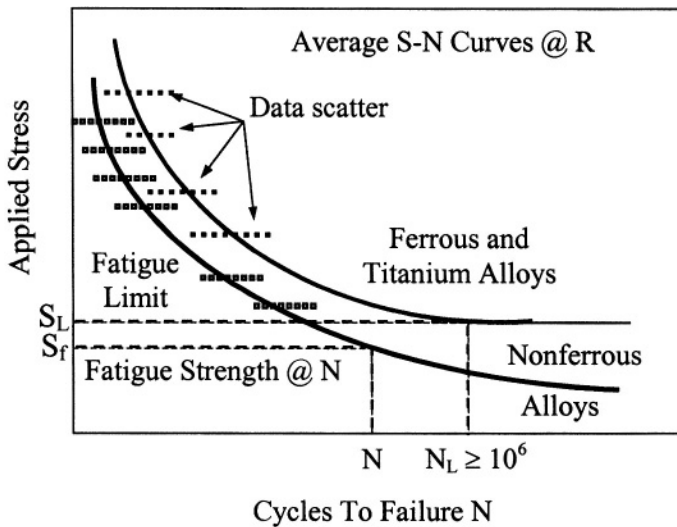
Figure 9.2 Schematic fatigue S-N curves

It should be pointed out that the fatigue limit (for infinite life) was formerly called the endurance limit and it is the stress level below which fatigue failure does not occur. Generally, ferrous alloys such as steels exhibit a stress limit, whilst nonferrous do not show an asymptote and the stress continues to decrease with increasing cycles to failure. The latter materials are characterized by determining the fatigue strength at a specific life (N). This stress is meaningless if the specific life is not identified.

Typically, fatigue life exhibits data scatter as schematically shown in Figure 9.1 for ferrous and titanium alloys. Nonferrous alloys also exhibit data scatter. Therefore, the difference in failure response of test specimens is due to microstructural defects and machining defects. In addition, a particular material having a fine-grained microstructure exhibit superior fatigue properties over coarse-grained microstructure.

Metal fatigue is a significant engineering problem because it can occur due to repeated or cyclic stresses below the static yield strength, unexpected and catastrophic failure of a vital structural part may occur and rack initiation may start at discontinuities in highly stressed regions of the component. Fatigue failure may be due to discontinuities such as inadequate design, improper maintenance and so forth.

Fatigue failure can be prevented by

- Avoiding sharp surfaces caused by punching, stamping, shearing and the like

- Preventing the development of surface discontinuities during processing.

- Reducing or eliminating tensile residual stresses caused by manufacturing

- Avoiding misuse and abuse

- Avoiding assembling errors, improper maintenance, manufacturing defects, design errors

- Using proper material and heat treatment procedures

- Using inert environments whenever possible

Furthermore, normally the nominal stresses in most structures are elastic or below the static yield strength of the base material. In pertinent cases, the strain-life (ϵ-N) can be determined instead of the stress-life (S-N) in high low cycle fatigue schemes.

9.3   FATIGUE CRACK INITIATION

It is not intended here to include a detailed background on crystallography, but a brief explanation on this subject can make the reader be aware of the implications in preventing and understanding fracture initiation at a atomic or nanoscale. With regard to common metallic structural materials, metals and engineering alloys are crystalline in nature since atoms are arranged uniformly forming unique repetitive three-dimensional arrays, which constitute what is known in crystallography as unit cells. As a result, the unit cells repeat themselves within grains (crystals) and their atomic mismatch is known as grain boundary. Figure 9.3a shows an schematic unit cell within the space lattice and Figure 9.3b depicts the atomic arrangement in a body-centered cubic (BCC) showing primary slip system $(110)[\bar{1}11]$. On the other hand, Figure 9.4 shows two real and different types of microstructures and therefore, the static and dynamic behavior of the corresponding alloys have distinct mechanical behavior. This means that the microstructure play a very significant role in mechanical behavior of solid bodies. Figure 9.5 exhibits two different dislocation networks as the representative line defects that develop during permanent deformation [54-56]. These figures are intended to show the different microstructural features of polycrystalline materials responsible for any observable mechanical behavior.

In general, fatigue crack initiation and growth depend on microstructural features, the maximum fluctuating stress and environment. Conversely, plastics or polymers are composed of molecules and are also important engineering materials; however, their fatigue mechanism is different from metals.

a) Space lattice

b) BCC unit cell
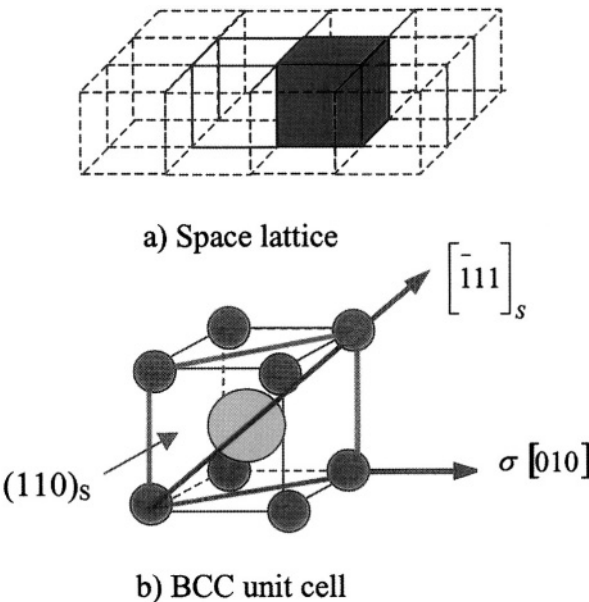
Figure 9.3 Atomic arrangement within a crystal. a) Repetitive array of unit cells and b) body-centered cubic (BCC) showing the slip direction (s), direction of the applied stress (σ) and the most dense plane for shear motion of atoms along the shown direction.

a) AISI 304 S.S.   b) RSA $Ni_{53}Mo_{35}Fe_9B_2$
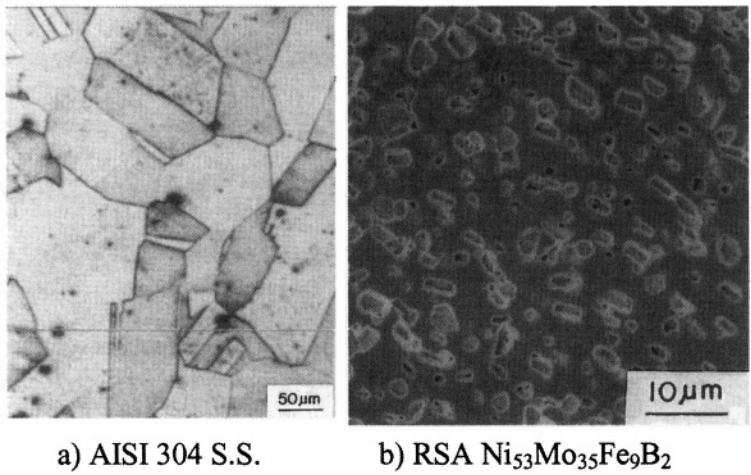
Figure 9.4 Microstructural features of a) 41% cold rolled stainless steel type AISI 304 showing austenite grains and b) rapidly solidified alloy exhibiting hard boride particles embedded in an Ni-Mo matrix [54-56].

a) Wrought 304 S.S.   b) RSA $Ni_{53}Mo_{35}B_9Fe_2$
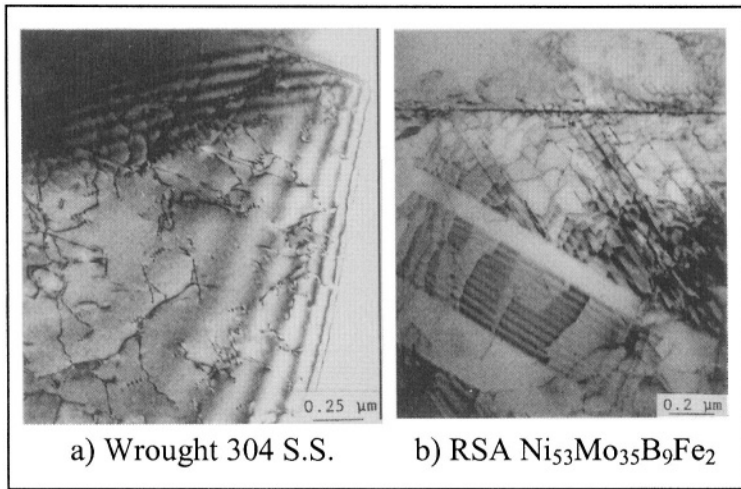
**Figure 9.5 Bright field TEM photomicrographs showing
dislocations networks [54]**

Consider a polycrystalline solid with a smooth surface being subjected to an elastic-cyclic stress range, in which $\sigma_{max} < \sigma_{ys}$ but σ_{max} is high enough to activate a slip mechanism such as the Cottrell-Hull modified mechanism [3-6] shown in Figure 9.6. Let the stress ratio be $R = -1$ for a fully reversed cyclic load system causing irreversible damage after many cycles. Take the slip planes A and B for convenience so that dislocation pile-ups occur on both sides of the planes, but having opposite signs as indicated in Figure 9.6a. When the slip system $\{hkl\} < uvw >$ is activated due to the local maximum shear stress τ, a surface step is created at $\sigma_{max} > 0$ (Figure 9.6b). Then dislocation motion is reversed once $\sigma_{min} > 0$ (Figure 9.6c). Also, the upper part moves toward its original position, leaving an inward step called intrusion in the order of the Burger's vector $b = 3\ mm$ [3]. This mechanism is repeated many times until a deeper intrusion acts as a micro-crack. During this stage I, many life cycles are consumed before crack growth in the direction perpendicular to the local principal normal tension stress, which governs the crack growth behavior, and the Cottrell mechanism no longer applies in a simple manner. This mechanism can take place in a few grains before the crack changes direction. Once this occurs other dislocation mechanisms such as the Frank-Read source may take place. When multiple cross-slip occurs, the Frank-Read source may not complete a loop cycle [4].
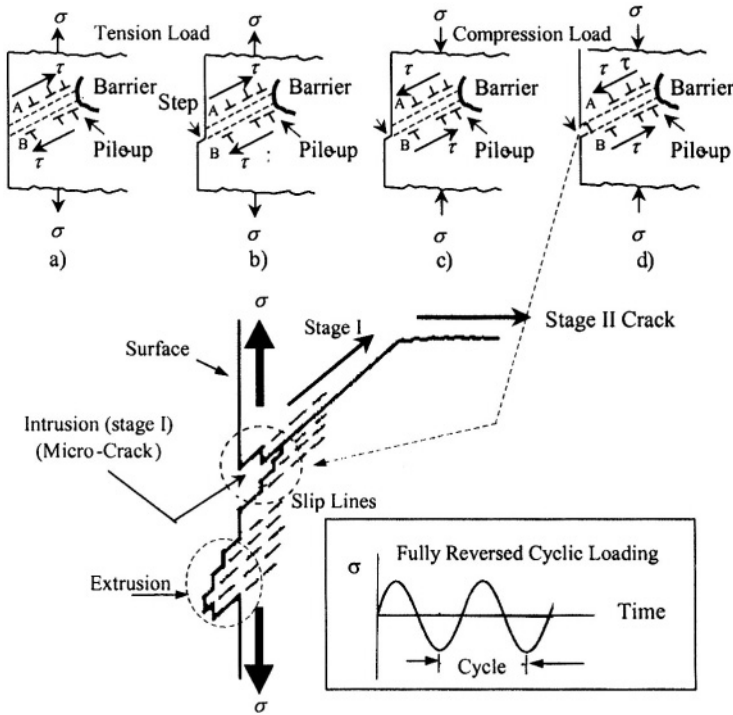
Figure 9.6 Cottrell-Hull fatigue mechanism in ductile materials

Nevertheless, the micro-crack becomes long enough, causing an increase in the stress concentration at the crack tip, and subsequently, the local stress is truncated to the yield strength of the solid. This leads to a stage II crack growth during which many grains are deformed making the plastic zone, which eventually reaches a critical size for crack growth continuation in the direction of the local principal stress which governs the stress field at the crack tip.

Since each grain has a different preferred orientation, crack growth may be in a zigzag manner due to different slip directions. As a result, fatigue surface features may consist of curved beach marks and striations in between. It is believed that each striation corresponds to a cycle and many striations are formed between beach marks. Therefore, it is possible that the plastic zone growth is related to sets of striations and its rupture at a critical size may be attributed to the formation of a beach mark. In addition, solid bodies subjected to a fluctuating load, as opposed to a monotonic load, may develop cracks that may grow very slowly. The fatigue maximum tension load (lower than the monotonic maximum) is attributed to cause crack opening. On the other hand, the minimum load closes the crack. At this point, crack closure will be neglected.

Fatigue Fracture is a cyclic mechanical process in which a stress range is applied at constant or varying stress amplitude until rupture occurs. It is a complex phenomenon since it may start from macroscopic pre-cracks, occur in

originally crack-free bodies or initiate in slip zones adjacent to the outer surface or in internal defects, such as voids or inclusions.

The mechanism of fatigue fracture may be initiated at a microscopic defect since

- A cumulative displacement between slip planes occurs

- An intrusion, as formed in a slip direction, may be the original source for a micro-crack.

- A triple point at grain boundaries may be a source of crack initiation or cracks may be developed by stress corrosion action, such as hydrogen embrittlement.

However, the direction of fatigue crack growth may change from the slip orientation (stage I) to an average cracking normal to the maximum tension direction corresponding to the stage II process. Thus, the characteristics of crack growth may be transcrystalline either by progressive plastic straining, which causes typical striations or by cleavage at low temperatures or in the presence of brittle inclusions.

On the other hand, crack growth may be intercrystalline due to bonding deficiency, aggressive environment or due to initiation and coalescence of voids within or between grains. Then, the final stage (III) of fatigue fracture is caused by a dynamic crack propagation mechanism, in which the applied maximum stress intensity factor reaches a critical value equals to the plane stress or plane strain fracture toughness of the material. Therefore, the final fatigue process leads to failure or rupture.

9.4   FATIGUE CRACK GROWTH RATE

Since fatigue is a cyclic dissipation of energy, in the form of hysteretic loops, which are related to a cumulative damage process, the elapsed time for damage is expressed in terms of the number of fatigue cycles *(N)*. The control parameter that is used to evaluate this process is the rate of crack growth per cycle (da/dN). Hence, da/dN depends on the applied stress intensity factor range (ΔK) and N is the well-known fatigue life term.

For crack initiation or stage I, the threshold stress intensity factor and threshold stress range are associated as

$$\Delta K_{th} = \alpha \Delta \sigma_{th} \sqrt{\pi a} \tag{9.5}$$

Here, α is the geometric correction factor introduced in Chapter 3 and $\Delta \sigma_{th}$ is analogous to fatigue limit S_L. This equation indicated that if $\Delta \sigma < \Delta \sigma_{th}$ crack growth does not occur. On the other hand, in the early 1960's, Paris [6] empirically expressed the phenomenon associated with the rate of fatigue crack

growth in stage II in terms of the stress intensity factor range (ΔK). Thus, the Paris law for stage II is defined by

$$\frac{da}{dN} = A(\Delta K)^n \tag{9.6}$$

$$\Delta K = \Delta\sigma\sqrt{\pi a} \quad \text{(Uncorrected)} \tag{9.7}$$

$$\Delta K = \alpha\Delta\sigma\sqrt{\pi a} \quad \text{(Corrected)} \tag{9.8}$$

where $\Delta K = K_{\max} - K_{\min}$
A = Constant $(MPa^{-n}.m^{1-n/2}/cycles)$
n = Exponent
α = Geometric correction factor introduced in Chapter 3
$\Delta\sigma = \sigma_{\max} - \sigma_{\min}$ = Stress range

Figure 9.7 shows the procedure da/dN for estimating stage II in an actual laboratory exercise. Notice that the tangential slope of $a = f(N)$ for a constant stress ratio R is da/dN, which increases rapidly as the crack grows and the number of applied cycles increases. Moreover, the effect of the stress ratio R on crack growth is remarkably noticeable since increasing R increases da/dN and fracture is accelerated. The Paris law has empirically been modified in order to incorporate the cyclic stress ratio.
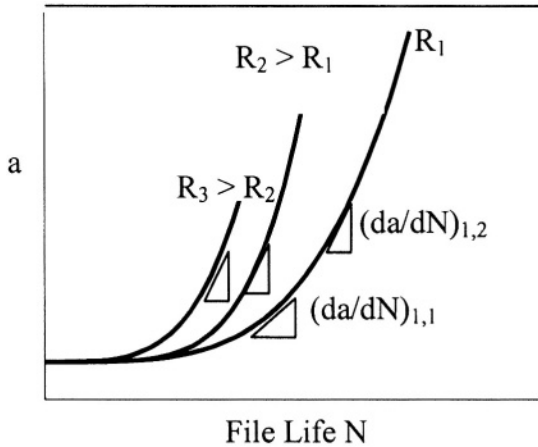
Figure 9.7 Schematic fatigue crack growth curves

In addition, some expressions cited in the literature are given as

• Forman equation [7]:

$$\frac{da}{dN} = \frac{A(\Delta K)^n}{(1-R)K_C - \Delta K} \qquad \text{For plane stress and } R > 1 \qquad (9.9)$$

$$\frac{da}{dN} = \frac{A(\Delta K)^n}{(1-R)K_{IC} - \Delta K} \qquad \text{For plane strain and } R > 1 \qquad (9.10)$$

- Broek and Schijve equation [8-9]:

$$\frac{da}{dN} = AK^2_{max}(\Delta K)^n \qquad (9.11)$$

- Walker equations [10]:

$$\frac{da}{dN} = AK^m_{max}(\Delta K)^n \qquad (9.12)$$

$$\frac{da}{dN} = A\sigma_{max}(1-R)\sqrt{\pi a} \qquad \text{For } R > 1 \qquad (9.13)$$

- Hartman and Schijve equation [11]:

$$\frac{da}{dN} = \frac{A(\Delta K - \Delta K_{th})^n}{(1-R)K_C - \Delta K} \qquad \text{For plane stress and } R > 1 \qquad (9.14)$$

Denote that the exponent n in the above equations is not have a fixed value.

9.5 FATIGUE LIFE CALCULATIONS

The goal here is to develop a mathematical model that predicts Fatigue Life (N) for a given stress range at a constant load amplitude. Since Mode I loading is the most studied, integration of eq. (9.6) is carried out for this mode for convenience; however, other mode of loading may be used instead. Nevertheless, the fatigue life *(N)* sought is

$$\int_{N_o}^{N} dN = \int_{a_o}^{a} \frac{da}{A(\Delta K)^n} \qquad (9.15)$$

Inserting eq. (9.8) into (9.15), integrating and arranging the resultant expression yields

$$N - N_o = \frac{2a}{A(n-2)(\alpha\Delta\sigma)^n (\pi^{n/2})} \left[\left(\frac{a}{a_o}\right)^{n/2-1} - 1 \right] \qquad \text{For } n \neq 2 \quad (9.16)$$

Assuming that final fracture occurs when the crack length reaches a critical (maximum) size so that $a = a_c$ and $\Delta K = K_{max}$. For plane strain conditions, the critical crack length along with $K_{max} = K_{IC}$ can be predicted by

$$a_c = \frac{1}{\pi} \left(\frac{K_{IC}}{\alpha}\right)^2 \Delta\sigma^{-2} \tag{9.17}$$

Substituting eq. (9.17) along with $a = a_c$ into (9.16) yields an important expression for determining the stress range $\Delta\sigma$ when the final crack size is unknown

$$C_1 \left(\Delta\sigma\right)^n + C_2 \left(\Delta\sigma\right)^{n-2} - C_3 = 0 \tag{9.18}$$

where

$$
\begin{aligned}
C_1 &= A\left(n-2\right)\left(N - N_o\right)\left(K_{IC}\right)^n \\[2mm]
C_2 &= \frac{2}{\pi} \left(\frac{K_{IC}}{\alpha}\right)^2 \\[2mm]
C_3 &= 2\left(a\right)^{1-n/2} \left(\frac{1}{\pi}\right)^{n/2} \left(\frac{K_{IC}}{\alpha}\right)^n
\end{aligned}
\tag{9.19}
$$

Example 9.1 *A high-strength steel string has a miniature round surface crack of* 0.09 *mm deep and a outer diameter of* 1.08 *mm. The string is subjected to a repeated fluctuating load* $(\sigma_{\min} = 0, \sigma_{\max} > 0$ *at a stress ratio* $R = 0$*. The threshold stress intensity factor is* $\Delta K_{th} = 5\ MPa\sqrt{m}$*, and the crack growth rate equation is given by*
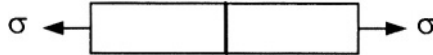
$$\frac{da}{dN} = \left(5x10^{-14}\ \frac{MN^{-4}.m^7}{cycles}\right)(\Delta K)^4$$

Determine a) the threshold stress $\Delta\sigma_{th}$ *the string can tolerate without crack growth, b) the maximum applied stress range* $\Delta\sigma$ *and c) the maximum (critical) crack size for a fatigue life of* $N = 10^4$ *cycles. Use the following steel properties:* $K_{IC} = 25\ MPa\sqrt{m}$ *and* $\sigma_{ys} = 795\ MPa$*.*

Solution: *It is assumed that the plastic-zone with a cyclic range* ΔK *is smaller than that for* K_I *applied monotonically, and that the surface crack can be treated as a single-edge crack configuration. Note that* $N_o = 0$ *since* a_o *already exists. Data:*

a) *From eqs. (3.56),*

$$a = \frac{D-d}{2} \tag{3.56}$$

$$d = D - 2a = 1.08 \ mm - 2(0.09 \ mm) = 0.90 \ mm$$

$$\frac{d}{D} = 0.8333 \quad \text{and} \quad \frac{D}{d} = 1.20$$

Thus, eqs. (3.54) and (9.5) yield respectively

$$f(d/D) = \frac{1}{2}\sqrt{\frac{D}{d}}\left[\frac{D}{d} + \frac{1}{2} + \frac{3}{8}\left(\frac{d}{D}\right) - \frac{5}{14}\left(\frac{d}{D}\right)^2 + \frac{11}{15}\left(\frac{d}{D}\right)^3\right] \tag{3.55}$$

$$\alpha = f(d/D) = 1.1989$$

$$\Delta\sigma_{th} = \frac{\Delta K_{th}}{\alpha\sqrt{\pi a_o}} = \frac{5 \ MPa\sqrt{m}}{(1.1989)\sqrt{\pi(0.09 \times 10^{-3} \ m)}} = 248.02 \ MPa$$

$$\Delta\sigma_{min} < \Delta\sigma_{th}$$

b) *Use eq. (9.19) and subsequently (9.18) to get*

$$C_1 = \left(5 \times 10^{-14} \ \frac{MN^{-4}.m^7}{cycles}\right)(4-2)\left(10^4 \ cycles\right)\left(25 \ \frac{MN}{m^2}\sqrt{m}\right)^4$$

$$C_1 = 3.9063 \times 10^{-4} \ m$$

$$C_2 = \frac{2}{\pi}\left(\frac{K_{IC}}{\alpha}\right)^2 = \frac{2}{\pi}\left(\frac{25 \ MPa\sqrt{m}}{1.1989}\right)^2 = 276.82 \ MPa^2.m \tag{9.19}$$

$$C_3 = 2\left(0.09 \times 10^{-3} \ m\right)^{1-4/2}\left(\frac{1}{\pi}\right)^{4/2}\left(\frac{25 \ MPa\sqrt{m}}{1.1989}\right)^4$$

$$C_3 = 4.2571 \times 10^8 \ MPa^4.m$$

and

$$3.9063 \times 10^{-4}\Delta\sigma^4 + 276.82\Delta\sigma^2 - 4.2571 \times 10^8 = 0$$

Solving the above biquadratic equation yields four roots. The positive root is

$$\Delta\sigma = 864.93 \ MPa$$

$$\sigma_{max} = \Delta\sigma = 864.93 \ MPa \quad \text{since} \quad \sigma_{min} = 0$$

$$\sigma_{max} \lessapprox \sigma_{ys}$$

b) *The critical crack size is calculated from eq. (9.17)*

$$a_c \;=\; \frac{1}{\pi}\left[\frac{K_{IC}}{\alpha}\right]^2 \Delta\sigma^{-2} = \frac{1}{\pi}\left[\frac{25\ MPa\sqrt{m}}{(1.198\,9)\,(864.93\ MPa)}\right]^2 \qquad (9.17)$$

$$a_c \;=\; 0.185\ mm = 2.056 a_o$$

$$\Delta a \;=\; a_c - a_o = 0.095\ mm$$

Therefore, $\Delta a = 0.095\ mm$ represents 5.56% increment at a maximum fluctuating stress $\sigma_{\max} \lesssim \sigma_{ys}$ for a fatigue life of 10^4 cycles.

9.6   CRACK GROWTH RATE DIAGRAM

In addition, a detailed fatigue-crack growth behavior (sigmoidal curve) is schematically shown in Figure 9.8 [12]. Stage I is a slow crack growth region in which the fatigue threshold stress intensity factor range is usually less than $DK < 9$ $MPa\sqrt{m}$ [12], and below this value fatigue crack growth does not occur. In addition, stage I is rather a complex region from a micro-scale point of view, but it is related to a non-continuum crack growth mechanism, which strongly depends on the materials microstructure, the applied stress ratio R and the environment.
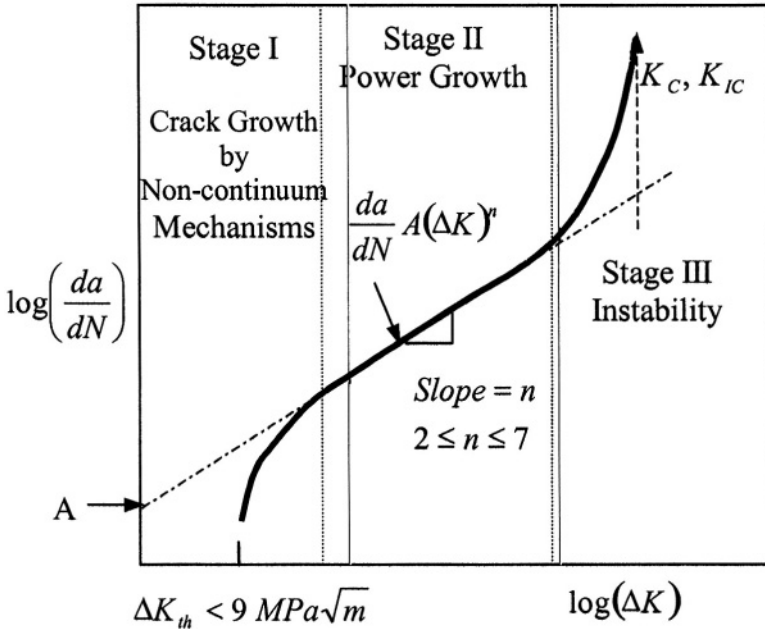
Figure 9.8 Schematic stages of fatigue crack growth rate

ANALYSIS OF Figure 9.8:

Stage I: This is a slow crack growth process which is related to non-continuum mechanisms and slow fatigue crack growth in the order of $da/dN \leq 10^{-6}$ $mm/cycle$. Thus, this fatigue process strongly depends on the

- a) Microstructural parameters such as grain size, precipitates, dislocation density, etc.

- b) Mean tress and stress ratio

- c) Aggressiveness of the environment

- d) Surface damage initiation

Stage II: This fatigue process is referred to as the power growth behavior usually characterized by the Paris law and it slightly depends on the parameters in stage I. Particularly, surface characteristics are the formation of beach marks and striations in some metallic materials. Furthermore, the specimen thickness does not strongly influence the fatigue crack growth rate.

Striations are microscopic fatigue features that can be observed with the scanning electron microscope (SEM) and the transmission electron microscope (TEM) at relatively high magnifications. Conversely, each striation indicates a successive advance of one stress cycle. The width of a striation represents the advance of the crack front during one stress cycle, but it depends on the magnitude of the applied stress range. Normally, the appearance of service fatigue striations is irregular due to changeable stress amplitude. Striation are dealt with in later section. Then, this irregularity in striation configuration is an indication of non-steady crack growth rate, which may be restricted to geometry-dependency and load history, leading to an enhanced or retarded rate.

Stage III: This fatigue process strongly depends on the microstructural parameters cited in stage I and on the specimen thickness. Since the applied stress intensity factor is sufficiently large, the fatigue crack growth is high and the process is under an instable damage process. Therefore, this is the instability region in Figure 9.8 and fracture occurs when the stress intensity factor reaches a critical value.

Figure 9.9 schematically shows the influence of R on stage I [13]. Figure 9.10 depicts experimental $da/dN = f(R, \Delta K)$ for a structural steel [14] For instance, the most common engineering metallic materials have a BCC, FCC, or HCP atomic structure; therefore, the fatigue behavior of these materials is expected to be different. Generally, surface crack initiation occurs in this State I in which the crack growth rate is very slow. In addition, stage II is known as the power crack growth, which is less dependent on the microstructure, stress ratio, and environment than stage I. The log-log linear fatigue behavior is referred to as the Paris Law, which empirically define by eq. (9.6). The characteristics of the surface fracture appearance may include beach marks and striations that are observable in certain materials such aluminum and aluminum alloys. Both

fatigue fracture features are concentric ridges of circular, semicircular or semi-elliptical shape. Beach marks (or clamshell marks) are macroscopic bands-containing striations, represent the position of the crack of length and are formed due to interruptions of the cyclic stress loading during service.
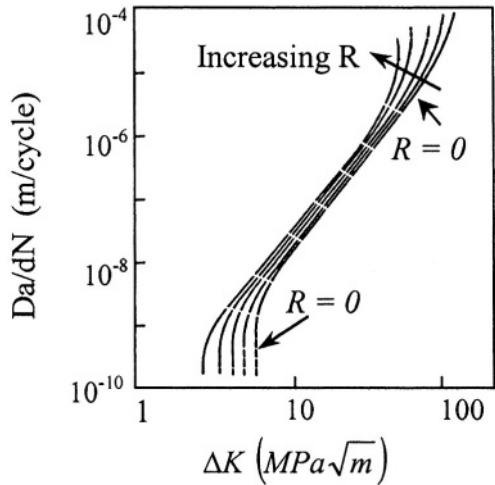
Figure 9.9 Schematic effects of stress ratio on the crack growth rate curves [13]
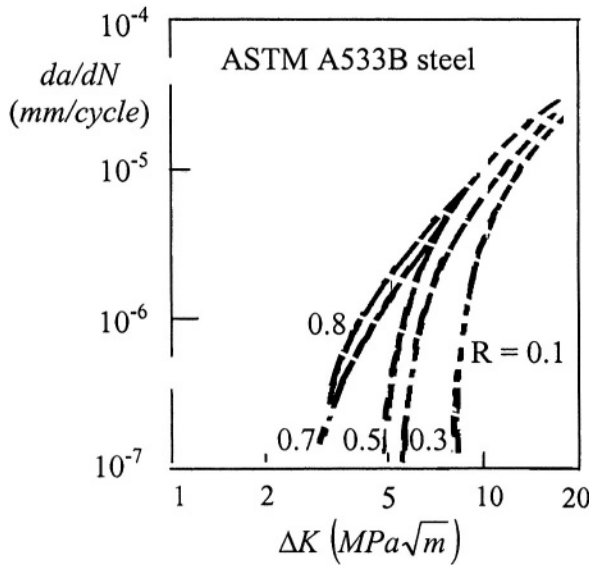
Figure 9.10 Effect of stress ration on fatigue crack growth rate of ASTM A533B steel [14]

Despite the experimental data scatter found in steels, Barsom and Rolfe [14] determined conservative crack growth rate expressions as given in Table 9.1. based on Paris equation for fatigue stage II at $R = 0$. If experimental data is not available for a particular steel, these equations can be used in designing with proper caution. Thus,

Table 9.1 Fatigue crack growth rate equations for steels [14]

Steel	Paris equation $(m/cycle)$	Strength
Martensitic	$\frac{da}{dN} = 1.35x10^{-10} (\Delta K)^{2.25}$ ΔK in $MPa\sqrt{m}$	$\sigma_{ys} > 483\ MPa$ $\sigma_{ts} > 621\ MPa$
Ferritic-Pearlitic	$\frac{da}{dN} = 6.90x10^{-12} (\Delta K)^{3}$	$207\ MP < \sigma_{ys} < 552\ MPa$
Austenitic	$\frac{da}{dN} = 5.60x10^{-12} (\Delta K)^{3.25}$	$207\ MP < \sigma_{ys} < 345\ MPa$

Fatigue crack growth data is quite abundant in the literature, but some selected experimental data are included in Table 9.2 as a reference. Useful experimental data can be found elsewhere [15-49].

Table 9.2 Fatigue crack growth data for some materials. $K_{IC}, \Delta K_{th}$ and ΔK in $MPa\sqrt{m}$ and A in $MN^{-n}.m^{1-n/2}/cycle$. S.S. = Stainless steel

Materials	σ_{ys} (MPa)	K_{IC}	R	ΔK_{th}	n	A	Ref.
12Cr S.S	730	102	0	5	3.5	1.70x10^{-9}	[19]
304 S.S.	1400	66	0	4.6	3.6	4.77x10^{-11}	[22]
403 S.S	100	115	0.5	5.52	2.6	1.90x10^{-11}	[24]
Ti-6Al-4V	1172	70	0.4	14.7	4.0	1.00x10^{-12}	[28]
Ti-6Al-4V	880	91	0.02	$\simeq 5$	3.6	1.91x10^{-13}	[27]
Nb-37Ti-13Cr	1107	26	0.1	7	5.5	3.40x10^{-14}	[45]
Nb-15Al-49Ti	660	110	0.1	$\simeq 5$	9.7	5.00x10^{-19}	[46]

With regard to Figure 9.8, the transition between stage II and III apparently is related to tearing mechanism when the crack tip strain reaches a critical value [49]. For a $R = 0$, $\Delta K = \Delta K_{max}$ and the onset of the transition apparently occurs at a constant crack tip opening displacement (δ_t), which can be estimated according to Barsom's relationship of the form [50]

$$\delta_{trans} = \frac{\Delta K_{tran}^2}{E\sigma_F} \tag{9.20}$$

and

$$\sigma_F = \frac{\sigma_{ys} + \sigma_{ts}}{2} \tag{9.21}$$

where ΔK_{tran} is the transition stress intensity factor, which can be set equals to the upper limit of the valid range of ΔK in stage II. Actually, σ_F is the flow stress for this transition and E is the modulus of elasticity.

In addition, Figure 9.11 shows recently published da/dN data using compact tension (CT) specimens according to the ASTM E647 Standard Test Method for Measurement of Fatigue Crack growth and a specific software [57]. The testing material apparently was a steel alloy. From this figure, the threshold stress intensity factor approximately $\Delta K_{th} \simeq 7.8 \sqrt{MPam}$, agrees with the information given in Figure 9.8 that $\Delta K_{th} < 9 \sqrt{MPam}$. The reason fro selecting this particular data is to inform the reader that fracture mechanics tests can be conducted using state-of-the-art instrumentation accompanied with reliable software to speed up calculations and avoid human errors.

The curve fitting equation for data in Figure 9.11 is

$$\frac{da}{dN} = 2x10^7 (\Delta K)^2 - 10^7 (\Delta K) - 4x10^7 \tag{9.22}$$
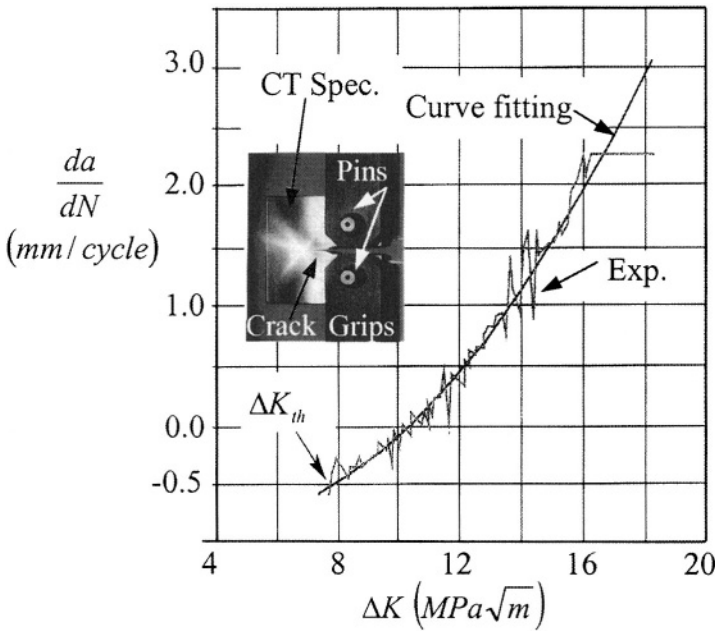
Figure 9.11 Fxperimentral fatigue crack growth data for a compact tension (CT) steel specimen [57]

From a metallurgical point of view, Paris [16] compared fatigue crack growth rate data for FCC, BCC and HCP metallic solids. For convenience, only FCC and BCC data are shown in Figure 9.12. Therefore, it is clear that this data set correlates with the Paris law, eq. (9.6).
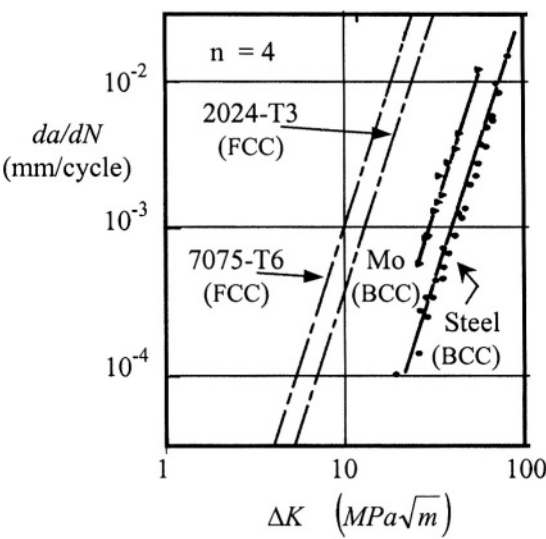
Figure 9.12 Comparison of FCC and BCC crack growth rates [16].

An analogous da/dN behavior for polymers is depicted in Figure 9.13. There-fore, fatigue crack growth behavior is mathematically described by the function $da/dN = f(\Delta K)$, the simplest being the Paris equation.
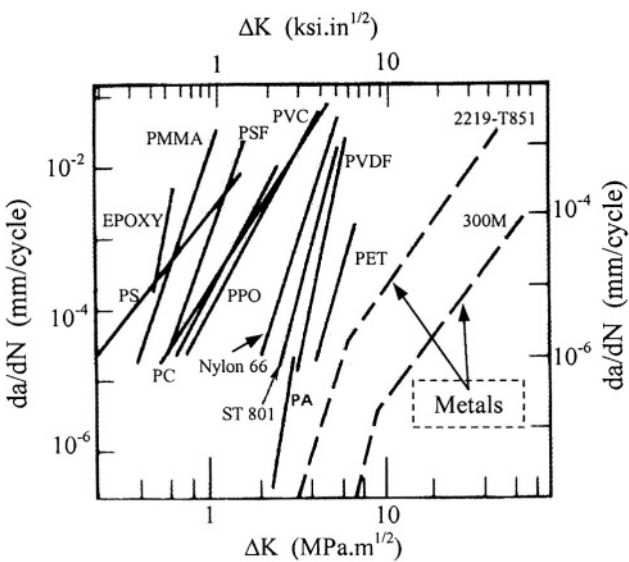
Figure 9.13 Fatigue crack growth behavior of polymers and two metals [63].

9.7   WELDMENTS

Welding is a fabrication process for joining two or more parts to form one single part.   The joining process is a localized metallurgical process related to solidification.   The resultant welded area is metallurgically heterogeneous with respect to microstructural features. Nevertheless, the joining process can be achieved by laser beam welding (LBW), arc and gas welding, brazing and soldering using relatively low melting temperature metals (Pb-Sn), explosive welding, ultrasonic welding, and by friction stir welding technique [58]. The reader should consult the American Welding Society, the Welding Institute of the United Kingdom and a new technical article published by American Society for Metals International. Figure 9.14 shows a typical plot for welded pressure vessel steel specimens [59-60].
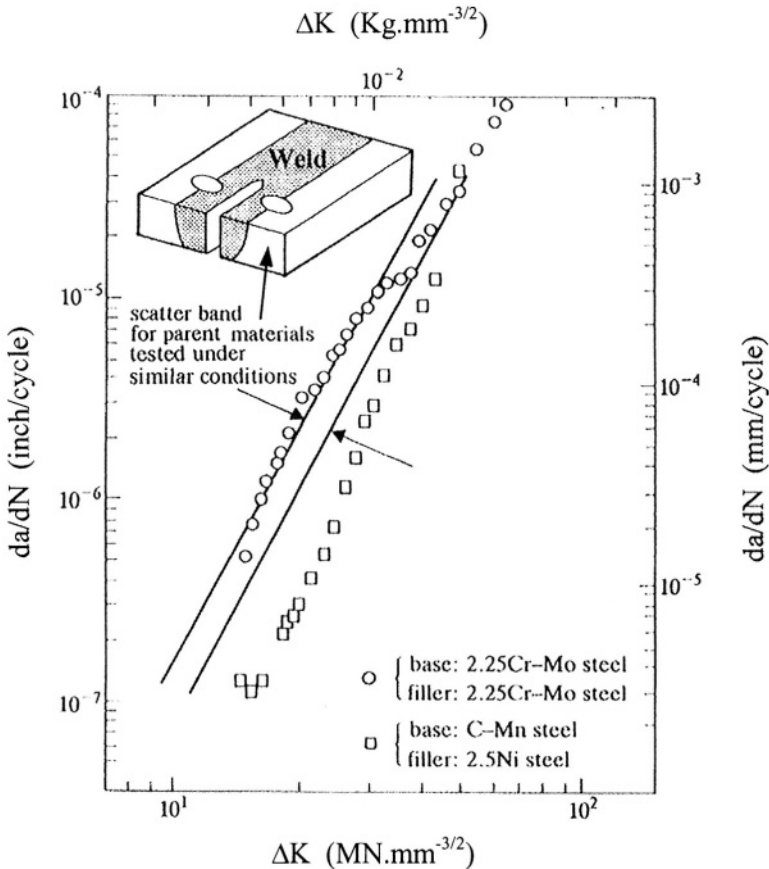
Figure 9.14 Fatigue crack growth behavior of pressure vessel steel weldments in air at $24^\circ C$ [59]. This refernce was taken from Lancaster [60].

Figure 9.15 depicts Viswanathan's model [61] for microstructural changes in the heat affected zone (HAZ) adjacent to the weld, which in turn is related to the Fe-C phase diagram. This schematic representation of the microstructural changes in the base metal with respect to grain size and grain morphology is typical in submerged arc welding *(SMAW)* process of Cr-Mo steels. Consequently, mechanical properties in the HAZ are affected by the cooling rate within the welded region and grain size in the HAZ. In alloy steels, martensite may form as an undesirable phase because it is brittle. The different microstructures are labeled schematically in Figure 9.15 as zones. These different microstructural zones disturb the microstructural symmetry of the parent metal and as a consequence, mechanical and corrosion properties vary through the HAZ. One particular solution to this metallurgical problem is to heat treat the welded part whenever possible to obtain a uniform microstructure.

In general, welding cracks or HAZ cracking may occur due to tensile residual stresses that develop upon contraction of the welding bead. Therefore, welding should be done properly in order to avoid welding defects because they have a strongly affect mechanical properties.
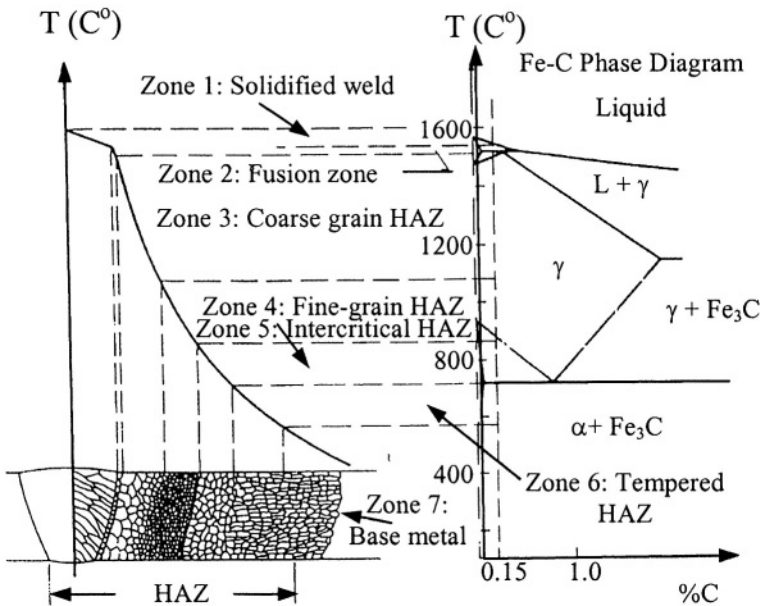
Figure 9.15 Heat affected zone (HAZ) adjacent to the weld [61].

The Paris law is the most common approach for correlating da/dN with ΔK in weldments. In fact, the weld bead or solid-phase weld is the part of the joined materials that is tested and characterized. It is apparent that a good correlation exists for $da/dN = f(\Delta K)$ in stage II, where the Paris law describes the observed fatigue behavior [59].

9.8   SURFACE FRACTURE APPEARANCES

This section is focussed on the appearance of fracture surfaces that are vital in failure analysis in conjunction with knowledge of the load history in a particular environment. Figure 9.16 shows Schijve's model [15] that provides details of a fracture surface exhibiting typical ductile fracture features encountered in many engineering materials under quasi-static loads. These features are affected by applied stress conditions, specimen geometry, flaw size, mechanical properties and environment. Subsequent fatigue crack growth or crack extension is associated with increasing applied stress, which in turn increases the stress intensity factor. Some solid materials can show a shear lip as an indicative of ductile fracture and as a result, the fracture surface exhibits a slant *(SL)* area. Some materials exhibit double-shear lips which are indications of ductile fracture due to an overload. Conversely, a brittle fracture surface is normally flat without shear lips.
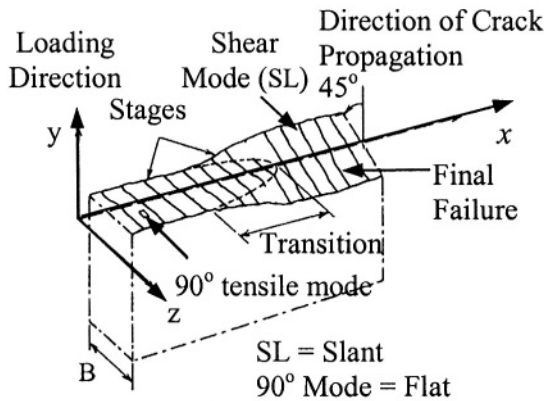
Figure 9.16 Schematic fracture surface transition from flat to slant appearance [15].

In addition, environmental effects, such as low and high temperatures and corrosive media, can have a significant impact on the mechanical behavior and fracture appearances of solid bodies. For instance, a ductile steel alloy may become brittle at relatively low temperatures.

Stage II Fatigue Failure: This is due to a change in crack growth direction of stage I as shown in Figure 9.6, in which the crack in a polycrystalline material advances along crystallographic planes of high shear stress. The characteristics for fatigue failure of stage II can be summarized as per schematically shown in Figure 9.17.

The fatigue events are described as follows:

• Crack growth occurs by repetitive plastic blunting and sharpening of the crack front.

- Shear deformation direction reverts to complete a full cycle in compression. This event may cause cleavage fracture.

- If rapid crack growth rate occurs, then rapid failure takes place, and beach marks and striations may be absent, regardless if the material is ductile or brittle.

- Intercrystalline fracture is possible, particularly at the lower range of stress.

- Formation of striations depends on the nature of the materials, such as aluminum and Al-alloys. However, steels may exhibit cleavage mechanism as a dominant fracture mode.
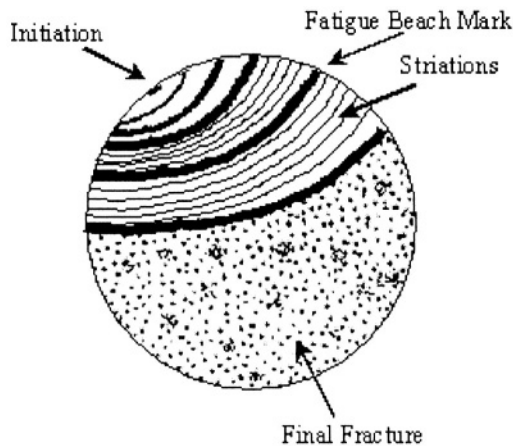
Figure 9.17 Schematic fatigue fracture surface.

- Striations indicate the changing position of the crack front with each new cycle of loading.

- Ripple (annual ring) patterns can form on the fracture surface.

- The domain of high-cycle fatigue prevails during stage II.

Model for the Formation of Striations: Figure 9.18 shows Broek's possible mechanism [33] for the formation of striations in certain materials, such as aluminum alloys and in some strain-hardened alloys.
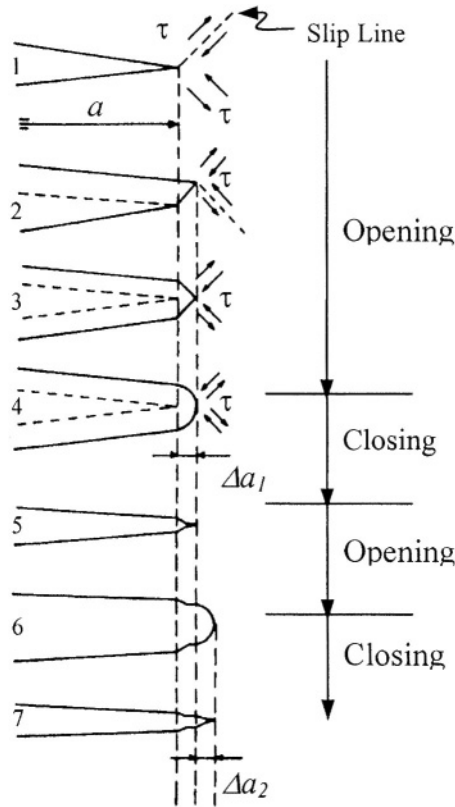
Figure 9.18 Model for the formation of fatigue striations [33].

The possible stages during the formation of striations are

- 1 & 2) Slip formation occurs at the crack tip due to a stress concentration. Slips form in the direction of maximum shear stress as explained by the Cottrell-Hull mechanism (Figure 9.6), and the crack opens and extends in length (Δa). A particular model for a slip system, $(100)[\bar{1}11]$, in BCC structure is shown in Figure 9.3b. In addition, Figure 9.19 shows a unique microphotograph of wavy slip lines in BCC niobium (Nb) [62].

- 3) Other slip planes are activated and consequently, cross-slip may occur.

- 4) Crack tip blunting occurs due to strain hardening, which may activate other slip planes.

- 5) The crack re-sharpens due to plastic deformation (plastic zone) embedded in the elastic surroundings. During load release, the elastic surroundings excerpt compressive stresses on the plastic zone. This reversed plastic deformation process closes and re-sharpens the crack tip.

- 6&7) Crack closure and re-sharpen occur due to repeated loading, leading to more crack growth (extension).
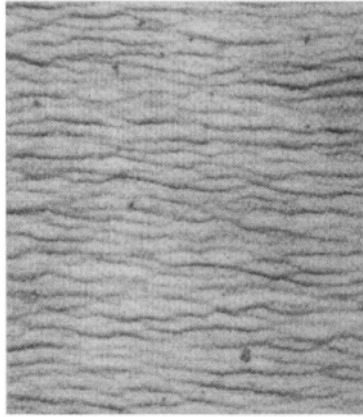
Figure 9.19 Wavy slip lines in niobium after static deformation [62].

The cyclic opening and closing of the crack develops a typical pattern of ripples called fatigue striations. The above model (Figure 9.18) of striation formation is a general representation of crack blunting and re-sharpening in ductile or sufficiently ductile materials. However, a cleavage mechanism may involve brittle striations, as opposed to ductile striations.

Figure 9.20 shows the characteristic fatigue striations of an Al-alloy having a modulus of elasticity approximately equals to $E = 72,000 \ MPa$.
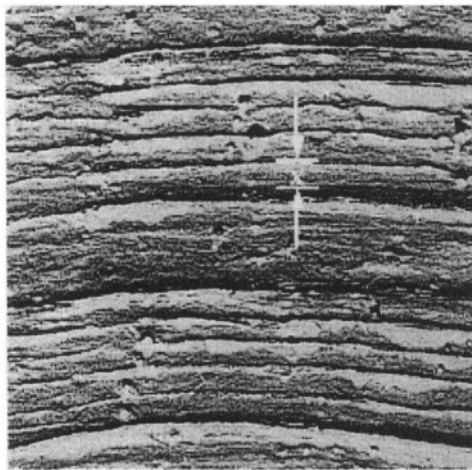
Figure 9.20 Fatigue striations on a crack surface of an Al-alloy. Magnification: 12,000X [18].

These striations are ripples on the fractured surface caused by perturbations in the cyclic stress system. The width of a striation depends on the fatigue stress, but it is in the order of 10^{-4} *mm* or less. For instance, the apparent stress intensity factor range is related to striation spacing as empirically proposed by Bates and Clark [34]

$$\Delta K = E\sqrt{\frac{x}{6}} \tag{9.23}$$

where E = Modulus of elasticity (MPa)
       x = Average striation spacing (μm)

The striation spacing is a measure of slow crack growth per stress cycle and it may be constant for constant stress amplitude. However, striations may not form when the stress range and the maximum stress are relatively large, leading to fast fatigue crack growth rate [35].

Example 9.2 *Determine the apparent stress intensity factor range and the fatigue crack growth rate for the aluminum alloy fracture surface shown in Figure 9.20. Use a modulus of elasticity of* $72,000$ *MPa.*

Solution:

The solution to this problem requires that the actual average striation spacing be calculated using the magnification given in Figure 9.10. The average striation spacing as denoted in Figure 9.20 is approximately

$$x = \frac{4\ mm}{12,000} = 3.3333x10^{-4}\ mm = 333.33\ \mu m$$

Then, using eq. (9.23) yields

$$\Delta K \quad = \quad E\sqrt{\frac{x}{6}} = (72,000 MPa)\sqrt{\frac{4x10^{-3}\ m}{(6)\,(12,000)}} \tag{9.23}$$

$$\Delta K \quad \simeq \quad 17\ MPa\sqrt{m}$$

Since the striation spacing is a measure of slow crack growth per stress cycle the estimated actual fatigue crack growth rate is

$$\frac{da}{dN} \simeq \frac{\Delta a}{\Delta N} = 333.33\ \frac{\mu m}{cycle}$$

Example 9.3 *Let's use Fuchs and Stephen problem 8.13* [13] *with reference to a fractograph reported by Crooker et al.* [64] *to illustrate another approximation technique in fatigue failure analysis. A 17-4 HP stainless steel plate*

containing a 6-mm single-edge crack was subjected to a constant cyclic loading with a stress ratio of R = 0. The plate was 5-mm thick, 20-mm wide and sufficiently long. Calculate the apparent stress intensity factor range and the maximum load. The crack growth rate as per Paris equation was

$$\frac{da}{dN} = \left(10^{-12} \ m/cycle\right) \left(\Delta K\right)^{3.5}$$

1 μm
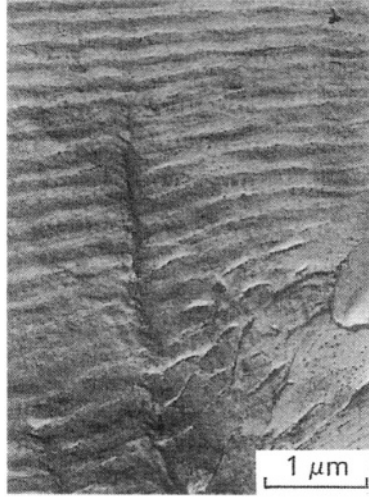
Solution:

Given data: $a = 6 \ mm$ $w = 20 \ mm$ $B = 5 \ mm$ $b = w - a = 14 \ mm$

$$a/w = 0.3 \qquad R = K_{min}/K_{max} = 0 \qquad K_{min} = 0$$

The geometric correction factor for this crack configuration is given in Table 3.1. Thus,

$$\alpha = 1.12 - 0.23 \left(\frac{a}{w}\right) + 10.55 \left(\frac{a}{w}\right)^2 - 21.71 \left(\frac{a}{w}\right)^3 + 30.38 \left(\frac{a}{w}\right)^4$$

$$\alpha = 1.66$$

From the micron marker on the fractograph, linear interpolation allows the determination of the fatigue crack growth rate. Firstly, the average striation spacing is calculated using linear interpolation. The micron bar is approximately 13-mm long and it is equivalent to 1 μm as magnification factor, then

$$13 \ mm \quad \rightarrow \quad 1 \ \mu m$$
$$1 \ mm \quad \rightarrow \quad x$$
$$x \quad = \quad \frac{(1 \ mm) \, (1 \ \mu m)}{13 \ mm} = 7.69x10^{-2} \ \mu m$$
$$x \quad = \quad 7.69x10^{-8} \ m$$

For one cycle, the average striation spacing represents the crack grown per cycle.   Thus,

$$\frac{da}{dN} \simeq \frac{\Delta a}{\Delta N} = \frac{x}{\Delta N} = 7.69x10^{-8} \ m/cycle$$

Using Paris equation yields

$$\Delta K \quad = \quad \left(\frac{da/dN}{A} \right)^{1/n} = \left(\frac{7.69x10^{-8}}{10^{-12}} \right)^{1/3.5}$$
$$\Delta K \quad = \quad 24.89 \ MPa\sqrt{m} = K_{\max}$$

For comparison purposes, eq. (9.23) along with $E = 207 \ GPa$ gives

$$\Delta K \quad \simeq \quad E\sqrt{\frac{x}{6}} = \left(207x10^3 \ MPa \right) \sqrt{\frac{7.69x10^{-8} \ m}{6}}$$
$$\Delta K \quad \simeq \quad 23.44 \ MPa\sqrt{m} = K_{\max}$$

which is approximately 6% lower than the previous result.   Therefore, both methods can yield reasonable results.

Secondly, taking $\Delta K \simeq 24.17 \ MPa\sqrt{m}$ as the average value one can calculate the maximum load as follows:

$$K_{\max} \quad = \quad \alpha \sigma_{\max} \sqrt{\pi a} = \frac{\alpha P_{\max}}{Bw} {}_{\max} \sqrt{\pi a}$$
$$\sigma_{\max} \quad = \quad \frac{K_{\max}}{\alpha \sqrt{\pi a}} = \frac{24.17 \ MPa\sqrt{m}}{(1.66) \sqrt{\pi \, (6x10^{-3} \ m)}} = 106.05 \ MPa$$
$$P_{\max} \quad = \quad Bw\sigma_{\max} = \left(5x10^{-3} \ m \right) \left(20x10^{-3} \ m \right) \left(106.05 \ \frac{MN}{m^2} \right)$$
$$P_{\max} \quad = \quad 10.61 \ kN$$

9.9 MIXED-MODE LOADING

The slow fatigue crack growth ΔK-dependency in elastic solids has been investigated under mixed-mode interactions [36-37] and biaxial cyclic loading [36-40]. A remarkable observation is that ΔK_{th} decreases as the stress ratio R increases as in the case of mode I loading depicted in Figure 9.10. However, if the starting crack size is large and the biaxial stress level is low, da/dN is independent of ΔK [38].

In conducting mixed-mode fatigue studies, a defined effective stress intensity factor ΔK_e may be used in the Paris law for brittle [36-40] or ductile [41-44] materials. Effectively, the definition of ΔK_{eff} depends on the mathematical technique and theoretical background one uses. Nevertheless, the Paris law [16-17] takes the general and empirical form

$$\frac{da}{dN} = A\left(\Delta K_e\right)^n \tag{9.24}$$

For a mixed-mode I and II interaction, eq. (8.17) and (8.18) may be used to defined the effective stress intensity factor range as

$$\Delta K_e^2 = \Delta K_I^2 + \Delta K_{II}^2 \tag{9.25}$$
$$\Delta K_e^2 = \pi a \left(\Delta \sigma\right)^2 \sin \beta \tag{9.26}$$

For pure mode I at fracture, $\Delta K_e = K_{IC}$ (similar argument was presented in Chapter 8) for $R = 0$ and eqs. (9.25) and (9.26) become

$$K_{IC}^2 = \Delta K_I^2 + \Delta K_{II}^2 \tag{9.27}$$
$$K_{IC}^2 = \pi a_c \left(\Delta \sigma\right)^2 \sin^2 \beta \tag{9.28}$$

Combining eqs. (8.15), (8.16), (9.27) and (9.28) yields a expression similar to eq. (8.18)

$$D_1 \left(\Delta \sigma\right)^n + D_2 \left(\Delta \sigma\right)^{n-2} - D_3 = 0 \qquad \text{For } n \neq 0 \tag{9.29}$$

where

$$
\begin{aligned}
D_1 &= A\left(n-2\right)\left(N-N_o\right)\left(K_{IC}\right)^n \\
D_2 &= \frac{2}{\pi}\left(\frac{K_{IC}}{\alpha \sin \beta}\right)^2 \\
D_3 &= 2\left(a\right)^{1-n/2}\left(\frac{1}{\pi}\right)^{n/2}\left(\frac{K_{IC}}{\alpha \sin \beta}\right)^n
\end{aligned}
\tag{9.30}
$$

An example can make the above analytical procedure clearly usable for solving mixed-mode problems under cyclic stress systems.

Example 9.4 *Assume that a solid cylinder of 25 mm in diameter has a round surface crack inclined at $\beta = 20°$ and that the material has an average plane strain fracture toughness and threshold stress intensity factor of 15 $MPa\sqrt{m}$ and 5 $MPa\sqrt{m}$, respectively. If the crack depth is 0.09 mm and the applied cyclic stresses are $\Delta\sigma = \sigma_{max}$ and $\sigma_{min} = 0$, calculate a) the minimum stress range $\Delta\sigma_{min}$ b) the applied stress range $\Delta\sigma = \sigma_{max}$ and c) the critical length a_c for a fatigue life of 10^4 cycles. How much will the crack grow? What will be the percent crack increment? The Paris equation is*

$$\frac{da}{dN} = \left(5x10^{-12} \ \frac{MN^{-4}.m^7}{cycles}\right)(\Delta K)^4$$
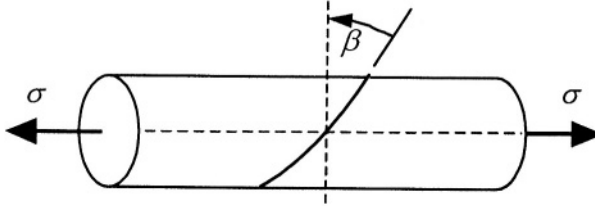
Solution:

Threat the surface defect as surface single-edge crack. Given data:

$$N = 10^4 cycles \quad K_{IC} = 15MPa\sqrt{m} \quad \Delta K_{th} = 15MPa\sqrt{m}$$

$$a_o = 0.09 \ mm \quad A = 5x10^{-12} \ \frac{MN^{-4}.m^7}{cycles} \quad n = 4 \quad \alpha = 1.12$$

a) *The minimum stress range can be calculated using eq. (9.26) by letting* $\Delta K_{th} = \Delta K_e$

$$\Delta\sigma_{th} = \frac{\Delta K_{th}}{\alpha\sqrt{\pi a_o}} = \frac{5 \ MPa\sqrt{m}}{(1.1989)\sqrt{\pi \ (0.09x10^{-3} \ m)} \sin(20)} = 776.25 \ MPa$$

$$\Delta\sigma_{min} < \Delta\sigma_{th}$$

b) *For maximum stress range,*

$$D_1 = A(n-2)(N-N_o)(K_{IC})^n = 5.0625x10^{-3} \ m$$

$$D_2 = \frac{2}{\pi}\left(\frac{K_{IC}}{\alpha\sin\beta}\right)^2 = 976.16 \ MPa^2.m \qquad (9.30)$$

$$D_3 = 2(a)^{1-n/2}\left(\frac{1}{\pi}\right)^{n/2}\left(\frac{K_{IC}}{\alpha\sin\beta}\right)^n = 5.2939x10^9 \ MPa^4.m$$

Then,

$$0 = 5.0625x10^{-3} (\Delta\sigma)^4 + 976.16 (\Delta\sigma)^2 - 5.2939x10^9$$
$$\Delta\sigma = 964.74 \ MPa$$

c) *From eq. (9.28), the critical crack size is*

$$a_c = \frac{K_{IC}^2}{\pi (\Delta\sigma)^2 \sin^2 \beta} = \frac{(15 \ MPa\sqrt{m})^2}{\pi (964.74 \ MPa) \sin^2 (20)}$$
$$a_c = 0.66 \ mm$$
$$\Delta a = a_c - a_o = 0.66 \ mm - 0.09 \ mm = 0.57 \ mm$$

Therefore, the crack grew $\Delta a = 0.57 \ mm$ which represents 6.33% crack increment.

9.10   GROWTH RATE MEASUREMENTS

In general, for small increments of the crack length in the order of $1 \ mm$ or less, the following procedure gives acceptable results. That is, the fatigue crack growth rate can be approximated by

$$\frac{da}{dN} \simeq \frac{a_i - a_{i-1}}{N_i - N_{-1}} \qquad \text{For } i = 1, 2, 3, 4, 5, ... \qquad (9.31)$$

Then, compute the average crack length and the specimen geometry correction factor, respectively, as

$$\bar{a} = \frac{a_i + a_{i-1}}{2} \qquad (9.32)$$
$$\alpha = f(\bar{a}/w) \qquad (9.33)$$

For $i = 0$, $a_i = a_o$ and $N_i = N = 0$ since the initial crack length exists. The American Society for Testing Materials (ASTM) E647 Standard Test Method is widely used for measuring the crack length and the elapsed fatigue cycles at constant loading stress amplitude and frequency. This method deals with the procedure for determining low and high steady-state fatigue crack growth rates. This particular test method does not restrict specimen geometry and specimen thickness as long as buckling is precluded and the specimen ligament is large enough.

9.11   CORROSION FATIGUE

In general, stress corrosion is a phenomenon caused by the combination of quasi-static or cyclic stress and a corrosive environment (hostile chemical solution). If a material is susceptible to deteriorate under these conditions, then a corrosion behavior is established. However, if the material undergoes anodic dissolution at the crack tip, a stress corrosion cracking *(SCC)* mechanism dominates with the aid of the static or cyclic stress. Secondary cracks may develop on the surface of a component, while the crack tip dissolves and the crack growth rate increases.

In general, the *SCC* mechanism can occur on ductile and brittle materials containing initially smooth surface. The purpose of conducting SCC experiments is to determine the effects of a particular fluid, temperature, applied strain rate or applied voltage on solid bodies.

Secondary crack formation on a smooth surface prevails as the source for a major crack to grow statically and cyclically (dynamically). Figure 9.21 shows tensile fracture surfaces of a 304 stainless steel tested in $0.1N$ H_2SO_4 solution at room temperature and at strain rate of $5.5x10^{-5}$ sec^{-1} [56]. This material was produced by rapidly solidification and subsequently, consolidated and 50% cold rolled. Smooth rods were prepared [56] for conducting slow strain rate (SSR) stress corrosion cracking tests in the mentioned environment.
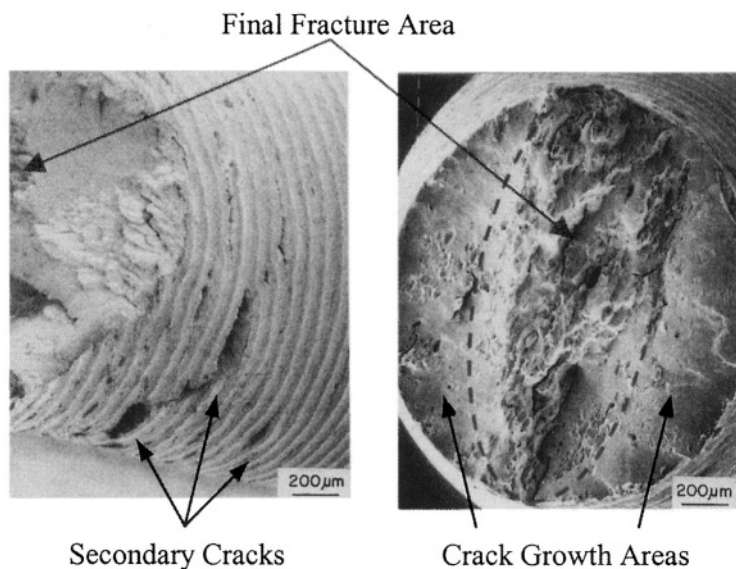
Figure 9.21 Secondary cracks and overload fracture areas in a 50% CR RSA 3004 [56].

Figure 9.21a shows secondary cracks on the specimen gage length. Figure 9.21b also showed secondary cracks tested at -200 mV under the same environmental conditions, but the primary crack grew in a semielliptical manner

from opposite sides of the specimen and the final fracture area due to an stress overload exhibited a elliptical configuration.

If a component has an initial crack, the fatigue crack growth rate process does not include an incubation period as in testing smooth components. Generally, the corrosion fatigue behavior relates to a high plastic strain at the crack tip [3], which is suitable for anodic dissolution. Apparently, the combination of high plastic strains enhances metal dissolution, which in turn, accelerates fatigue crack growth rates. In addition, if a material is susceptible to develop beach marks and striations as fatigue fracture features in a suitable environment, these features may not be observed or not be cleared enough if metal dissolution takes place on the fracture surface, coating these features with a corrosive product. This corrosion product may be difficult to remove; however, the ultrasonic cleaning technique may be appropriate for this task.

On the other hand, if the corrosive environment, containing hydrogen ions, does not provoke metal dissolution at the crack tip, a phenomenon called hydrogen embrittlement *(HE)* may control the corrosion fatigue behavior. HE has its effect on materials under static and cyclic conditions. This is a mechanism, in which a highly localized brittle region develops at the crack tip [51-53]. This, then, indicates that the applied cyclic stresses, which induce cyclic strains at the crack tip, and the action of hydrogen atoms, enhance the crack growth rate due to an accelerated breakage of atomic bonds at the crack tip. Thus, atomic hydrogen *(H)*, as oppose to molecular hydrogen (H_2), diffuses into the metal, especially if the amount of hydrogen exceeds that of the solubility limit, at favorable atomic sites at the crack tip. Therefore, the accelerated crack growth rate, specifically in stage II fatigue, may be attributed to this hydrogen diffusion-controlled mechanism since the atomic hydrogen radius is relatively small. These atomic sites are grain boundaries, voids, and inclusions.

However, atomic hydrogen can precipitate in a gaseous or solid form when it reacts with the exposed metal, such as irons and steels, under appropriate environmental (thermodynamics) conditions. Apparently, gaseous precipitation of hydrogen atoms located at these sites react to form hydrogen molecules, which in turn combine themselves to form bubbles at extremely high pressure of 1.3 GPa as an upper limit [3]. Moreover, the solid precipitation of hydrogen with Ti and Zr, among many other elements, is referred to as hydride precipitation, which hardens the material in question [35].

Many investigators have reported the application of linear elastic fracture mechanics *(LEFM)* to many material-environment systems, and the literature in this particular engineering field is quite abundant for Al-alloys, Fe-alloys (steels), Ti-alloys, and so on. However, the controlling macroscopic parameter for assessing crack growth has been the stress intensity factor K_I for mode I loading.

In general, many materials are sensitive to combinations of stress, environments and microstructure. One particular case is shown in Figure 9.22 for a Ni-base alloy steel tested in 3% NaCl saline solution and in air at different test frequencies (cpm = cycles per minute) [65].
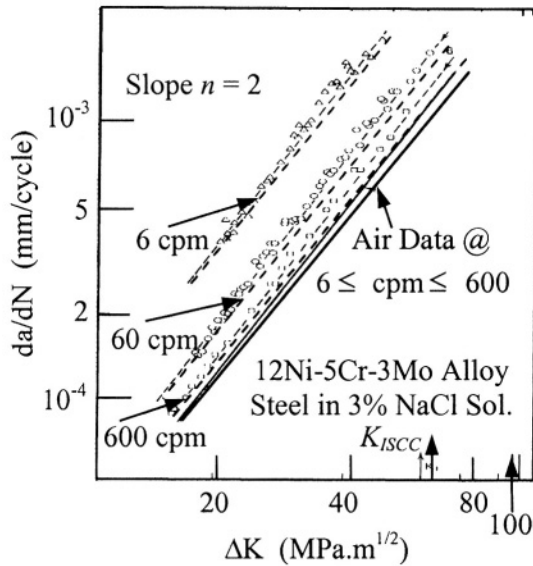
Figure 9.22 Corrosion fatigue crack growth behavior as a function of different test frequency for 12Ni-5Cr-3Mo alloy steel in 3% NaCl solution and air. All test conducted at $K_{max} < K_{ISCC}$ [65].

Despite that the experimental data obeyed the Paris equation with a common exponent of 2, the environmental effect on the da/dN for the Ni-base alloy steel is evident even at $K_{max} < K_{ISCC}$, which contradicts the stress corrosion cracking behavior depicted in Figure 9.23. The term K_{ISCC} stands for the stress intensity factor for mode I loading below which stress corrosion cracking does not occur. One possible reason for this discrepancy is that crack growth does not occur at $K_{max} < K_{ISCC}$ for constant load tests due to a protective passive film at the crack tip. However, this film is sensitive to cyclic stresses and consequently, fatigue crack growth occurs [66]. The phrase stress corrosion cracking (SCC) is also known as environment-assisted cracking *(EAC)*.

Figure 9.23 illustrates important criteria described by Hertzberg [66] when stress intensity factor is time-dependent at constant load. Thus,

- If $K_I < K_{ISCC}$, then failure is not expected in an aggressive or corrosive fluid

- If $K_{ISCC} < K_I < K_{IC}$, then crack growth and fracture occur after a prolong period of time

- If $K_I > K_{IC}$, then sudden fracture is expected upon loading
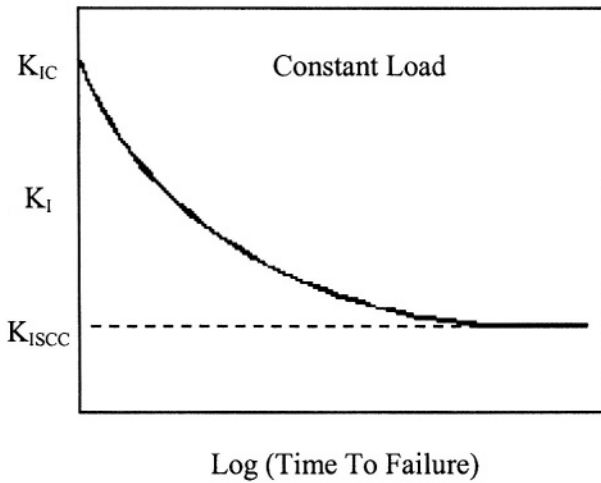
Figure 9.23 Stress intensity factor as a function time to break.

Figure 9.23 represents the possible mechanical behavior of a stressed structural component exposed to an aggressive environment during service. Therefore, care should be taken when using this type of data in designing against stress corrosion cracking.

9.12   PROBLEMS

9.1   Show that Paris equation can take the form

$$da/dN = A\left[E\sigma_{ys}/\left(1 - v^2\right)\right]^{n/2} \cdot (\Delta\delta_t)^{n/2}$$

where $\Delta\delta_t$ is the change of crack tip opening displacement, E is the modulus of elasticity, and A is a constant.

9.2   a) Show that $da/dN = C\left(\Delta K_e\right)^n$, where $C = A\left(1 - R\right)^{-n(1-\alpha)}$ and $\Delta K_e = K_{\max}\left(1 - R\right)^{\alpha}$ is Walker's effective stress intensity factor range. b) Plot and for a 4340 steel having. b) Plot $da/dN = C\left(\Delta K_e\right)^n$ and $da/dN = A\left(\Delta K_e\right)^n$ for a steel having $\sigma_{ys} = 1,254\ MPa$, $\sigma_{ts} = 1,296\ MPa$, $K_{IC} = 130$ $MPa\sqrt{m}$, $\alpha0.42$, $n = 3.24$, $R = 0.7$ and $A = 5.11x10^{-11}\ MN^{-n}.mm^{1-n/2}/cycle$.

9.3   Suppose that a single-edge crack in a plate grows from $2\ mm$ to $10\ mm$ at a constant loading frequency of 20 Hz. The applied stress ratio and the maximum stress are zero and 403 MPa, respectively. The material has a plane strain fracture toughness of $80\ MPa.m^{1/2}$ and a crack growth behavior described by $da/dN = 3.68x10^{-12}\left(\Delta K\right)^4$. Here, a/dN and ΔK are in $mm/cycle$ and $MPa\sqrt{m}$ units, respectively. Determine a) the critical crack size and b) the time it takes for rupture to occur. [Solution: a) $a_c = 10\ mm$ and b) $t = 1.47\ hours$].

9.4   If a large component is subjected to a cyclic loading under $\Delta\sigma = 300$ MPa and $R = 0$. The material behaves according to Paris law $da/dN = 2x10^{-8}\left(\Delta K\right)^{2.45}$, where a/dN and ΔK are in $mm/cycle$ and $MPa\sqrt{m}$ units, respectively. Determine the plane-strain fracture toughness for the component to endure 54,532 cycles so that a single-edge crack grows from 2 mm to a_c.

9.5   Consider a part made of a polycrystalline metal that is stresses in the elastic stress range. If the metal contains inclusions, has an imperfectly smooth exterior surface, and natural dislocation, would the metal experience irreversible changes in a micro-scale? Explain.

9.6   Why most service fatigue fractures are normally not clear?

9.7   What is the physical meaning of the slope of the stage II line in the Paris model?

9.8   Suppose that $d\left(2a\right)/dN = 0.001\ mm/cycle$ and $n = 4$ in the Paris equation for 7075-T6 (FCC), 2024-T3 (FCC), Mo (BCC), and steel (BCC). Determine a) the constant A and its units, and b), which of this material will have the higher crack growth, rate?

9.9   A Ti-6Al-4V large plate containing a 4-mm long central crack is subjected to a steady cyclic loading R = 0.10. The plane strain and the threshold

fracture toughness *are* 70 and 14.7 $MPa\sqrt{m}$, respectively. Determine a) the minimum stress range, b) the maximum applied stress range for a fatigue life of 3,000 cycles, and c) the critical crack size for 3,000 cycles. Let the Paris equation be applicable so that $n = 4$ and $A = 10^{-12}\ MN^4.mm^{-1}/cycle$. [Solution: a) $\Delta\sigma_{min} < 185.45\ MPa$, b) $\Delta\sigma = 642\ MPa$ and c) $a_c = 3.10\ mm$].

9.10 Plot $da/dN = f(\Delta K)$ for 403 S.S. using the Paris, Forman and Broek/Schijve equations. Use the data given in Table 9.2 and a (20 mm)x(300 mm)x(900 mm) plate containing a single-edge crack of 2-mm long. Let 20 $MPa\sqrt{m} \le \Delta K \le 80\ MPa\sqrt{m}$.

9.11 Plot the data given below and use eq. (9.6) as the model to draw a curve fitting line on log-log scales. Determine the constants in such an equation. [Solution: $n = 3.50$ and $A = 5.98x10^{-13}\ PMa^{-3.5}.m^{3/4}$].

ΔK	$(MPa\sqrt{m})$	20	30	40	50	60	70
da/dN	$(x10^{-7}\ m/cycle)$	0.241	0.884	2.42	5.29	10	17.20

9.12 A steel plate containing a single edge crack was subjected to a uniform stress range $\Delta\sigma$ and a stress ratio of zero. Fatigue fracture occurred when the total crack length was $0.03\ m$. Subsequent fatigue failure analysis revealed a striation spacing per unit cycle of $7.86x10^{-8}\ m$. The hypothetical steel has a modulus of elasticity of $207\ GPa$. Predict a) the maximum cyclic stress for a crack length of $0.01\ m$, b) the striation spacing per unit cycle when the crack length is $0.02\ m$, c) the Paris equation constants and d) the plane strain fracture toughness and e) the fatigue crack growth rate assuming that the Paris equation is applicable nearly up to fracture.

9.13 A 2-*cm* thick pressure vessel made of a high strength steel welded plates burst at an unknown pressure. Fractographic work using a scanning electron microscope (SEM) revealed a semielliptical fatigue surface crack $(a = 0.1\ cm$ and $2c = 0.2\ cm)$ located perpendicular to the hoop stress and nearly in the center of one of the welded plates. The last fatigue band exhibited three striations having an average length of $0.34\ mm$ at 10,000 magnification. The vessel internal diameter was $10\ cm$. Calculate a) the pressure that caused fracture and b) the time it took for fracture to occur due to pressure fluctuations. Assume a pressure frequency of $0.1\ cpm$ Given data: $\sigma_{ys} = 600\ MPa$, $E = 207\ GPa$ and $da/dN = 4.50x10^{-7}(\Delta K)^2$. [Solution: $P = 154.40\ MPa$].

9.13   REFERENCES

[1]   J.A. Collins, "Failure of Materials in Mechanical Design: Analysis, Prediction, Prevention," Second Edition, John Wiley & Sons, New York (1993) 181

[2]   W.A. Wood. Bulletin Inst. Of Metals, Vol. 3 (1955)

[3]   D.K. Felbeck and A.G. Atkins, "Strength and Fracture of Engineering Solids," Second Edition, Prentice Hall, Inc., Upper Saddle River, NJ, (1996) 430-443

[4]   G.E. Dieter, "Mechanical Metallurgy," McGraw-Hill, Inc., (1986) 178

[5]   K. Hellan, "Introduction to Fracture Mechanics," McGraw-Hill Book company, New York, (1984)

[6]   P.C. Paris and F. Erdogan, "A Critical Analysis of Crack Propagation Laws," J. Basis Engineering, Trans. ASME, Vol. 85(1963) 528-534

[7]   R.G. Forman at el., Trans. ASME 89 (1967) 459-464

[8]   D. Broek and J. Schijve, National Aerospace Laboratory, Amsterdam, Report NLR-TR-M-2111, (1963)

[9]   F. Endorgan, "Crack Propagation Theories," NASA-CR-901, (1967)

[10] E.K. Walker, ASTM STP 462 (1970) 1-14

[11] A. Hartman and J. Schijve, Eng. Fracture Mechanics, 1(1970)

[12] R.O. Ritchie, "Near-Threshold Fatigue Crack Propagation," Inter. Metals Reviews, Vol. 24(5) (1979)

[13] H.O. Fuchs and R.I. Stephens, "Metal Fatigue in Engineering," John Wiley & Sons, New York, 1980

[14] J.M. Barsom and S.T. Rolfe, "Fracture and Fatigue in Structure: Application of fracture Mechanics," Third edition, American Society for Testing and Materials, Philadelphia, PA, (1999).

[15] J. Schijve, Fatigue Thresholds, Vol. 2 EMAS Ltd., West Midlands, England, (1982)

[16] P.C. Paris, "Fracture Mechanics Approach to Fatigue." Fatigue-An Interdisciplinary Approach, J.J. Burke at el., Editor. Proc. 10th Sagamore Army Matl. Research Conf., Syracuse University Press, Syracuse, NY (1964)

[17] P.C. Paris et al., ASTM STP 513 (1972) 141-176

[18] E.J. Imhoff and J.M. Barsoum, ASTM STP 536 (1973)

[19] M.D. Speidel, NACE Stress Corrosion Cracking and Hydrogen Embrittlement of Iron Base Alloys, Vilieux, France, (June 1973)

[20] W.W. Gerberich et al., Corrosion Fatigue, NACE-2, Houston, (1972)

[21] A.J. McEvily and J.L. Gonzalez, Metallurgical Trans. A, Vol. 23A (Aug. 1992)

[22] P. Shahinian et al., ASTM STP 520 (1973)

[23] W.A. Logsdon, Eng. Fracture Mechanics, Vol. 7(1) (March 1975)

[24] L. Abrego and J.A. Begley, in International Corrosion Forum, Palmer House, Chicago, March 3-7 (1980)

[25] W.J. Mills, J. Eng. Materials and Technology, Trans. ASME Vol. 100(2) (1978)

[26] L.A. James, Report HEDL-TME-75-82, Westinghouse Hanford Co., Richland, WA, (January 1976)

[27] Report MDC-A0913, Phase B Test Program, McDonnell Aircraft Co., McDonnell Douglas Corp., St. Louis, (May 1971)

[28] J.C. Zola, Case Studies in Fracture Mechanics, edited by T.P. Rich and D.J. Cartwright, AMMRC MS 77-5 Army Materials and Mechanics Research Center, Watertown, MA (1996)

[29] R.L. Tobler, Cryogenics, Vol. 16(11) (1976)

[30] W.J. Mills and L.A. James, ASME Publication 7-WA/PUP-3, (1979)

[31] R.W. Bush et al., "Fracture Mechanics Characteristics of High Strength Aluminum Alloy Forging," ALCOA Forged Products, Report Q-395 (1993)

[32] H.M. Westergaard, "Bearing Pressures and Cracks," J. Appl. Mech., G1 (1939) A49 - A53

[33] D. Broek, "Elementary Engineering Fracture Mechanics," Fourth edition, Kluwer Academic Publisher, Boston, (1986)

[34] R.C. Bates and W.G. Clark, Jr., Trans. Quarterly ASM 62(2) (1969)

[35] T.H. Courtney, "Mechanical Behavior of Materials," McGraw-Hill Publishing Co., N.Y. (1990)

[36] K.J. Miller and A.P. Kfouri, Inter. J. Fracture, Vol. 10(3) (1974)

[37] N.J. Adams, Eng. Fracture Mechanics, Vol. 5 (1973)

[38] H. Kitagawa et al., ASTM STP 853, (1985)

[39] T. Hishide et al., Fatigue Eng. And Materials Structure, Vol. 4, No. 4, (1981)

[40] A. Liu et al., ASTM STP 677, (1979)

[41] W. Elber, ASTM STP 486 (1971) 230

[42] F. Erdogan and G.C. Sih, J. Basic Eng., 85 (1963) 519

[43] H. Qingzhi, Fatigue Eng. Mat. Structure, 7 (1984) 41

[44] W. Wei and H. Qingzhi, Proc. Far East Fracture Group Workshop, Tokyo Institute of Technology, Japan, Nov. 28-30 (1988) 193.

[45] E.A. Loria, Mat. Sci. Eng., A254 (1998) 63.

[46] F.Y.C. Mercer and W.D. Soboyego, Metall. Mat. Trans. A, Vol. 29A (1998) 2361

[47] A. Tonneau et al., Mat. Sci. Eng, A256 (1998) 256.

[48] M.A. Daeubler et al., Metall. Tran A, Vol. 21 A (1990) 925.

[49] J.M. Barsom, Ph.D. Dissertation, University of Pittsburgh, PA (1969)

[50] J.M. Barsom, ASTM STP 486, (1971) 1-15

[51] H. Vehoff and H.K. Klameth, "Hydrogen Embrittlement and Trapping at Crack Tips in Ni-Single Crystals", Perspect in Hydrogen in Met., (1986) 661-668

[52] J.S. Wang, "Hydrogen Induced Embrittlement and the Effect of the Mobility of Hydrogen Atoms," Proc. of the 1994 5th Inter. Conf. on the Effect of Hydrogen on the Behavior of Materials, , Mora, WY, USA, (Sept. 11-14, 1994) 61-75

[53] R.P. Gangloff, "Crack Tip Modeling of Hydrogen Environment Embrittlement: Application to Fracture Mechanics Life Prediction," Materials & Engineering A, Vol. A103, 1 (Aug. 1988) 157-166

[54] N. Perez, "Strengthening Mechanism of Alloy," Journal of Mechanical Behavior of Materials, March (1999)

[55] N. Perez and T.A. Place, "X-Ray Diffraction of a Heat Treated Rapidly Solidified Alloy", Journal of Materials Science Letters, 9 (1990) 940-942.

[56] N Perez, Ph.D. Dissertation, University of Idaho, USA,(1989)

[57] A. Riddick, "Testing for Fatigue Crack Growth," Advance Materials & Processing, (October 2003) 53-55

[58] R.S. Mishra, "Friction Stir Processing Technologies," Advance Materials & Processing, (October 2003) 43-46

[59] L.A. James, Elding Journal, 56 (19777) 386-391

[60] J.F. Lancaster, "Metallurgy of Welding," Fifth edition, Chapman & Hall, New York, (1993) 356

[61] R. Viswanathan, "Damage Mechanisms and Life Assessment of High-Temperature Components," ASM international, (1989)

[62] A. Kelly and G.W. Groves, "Crystallography and Crystal Defects," Addisson-Wesley Publishing Company,Reading, Massachusetts, (1970) 212

[63] J.A. Manson et al., Advances in Fracture Research, D. Francois et al. editors, Pergamon Press, Oxford, (1980)

[64] T.W. Crooker, D.F. Hasson and G.R. Yoder, "Micromechanistic Interpretation of Cyclic Crack Growth Behavior in 17-4 PH Stainless Steel," Fractography: Microscopic Cracking Processes, ASTM STP 600, (1976) 205

[65] E.J. Imhof and J.M. Barsom, ASTM STP 536, (1973) 182

[66] R.W. Hertz berg, "Deformation and Fracture Mechanics of Engineering Materials", third edition, John Wiley & Sons, New York, (1989)

Chapter 10

FRACTURE TOUGHNESS CORRELATIONS

10.1 INTRODUCTION

This chapter is devoted to a brief review of fracture toughness of crack-free and notched specimens. Fracture toughness can be defined as the strain energy absorbed by a material prior to fracture. Thus, this energy is defined as the strain energy density in a tension test, the intensity of the stresses (K_I) ahead of a crack tip, the strain-energy release rate also known as the crack driving force $(G_I$ or $J_I)$ for crack growth or the dynamic strain energy (U) for conventional and instrumented Charpy impact tests. Some useful empirical correlations for determining the plane strain fracture toughness (K_{IC}) from Vickers microhardness measurements and impact tests are included.

Furthermore, impact testing and microhardness measurement techniques are widely used in materials evaluation since they are simple and cost effective. Thus, fracture toughness correlations have evolved indicating the usefulness of the impact and indentation techniques when proper precautions are taken in conducting experiments. For instance, the dynamic behavior of the Charpy impact test can be understood by modeling the striker and specimen as a spring-mass system.

10.2 CRACK-FREE BODIES UNDER TENSION

In general, the mechanical behavior of a material under a stress-loading mode depends on the microstructure, strain rate, and environment. The behavior of an initially crack-free material is characterized by one of the typical stress-strain curves shown in Figure 10.1. Typical tension properties, such as yield strength, tensile strength, ductility, and the modulus of elasticity are obtained from these curves. The strength refers to a property and stress is a parameter related to an

applied loading mode. Nevertheless, the area under the stress-strain $(\sigma\text{-}\epsilon)$ curve is a measure of fracture toughness in terms of strain energy density, which is not a common variable used by engineers in structural analysis, but it may be used as a controlling parameter in classifying structural materials. Particularly, the SMA curve in Figure 10.1 is for a shape memory alloy (SMA), such as 55Ni-45Ti (Nitinol), which exhibits significant high strain to failure (superelastic) and high total strain energy density [1-2].
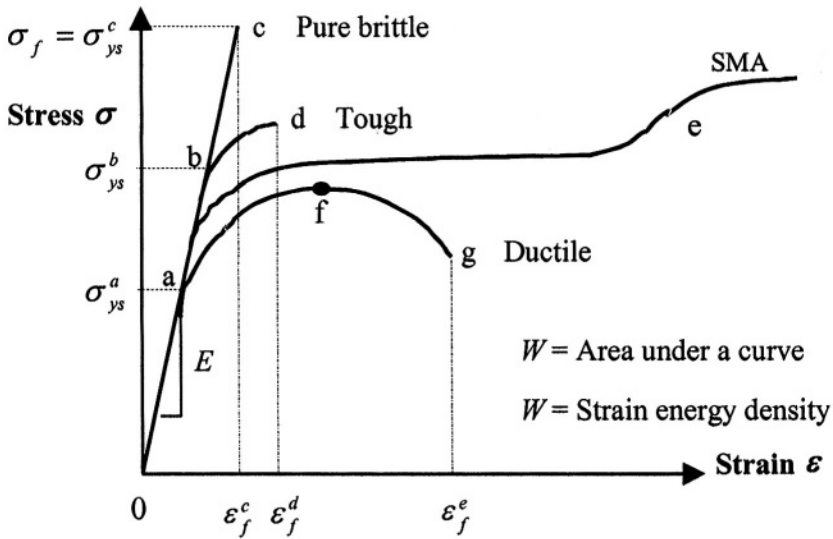
Figure 10.1 Schematic stress-strain curves for different materials.

This strain energy density W (Joules/m^3) is the energy required to deform the material. According to Figure 10.1, the energy is the area under the $\sigma\text{-}\epsilon$ curve. For elastic behavior (up to the yield point), fracture toughness is the elastic strain energy density, which is called Resilience. Thus,

$$W_e = \int_o^{\epsilon_{ys}} \sigma\, d\epsilon = \frac{1}{2}\epsilon_{ys}E = \frac{\sigma_{ys}^2}{2E} \qquad (10.1)$$

since Hooke's law is $\sigma = \epsilon E$. For tough, SM and ductile materials, strain energy density, which can be defined as the tensile fracture toughness of crack-free solid bodies, the strain energy density takes the form

$$W = \int_o^{\epsilon_f} \sigma\, d\epsilon = \int_o^{\epsilon_{ys}} \sigma\, d\epsilon + \int_{\epsilon_{ys}}^{\epsilon_u} \sigma\, d\epsilon = W_e + W_p \qquad (10.2)$$

where W_p is the plastic strain energy density. These integrals can be solved once stress functions in terms of strain, $\sigma = f(\epsilon)$, are available. From Chapter

7, the most common plastic stress functions are known as Ramberg-Osgood and Hollomon equations, respectively

$$\sigma = \sigma_{ys} \left(\frac{\epsilon}{\alpha' \epsilon_{ys}} \right)^{1/m} \qquad \text{For } \sigma \geq \sigma_{ys} \text{ (Ramberg-Osgood)} \qquad (10.3)$$

$$\sigma = k\epsilon^n \qquad \text{For } \sigma \geq \sigma_{ys} \text{ (Hollomon)} \qquad (10.4)$$

These equations are valid from the yield strength to the maximum or ultimate tensile strength stress on the stress-strain curves. In other words, the limit points are $(\epsilon_{ys}, \sigma_{ys})$ and (ϵ_u, σ_u).

For a strain hardenable material, the Ramberg-Osgood or Hollomon equation may be used as an effective stress expression so that the integral can easily be solved. Substituting eqs. (10.3) and (10.4) into (10.2) yields general solutions

$$W = \frac{\sigma_{ys}^2}{E} \left[\frac{1}{2} + \alpha' \left(\frac{m}{1+m} \right) \left(\frac{\sigma}{\sigma_{ys}} \right)^{1+m} \right] \qquad \text{(Ramberg-Osgood)} (10.5)$$

$$W = \frac{\sigma_{ys}^2}{2E} + \frac{\sigma}{1+n} \left(\frac{\sigma}{k} \right)^{1/n} \qquad \text{(Hollomon)} \qquad (10.6)$$

Using proper integral limits, these equations become, respectively

$$W = \frac{\sigma_{ys}^2}{2E} + \frac{m}{\alpha'(1+m)} \left(\frac{\sigma_{ys}}{E} \right)^{1-1/m} \left[E\epsilon_u^{1+1/m} - \sigma_{ys} \left(\frac{\sigma_{ys}}{E} \right)^{\frac{1}{m}} \right] \quad (10.7)$$

$$W = \frac{\sigma_{ys}^2}{2E} + \frac{\sigma}{1+n} \left[\epsilon_u^{1+n} - \left(\frac{\sigma_{ys}}{E} \right)^{1+n} \right] \qquad (10.8)$$

An ideal tough material must exhibit high strength and ductility. Despite ductile materials are considered tough; they have low strength and high ductility. However, if a notched tensile specimen, made of a ductile material, is loaded in tension, the plastic flow is shifted upwards since a triaxial state of stress is developed at the root of the notch. This is a constraint against plastic flow, but it enhances the magnitude of the elastic stresses at the notch root [3].

In summary, the yield strength and the fracture toughness in terms of total strain energy density of crack-free materials can be compared using the inequalities shown below

$$\sigma_{ys}^{ductile} < \sigma_{ys}^{tough} < \sigma_{ys}^{brittle} \qquad (10.9)$$

$$W_{brittle} < W_{tough} < W_{ductile} \qquad (10.10)$$

This analogy implies that fracture toughness decreases with increasing strength and decreasing strain to failure.

10.3   GRAIN SIZE REFINEMENT

The grain size refinement technique, which has been successfully applied to some Body-Centered Cubic (BCC) steels containing molybdenum (Mo), vanadium (V), titanium (Ti), and aluminum (Al), is one approach for enhancing both yield strength and fracture toughness. These alloying elements react in the solid-solution state to form either particles or cause microstructural changes that are accountable for pinning grain boundaries, and therefore, austenite grain growth is retained on cooling.

In addition, these elements can restrain the coarsening of carbide particles, which in turn pin dislocation motion on deformation by external stresses. The exact microstructural and phase transformation mechanism evolved in adding these elements to carbon steels is a particular metallurgical topic that can be found elsewhere [4]. Subsequently, the controlling property, such as yield strength or fracture toughness, is limited to 1) the strength if an applied external load exists, 2) the fracture toughness if absorption of strain energy occurs prior to fracture, and 3) the ductility if metal shaping or forming is required.

The addition of small amounts of alloying elements, such as Al, Ti, V, and the like, to carbon steels enhances the strength and fracture toughness of these important engineering materials. As mentioned in Chapter 2, this is referred to as the grain-size refinement technique. Thus, the yield strength, fracture strength, and fracture toughness can be correlated with grain size and correlations can be accomplished experimentally [5-7] and empirically by using the Orowan [8] and the Hahn-Rosenfield [9] plastic constraint factor (λ) at the crack tip, respectively, defined by

$$\lambda \;=\; \frac{\sigma_f}{\sigma_{ys}} \qquad \text{(Orowan)} \qquad\qquad (10.11)$$

$$\lambda \;=\; 1 + \beta \left(\frac{K_{IC}}{\sigma_{ys}} \right) \qquad \text{(Hahn-Rosenfield)} \qquad (10.12)$$

where $\beta = 20 \; m^{-1/2}$ for strain hardening mild steels [9].

The most common relationships for correlating the yield and fracture strengths with grain size is known as the Hall-Petch type equation defined as

$$\sigma_{ys} \;=\; \sigma_{oy} + k_y d^{-1/2} \qquad\qquad (10.13)$$

$$\sigma_f \;=\; \sigma_{of} + k_f d^{-1/2} \qquad\qquad (10.14)$$

where σ_{oy} = Friction stress due to particle, dislocations, grain boundary and the like (MPa)

σ_{of} = Stress constant (MPa)
k_y = Dislocation locking term $(MPa.mm^{1/2})$
k_f = Constant $(MPa.mm^{1/2})$
d = Grain size (mm)

Combining eqs. (10.11) and (10.12) along with eqs. (10.13) and (10.14) yields the plane strain stress intensity factor as

$$K_{IC} = \frac{1}{\beta}(\sigma_f - \sigma_{ys}) \tag{10.15}$$

$$K_{IC} = \frac{1}{\beta}(\sigma_{of} - \sigma_{oy}) + \frac{1}{\beta}(k_f - k_y)d^{-1/2} \tag{10.16}$$

$$K_{IC} = K_o + K_d d^{-1/2} \tag{10.16}$$

Example 10.1 *Using Stonesifer and Armstrong [10] linear regression analysis for A533B steel at room temperature having an average grain size of* **10** *μm and modulus of elasticity of* 207 *GPa, calculate Calculate a)* λ *and* β *and b) predict the elastic strain energy density as a measure of elastic fracture toughness for sound specimens subjected to tension loading an determine.*

$$\sigma_{ys} = 572\ MPa + \left(0.11\ MPa.m^{1/2}\right)d^{-1/2} = 606.79\ MPa$$

$$\sigma_{ys} = 1,750\ MPa + \left(3.30\ MPa.m^{1/2}\right)d^{-1/2} = 2,793.55\ MPa$$

$$K_{IC} = 60\ MPa\sqrt{m} + (0.16\ MPa.m)\,d^{-1/2} = 110.60\ MPa\sqrt{m}$$

Solution:

a) *From eq. (10.11) and (10.12),*

$$\lambda = \frac{\sigma_f}{\sigma_{ys}} = \frac{2,793.55\ MPa}{606.79\ MPa} = 4.60$$

$$\beta = (\lambda - 1)\left(\frac{\sigma_{ys}}{K_{IC}}\right) = (4.60 - 1)\left(\frac{606.79\ MPa}{110.60\ MPa\sqrt{m}}\right)$$

$$\beta = 19.75\ m^{-1/2}$$

which agrees with Hahn and Rosenfield [9] approximation given above.

b) *From eq. (10.1),*

$$W_e = \frac{\sigma_{ys}^2}{2E} = \frac{(606.79\ MPa)^2}{2\,(207x10^3\ MPa)} = 0.89\ MJ/m^3$$

10.4   INDENTATION-INDUCED CRACKING

In this section, the theory of indentation is strictly used to measure "indentation hardness" which implies resistance to penetration as depicted in Figure 120.2. The most common hardness tests are mechanically static in nature, which have industrial and research applications. Thus, "hardness" can be measured by using the Brinell, Rockwell, and Meyer tests. On the other hand, "microhardness" can be measured using the Knoop and Vickers indentation techniques. The term microhardness indicates the hardness of a very small area such as a grain and/or a particle that constitute the microstructure of a polycrystalline material. Herein, attention is devoted to the Vickers indentation-hardness measurement technique, which has been used very extensively in research for predicting Vickers fracture toughness of brittle materials. The technical procedure for employing the Vickers hardness testing can be found in the ASTM E92 (1997) Standard Test Method. The term microhardness refers to as small microindentation hardness due to relatively common light applied load that ranges from 1 Kg_f to 120 Kg_f.
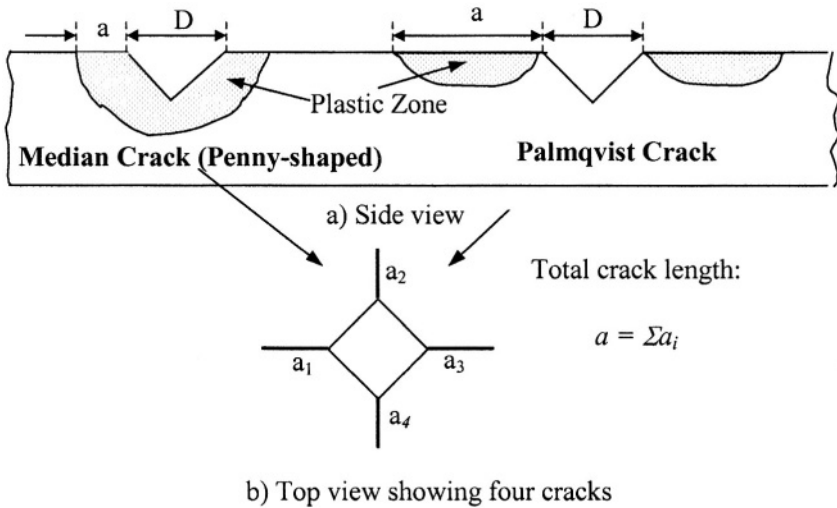
Figure 10.2 Schematic indentation-induced cracking systems [11].

The Vickers indentation is made with a diamond pyramidal-shaped indenter. In fact, the indenter impression schematically shown Figure 10.2 is a square-based inverted pyramid with a face angle of 136° and it is so small that it must be observed with a microscope. For brittle materials, such as ceramics (fused, sintered or cemented metallic oxides), cermets (powder metallurgy products containing ceramic particles), polymers, and amorphous metallic materials, indentation-induced cracking overcome difficulties in specimen preparation in a

conventional manner as recommended by the American Society for Testing Materials (ASTM) E399 for plane strain fracture toughness and for the J-integral approach. As a result, an empirical equation may be used to determine the Vickers fracture toughness.

The Vickers hardness (H_v) can be calculated as follows

$$H_v = \frac{2P \sin(\theta/2)}{D^2} = \frac{1.8544P}{D^2} \tag{10.17}$$

where P = Applied load (Kg)

D = Mean diagonal (mm)

$\theta = 136° =$ Face angle

The advantages of Vickers hardness measurements are 1) its simplicity, 2) it can be applied to microstructural constituents, 3) it does not require fatigue precracking, which is difficult to accomplish in brittle materials, 4) it is cost effective since small specimens are needed, 5) the tests are considered non-destructive in a macroscale. However, specimen preparation is a slightly time consuming procedure since a polished surface is required so that uniform indentations are made on a reflective flat plane, which it is must in order to obtain consistent and reproducible results.

In fact, hardness measurements are made for screening materials and characterizing microstructures, subsequent use is made for determining the Vickers fracture toughness, which inevitably shows some degree of inaccuracy when compared with conventional fracture toughness. Nevertheless, this technique has become an excellent approach for characterizing ceramics, cermets (e.g. $TiC\text{-}Al_2O_3$, $WC\text{-}Co$ composites), and amorphous metals and their alloys.

In 1950's, Palmquist [12] recognized that indentation-induced cracking observed on cermets was related to fracture toughness and he developed a procedure to predict fracture toughness. Vickers is the most common and suitable test method due to four possible cracks that may emanate from the corners of the indenter. A typical Palmquist fracture toughness analysis requires a linear plot of total crack length (a) vs. applied load (P); that is, $a = f(P)$. This is shown in Figure 10.3 for an Alumina-Titanium carbide cermet $(Al_2O_3\text{-}TiC)$. The inverse of the slope of the line is a measure of Palmquist Fracture Toughness in terms of work done (W_C), which may be taken as the strain-energy release rate (G_C) [13].

The prediction of fracture toughness for many brittle materials using empirical formulations can be found in the literature [14-18]. However, the most common expression is the following general form
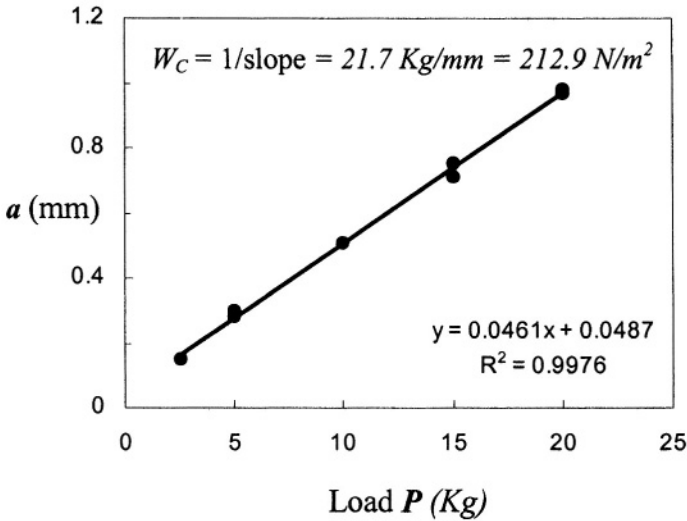
Figure 10.3 Palmquist fracture toughness plot for Al_2O_3-TiC cermet [13].

$$K_{IC} = \xi \left(\frac{E}{H_v} \right)^x \left(\frac{P}{a^{3/2}} \right) \tag{10.18}$$

where ξ = Indentation geometric factor ($\xi < 1$)
      E = Modulus of Elasticity (MPa)
      P = Indenter load (MN)
      H_v = Vickers hardness (MPa)
      x = Exponent
      a = Average crack length (m)

Rearranging and manipulating eq. (10.18) gives

$$K_{IC} = \sqrt{\pi} \alpha p a^{-3/2} \tag{10.19}$$

$$\alpha = \frac{\xi}{\sqrt{\pi}} \left(\frac{E}{H_v} \right)^x \tag{10.20}$$

Observe that eq. (10.18) resembles eq. (3.29) for the conventional plane stress fracture toughness. Moreover, the exact numerical form of eq. (10.18) depends on the crack configuration (Figure 10.2) and the material's properties [14-17,19]. In order to illustrate the usefulness of eq. (10.18) or (10.19), let's curve fit Laugier [17] and Anstis et al. [19] data for several ceramics and cermets, respectively. Notice the remarkable correlation depicted in Figure 10.4 for Vickers fracture toughness and conventional fracture toughness testing method

(ASTM E399). The pertinent values for each parameter in eq. (10.18) can be found in the cited references [17,19].
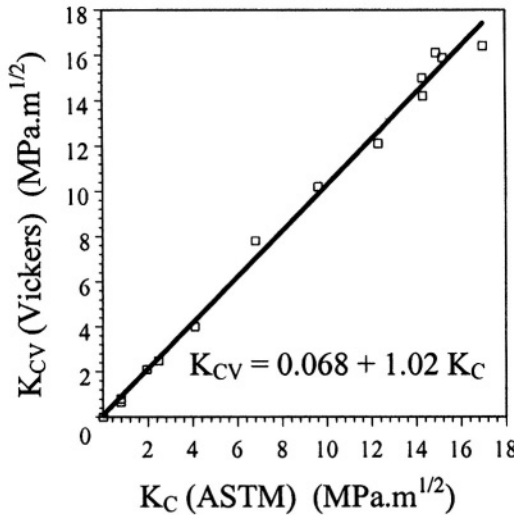
Figure 10.4 Comparison of Vickers and conventional fracture toughness for brittle ceramics and WC-Co cermets. Experimental data was taken from references [17] and [19].

Despite that Vickers hardness technique has been used for decades, it is still a classical research tool for characterizing materials. For instance, Phelps et al. [20] evaluated toughness of female baboon femurs of 6 to 27 year old using this technique. On the other hand, Iost and Bigot [21] made use of the Vickers hardness measurements to characterize the brittleness index, which depends on fracture mechanics and hardness, for metallic and ceramics materials, and flux-grown ErFeO3 single crystals [22]. Furthermore, Sridhar and Yovanovich [23] found a power law relation, $H_v = cD^n$, that fitted hardness data for a tool steel 01, AISI 304 stainless steel, and Ni200. In addition, Berces et al. [24] determined the dynamic Vickers hardness as $H_v = P/D^2$ for the characterization of plastic instability of an Al-3.3Mg binary alloy at a loading range of 1.4-70 MN/s. The search for finding different avenues to characterize materials continues beyond a researcher's imagination, but apparently, the Vickers hardness measurement technique remains as a research tool.

Recently, Milekhine et al. [18] used Vickers indentation-induced cracking for evaluating the plane strain fracture toughness of FeSi using Palmquist type cracks. The average reported result is $K_{IC}(\text{Vickers}) = K_{IC}(\text{ASTM}) = 2.46$ $MPa\sqrt{m}$.

10.5   CHARPY IMPACT TESTING

In general, impact tests are performed to measure the response of a material to dynamic loading. The most common laboratory test configurations are the pendulum machine and the drop tower. The results obtained from a standard impact tests are usually a single value of the impact energy or energy spent on a single specimen. This is of limited value in describing the dynamic behavior of a particular sample material. Therefore, instrumenting an impact machine yields information on the impact forces, impact velocities, displacements, and strain energies of the striker at any time during the dynamic test. Figure 10.5 shows a conventional Charpy impact testing machine used to measure fracture toughness of a three-point bending specimen (3PB) under an impact loading system at low velocity.
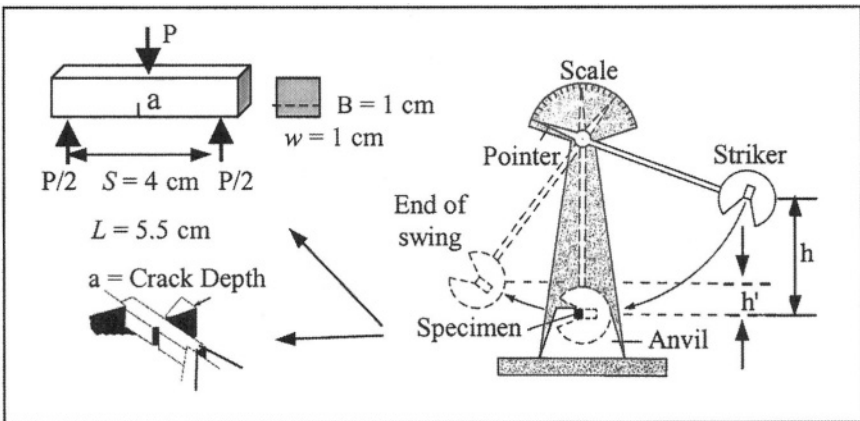
Figure 10.5 The three-point bending (3PB) specimen and the conventional Charpy impact testing machine [48].

Impact loads generate high strain rates in solid materials. For instance, conventional and instrumented Charpy impact testing machines impart low strain rates at low velocity when compared to ballistic impact velocity. The former technique has been used for characterizing the dynamic behavior of some particular composite materials [25-32] and the latter technique promotes impact at a high velocity, which varies according to the type of gun projectile being used. Excellent work in the ballistic field can be found elsewhere [33-36].

The instrumented Charpy impact machine remains a key means for fracture toughness testing due to its low cost, convenience, reliability based on certification standards, and simple use. A particular instrumented Charpy impact machine is shown in Figure 10.6. Thus, the transient load history during a Charpy test is readily obtained by placing strain gages on the striker so that it becomes the load cell. Using software during an impact one can record the displacements by integrating the acceleration versus time twice with respect to

time. The accuracy of these measurements may be affected by the inertial forces in the striker, variations in the contact force distribution between the striker and the specimen, striker geometry, and by strain gage location on the striker [37].

Figure 10.7 illustrates a typical load history for a relevant case [37].
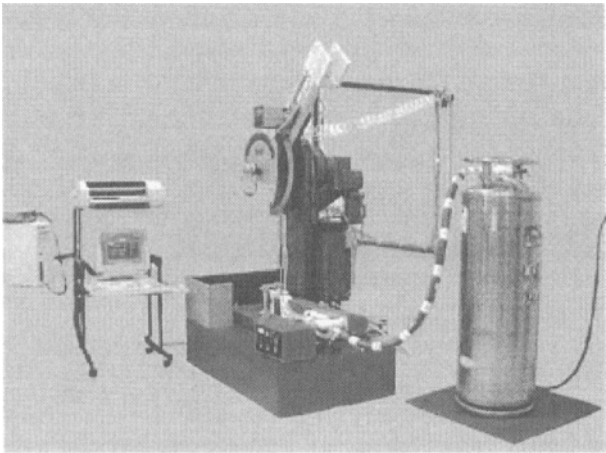
Figure 10.6 Tinius Olsen Model 84 Instrumented Charpy impact machine equipped with in-situ heating and cooling system, optical encoder for measuring the impact velocity, and motorized hammer (striker) return [39].
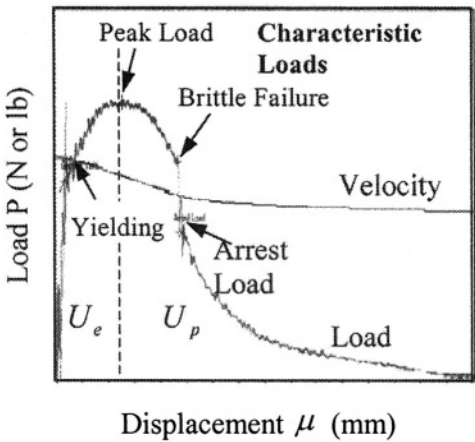
Figure 10.7 a) Schematic load history for brittle materials and b) Load history and velocity plot obtained using MPM ImpactTM v3.0 software [32].

The interpretation of Figure 10.7 is very vital for characterizing a material dynamic behavior. Denote the characteristic load information and the velocity profile in this figure. This type of plot represents the dynamic load response to dynamic displacement cause by the impact process in a Charpy specimen.

The use of instrumented Charpy impact machine has the advantage of providing information on the toughness characteristics of a specimen [37,40-46]. In general, the load-time history for a three-point bending (3PB) Charpy specimen can be divided into fracture initiation and fracture propagation regions expressed in terms of areas under the curve (Figure 10.7). These areas are measures of the elastic strain energy (U_e) and plastic strain energy (U_p). These energies are strongly dependent on the temperature, specimen size, and impact velocity imparted by the kinetic energy of the striker. Thus, the total impact or strain energy a specimen can absorb during impact is known as the Charpy V-notch (CVN) energy defined by the following general relationship [4]

$$U = U_e + U_p = \qquad (10.21)$$

$$U = v \int P dt \qquad (10.21a)$$

$$v = \sqrt{2gh} \qquad (10.22)$$

where v = Striker velocity on contact with the specimen (m/s)
$\quad P =$ Impact load (N)
$\quad \int P dt =$ Impulse $(N.s)$
$\quad h =$ Pendulum initial height (m)
$\quad g = 9.81 \ m/s^2$

Thus, one must analyze the load-time curve very carefully with respect to the elastic and plastic strain energies. These energies may be used for classifying solid materials as $U_e > U_p$ for brittle materials and $U_e < U_p$ for tough and ductile materials.

The Charpy or Izod notched specimens are used for this purpose; the Charpy V-notched specimen being the most common. This technique became a conventional testing method when it was revealed in the 1940's that welded ships, large pipelines, and other monolithic steel structures fractured at notch roots. This is a dynamic (impact) testing technique recommended by the ASTM E23 standard test method. The applied impact load (P) is through an impact blow from a falling pendulum hammer (striker).

The resultant energy measurement is commonly referred to as Charpy impact energy (U), which is a measure of the fracture toughness of a material at testing temperatures. Thus, $U = f(T)$ is normally determined experimentally in order to reveal the effects of impact loads on the dynamic behavior of materials at relatively low and high temperatures. For instance, structural steels usually have low fracture toughness at relatively low temperatures.

10.6 DYNAMIC EFFECTS

The Charpy impact testing machine and its dynamic characteristic can be understood using Williams' [47] one-degree of freedom spring-mass model as shown in Figure 10.8. For a perfectly elastic deformation on impact, the contact stiffness k_1 (= 1/compliance) is high compared with that of the specimen k_2 and consequently, considerable load oscillations are likely over a short period of time
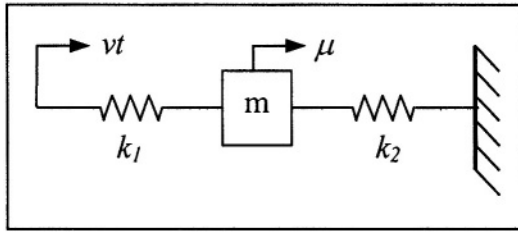
Figure 10.8 Spring-mass model of the Charpy Impact machine. After Ref. [47].

Firstly, the equation of motion of the system shown in Figure 10.8 is [47]

$$m\ddot{u} + (k_1 + k_2)\,u = k_1 vt \qquad (10.23)$$

where k_1 = Stiffness of the striker-specimen interface
    k_2 = 1/C = Stiffness of the specimen
    C = Compliance of the specimen
    m = Mass of the specimen

Using the boundary conditions $\dot{u} = \mu = 0$ at yields the solution of eq. (10.19)

$$u = \frac{v}{\omega}\left(\frac{k_1}{k_1 + k_2}\right)[\omega t - \sin(\omega t)] \qquad (10.24)$$

where the natural angular frequency and the period of oscillations are, respectively

$$\omega = \sqrt{\frac{k_1 + k_2}{m}} \qquad (10.25)$$

$$\tau = \frac{2\pi}{\omega} \qquad (10.26)$$

Secondly, assume that the striker slows down insignificantly upon striking the specimen mass (m) so that the spring k_2 expands at velocity v and the spring k_1 compresses. In this case, the impact load (force) can be defined by

$$P = k_1\,(vt - \mu) \qquad (10.27)$$

Substituting eq. (10.24) into (10.27) and rearranging the resultant expression yields

$$P = \frac{vk_2}{\omega} \left(\frac{k_1/k_2}{1 + k_1/k_2} \right) \left[\omega t - \left(\frac{k_1}{k_2} \right) \sin(\omega t) \right] \qquad (10.28)$$

Let

$$\lambda = \frac{\omega P}{vk_2} \left(\frac{1 + k_1/k_2}{k_1/k_2} \right) = \left[\omega t - \left(\frac{k_1}{k_2} \right) \sin(\omega t) \right] \qquad (10.29)$$

The oscillatory behavior of eq. (10.29) is shown in Figure 10.9 as a diagram exhibiting two discrete values of λ. This diagram illustrates that the spring-mass system oscillates as k_1/k_2 increases. The ideal elastic case dictates that $k_1/k_2 = 0$ and load oscillations do not occur as indicated by the straight line. However, real systems are bound to experience load oscillations after the initial contact between the striker and the specimen. These oscillations are likely over a small interval of time.
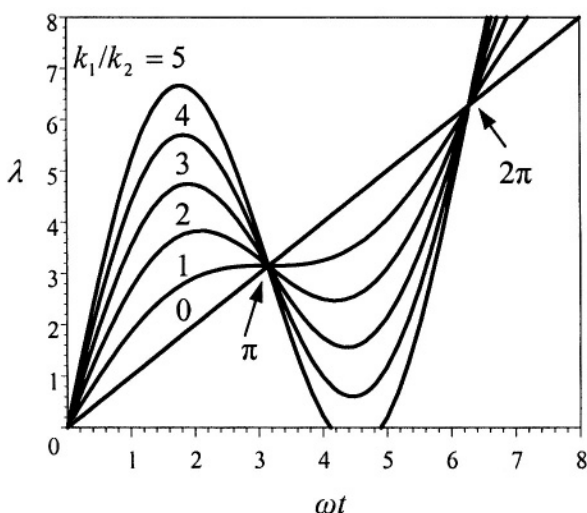
Figure 10.9 Load-time diagram showing oscillations when $k_1/k_2 > 0$.

If loss of contact occurs when the striker bounces in the opposite direction, then the impact load is zero at that instance, but impact reloading resumes in a short interval of time as shown by lines 1 through 5 in Figure 10.9. In this case, the specimen undergoes free oscillations and the dynamic behavior that describes this event is defined by the following equation of motion

$$m\ddot{u} + (k_1 + k_2)\, u = 0 \qquad (10.30)$$

The loss of contact occurs when $P = 0$ and as a result, eq. (10.28) gives

$$\omega t - \left(\frac{k_1}{k_2}\right) \sin(\omega t) = 0 \tag{10.31}$$

and

$$\omega t \simeq \pi (1 + k_2/k_1) \tag{10.32}$$

Combining eqs. (10.21a) and (10.28) and integrating the resultant expression yields the impact energy lost by the striker

$$U = \frac{k_1/k_2}{(1 + k_1/k_2)^2} \left\{ \frac{(\omega t)^2}{2} + \frac{k_1}{k_2} [1 - \cos(\omega t)] \right\} mv^2 \tag{10.33}$$

This expression illustrates that the striker kinetic energy (mv^2) is transformed into strain energy U, which is absorbed by the specimen during the impact process. However, this dynamic event exhibits an oscillation behavior to the impact response as indicated by the cosine term in eq. (10.33). Consequently, bouncing generates load oscillations and gives discrete values of energy as illustrated in Figure 10.9 where all curves coincide when $\omega t = \pi$. Thus, eq. (10.33) becomes [47]

$$\frac{U}{mv^2} = \frac{k_1/k_2}{(1 + k_1/k_2)^2} \left[\frac{\pi^2}{2} + 2 \left(\frac{k_1}{k_2}\right) \right] \tag{10.34}$$

For rigid body contact, the stiffness ratios becomes $k_2/k_1 \to 0$ or $k_1/k_2 \to \infty$ and eq. (10.34) yields a simplified form of the impact strain energy

$$U \simeq 2mv^2 \quad \text{For } \frac{k_1}{k_2} \to \infty \tag{10.35}$$

Analysis of theoretical and experimental data is a very important issue because erroneous conclusions may be drawn. For example, plotting eq. (10.33) when $k_1/k_2 \leq 1$ and $k_1/k_2 > 1$ yields different dynamic behavior, while kinetic energy is converted to strain energy as the specimen bends and slows down. The obvious significance of this observation is shown in Figure 10.10. The curves for $k_1/k_2 > 1$ coincide at $\omega t = \pi$. This is attributed to the first load oscillation since this behavior is also observed in Figure 10.9. Eventually, a second impact may occur at time predicted by eq. (10.26) for further kinetic energy transfer.
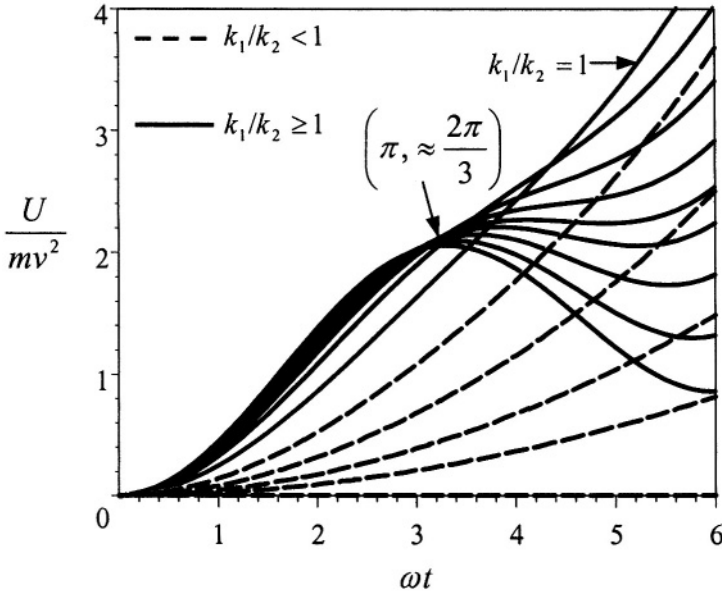
Figure 10.10 Energy ratio-time diagram ofr impact loading.

ENERGY LOSSES. Despite there are different sources of motion in an impact test, the rigid body motion is considered in the Charpy test analysis. The general overview of the striker kinetic energy (KE) transformation is depicted in Figure 10.11 [66].

The general equation for kinetic energy is [47,66]

$$U_{KE} = \frac{1}{2}\left(Mv^2 + I\omega^2\right) = Mgh + \frac{1}{2}I\omega^2 - U_w - U_f \qquad (10.36)$$

where M = Mass of the striker
I = Moment of inertia
ω = Rotational velocity
U_w = Windage energy
v = Translational velocity
U_f = Friction energy

This expression takes into account the force transmitted to the points of rotation when the center of percussion is at an eccentric point from the specimen axis of rotation, the energy losses due to windage and friction of the pendulum.
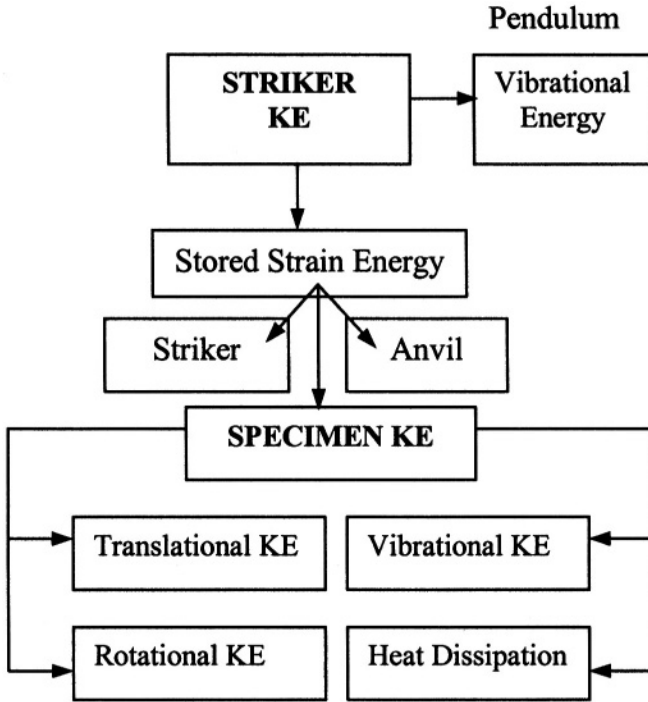
Figure 10.11 Energy conversion and energy losses.

A convenient and realistic model considers a heavy striker (large mass M) and a light specimen (small mass m) in which the displacement is due to relative motion of both bodies. The equation of motion for $M > m$ is [47]

$$m\ddot{u} + \left(1 + \frac{m}{M}\right) f_e(u) + \left(1 + \frac{m}{M}\right) f_d(\dot{u}) = 0 \qquad (10.37)$$

Here, $f_e(u)$ is the elastic constant stiffness function and $f_d(\dot{u})$ is the dissipation function. The solution of this differential equation, eq. (10.37), along with the coefficient of restitution

$$e = \frac{\text{Rebound } v}{\text{Initial Impact } v} \qquad (10.38)$$

is the kinetic energy loss of the striker, from which the strain energy absorbed by the specimen and that lost in impact are deduced as [47]

$$U_S = \left(\frac{1+e}{1+m/M}\right)\left[1 - \frac{m}{2M}\left(\frac{1+e}{1+m/M}\right)\right]mv^2 \text{ (Striker)} \quad (10.39)$$

$$U_A = \frac{1}{2}\left(\frac{1+e}{1+m/M}\right)mv^2 \quad \text{(Specimen)} \quad (10.40)$$

$$U_A \simeq \frac{1}{2}(1+e)^2 \quad \text{For } m/M \ll 1 \text{ and } 0 \le e \le 1 \quad (10.41)$$

$$U_L = \frac{1}{2}\left(\frac{1-e^2}{1+m/M}\right)mv^2 \simeq \left(\frac{1-e^2}{2}\right)mv^2 \quad \text{(Impact)} \quad (10.42)$$

10.7 DYNAMIC STRAIN-ENERGY RELEASE RATE

This section describes the fracture mechanics of impact testing and how dynamic corrections are derived, and demonstrates how impact tests are a coherent part of fracture mechanics. A basic analysis is outlined using elementary linear elastic fracture mechanics (LEFM) for mode I loading. It is possible to measure G_I concurrently with an impact test by measuring Charpy elastic strain energy U. The mathematical connection between these energies requires a dynamic correction factor ϕ. This is defined by [47]

$$G_I = \frac{U}{\phi Bw} = \frac{K_I^2}{E'} \quad (10.43)$$

The general stress intensity factor and that for a 3PB Charpy specimen are, respectively

$$K_I^2 = \frac{\pi a f^2 (a/w) P}{Bw} \quad (10.44)$$

$$K_I^2 = f^2(a/w)\left(\frac{6M}{Bw^2}\right)a = \frac{EP^2}{2B}\frac{dC}{da} \quad (10.45)$$

and the bending moment is

$$M = \frac{PS}{4} \quad (10.46)$$

where E' has been defined in eqs. (3.5), (6.34) and (8.11). Specimen variables are given in Figure (10.5). For brittle materials, this analytical procedure incorporates the Charpy elastic strain energy into G_I as deduced from Williams [47] relationships using a Charpy three-point bending (3PB) specimen. Experimentally, measure $U = f(x = a/w)$ and subsequently, plot $U = f(\phi Bw)$ to obtain $G_I = G_{IC}$ from the slope of the straight line. A particular case is shown in Figure 10.12 for a HDPE polymer.
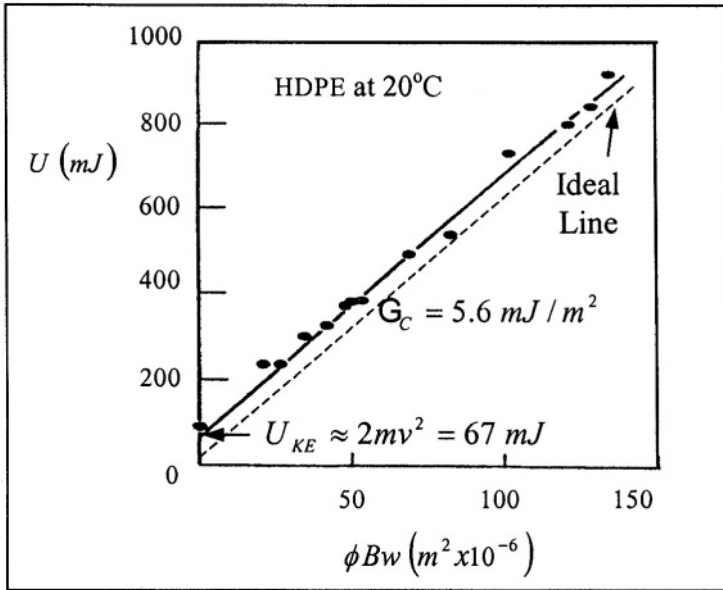
Figure 10.12 Charpy impact data on HDPE specimen showing the kinetic energy value. Data: $v = 3.36\ m/s$, $\phi \geq 4$, $\rho = 10^3\ Kg/m^3$, **L = 41 mm, B = 12 mm, and w = 6mm [47]**

The significance of this method is shown in Figure 10.12, which exhibits the apparent linearity of the strain energy. The slope of this linear plot is the critical strain-energy release rate as $G_{IC} = 5.6\ mJ/M^2$ and the intercept is to the kinetic energy of the striker $U_{KE} \simeq 2mv^2 \simeq 67\ mJ$. The energy absorbed by the HDPE specimen as strain energy is approximately

$$U_{spec} \simeq U_{KE} - U = U_{KE} - \phi BwG_{IC} \simeq U_{KE} \simeq 67\ mJ \qquad (10.47)$$

Furthermore, rearranging eq. (10.45) yields the derivative of the compliance with respect to the crack length along with $x = a/w$

$$\frac{dC}{da} = \left(\frac{9S^2}{2Bw^2E'}\right) xf^2(x) \qquad (10.48)$$

Integrating eq. (10.48) gives the total compliance

$$C = \frac{9S^2x^2f^2(x)}{4Bw^2E'} + C_o \qquad (10.49)$$

where C_o is an integration constant defined as the compliance for a crack-free specimen. Thus, [47]

$$C_o = \frac{S}{BwE'} \qquad \text{For tension loading} \qquad (10.50)$$

$$C_o = \frac{S^3}{4Bw^3E'} \qquad \text{For 3-point bending loading} \qquad (10.51)$$

From eq. (10.49), the new compliance equation is

$$\frac{dC}{dx} = \frac{9S^2 x f^2 (x)}{2Bw^2 E'} \tag{10.52}$$

$$C = \int \frac{9S^2 x f^2 (x)}{2Bw^2 E'} dx + C_o \tag{10.53}$$

Now, the energy calibration factor for a 3PB specimen is defined along with $x = a/w$ by

$$\phi = \frac{C}{dC/dx} = \frac{\int x f^2 (x)\, dx}{x f^2 (x)} + \frac{S}{18 w x f^2 (x)} \tag{10.54}$$

The geometric calibration factor, $f(x)$, for a Charpy 3PB specimen is given by Brown and Strawley [48] in polynomial form for two span-to-width ratios. The resultant polynomials for $S/w = 4$ and $S/w = 8$ are

$$f_4 (x) = 1.93 - 3.07x + 14.53x^2 - 25.11x^3 + 25.80x^4 \tag{10.55}$$
$$f_8 (x) = 1.96 - 2.75x + 13.66x^2 - 23.98x^3 + 25.22x^4 \tag{10.56}$$

Inserting eqs. (10.55) and (10.56) into (10.54) and evaluating yields 10th order polynomials which can be approximated by the following functions

$$\phi_4 \simeq \frac{2}{7\pi x} \quad \text{For } S/w = 4 \tag{10.57}$$

$$\phi_8 \simeq \frac{1}{2\pi x} \quad \text{For } S/w = 8 \tag{10.58}$$

Figure 10.13 shows the numerical result for the energy calibration factor. Denote that the functions defined by eqs. (10.57) and (10.58) give slight higher results than the polynomials at $a/w \leq 0.18$ for both $S/w = 4$ and $S/w = 8$.
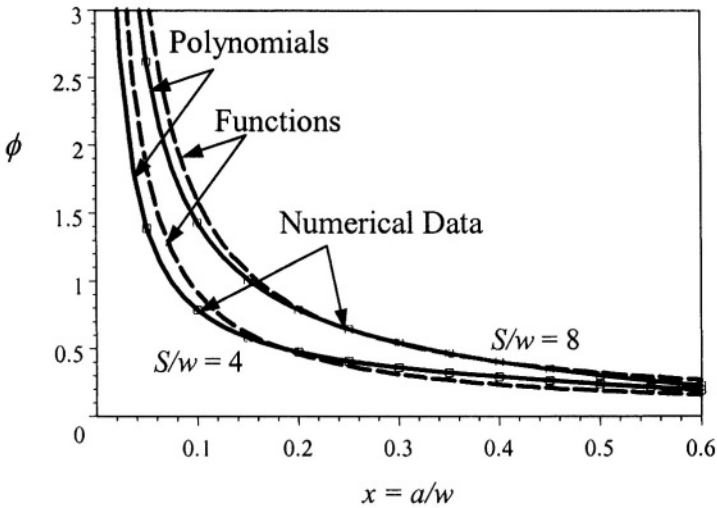
Figure 10.13 Energy calibration factor.

10.8 CORRELATIONS

Ideally, Figure 10.14 shows complete S-Shaped Curves, $U = f(T)$, for quasi-static (slow-bend) and dynamic testing conditions. Note that the dynamic ductile-to-brittle transition, known as the Nil-Ductility-Transition (NDT) Temperature, which is referred to as To, is shifted to the left for the quasi-static testing and the upper region is shifted downwards. This temperature shift in Figure 10.14 is $To* = To - \Delta T$, and it defines the upper limit of the plane-strain condition. This clearly indicates that the loading rate affects the transition region. Below the NDT point, the elastic behavior prevails, but it is strongly dependent on the notch acuity and thickness.

On the other hand, above the NDT, the elastic-plastic behavior occurs in the transition region, while a pure plastic behavior becomes asymptotic accompanied by a tearing type of fracture, and the material energy consumption is increased at relatively high temperatures. All this implies that the material behaves elastically at low temperatures (below the NDT temperature) and plastically at high temperatures. In addition, increasing the notch acuity increases the stress concentration and decreases the impact energy.

Failure analysis on brittle fracture or low energy fracture would reveal a shiny and flat surface appearance since small amounts of energy is absorbed prior to fracture due to an elastic deformation fracture mode. This type of fracture is caused by a cleavage fracture mechanism in which individual grains separate along definite crystallographic planes.
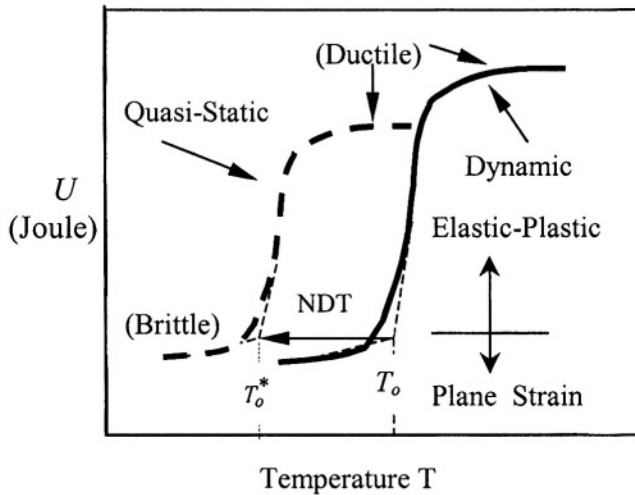
Figure 10.14 Schematic quasi-static and dynamic dynamic fracture toughness.

Brittle fracture literally indicates that only elastic flow occurs and the impact force provides the absorbed energy. However, in order for the notch to grow as crack, the structure strain energy must be released so that new crack surfaces are generated until total separation occurs. On the other hand, the ductile fracture or shear fracture has different characteristics since yielding occurs due to plastic flow, which causes a dull fibrous surface appearance. In general, the transition from ductile-to-brittle depends on the microstructure, testing temperature, strain rate, and notch acuity. This may be reflected on ductile and notch insensitivity steels, which may become brittle if tested at a relatively low temperature or at a relatively high strain rate. At the transition region, the fracture appearance is a mixture of both shiny and flat, and dull fibrous fracture surfaces. If the material has an extended degree of anisotropy and if it is tested several times at a fixed temperature in the transition region, then it may exhibit a brittle behavior at one time and ductile behavior later. Therefore, this transition behavior causes the normal wide data scatter encounter in most *BCC* low carbon steels.

Figure 10.15 illustrates the variation of the Charpy V-notch impact energy as a function of testing temperature [49]. Denote the continuous increase of this dynamic energy trend of face-centered cubic (*FCC*) aluminum , and high strength steel.. However, among many practical ferrous alloys, low carbon steels being used as structural materials, have *BCC* structures and exhibit a ductile-to-brittle transition dynamic behavior, which in turn depends on the carbon content as shown in Figure 10.16. The microstructures of these steels are composed of ferrite and pearlite phases. If the carbon content is increased, then the amount of pearlite increases.
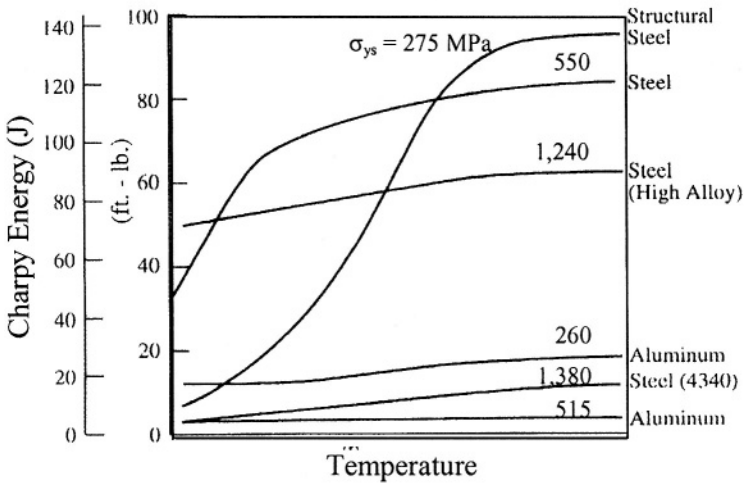
Figure 10.15 Charpy V-notch impact energy for BCC steels and FCC aluminum engineering materials [49].
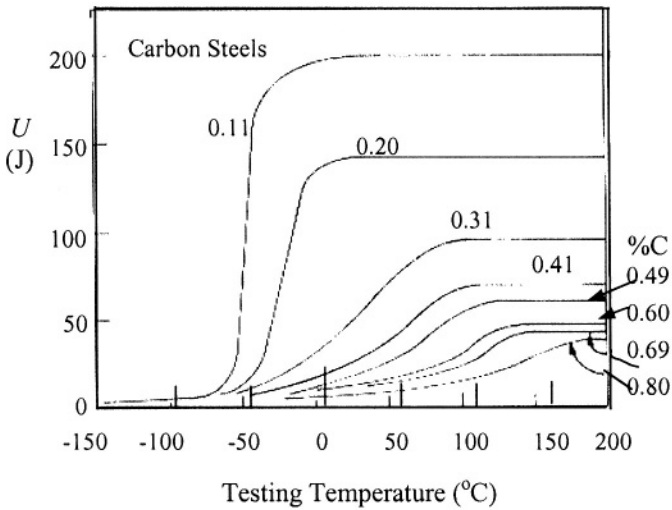
Figure 10.16 Charpy V-Notch energy vs. Temperature for carbon steels [5].

The strengthening mechanism has a strong effect on the U energy trend by increasing the transition temperature and decreasing the upper shelf energy.

In general, carbon content, alloying elements, impurities, microstructure, grain size, fabrication process, and specimen orientation influence the $U = f(T)$ behavior [50]. For instance, the eutectoid steel AISI 1080 (0.80%C) consists of 100% pearlite, which is a harder phase than ferrite, does not exhibit a transition region, making the upper shelf decrease drastically. In contrast, large amounts of ferrite phase govern the mechanical behavior of steels containing small amounts of carbon, such as the 0.11%C curve. This is clearly shown in Figure 10.16.

Moreover, Figure 10.17 shows a schematic $U = f(T)$ reference curve for a nonlinear regression procedure. Consequently, among several mathematical models that can fit U data, a model based on the hyperbolic tangent function can give reasonable results.
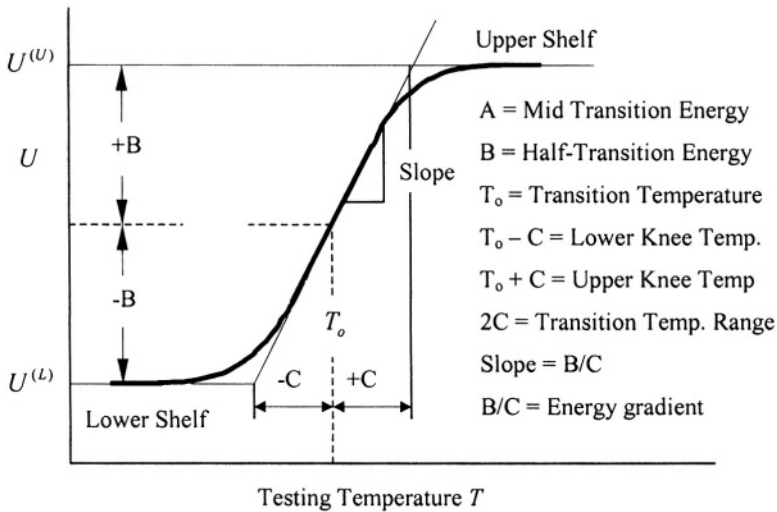
Figure 10.17 Schematic $U = f(T)$ curve showing regression parameters [51].

Oldfield [51-52] used such a function to interpret the physical meaning of the nonlinear curve fitting parameters. Thus,

$$U = A + B \tanh \left(\frac{T - T_o}{C} \right) \qquad (10.59)$$

where A, B, C, T_o = Regression parameters, which are defined in Figure 10.17

T = Testing temperature

The lower shelf energy in Figure 10.17 represents a brittle behavior in which plane strain condition should exist. Thus, brittle fracture requires a low consumption of energy. On the other hand, the upper shelf energy is a ductile

response and fracture occurs by tearing, which is a fracture process that absorbs a large amount of strain energy.

The slope of the transition region can mathematically be defined by

$$\frac{\partial U}{\partial T}\bigg|_{T=T_o} = \frac{B}{C}\sec h^2\left(\frac{T-T_o}{C}\right) = \frac{B}{C} \tag{10.60}$$

This expression yields the same definition given in Figure 10.17. Moreover, the following additional functions give good results

$$U = A + B\arctan\left(\frac{T-T_o}{C}\right) \tag{10.61}$$

$$U = \frac{D}{1 + F\exp(-ET)} \tag{10.62}$$

Figure 10.18 shows data for a 25% cold rolled (*CR*) *AST M A*710 steel and the nonlinear least squares fitting curves as per eqs. (10.59) and (10.61). The curve fitting equations along with T in $^{\circ}C$ and U in joules (J) are

$$U = 64.07 + 53.55\tanh\left(\frac{T-70.62}{10.67}\right) \tag{10.63}$$

$$U = 64.34 + 36.66\arctan\left(\frac{T-70.57}{5.38}\right) \tag{10.64}$$

$$U = \frac{119.46}{1 + 23,703.73\exp(-0.15T)} \tag{10.65}$$
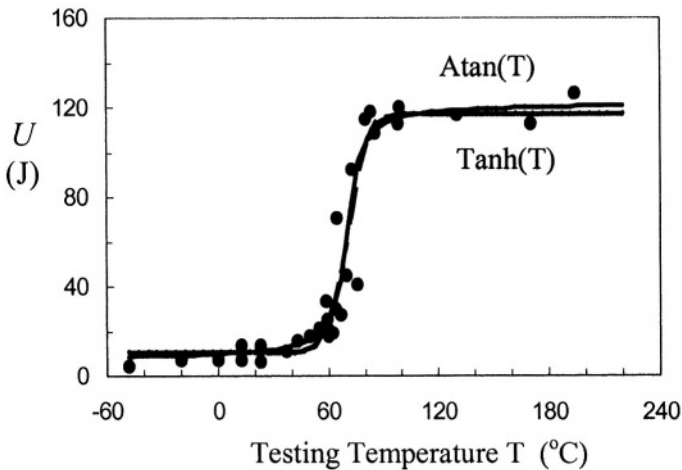
Figure 10.18 Notch-toughness of a 25%CR A710 steel.

Extensive efforts have been devoted to correlate impact fracture toughness (U) and plane strain fracture toughness (K_{IC}) data [51-61]. In fact, correlations can be derived very easily using nonlinear curve fitting. Let fracture toughness be empirically defined by

$$K_{IC} \quad = \quad A + B \tanh\left(\frac{T - T_o}{C}\right) \qquad (10.66)$$

$$K_{IC} \quad = \quad D + E \tanh\left(\frac{T - T_o}{F}\right) \qquad (10.67)$$

These two expressions give a similar S-shaped trend and the transition temperature should be the same for a particular data set. Solving eq. (10.67) for T and substituting the result expression into eq. (10.66) yields

$$K_{IC} = A + B \tanh\left[H\left(U - D\right)\right] \qquad (10.68)$$

where $H = F/(CE)$.

Since the transition temperature sets an upper limit for plane strain conditions, suitable expressions for characterizing the fracture toughness K_{IC} from the lower shelf up to T_o can readily be obtained from eqs. (10.66) and (10.68). This can be accomplished by letting the testing temperature be $T \leq T_o$.

Other empirical expressions for $U = f(T)$, $K_{IC} = f(T)$, and $K_{IC} = f(U)$ have been successfully used by Nogata and Takahashi [53] for evaluating sound and irradiated materials. In general,

$$K_{IC} = A + B \exp\left(CT\right) \qquad (10.69)$$

Combining eqs. (10.62) and (10.69) and eliminating T yields

$$K_{IC} = A + q\left(\frac{D}{U} - 1\right)^m \qquad (10.70)$$

where $m = -C/E$
$\qquad q = B/F^m$
$\qquad D = $ Upper shelf fracture toughness

This particular correlation, eq. (10.70), was suitable for evaluating pressure vessels made of ASTM A533B-1 steel [53]. Furthermore, eqs. (10.62) and (10.69) were fitted to experimental data for evaluating this particular steel. The resultant empirical equations as functions of testing temperatures (^oC) take the numerical form [53]

$$K_{IC} \quad = \quad 20 + 95.5 \exp\left(0.016T\right) \quad \text{(in } MPa\sqrt{m}) \qquad (10.71)$$

$$U \quad = \quad \frac{196}{1 + \exp\left(-0.0297T\right)} \quad \text{(in } Joules) \qquad (10.72)$$

Combining eqs. (10.57) and (10.58) to eliminate T yields [53]

$$K_{IC} = 20 + 139 \left(\frac{196}{U} - 1 \right)^{-0.54} \quad \text{(in } MPa\sqrt{m}) \qquad (10.73)$$

This expression, eq. (10.73), requires that $U \leq 196$ *joules*; otherwise, K_{IC} cannot be determined. Figure 10.19 shows the response of eq. (10.73) for the structural steel type A533B-1. Observe that there is a linear correspondence in the selected **lower shelf energy**.
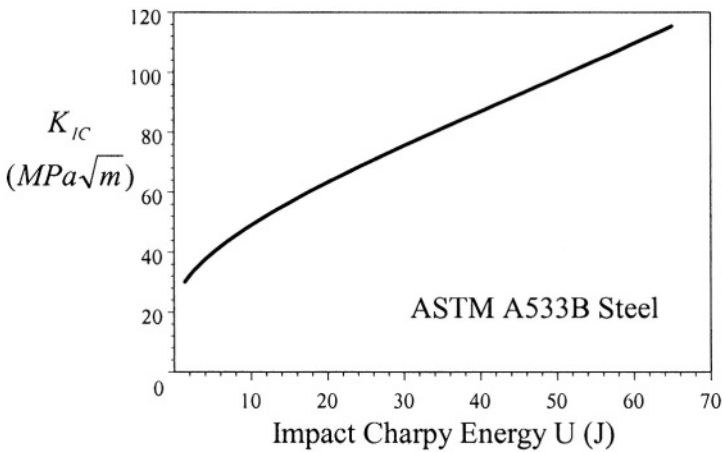
Figure 10.19 Lower shelf fracture toughness for A533B structural steel.

For the **upper energy shelf**, the fracture toughness of the ASTM A723 steel is correlated with both impact energy and yield strength [61]

$$K_{IC} = \sqrt{0.644 U \sigma_{ys} - 0.006 \sigma_{ys}^2} \qquad (10.74)$$

where U is in Joules, σ_{ys} in MPa and K_{IC} in $MPa\sqrt{m}$.

Other empirical correlations can be found in the literature. Of significance is the Hertzberg's book [62], which contains many compiled expressions in a tabular form. Ideally, K_{IC} and U correlations should correspond to the same loading rate, but quasi-static K_{IC} values can be estimated from dynamic U experimental data, taking into account the related temperature shift.

In this regard, a simple correlation for ABS-C, A302-B, and A517-F steels in the **transition region** has been reported [61,63] to give conservative results. The reported mathematical expression is of the form

$$K_{IC} = \sqrt{AEU} \qquad \text{For } \sigma_{ys} \geq 690 \ MPa \qquad (10.75)$$

where E = Modulus of elasticity (MPa)

$\quad\quad U$ is in Joules (J)

$\quad\quad A$ = 37.51 for dynamic tests (MPa/J)

$\quad\quad A$ = 46.89 for quasi-static tests (MPa/J)

For the upper shelf, which is not strongly dependent on notch acuity and loading rate, Barsom and Rolfe [61) and Rolfe and Novak [64] evaluated several medium-strength high-toughness steels listed in Table 10.1 by normalizing eq. (10.75) with the room temperature yield strength. Curve fitting such a data set yields an empirical expression with a correlation coefficient of 0.99

$$\left(\frac{K_{IC}}{\sigma_{ys}}\right)^2 = 4.69\left(\frac{U}{\sigma_{ys}}\right) - 0.20 \qquad (10.76)$$

The units of K_{IC} and U in eq. (10.76) are given in Table 10.1. Figure 10.20 shows the curve fitting results.

Table 10.1 Longitudinal mechanical properties of some steels at 27°C. The 0.2% offset method for the yield strength [49].

No	Steel	σ_{ys} (MPa)	σ_{ts} (MPa)	%EL	%RA	U (J)	K_{IC} (MPa$\sqrt{m}$)
1	A517-F	758	834	20	66	84	187
2	4147	945	1,062	15	49	35	120
3	HY-130	1,027	1,096	20	68	121	271
4	4130	1,089	1,151	14	49	31	110
5	12Ni-5Cr-3Mo	1,262	1,317	15	61	81	242
6	12Ni-5Cr-3Mo	1,282	1,324	17	67	88	249
7	18Ni-8Co-3Mo (200 Grade)	1.310	1,351	12	54	34	123
8	18Ni-8Co-3Mo (190 Grade)	1,289	1,345	15	66	66	176
10	18Ni-8Co-3Mo (190 Grade)	1,696	1,772	12	54	22	96

The valid range for each property listed in Table 10.1 is give below [49]:

$$\begin{aligned}
690 \ MPa &\leq \sigma_{ys} \leq 1,696 \ MPa \\
834 \ MPa &\leq \sigma_{ts} \leq 1,772 \ MPa \\
22 \ J &\leq U \leq 88 \ J \\
96 \ MPa\sqrt{m} &\leq K_{IC} \leq 270 \ MPa\sqrt{m}
\end{aligned} \qquad (10.77)$$
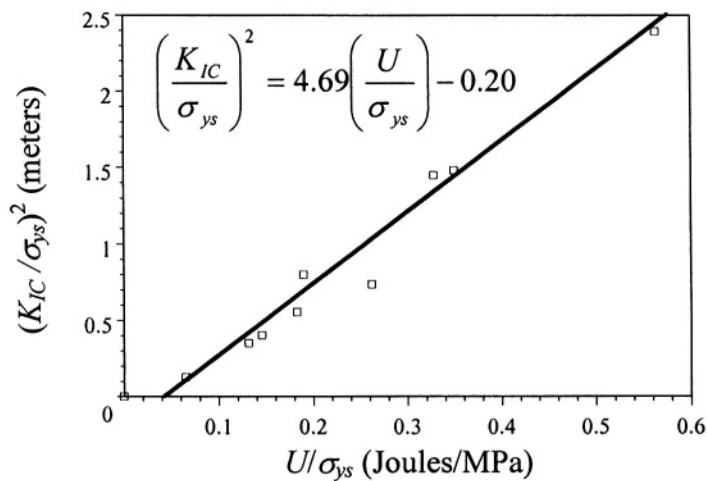
Figure 10.20 Fracture toughness correlation for the steels in Table 10.1

Plotting the $K_{IC} = f(\sigma_{ys})$ data given in Tables 3.2 and 10.1 one can determine that there is not a good correlation between these properties due to the data scatter shown in Figure 10.21. However, a good correlation is found for 4147 and 4340 steels since they have similar microstructure.
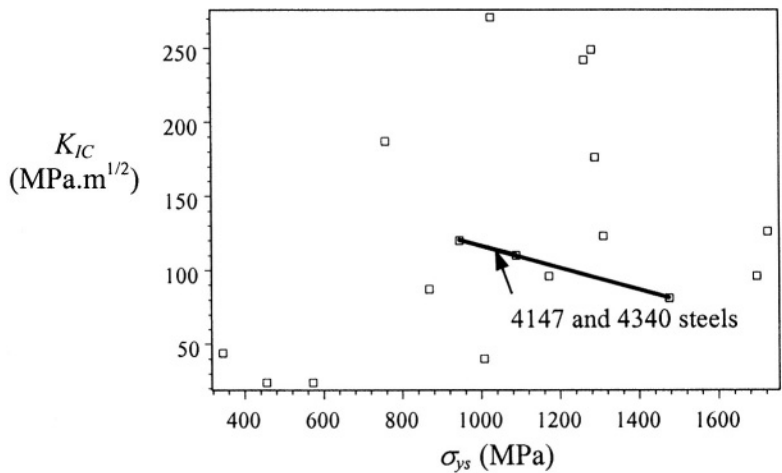
Figure 10.21 Correlation between ASTM plane strain fracture toughness and yield strength for materials given in Tables 3.2 and 10.1.

10.9   SMART HYBRID COMPOSITES

This section is devoted to composite materials because of their technological importance in manufacturing lightweight structures. Some theoretical and experimental results obtained by using the instrumented Charpy impact machine are included. The effect of low velocity imparted by the Charpy striker may be considered as a non-penetrating striker. A common low velocity impact is the event of dropping a hard and sharp tool or a falling bulk and heavy object on a substrate surface. This event may cause permanent surface damage on metals and alloys due to the irreversible plastic deformation mechanism. If the substrate is a composite laminated material, then the surface damage may be severe enough for reducing the load carrying capacity of composites or for premature failure or fracture since the type of reinforcing fiber and matrix are brittle for absorbing impact energy [65].

Figure 10.22 schematically shows a three-point bending (3PB) model indicating the possible failure mechanisms encounter in unidirectional composite bars subjected to impact bending loading at low velocity. The model indicates that the impact energy provided by an object traveling at low velocity is absorbed by the composite bar generating defects and if the plate is thin enough and sufficiently long some of the impact energy is absorbed by general bending [65]. Thus, the composite specimen damage caused by the impact is represented by delaminations, cracks and fiber breakage on the opposite side of the impact point *P* in Figure 10.22.
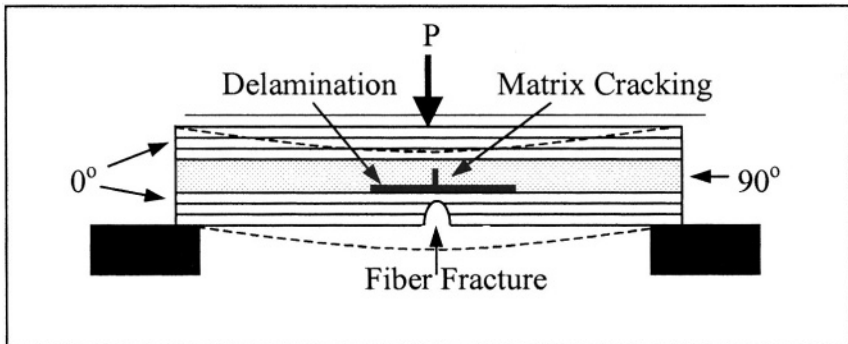
**Figure 10.22 Schematic principal failure mechanisms of a
$[0/90]_s$ unidirectional three-point bending (3PB) composite bar under bending. Delamination is due to fiber-matrix debonding for weak interface, the matrix cracking occurs due to brittle matrix, and fiber fracture forms a crack. The dashed lines represent the bending path of the composite.**

Adding tough fibers to the matrix can enhance the impact and fracture resistance of brittle composite materials. For instance, hybrid composites containing

embedded shape memory alloy (SMA containing $55Ni$-$45Ti$ or $Ni_{42}Ti_{45}Cu_{13}$) fibers or particulates into the matrix materials, such as polymers, fiber-reinforced polymers, have good impact properties due to the superelastic behavior of SMA materials.

The SMA material undergoes martensitic transformation due to high strain levels. Thus, the stress-induced martensitic transformation mechanism imparts strain energy dissipation, which suppress, to an extent, the formation of defects. Consequently, brittle composites containing SMA fibers become tough to an extent because of the strain energy dissipation upon impact loading. Nevertheless, improving the impact resistance may be accomplished at the expense of material strength.

According to Elber [1], the matrix properties govern the damage initiation and its extent and fiber properties, on the other hand, control the penetration resistance or the impact resistance. In fact, a super-elastic shape memory alloy has a remarkably high strain-to-failure primarily due to the stress-induced martensitic phase transformation creating a plateau region in the stress-strain curve and a recoverable elastic strain up to 8% [2,48]. Consequently, SMA fibers in composites absorb much more strain energy than other fibers before their failure. Thus, SMA hybrid composites become tough.

Figure 10.23 shows the relationship between the absorbed strain energy and the martensite fraction on the surface of a SMA beam under bending load. Observe that the martensitic phase transformation absorbs most of the strain energy in the structure. For a martensite fraction of 0.9%, the superelastic SMA absorbs at least twice the strain energy of the martensitic SMA [48].
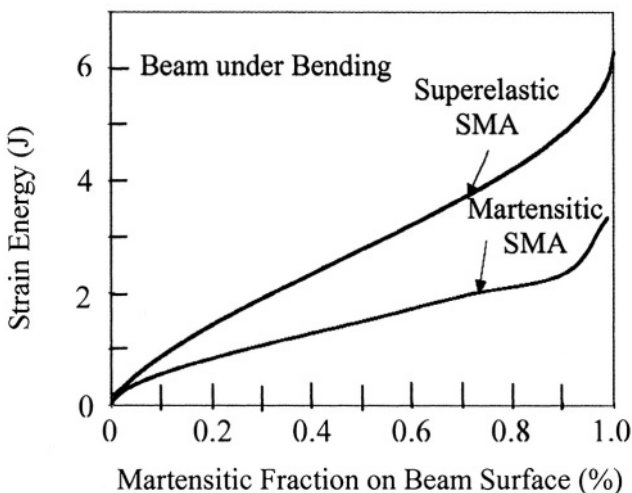
Figure 10.23 Strain energy plot for SMA [63].

With respect to impact testing, the improved energy absorption mechanism

in SMA-composites may be attributed to the small volume fraction of SMA fibers embedded in the matrix. If this is the case, the absorbed strain energy of SMA-composites is $U(T, B, SMA) > U((T, B))$, which is an indication of improved impact damage resistance of plane brittle composites at the expense of strength and stiffness [28].

10.10   PROBLEMS

10.1 a) Plot the given $U = f(T)$ data for a hypothetical steel. b) Calculate K_{IC} using the Charpy impact energy U values up to zero °C. Plot K_{IC}-cal. vs. Temperature and K_{IC}-exp. vs. Temperature. Is there a significant difference between these plots? If so, explain.

T (°C)	-125	-100	-60	-40	-12	0	10	25	40	45
U (J)	12	18	20	28	40	78	98	110	125	126
$K_{IC} - $ exp. (MPa.m$^{1/2}$)	40	50	80	88	150	210				

10.2 A mild steel plate has a through the thickness single-edge crack, a yield strength of $800\ MPa$ and a static fracture strength is $\sigma_f = 3.2\sigma_{ys}$. If the plate is loaded in tension and fractures at $600\ MPa$, calculate the plane strain fracture toughness of the steel plate and the critical crack length.

10.11   REFERENCES

[1]   R.L. Ellis, "Ballistic Impact Resistance of Graphite Epoxy Composites With Shape Memory Alloy And Extended Chain Polyethylene Spectra TM Hybrid Components," Ph.D. Dissertation, Virginia Polytechnic Institute and State University, (1996)

[2]   H. Jia, "Impact Damage Resistance of Shape Memory Alloy Hybrid Composite Structures," Ph.D. Dissertation, Virginia Polytechnic Institute and State University, Mechanical Engineering Department, May 26, 1998

[3]   W.S. Peeling, "Design Options for Selection of Fracture Control Procedures in the Modernization of Codes, Rules, and Standards," Proceedings: Joint United States–Japan Symposium on Applications of Pressure Component Codes, Tokyo, Japan. (March 1973)

[4] R.W.K. Honeycombe, "Steels: Microstructure and Properties," Edward Arnold Publisher Ltd., and American Society for Metals, (1982)

[5]   A.R. Rosenfield, G.T. Hahn, and J.D. Embury, "Fracture of Steel Containing Pearlite," Metallurgical Trans., Vol. 3, (1972) 2797-2803

[6]   D.A. Curry and J.F. Knott, "The Relationship between Toughness and Microstructure in the Cleavage Fracture of Mild Steel," Metal Science, Vol. 10, (1976) 1-5

[7]   R.O. Ritchie, J.F. Knott, and J.F. Rice, "On the Relation ship Between Critical Tensile Stress and Fracture Toughness in Mild Steel," Journal of the Mechanics and Physics of Solids, Vol. 21, (1973) 395-410

[8]   E. Orowan, Trans. Inst. Eng. Shipbuild Scot., Vol. 89, (1945)

[9]   G.T. Hahn and A.R. Rosenfield, "Experimental Determination of Plastic Constraint Ahead of a Sharp Notch under Plane-Strain Conditions," Trans. ASM, Vol. 59, (1966) 909-919

[10] F.R. Stonesifer and R.W. Armstrong, "Effect of Prior Austenite Grain Size on the Fracture Toughness Properties of A533B Steel," in Fracture 77, Vol. 2A, Edited by D.M.R. Taplin, Pergamon Press (1977) 1-5

[11] M.W. Barsoum, "Fundamentals of Ceramics," The McGraw-Hill Companies, Inc., New York, (1997) 404-405

[12] S. Palmquist, "Method of Determining the Toughness of Brittle Materials, Particularly Sintered Carbides," Jernkontorest Ann., Vol. 141 (5) (1957) 300-307

[13] G.F. Vander Voort, "Metallography: Principles and Practice," McGraw-Hill, Inc., New York, (1984) 350-389

[14] C.B. Ponton and R.D. Rawlings, "Vickers Indentation Fracture Toughness Test Part 1: Review of Literature and Formulation of Standardized Indentation Toughness Equations," Materials Sci. and Technology, Vol. 5, (Sept. 1989) 965-872

[15] C.B. Ponton and R.D. Rawlings, "Dependence of the Vickers Indentation Fracture Toughness on the Surface Crack Length," Br. Ceramic Trans. J., 88(1989) 83-90

[16] K.K. Sharma, P.N. Kotru, and B.M. Wanklyn, "Microindentation Studies of Flux-Grown ErFeO3 Single Crystals," Applied Surface Science, Vol. 81 (2) (Oct. 1994)

[17] M.T. Laugier, "Comparison of toughness in WC-Co determined by a Compact Tensile Technique with Model Predictions," J. Mat. Sci. Letters, 6 (1987) 779-780

[18] V. Milekhine, M.I. Onsoien, J.K. Solberg, and T. Skaland, "Mechanical Properties of $FeSi(\epsilon)$, $FeSi_2(\alpha)$ and Mg_2Si," Elsevier, Intermetallics, 10 (2002) 743-750

[19] G.R. Anstis, P. Chantikul, B.R. Lawn, and D.B. Marshall, J. Amer. Cer. Soc., 64(9), (1981) 533-538

[20] J. Phelps, J. Shields, X. Wang, and C.M. Agrawal, "Relationship of Fracture Toughness and Microstructural Anisotropy of Bone," Southern Biomedical Engineering Conference Proc., Sponsored by IEEE, (6-8 Feb. 1998) 23

[21] A. Iost and R. Bigot, "Reply to comment on indentation size effect: reality or artifact?" J. Mat. Sci. Letters, Vol. 17 (22) (1998) 1889-1891

[22] K.K. Sharma, P.N. Kotru, and B.M. Wanklyn, "Microindentation Studies of Flux-Grown ErFeO3 Single Crystal," Applied Surface Sci., Vol. 18 (2)

(1994) 251-258

[23] M.R. Sridhar and M.M. Yovanovich, "Empirical Methods to Predict Vickers Microhardness," Wear 193, (April 1996) 91-98

[24] G. Berces, N.Q. Chinh, A. Juhasz, and J. Lendvai, "Kinetic Analysis of Plastic Instabilities Occurring in Microhardness Tests," Acta Mat., Vol. 46 (6) (23 March 1998) 2029-2037

[25] Z. Gurdal, R.T. Haftka, and P. Hajela, "Design and optimization of laminated composite materials," Wiley-Interscience, John Wiley & Sons, Inc., (1999)

[26] R. M. Jones, "Mechanics of Composite Materials," Book News, Inc.®, Portland, OR, 2nd edition (June 1998)

[27] A. Hazizan and W.J. Cantwell, "The Low Velocity Impact Response of Foam-Based Sandwich Structures," Composites Part B: Vol. 33, No. 3, (2002) 193-204

[28] J.S.N. Paine and C.A. Rogers, "The Response of SMA Hybrid Composite Materials to Low Velocity Impact," J. Intelligent Material Systems and Structures, Vol. 5, (1994) 530-535

[29] W.J. Cantwell and J. Morton, "Geometrical Effects in the Low Velocity Response of CFRP," Composite Structures, Vol. 12, (1989) 39-59

[30] L.J. Broutman and A. Rotem, "Impact Strength and Toughness of Fiber Composite Material," ASTM STP 568, (1975) 114-133

[31] J.C. Aleszka, "Low Energy Impact Behavior of Composite Panels," J. Test. Eval., 6 (3) (1978) 202-210

[32] M.P. Manahan, "In-situ Heating and Cooling of Charpy Test Specimens," ASTM STP 1380, (1999)

[33] R.L. Ellis, F. Lalande, H. Jia and C.A. Rogers "Ballistic Impact Resistance of SMA and Spectra Hybrid Graphite Composites," J. Reinf Plast and Compos, Vol. 17, 2 (1998) 147-164

[34] J.G. Hetherington and P.F. Lemieux, "The Effect of Obliquity on the Ballistic Performance of Two Component Composite Armour," Int. J. Impact Engng Vol. 15, No. 2, (1994) 131-137

[35] J.D. Walker and C.E. Anderson, Jr., "The Influence of Initial Nose Shape in Eroding Penetration," Int. J. Impact Engng Vol. 15, No. 2, (1994) 139-148

[36] W.J. Cantwell and J. Morton, "Comparison of the Low and High Velocity Impact Response of CFRP," Composites, Vol. 20, No. 6 (1989) 545-551

[37] M.P. Manahan and R.B. Stonesifer, "Studies Toward Optimum Instrumented Striker Designs," MPM Technologies, Inc., State College, PA 16803

[38] H.W. Hayden, W.G. Moffatt, and J. Wulff, "The Structure and Properties of Materials," Vol. III, Mechanical Behavior, John Wiley & Sons, (1965)

[39] MPM Technologies, Inc., www.mpmtechnologies.com, (2003)

[40] M.P. Manahan, "Advances in Notched Bar Impact Testing," ASTM Standardization News, (October 1996) 23-29

[41] H.J. Schindler, T. Varga, H. Njo, and G. Prantl, "Key Issues of Instrumented Pre-cracked Charpy-Type Testing in Irradiation Surveillance Pro-

grams," Proc. Int. Symposium on Materials Aging and Component Life Extension, Milan, Italy, Vol. II, (10-13 October 1995) 1367-1377

[42] H.J. Schindler, "The Use of Instrumented Pre-cracked Charpy Specimens," Engineering Integrity Assessment Evaluating Material Properties by Dynamic Testing, ESIS 20, Mechanical Engineering Publications, London, (1996) 45-58

[43] H.J. Schindler, "Estimation of the Dynamic JR Curve from a Single Impact Bending Test," Proc. ECF 11 – Mechanical and Mechanics of Damaged and Failure, Vol. II, Editor J. Petit, EMAS Publishing, (1996) 2007-2012

[44] H.J. Schindler and M. Veidt, "Fracture Toughness Evaluation from Instrumented Sub-size Charpy-Type Tests," ASTM STP 1329, (1997) 48-62

[45] W. Böhme and H.J. Schindler, "Application of Single-Specimen Methods on Instrumented Charpy Tests: Results of DVM Round-Robin Exercises," ASTM STP 1380, (1999) 327-336

[46] H.J. Schindler, "Preferable Initial Length for Fracture Toughness Evaluation Using Sub-sized Bend Specimens," ASTM STP 1418, (2002) 67-79

[47] J.G. Williams, "Fracture Mechanics of Polymers," Ellis Horwood Limited Publishers, Halsted Press a division of John Wiley & Sons, New York, (1984)

[48] W.F. Brown and J.E. Strawley, ASTM STP 410, (1966)

[49] J.M. Barsom and S.T. Rolfe, "Fracture and Fatigue in Structure: Application of fracture Mechanics," Third edition, American Society for Testing and Materials Philadelphia, PA, (1999)

[50] Metals Handbook, Edited by H.E. Boyer and T.L. Gall, American Society for Metals (ASM) (1985)

[51] W. Oldfield, "Curve Fitting Impact Test Data: A Statistical Procedure," ASTM Standardization News, Vol. 3, No. 11, (Nov. 1975) 24-29

[52] W. Oldfield, "Fitting Curves to Toughness Data," J. Testing and Evaluation, JTEVA, Vol. 7, No. 6, (Nov. 1979) 326-333

[53] F.N. Nogata and H. Takahashi, "Fracture Mechanics Evaluation of Irradiated Embrittlement in Reactor Vessel Steels Based on the Rate Process Concept," J. Testing and Evaluation, JTEVA, Vol. 14, No. 1, (Jan. 1986). 40-48

[54] J.D. Varsik and S.T. Byrne, "An Empirical Evaluation of the Irradiation Sensitivity of Reactor Pressure Vessel Materials," ASTM STP 683, (1979) 252-266

[55] R.H. Sailors and H.T. "Relationship Between Material Fracture Toughness Using Fracture Mechanics and Transition Temperature Tests," ASTM STP 514 (1972) 164-191

[56] S. Tauscher, "The Correlation of Fracture Toughness with Charpy V-Notch Impact Test Data," USA ARRADCOM Technical Report ARLCB-TR-81012, Benet Weapons Laboratory, Watervliet, NY, (March 1977)

[57] J.A. Kapp and J.H. Underwood, "Correlations between Fracture Toughness, Charpy V-Notch, and Yield Strength for ASTM A723 Steel," ASME, Pressure Vessels & Piping Division, (June 21-25, (1992) 219-221

[58] B. Nageswara and A.R. Acharya, "Comparative Study on Evaluation of Fracture Toughness from Charpy V-Notch Impact Energy and Reduction in Area," Eng. Fracture Mechanics (Jan. 1992) 85-90

[59] J.H. Underwood and G.S. Leger, "Fracture Toughness of High Strength Steel Predicted from Charpy Energy or Reduction in Area," ASTM STP 833, (1984) 481-498.

[60] S.T. Rolfe, W.A. Sorem, and G.W. Wellman, "Fracture Control in the Transition-Temperature Region of Structural Steels," J. Constructional Steel Res. (1989) 171-195

[61] J.M. Barsom and S.T. Rolfe, "Correlations Between K_{IC} and Charpy V-Notch Test Results in the Transition-Temperature Range," ASTM STP 466, (1970) 281-302

[62] R. W. Herztberg, "Deformation and Fracture Mechanics of Engineering Materials," Third Edition, John Wiley & Sons, Inc., (1989)

[63] J.M. Barsom, "The Development of AASHTO Fracture Toughness Requirements for Bridge Steels," Engineering Fracture Mechanics, Vol. 7, No. 3, (Sept. 1975) 605-618

[64] S.T. Rolfe and S.R. Novak, "Slow-Bend K_{IC} Testing of Medium Strength High-Toughness Steels," ASTM STP 463 (1970) 124-159

[65] W. Elber, "Effect of Matrix and Fiber Properties on Impact Resistance," Tough Composite Materials: Recent developments, Noyes, Park Ridge, NJ, (1985) 89-110

[66] M.P. Manahan and R.B. Stonesifer, "The Difference Between Total Absorbed Energy measured Using an Instrumented Striker and that Obtained Using an Optical Encoder," ASTM STP 1380, (1999)

Appendix A

METRIC CONVERSIONS

Table A-1 Prefixes

Factor	Prefix	SI Symbol
10^{18}	exa	E
10^{15}	peta	P
10^{12}	tera	T
10^{9}	giga	G
10^{6}	mega	M
10^{3}	kilo	k
10^{-3}	milli	m
10^{-6}	micro	μ
10^{-9}	nano	n
10^{-12}	pico	p
10^{-15}	femto	f
10^{-18}	atto	a

Table A-1 Physical constants

Avogadro's number	$N_A = 6.023 \times 10^{23}$ atom/mol
Boltzmann's constant	$k = 1.38 \times 10^{-23}$ J/atom°K
Gas constant	$R = 8.315$ J/°K.mol
Plank's constant	$h = 6.63 \times 10^{-34}$ J.s

Length	
$1 \text{ m} = 10^{10} \text{ Å}$	$1 \text{ Å} = 10^{-10} \text{ m}$
$1 \text{ m} = 10^9 \text{ nm}$	$1 \text{ nm} = 10^{-9} \text{ m}$
$1 \text{ m} = 10^6 \,\mu\text{m}$	$1 \,\mu\text{m} = 10^{-6} \text{ m}$
$1 \text{ m} = 10^3 \text{ mm}$	$1 \text{ mm} = 10^{-3} \text{ m}$
$1 \text{ m} = 10^2 \text{ cm}$	$1 \text{ cm} = 10^{-2} \text{ m}$
$1 \text{ m} = 3.28 \text{ ft}$	$1 \text{ ft} = 0.3049 \text{ m}$
$1 \text{ m} = 39.36 \text{ in}$	$1 \text{ in} = 0.0275 \text{ m}$
$1 \text{ cm} = 10 \text{ mm}$	$1 \text{ mm} = 0.10 \text{ cm}$
$1 \text{ cm} = 3.28\text{x}10^{-2} \text{ ft}$	$1 \text{ ft} = 30.48 \text{ cm}$
$1 \text{ cm} = 0.394 \text{ in}$	$1 \text{ in} = 2.54 \text{ cm}$
$1 \text{ mm} = 3.28\text{x}10^{-3} \text{ ft}$	$1 \text{ ft} = 304.8 \text{ mm}$
$1 \text{ mm} = 3.94\text{x}10^{-2} \text{ in}$	$1 \text{ in} = 25.4 \text{ mm}$

Area	
$1 \text{ m}^2 = 10^{20} \text{ Å}^2$	$1 \text{ Å}^2 = 10^{-20} \text{ m}^2$
$1 \text{ m}^2 = 10^{18} \text{ nm}^2$	$1 \text{ nm}^2 = 10^{-18} \text{ m}^2$
$1 \text{ m}^2 = 10^{12} \,\mu\text{m}^2$	$1 \,\mu\text{m}^2 = 10^{-12} \text{ m}^2$
$1 \text{ m}^2 = 10^6 \text{ mm}^2$	$1 \text{ mm}^2 = 10^{-6} \text{ m}^2$
$1 \text{ m}^2 = 10^4 \text{ cm}^2$	$1 \text{ cm}^2 = 10^{-4} \text{ m}^2$
$1 \text{ m}^2 = 10.76 \text{ ft}^2$	$1 \text{ ft}^2 = 9.29\text{x}10^{-2} \text{ m}^2$
$1 \text{ m}^2 = 1.55\text{x}10^3 \text{ in}^2$	$1 \text{ in}^2 = 6.45\text{x}10^{-4} \text{ m}^2$

Volume	
$1 \text{ m}^3 = 10^{27} \text{ nm}^3$	$1 \text{ nm}^3 = 10^{-27} \text{ m}^3$
$1 \text{ m}^3 = 10^{18} \,\mu\text{m}^3$	$1 \,\mu\text{m}^3 = 10^{-18} \text{ m}^3$
$1 \text{ m}^3 = 10^9 \text{ mm}^3$	$1 \text{ mm}^3 = 10^{-9} \text{ m}^3$
$1 \text{ m}^3 = 10^6 \text{ cm}^3$	$1 \text{ cm}^3 = 10^{-6} \text{ m}^3$
$1 \text{ m}^3 = 35.20 \text{ ft}^3$	$1 \text{ ft}^3 = 2.83\text{x}10^{-2} \text{ m}^3$
$1 \text{ m}^3 = 6.10\text{x}10^4 \text{ in}^3$	$1 \text{ in3} = 1.64\text{x}10^{-8} \text{ m}^3$
$1 \text{ cm}^3 = 3.53\text{x}10^{-5} \text{ ft}^3$	$1 \text{ ft}^3 = 2.83\text{x}10^4 \text{ cm}^3$
$1 \text{ cm}^3 = 6.010\text{x}10^{-2} \text{ in}^3$	$1 \text{ in}^3 = 16.39 \text{ cm}^3$
$1 \text{ cm}^3 = 2.642\text{x}10^{-4} \text{ gal (US)}$	$1 \text{ gal (US)} = 3.79\text{x}10^3 \text{ cm}^3$
$1 \text{ liter (l)} = 10^3 \text{ cm}^3$	$1 \text{ cm}^3 = 10^{-3} \text{ liter}$
$1 \text{ liter (l)} = 0.2642 \text{ gal (US)}$	$1 \text{ gal (US)} = 3.785 \text{ liters}$

Mass	
$1 \text{ Kg} = 10^3 \text{g}$	$1 \text{ g} = 10^{-3} \text{ Kg}$
$1 \text{ Kg} = 2.205 \text{ lb}_m$	$1 \text{ lb}_m = 0.454 \text{ Kg}$
$1 \text{ g} = 2.205\text{x}10^{-3} \text{ lb}_m$	$1 \text{ lb}_m = 454 \text{ g}$
$1 \text{ g} = 3.53\text{x}10^{-2} \text{ oz}$	$1 \text{ oz} = 28.35 \text{ g}$
$1 \text{ lb}_m = 16 \text{ oz}$	$1 \text{ oz} = 6.25\text{x}10^{-2} \text{ lb}_m$

Density	
$1\ Kg/m^3 = 10^{-3}\ g/cm^3$	$1\ g/cm^3 = 10^3\ Kg/m^3$
$1\ Kg/m^3 = 0.0624\ lb_m/ft^3$	$lb_m/ft^3 = 16.03\ Kg/m^3$
$1\ Kg/m^3 = 3.61 \times 10^{-5}\ lb_m/in^3$	$lb_m/in^3 = 2.77 \times 10^4\ Kg/cm^3$
$1\ g/cm^3 = 0.0361\ lb_m/in^3$	$lb_m/in^3 = 27.70\ g/cm^3$

Force	
$1\ N = 1\ Kg.m/sec^2$	$1\ dyne = 1\ g.cm/sec^2$
$1\ N = 10^5\ dynes$	$1\ dyne = 10^{-5}\ N$
$1\ N = 0.2248\ lb_f$	$1\ lb_f = 4.448\ N$
$1\ dyne = 2.248 \times 10^{-6}\ lb_f$	$1\ lb_f = 4.448 \times 10^5\ dyne$

Stress	
$1\ MPa = 0.145\ ksi$	$1\ ksi = 6.895\ MPa$
$1\ MPa = 145\ psi$	$1\ psi = 6.90 \times 10^{-3}\ MPa$
$1\ MPa = 0.1019\ Kg_f/mm^2$	$1\ Kg_f/mm^2 = 9.81\ MPa$
$1\ MPa = 7.25 \times 10^{-2}\ Ton_f/in^2$	$1\ Ton_f/in^2 = 13.79\ MPa$

Energy	
$1\ J = 10^7\ ergs$	$1\ erg = 10^{-7}\ J$
$1\ J = 6.24 \times 10^{18}\ eV$	$1\ eV = 1.60 \times 10^{-19}\ J$
$1\ J = 0.239\ cal$	$1\ cal = 4.184\ J$
$1\ J = 9.48 \times 10^{-4}\ Btu$	$1\ Btu = 1054\ J$
$1\ J = 1.3558\ ft.lb_f$	$1\ ft.lb_f = 0.7376\ J$
$1\ cal = 3.97 \times 10^{-3}\ Btu$	$1\ Btu = 252\ cal$

Fracture Toughness	
$1\ MPa\sqrt{m} = 0.91\ ksi\sqrt{in}$	$1\ ksi\sqrt{in} = 1.10\ MPa\sqrt{m}$
$1\ MPa\sqrt{m} = 910\ psi\sqrt{in}$	$1\ psi\sqrt{in} = 1.10 \times 10^{-3}\ MPa\sqrt{m}$
$1\ ksi\sqrt{in} = 10^3\ psi\sqrt{in}$	$1\ psi\sqrt{in} = 10^{-3}\ ksi\sqrt{in}$

A.1   FRACTURE TOUGHNESS DATA

The average data below can be foundelsewhere [1-3]

Table B-1 Mechanical Properties [1-3]

Material	Temp.	σ_{ys} (MPa)	K_{IC} (MPa$\sqrt{m}$)
Steel			
AISI 1045	$-4°C$	269	50
AISI 4340	RT	1,567	57
AISI 4340	RT	1,408	85
D6AC	RT	1,495	93
HP 9-4-20	RT	1,295	143
18Ni (200)	RT	1,450	110
18Ni (300)	RT	1,931	74
ASTM A538	RT	1,722	111
Aluminum Alloys			
2020-T651	RT	532	25
2024-T351	RT	378	38
2024-T851	RT	450	26
6061-T651	RT	296	28
6061-T651	$-80°C$	310	33
7075-T651	RT	538	29
7075-T7351	RT	428	33

[1] H.O. Fuchs and R.I. Stephens, "*Metal Fatigue in Engineering*", John Wiley, NY, 1980

[2]   J.A. Collins, "*Failure of Materials in Mechanical Design: Analysis, Prediction, Prevention,*" John Wiley & Sons, New York, (1981)

[3]   R.W. Hertz berg, "*Deformation and Fracture Mechanics of Engineering Materials*", third edition, John Wiley & Sons, New York, (1989)

Index